The University Of Sheffield.

Fabrication of Calcium Phosphate Scaffolds via Honeycomb Extrusion

By:

Mohammed Elbadawi

A thesis submitted in partial fulfilment of the requirements for the degree of Doctor of Philosophy

The University of Sheffield
Faculty of Engineering
Department) of Mechanical Engineering

August 2018

Acknowledgements

I would like to thank my project supervisors Dr. James Meredith and Prof. Ian Reaney for their continued guidance and inspiration. I would like to thank many of the staff as their assistance was very much appreciated. Thanks go to Michael Jackson, Richard Kay, Austin Lafferty, Lisa Holland, Dean Haylock, Ben Palmer, Michael Bell, Andrew Mould, Robert Moorehead and The Sorby Centre staff for going above and beyond your duty.

Thanks also go to my colleagues Lynne, Hande, Rod, Ben, Phil, Whitney, Jen, Zuheir, Edgar, Ed and Altair, and the many more in G-floor and J-loor. I am privileged to have worked beside you all. Special thanks to Carl, Moss and Shbeh. I hope our collaborations continue for many years to come.

Above all, I wish to thank my family as this PhD would not be complete without their support.

Declarations

This thesis represents my original research work. Where others have contributed, their content was duly acknowledged in the text. I declare the following publications related to this project:

‘Progress in Bioactive Metal and Ceramic Implants for Load-Bearing Application’ by M. Elbadawi, J. Meredith, L. Hopkins and I. Reaney

DOI: 10.5772/62598

‘Porous hydroxyapatite scaffolds fabricated from nano-sized powder via honeycomb extrusion’ by M. Elbadawi, J. Meredith. M.Mosalagae and I. Reaney

DOI: 10.5185/amlett.2016.7063

‘Guar gum: A novel binder for ceramic extrusion’ by M. Elbadawi, M. Mosalagae, I. Reaney and J. Meredith

DOI: 10.1016/j.ceramint.2017.09.066

‘High strength yttria-reinforced HA scaffolds fabricated via ceramic honeycomb extrusion’ by M. Elbadawi and M. Shbeh

DOI: 10.1016/j.jmbbm.2017.10.09

‘Porous hydroxyapatite-bioactive glass hybrid scaffolds fabricated via ceramic honeycomb extrusion’

Accepted – Journal of American Ceramic Society

‘Investigation of the processing and biocompatibility of Ti-HA biocomposite foams’

Submitted

Mohammed Elbadawi

Abstract

For Hydroxyapatite (HA) bone graft substitutes, the choice of fabrication technique is an important aspect of design. Using HA ceases concerns with regards to biocompatibility, however other facets of design need to be addressed, particularly achieving high porosity and high mechanical properties. These two facets are mutually exclusive, however, if porosity can be achieved in a controlled manner, then it is possible for them to coincide. Honeycomb extrusion is a technique capable of achieving the aforementioned feat, with the added advantage of a high degree of pore interconnectivity. Extrusion is also relatively simple, inexpensive, and can achieve large-sized scaffolds. Thus, it was hypothesised that the aforementioned advantages can be translated to bone tissue engineering.

Dynamic mechanical analysis revealed that ceramic pastes formulated using guar gum and Methocel™ (MC) binders, required a shear modulus of 10^{-1} and 10^{1} MPa, respectively, for extrusion. A higher solids loading was achieved with MC, by 7.6 vol%, and accordingly was used for further studies. The extrusion setup favoured calcined powders for maximising scaffold compressive strength. Initially, a calcined β-tricalcium (β-TCP) and uncalcined HA scaffolds has compressive strengths of 23.6 ± 5.7 and 29.8 ± 8.6 MPa, respectively. When HA was calcined, the strength soared to 105.9 ± 12.2. Calcined powders were less susceptible to both agglomeration and enhanced densification, which resulted in higher solids loading and a higher thermal stability. The calcined powders all possessed a surface area < 10 m^2/g, which was regarded as the ideal value to ensure sufficient binder coating of the ceramic primary particles.

HA was also composited with 10 wt% Bioglass® (BG) and 10 wt% canasite glass (CAN), which have been documented to possess improved biological properties over the ceramic. A maximum compressive strength of 30.3 ± 3.9 and 11.4 ± 3.1 MPa, for BG and CAN, respectively, were achieved, and hence revealed that BG was the stronger compositing glass. The calcium oxide (CaO) content in raw BG was then increased by 5 wt%, which resulted in a maximum strength of 56.7 ± 6.9 MPa. The increased CaO was found to lessen the effect of glass-induced HA phase transformation into the mechanically weaker β-TCP, from a β-TCP:HA ratio of 1.01 to 0.84, as determined by XRD; and thus demonstrating that a 5 wt% change was able to have a profound effect on scaffold strength. The compressive strength values obtained herein are a considerable improvement on traditional and commercially-available products, thereby demonstrating the potential of honeycomb extrusion for fabricating porous scaffolds.

Table of Contents

List of Figures

List of Tables

Chapter 1: Project Introduction

The present thesis details the investigation into the use of ceramic honeycomb extrusion for the fabrication of bone graft substitutes. The motivation for this study was the fact that the demand for bone replacement far exceeds the current supply of transplantable tissue; the consequences of which vary from a reduced quality of life to mortality. A concerted effort has been devoted by the scientific, engineering and medical community to develop strategies to address this challenge. One approach that has garnered much attention is the use of synthetic materials to produce scaffolds for tissue engineering. These vary in material class (e.g. polymer, metal, ceramic) and in design (dense, porous scaffold, granules), and hence there are a myriad of options to pursue as research topics. However, as our knowledge of bone and fracture healing develops, ceramics, namely calcium phosphates, have been highlighted as possessing a great potential for addressing the aforementioned issue.

The principal component of the mineral phase of bone is hydroxyapatite (HA), a form of calcium phosphates (CaP) that can be easily synthesised in the laboratory. Laboratory-synthesised HA induces bone growth and can degrade within the body. Such feats are desirable as HA can expedite the healing process and be removed from the body without having to perform a second surgery, thereby obviating further surgery-associated risks. Bioactive glasses also possess these inherent biological properties.

Honeycomb extrusion, the fabrication process in which materials are forced through a given orifice, was selected as the fabrication route herein because of the additional benefits that can be conferred upon CaP scaffolds. By using a die with a honeycomb design, a reciprocal honeycomb structure can be fashioned, whereby the added open and interconnected porosity is expected to enhance biological properties. Furthermore, imparting porosity hastens bioresorbability as less material needs to be resorbed. In addition to porosity, extrusion has been reported to yield high strength, an existing constraint of HA scaffolds fabricated through traditional routes. This technique has been extensively used for the fabrication of cordierite catalytic supports for catalytic convertors, in which the fabrication technique has demonstrated its necessity and utility

therein. However, the use of ceramic honeycomb extrusion for bone graft substitutes has not thoroughly been explored, and there lies the basis for the current investigation.

This research branches out from prior work in that it investigated the effects of binders, particle properties and HA-bioactive glass composites on honeycomb extruded scaffolds: all of which resulted in original findings. Binders are polymers used to impart plasticity to a particulate system, thus allowing it to be shaped. Particle properties were explored as they are key determinants of the final properties of scaffolds. Finally, composites were examined to further enhance the already exceptional properties of HA.

The thesis is structured in the following manner. The aims and objectives of the project are outlined in section **1.1**. A background to the research project is given in **Chapter 2**, covering the biological properties of bones in order to understand how synthetic materials can be used to exploit their healing properties. **Chapter 3** specifies the characterisation techniques used herein. **Chapter 4** details the fabrication stages used for the present work. **Chapter 5, Chapter 6**, and **Chapter 7** are results chapters, each investigating the effects of different raw materials on the final scaffold products. **Chapter 8** contains both the concluding remarks, limitations and recommendations for future work.

1.1 Aims and Objectives of the Project

The overall aim of this project was to explore the means of achieving high-strength scaffolds fabricated by ceramic honeycomb extrusion. In order to achieve this aim, the following objectives were pursued:

- **Identify suitable binders capable of formulating ceramic pastes suitable for extrusion.**

  The objective here is to use a binder that permits a high ceramic solids loading, and both easy- and clean-burnout without leaving residues that are crack-inducing.

- **Optimise the extrusion process.**

Exploring different extrusion parameters and their effects on the quality of the extrudate, including extrusion speed, travel distance and pre-extrusion conditions.

- **Optimising the thermal treatments following extrusion.**
  Once extruded, the green body requires a careful thermal treatment to prevent the formation of defects. The objective here is to seek a balance between obtaining a defect-free scaffold and fast processing. In addition, the sintering temperature affects both mechanical strength and biological properties; hence the ideal sintering temperature, which will depend on the raw material, will need to be determined. Factors that limit the use of high sintering temperatures include grain growth, chemical phase transformation, and defect formation.

- **To determine the effects of the raw ceramic powders.**

  The final product for most powder fabrication techniques is affected by the raw powders selected. Although it has been acknowledged that key powder properties include particle morphology and chemical purity, the ideal characteristics are inconclusive, and are likely to vary for each fabrication technique. For example, previous work has identified that nano-particles lead to better mechanical properties, whereas other work has reported macro-particles yielded higher mechanical strengths. Such properties have not been explored for ceramic honeycomb extrusion, and hence research will need to be performed to determine the optimal powder characteristics.

- **To fabricate a ceramic-glass composite scaffold.**
  One means of enhancing the mechanical properties of ceramics is to add glass that can result in liquid-phase sintering. Thus, if this can be achieved with bioactive-glass, then two benefits would be obtained: enhanced mechanical properties and enhanced biological activity. Hence, research was undertaken into determining the feasibility of fabricating HA-bioactive glass composites using ceramic honeycomb extrusion.
- **To collate of the results and draw a pertinent conclusion to assess the necessity and utility of ceramic honeycomb extrusion for the fabrication of synthetic bone graft substitutes.**

Chapter 2: Background

1.1 Introduction

The chapter serves as a backdrop to the project. An overview of bone physiology is provided in order for the reader to understand the healing capacity of bone and how it can be exploited through the use of synthetic materials. The chapter then provides information that will rationalise the use of honeycomb ceramic extrusion for fabricating porous calcium phosphate scaffolds.

2.1 The Skeleton and Bone Physiology

2.1.1 The Skeleton

The role of the skeleton is to maintain physical support for the rest of the body, allow movement and locomotion by functioning as levers for muscles, protection of vital organs and other tissues, and serves as a reservoir for calcium and haematopoiesis formation [1].The skeleton consists of over 200 bones that are anatomically classed into the following groups: long bones, short bones, flat bones, and irregular bones [1]. Short bones provide strength and compactness, as well as providing some movement, and include the patellae, tarsal and carpal bones, and sesamoid bones. Flat bones, which have a protective role, include the skull, mandible and ribs. Irregular bones comprise the vertebrae, sacrum and hyoid bone. Long bones are found in limbs where their main role is providing locomotion, and include the radii, humeri, fibula, tibia and femurs. Flat bones are formed by membranous bone formation, whereas long bones are formed by a combination of endochondral and membranous bone formation. [2]. **Figure 2-1** portrays examples of the different classes of bones.

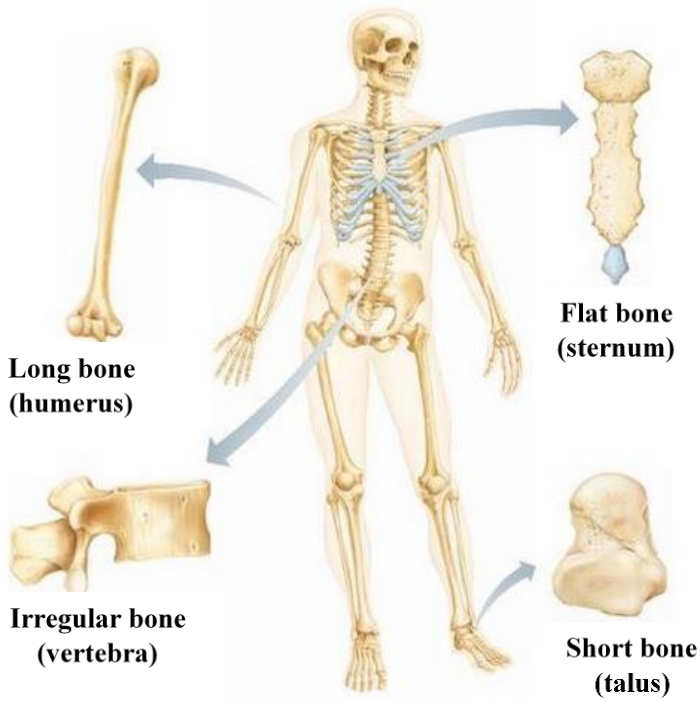

Figure 2-1. *Bone groups as classified by shape, which are long bone, short bone, flat bone and, for those that cannot be classed in the aforementioned group, irregular bone; The different anatomical structure serves a functional purpose. Adapted from ref. [3].*

1.1.1.1 Gross Anatomy of Long Bone

Long bones are an example of bones that bear load during locomotion, and **Figure 2-2** illustrates the components thereof. A long bone comprises a shaft and two extremities. The central long tubular shaft is called the diaphysis, and the two extremities are called the epiphysis, and the area delineating the diaphysis from the epiphysis is the metaphysis. The diaphysis is narrowed to afford greater space for the bellies of muscles; and curved, which is theorised to counteract bending by distributing stresses, and thus affording greater strength to the bone [1]. The diaphysis is primarily composed of dense bone with a hollow region called the medullary canal, which is filled with yellow marrow that is responsible for producing cartilage, bone and white blood cells [1].

The epiphysis and metaphysis consist of spongy bone encased by a relatively thin layer of dense bone. The spongy and dense bones are, respectively, referred to as trabecular and cortical bone. Trabecular bone is composed of a predominantly porous, honeycomb-like structure, whereas the cortical bone is markedly dense. The adult human skeleton is composed of 80% cortical bone and 20% trabecular bone [4].

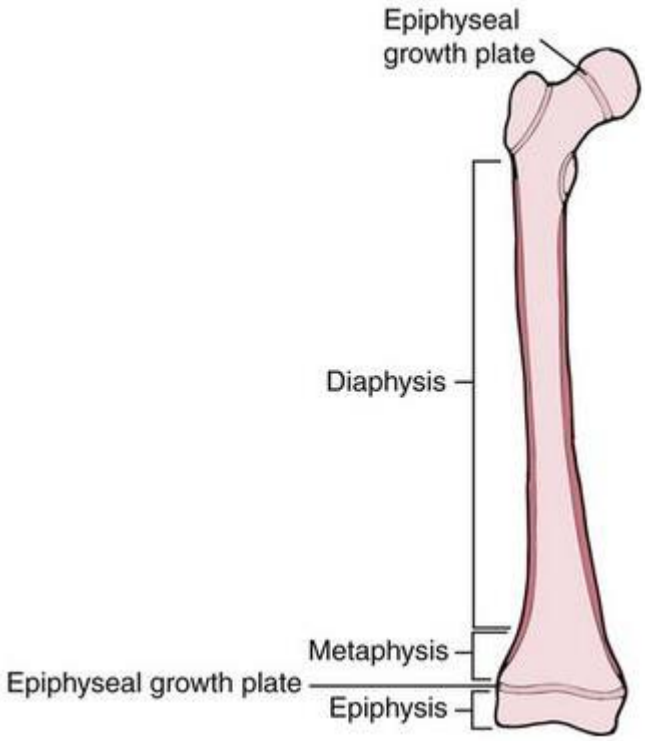

***Figure 2-2**. Components of long bone, where it can be observed to comprised of two extremities called the epiphysis; a central, long shaft called the diaphysis; and the metaphysis, an area delineating the epiphysis from the diaphysis. Each section differs from the other with regards to its microstructure [5].*

The volume ratio of cortical to trabecular bone varies between bones and skeletal sites. The ratio for the femoral head is 52:48 [4, 6], whereas for the lumbar spine it is 96:4 [6]. **Figure 2-3** presents microradiographs highlighting the difference between trabecular and cortical bone microstructure, namely the level of porosity.

Cortical bone has an outer membrane called the periosteum and is lined by an inner surface called the endosteum. Within the periosteum there is an osteogenic layer where progenitor cells can develop into osteoblasts: the bone-forming cells. Hence, the periosteal surface is necessary for appositional growth and fracture repair. The endosteum is more frequently remodelled than the periosteum, which is putatively due to exhibiting a greater biomechanical strain [2]. In contrast to the periosteum, bone resorption exceeds bone formation in the endosteum [7]; hence, bone diameter decreases therein, and consequently the marrow space enlarges with age [8].

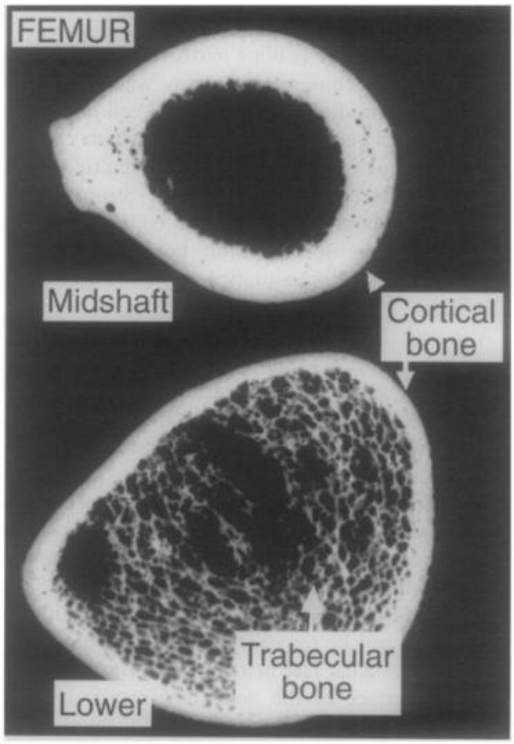

Figure 2-3. *Cortical and trabecular bone observed in a human femur by microradiographs [9]. Note the difference in porosity between cortical and trabecular regions.*

2.1.1.1 Microscopic Anatomy

Differences between cortical and trabecular bone can also be observed at the cellular and histological level. The basic functional units in both cortical and trabecular bone are called Haversian systems, which are separately referred to as osteons and packets, respectively. The Haversian systems contain mature bone cells called osteocytes; and also blood vessels and nerves, which facilitates oxygen and nutrient supply to bone cells [10]. An illustration of the aforementioned microscopic anatomical features is provided in **Figure 2-4**. It is believed that the size of the osteocytes determines the level of nutrient supply, and in turn governs the bone size. Osteons can be both active and inactive in bone remodelling, and it is this ratio that governs the level of porosity within cortical bone. A higher cortical remodelling results in greater cortical porosity and hence lower cortical bone mass. The cortex thins and the porosity increases in healthy aging adults [2]. In addition to a thinning cortex, Haversian system volume decreases with age [11].

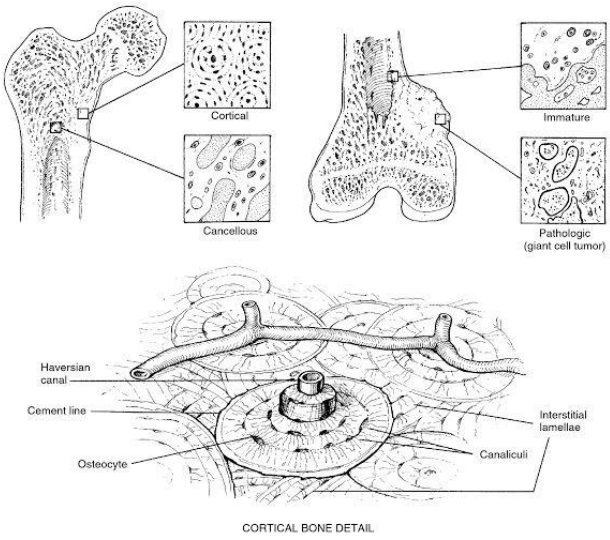

***Figure 2-4**. Schematic illustrating microscopic anatomy of bone [5]. The figure illustrates the components that make up the microscopic anatomy of bone: osteocytes, canaliculi, and Haversian canal.*

Trabecular and cortical bone are normally formed in a lamellar pattern, whereby collagen fibrils are laid down in alternating orientations. The mechanism of this phenomenon is unknown; however, the alternating layering of collagen fibrils provides lamellar bone with significant strength [12]. Bone formation can also be randomly oriented, which is referred to as woven bone. Although the mineral content is higher in woven bone, this stochastic orientation makes it weaker than its counterpart [13]. Woven bone is typically created during primary bone development. The densities of trabecular and cortical bone are, respectively, 0.07 to 0.97 Mg/m^3, and 1.8 to 2 Mg/m^3 [14].

2.1.1.2 Compositional Difference Between Trabecular and Cortical Bone

Aside from the microstructural differences, animal studies have reported a difference in chemical composition, which are presented in **Table 2-1**. As listed, cortical bone possessed a statistically-significant higher inorganic phase, carbonate content and Ca/P ratio. The higher inorganic phase in cortical bone may partly contribute to its higher mechanical strength over trabecular bone, as the strength is a function of the mineral phase [15-18]. High carbonate content is associated with a more stable phase of apatite [19], which may contribute to the lower turnover rate observed in cortical bone [20].

Furthermore, a higher carbonate content indicates a more mature bone [21]. A decrease in carbonate content is associated with osteoporosis [22], a disease characterised by loss of bone strength [23]. Furthermore, the Ca/P has also been implicated in the rate of bone turnover. With a lower Ca/P known to be more soluble, which, again, the higher rate observed in trabecular could be partly ascribed to its lower Ca/P [23, 24]. Considering that trabecular bone is more susceptible to fracturing [23], the higher bone turnover appears to be an evolutionary necessity to mitigate the build-up of fractures. It is also worth noting that decreasing Ca/P ratio has been found to compromise the mechanical strength of bone [25, 26]. Thus, to summate, the chemical composition of trabecular and cortical bone differs, which in turn may contribute to the difference between their stability, solubility and mechanical properties.

Table 2-1. *The difference in bone composition between trabecular and cortical bones extracted from the femur and tibia of Sprague-Dawley rats. The table also includes the statistical analysis between the two, where it was determined that there was a significant difference between the inorganic phase, carbonate content (CO) and calcium-to-phosphate ratio (Ca/P), but no significant difference (NS) between the magnesium (Mg) content. (adapted from ref. [19])*

Bone	Inorganic Phase (wt%)	CO (wt%)	Mg (wt%)	Ca/P Molar Ratio
Trabecular	62.0 ± 0.3	2.3 ± 0.2	3.6 ± 0.2	1.50 ± 0.2
Cortical	66.4 ± 0.3	3.8 ± 0.2	3.7 ± 0.2	1.63 ± 0.2
	P < 0.001	P < 0.001	NS	P < 0.001

2.1.2 Mediators of Remodelling

To understand how bone heals, it is necessary to grasp how bone remodels itself under normal condition and the mediators involved therein. The remodelling process is a cyclical event of bone formation that is preceded by bone resorption, and are mediated by various components of bone, including the four cell types found in bone: osteoclasts, osteoblasts, osteocytes and bone lining cells. A tree diagram representing the hierarchal composition of bone is presented in **Fig. 2-5**.

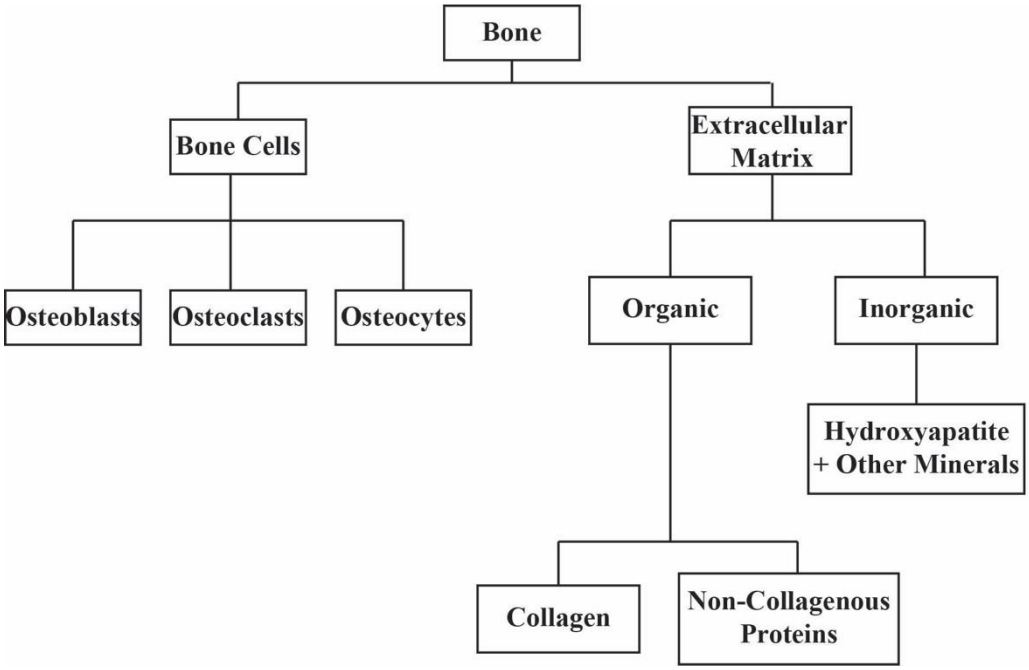

Fig. 2-5. *Tree diagram depicting the hierarchical structure of bone composition.*

2.1.2.1 Osteoclasts

Osteoclasts are the only cells known to be capable of bone resorption, and are the target of the majority of osteoporosis medication: a condition that results in weakening of the bones [27]. Osteoclasts are derived from mononuclear precursor cells of the monocyte macrophage lineage, which also form tissue-resident macrophages that are known for their digestive capabilities of other cells [28].

Osteoclasts bind to receptors on the bone matrix that causes them to become more polarised [29]. The cell undergoes a conformational change and forms a sealing zone surrounding the resorption site. During this process, the mineral part of bone is dissolved by the osteoclasts, which secrete hydrogen ions that acidify the resorption region below where the cells are anchored. Simultaneously, the osteoclasts also secrete an enzyme (cathepsin K) that lyse the proteinaceous matrix, wherein collagen is its main component [2, 30].

2.1.2.2 Osteoblasts

Osteoblasts, or bone-forming cells, synthesise new bone matrix on bone-forming surfaces. Population of osteoblasts are heterogeneous, with diverse cells expressing

distinctive genes that could explain the differences of the trabecular micro-architecture at various skeletal sites, site-specific anatomical differences due to disease, and local differences when in response to active pharmaceutical ingredients for bone therapy by the osteoblasts [31].

2.1.2.3 Osteocytes

Unlike osteoclasts, osteoblasts and lining cells, which reside at the bone surface, osteocytes are embedded within calcified bone, residing in the Haversian systems. Osteocytes account for more than 95% of bone cells [32], and their role is to support bone structure and metabolism. They are also involved in both the demineralisation and remineralisation of bone [33]. Osteocytes are terminally differentiated from osteoblasts [34], and the products they secrete [35].

Osteocytes possess different factors that assist in intracellular adhesion and regulate the exchange of minerals within osteons [36]. The cells are combined together metabolically and electrically through gap junctions consisting of primarily connexion 43, a protein that regulates intercellular communication with regards to cell differentiation, proliferation and cell death. Osteocytes transduce stress signal from stretching or bending of the bone into biological activity flow of canalicular fluid, in response to the stimulation of osteocytes through said external forces. Transient calcium diffusion across filipodial gap junctions in bone are thought to relay the transmission of information between osteoblasts on the bone surface and osteocytes situated within the bone [2, 37].

Osteocytes may survive for decades in human bone that is not turned over [34]. The presence of empty lacuna suggests that osteocytes may undergo cell death. Causes of osteocyte cell death can arise from estrogen deficiency or glucocorticoid treatment [38], such as for asthma, allergy or adrenal deficiency, and is harmful to bone structure. **Fig. 2-6** is an illustration depicting osteocytes, osteoblasts and osteolcasts.

2.1.2.4 Bone lining cells

Bone lining cells (BLC) are also differentiated from osteoblasts. They have multiple functions, including communicating with osteons, inducing the proliferation and

differentiation of osteogenic cells, respond to mechanical stimuli, and evidence suggests that they are involved in the propagation of the activation signal that initiates the remodelling cycle [39].

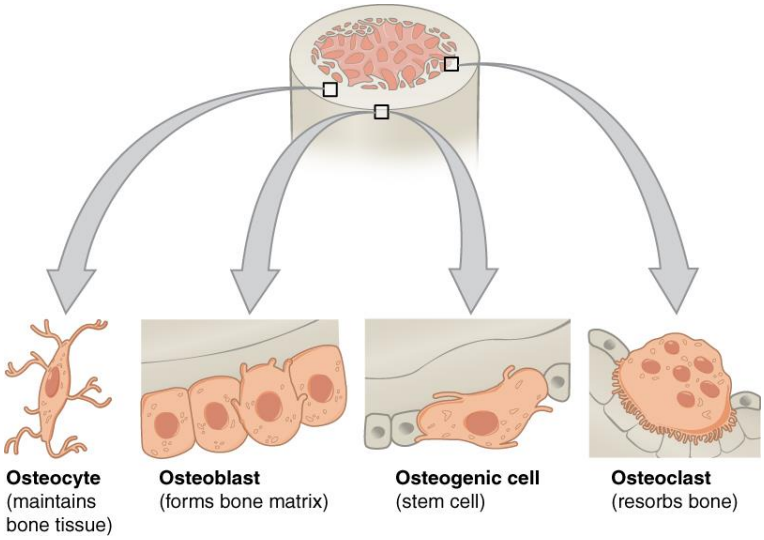

Fig. 2-6. *Illustration of the aforementioned bone cells: osteoclasts are recruited for bone tissue absorption; osteoblasts form new bone tissue; osteocytes are mature osteoblasts that are embedded within bone tissue; and Osteogenic cells are undifferentiated pre-osteoblast cells [40].*

2.1.2.5 Bone Matrix

The bone matrix is a hierarchal structure and comprises the majority of bone tissue, as demonstrated in **Fig. 2-7**. Its role is to bind cells and non-cellular components (i.e. extracellular matrix) together to form an organised structure, which will allow the bone to perform its functions. Bone matrix consists of 50 to 70% mineral, 20 to 40% organic matrix, 5 to 10% water and less than 3% lipid [41]. The mineral phase provides the mechanical rigidity and load-bearing capabilities of bone. The principal component of the mineral phase is hydroxyapatite [42], with small amounts of carbonate, magnesium, acid phosphate, as well as being hydroxyl-deficient. Examples of bone compositions reported in the literature are provided in **Table 2-2**.

Hydroxyapatite (HA) crystal size and concentration are promoted by calcium- and phosphate-binding proteins (e.g. alkaline phosphatase) secreted by osteoblasts, which

results in ordered formation of the bone mineral phase [43]; irregularities thereof are ascribed to several pathological conditions [44]. The process thereof is referred to as bone mineralisation. The exact mechanism of mineralisation is yet to be determined, with multiple theories, including collagen template-mediated and matrix vesicle-mediated mineralisations, postulated. The theories are beyond the scope of this thesis; a summary thereof can be obtained from ref. [45]. One such theory is that bone mineral formation initiates in the hole zone of collagen fibrils, and gradually develops into the inter- and intrafibrillary space [46]. A study by Meunier and Boivin (1997) revealed two distinct stages in the mineralisation process: (i) an initial rapid process, with a time frame of a few days) that results in bone tissues containing approximately 60-70% of the mineral load of fully mineralised bone; (ii) a subsequent stage that is contrastingly slower and lasts for at least a few months, whereby complete bone tissue mineralisation is attained [47].

Suffice it to say, the mineralisation process of bone determines the strength of bone [48], which can be compromised by pathological disorder. For example, sufferers of osteomalacia, a common bone disorder caused by pathological mineralisation, have a lower rate of calcification during mineralisation, yet a larger bone surface area that is covered unmineralised tissue. Another pathology is osteoclasia, whereby the over activity of osteoclasts during the mineralisation process results in fibrous connective tissue replacing osseous tissue. There are several other disorders, such as fibrous osteodystrophy and osteoitis deformans to name two, attributed to the disruption of the biomineralisation process, which can lead to bone unable to bear load [45].

Furthermore, formation of HA crystals with a sharp, mono-modal size distribution, in contrast to a wide distribution, are believed to result in mechanically weaker bones [49]. **Fig. 2-7** displays the hierarchal structure of bone, wherein the relation of hydroxyapatite crystals to said structure is demonstrated. The mean length and width of the crystals are approximately 20-50 nm and 12-20 nm, respectively, which vary depending on several factors, including age, nutrition, location of the tissue [50]. These in turn impact the structure and composition of the mineral phase of bone. Unlike dental enamel, calcium phosphates are poorly crystallised. Hence their study by either x-ray diffraction or infrared spectroscopy reveals broad peaks or bands, respectively [51].

Table 2-2. *Examples of the elemental composition of bone apatite by weight. The table demonstrates that bone apatite comprises of several impurities, with carbonate being the largest in terms of content. (adapted from ref. [51]).*

Element	**Carlstrom**	**Woodward**	**Triffitt et al.**	
			Young	Old
Calcium	27	22.2	23.4	24.6
Phosphor	12	10.2	11.9	12.6
Magnesium	0.5	0.12	0.40	0.51
Sodium	0.5	0.06	0.55	0.64
Potassium	0.05	-	0.15	0.05
Fluorine	0.02	-	-	-
Chloride	-	-	0.14	0.08
Carbonate	4	-	3.57	3.99
Ca/P mol	1.79	1.68	1.52	1.52

The degree of maturity of calcified tissues also varies, with respect to crystallinity, Ca/P ratio and impurities; which all increase with age. In contrast, magnesium content decreases at the same time [51].

In contrast to geological hydroxyapatite, bone hydroxyapatite crystals are small, poorly crystalline, and are more soluble; the latter is thought to allow support of mineral metabolism [52].

As bone matures, HA crystals increase in length and perfection (e.g. less impurities), but decrease in thickness [49], which is again regulated by proteins. Increase in crystal size occurs by crystal growth, whereby free ions are recruited; through secondary nucleation; and by fusion or aggregation of existing crystals. Cell viability, genetic factors and diet also affect crystal enlargement [49]. An additional factor that has also been postulated is the presence of impurities in the crystal lattice, which results in a driving force for the crystal to minimise its chemical imperfection [53]. The most relevant substitution concerning bone, notwithstanding minor and trace element substituents, is

the replacement of trivalent phosphate anions of the HA structure with divalent species such as carbonate (type B) and hydrogen phosphate ions. These substituents have been detected in large and variable amounts in bone mineral using different spectroscopic and chemical techniques [54]. The charge compensation mechanism for synthetic apatites containing these bivalents ions involves the formation of two ionic vacancies: one on a cationic site and one on a monovalent anionic site, which lead to the general formula [54]:

$$Ca_{10-x}(PO_4)_{6-x}(HPO_4 \text{ or } CO_3)_x(OH)_{2-x}$$

The replacement of phosphate with divalent ions is associated with a loss of hydroxyl ions, hence the depleted hydroxide ions observed in bone apatite. In addition, the substitution of carbonate (Type A) into the monovalent anionic sites could deplete hydroxyl content [55].

The organic phase of bone provides flexibility for minimising brittle fracture. The organic phases comprise 85 to 90% collagenous protein, and 10 to 15% non-collagenous proteins. Members of the latter include serum albumin and α2-HS-glycoprotein, which bind to hydroxyapatite because of their acidic properties. Both serum albumin and α2-HS-glycoprotein are believed to regulate matrix mineralisation and regulate bone cell proliferation, respectively. Both collagenous and non-collagenous proteins are synthesised and secreted by osteoblasts, and are degraded by proteins secreted by osteoclasts [56, 57]. **Fig. 2-7** is a schematic portraying the hierarchical structure of bone tissue, encompassing the aforementioned components.

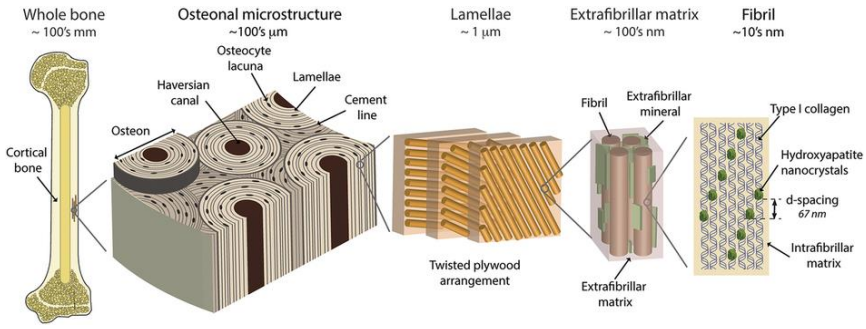

Fig. 2-7. *The hierarchical structure of bone [58]. Note the atomic scale components used to build-up from into this remarkable tissue. Hydroxyapatite will be discussed in* ***Section 2.3.4***

2.1.3 Bone Growth, Modelling and Remodelling

2.1.3.1 Bone Growth and Modelling

Bone growth occurs both radially and longitudinally during childhood and adolescence. Tissue proliferation occurs in the metaphyseal and epiphyseal sections of long bones, and is followed by mineralisation that forms primary new bone [2]. Diet affects bone growth, with long-term consumption of soft drinks and proteins are associated with a negative and positive effect, respectively, on bone growth [59, 60].

Bone modelling is the shaping process of new bone deposition without prior complete resorption, in response to physiological or mechanical stimuli. During this process, bones widen with age in response to periosteal apposition of new, and endosteal resorption of old, bone. In addition, bones may expand or change axis by addition or removal of bone-appropriate surfaces by the actions of osteoblasts and osteoclasts, in accordance to external stimuli. This phenomenon is known as Wolff's Law: an observation that describes the change in bone density in response to stresses applied thereto. The modelling process occurs right through to old age but markedly less so than the early years after completion of growth [61, 62]. An example of mechanical stimuli is seen in tennis player, where the physical activity undertaken results in individuals exhibiting a higher bone mass in their dominant playing arm compared to their passive arm [63]. The modelling process is also observed in bones that are not axially loaded, hence other factors are involved [64].

2.1.3.2 Bone Remodelling

Bone modelling occurs minimally in adulthood, and is replaced by a remodelling process, in which existing bone matrices are replaced by new matrices to maintain bone strength. The process is vital for preventing the accumulation of micro-cracks, combatting diseases such as osteoporosis, and mineral homeostasis [65, 66]. The process entails the sequential process of osteoclast-osteoblast activity, whereby old discrete parts of bone are removed and are replaced by newly-mineralised bone, which precede the deposition of a proteinaceous matrix. In contrast to modelling, the coordination between osteoclasts and osteoblasts aims to keep bone shape and structure unchanged during adulthood. The remodelling process consists of four stages: activation, resorption, reversal and formation; which may occur randomly but can also be directed to sites requiring repair

[67]. The remodelling process is briefly detailed below, summarised from the following references [2, 67, 68]. **Fig. 2-8** is a schematic depicting the remodelling process.

Activation involves the recruitment and initiation of osteoclast precursors that originate from blood circulation, after which the surface of bone is lifted. During this stage, the precursor cells fuse to form multinucleated pre-osteoclasts that bind to the bone surface at the remodelling site. Following activation is the resorption stage, which occurs for approximately 2-4 weeks for each remodelling cycle. Here, the osteoclasts secrete hydrogen ions to lower the pH within the bone-resorbing site to as low as 4.5 to aid bone mineral disintegration. Simultaneous to hydrogen ion secretion, proteins are released by the cells to digest the organic phase of bone. The resorption phase is terminated when the osteoclasts undergo apoptosis.

The intermediate phase between resorption and formation is called the reversal phase. Current knowledge suggests the cavities formed during resorption possess a variety of mononuclear cells released from the bone matrix, such as osteocytes that were recently shown to be able to revert into mature osteoblasts. In addition, preosteoblasts further enrich the site with bone-forming cells, and are recruited to commence new bone formation. Although the coupling signals linking resorption to the beginning of formation are not known, it putatively involves molecules decreasing osteoclast activity.

The final stage is formation, and takes approximately six weeks to complete. Osteoblasts synthesise new collagenous organic matrix, and regulate mineralisation of matrix by releasing calcium and phosphate that enzymatically lyse mineralisation inhibitors, such as pyrophosphate. It is also during this stage that the osteoblasts convert to osteocytes, however, approximately 50 to 70% undergo apoptosis.

The remodelling cycle is the same for both trabecular and cortical bone, with the end product of each remodelling sequence is the production of new osteons. Remodelling results in newer, healthier bone that preserve bone strength and other functions reported above. Again, the remodelling processes is governed by Wolff's Law. The annual turnover rate of the whole skeleton is 10%, and cortical turnover on average is 4% per year, which is sufficient to maintain bone strength [2, 69]. However, the difference between old bone resorbed and new bone formed results in thinning of both trabecular and cortical bone with age.

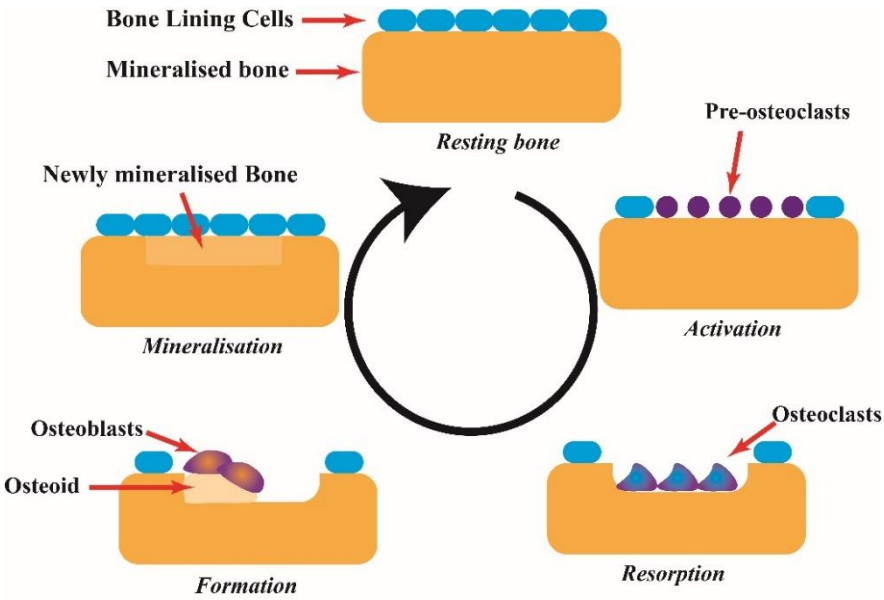

***Fig. 2-8**. Schematic illustrating the remodelling stages of bone. The activation stage entails pre-osteoclasts moving to the site of interest and binding thereto, which takes 3-5 days. This is followed by the resorption stage, which occurs for approximately 22 days, whereby the bone site is resorbed. The final stage of formation is where osteoblasts synthesis new collagenous and mineral matrices, which occurs for approximately 2-4 months [70, 71].*

2.1.4 Determinants of Bone Strength

Bone strength is dependent on large variety of interconnected factors. Bone mass accounts for 50 to 70% of bone strength [68]. Bone composition and geometry are important; however, larger bones are typically stronger than smaller bones, even with equivalent bone density. As the bone density increases radially, so does the strength by the radius raised to the power of four. The ratio of cortical to trabecular also affects bone strength. Bone strength is further determined by diseases affecting both the organic and inorganic matrices [72]. Pathologies such as osteogenesis imperfecta and scurvy demonstrate the importance of collagen for bone strength, as deficiency thereof results in substantial increases to fracture risks. Lastly, as previously alluded to, individual lifestyles such as diet and exercise affect bone strength.

2.1.5 Fracture Healing

Bone is one of few tissues that is able to heal without forming a fibrous scar. This is a great feat considering bone is biphasic in more ways than one, wherein the regeneration

of both a mineral and organic phase is achieved. For fracture healing, there are two methods in which the process can occur: direct or indirect. A concerted effort was applied in elucidating the healing process, including examining from a biological, mechanical and electrical perspective [73, 74]. A brief overview from a biological perspective is provided herein, summarised from Kalfas (2001) [75] Marsell and Einhorn (2011) [73], and Manske and Shankman (2011) [5]; to illustrate the key biological factors involved in the process: factors one should bear in mind when designing a scaffold.

2.1.5.1 Direct fracture healing

Direct healing, also referred to as primary healing, is the process of bone directly restoring anatomical and biomechanical properties of the lamellar structure. Bone on one side of the fracture site must bond with bone on the other side of the defect site to reinstate mechanical continuity. This form of healing only proceeds when anatomical restoration of the fracture fragments is achieved and rigid fixation is provided, externally if needed, that substantially reduces inter-fragmentary strain. Direct healing of fractures can either occur through contact healing or gap healing, which are briefly described below.

2.1.5.1.1 Contact healing

The fracture unites if the defect gap is less than 10 μm. In this process, cavities are formed at the periphery of osteons closest to the fracture site, by osteoclasts. The osteoclasts proceed to remove damaged fragments and the cavity is refilled with osteoblasts that initiate new bone formation, including simultaneously forming new Haversian systems. The bridging Haversian systems later mature into lamellar bone resulting in fracture healing without the formation of periosteal callus.

2.1.5.1.2 Gap Healing

For gap healing to occur, the defect gap is greater than 10 μm but less than 1 mm. The process differs from contact healing in that bone union and Haversian system are not simultaneously remodelled, and as a result this form of healing is the slower of the two. The process occurs in two stages, where the first stage establishes a mechanically weak lamellar bone that occurs approximately between one to two months; prior to the secondary stage that resembles the activity occurring during contact healing process.

2.1.5.2 Indirect fracture healing

Indirect healing is the most frequent form of fracture healing. It differs from direct healing in that anatomical reduction or stable mechanical conditions are not required. The process can be grouped into six distinct, yet overlapping stages [73]. The stages are detailed below to illustrate the role of cells and calcium in healing, as well as blood vessel formation.

2.1.5.2.1 Acute Inflammatory Response

Immediately following the trauma, a hematoma is formed, which contains bone marrow cells. An acute inflammatory response is also triggered by the release of pro-inflammatory molecules at the fracture site. The pro-inflammatory molecules include molecules that recruit inflammatory cells, and is also involved in facilitating angiogenesis and stimulating the differentiation of osteoclasts and osteoblasts. The response causes the hematoma to coagulate throughout the defect site forming a template for callus formation. The acute inflammatory response peaks within the first twenty-four hours and finishes after seven days, although the pro-inflammatory molecules remain for regulating subsequent process.

2.1.5.2.2 Recruitment of Mesenchymal Stem Cells

Mesenchymal stem cells (MSCs), which ostensibly originate from the surrounding tissues and bone marrow, are vital for bone regeneration, as they proliferate and differentiate into osteogenic cells. The molecules involved in the process are yet to be determined, with molecules involved in both the MSCs recruitment and the revascularisation of the defect site have been purported to be involved. The recruitment of MSCs initiates a cascade of collagen release and other peptide molecules that facilitate the generation of cartilaginous and periosteal bony callus, which are needed to provide an initial mechanical support to the fracture site.

2.1.5.2.3 Generation of Cartilaginous and Periosteal Bony Callus

A fibrin-rich, cartilganious granulation tissue ensues the hematoma formation, whereby an endochondral formation occurs at the defect site. The formation of fibrin is to provide

stability to the mechanically-weak defect site. In addition, the simultaneous formation of intramembranous ossification occurs forming a hard callus, whereby the bridging thereof from both ends of the defect site results in a partially-rigid structure that allows load-bearing.

2.1.5.2.4 Revascularisation and Neoangiogensis

Pro-angiogenic signalling molecules that promote blood vessels and their penetration into the endochondral tissue continue to be secreted in and around the fracture site. Furthermore, cells that remove the extracellular matrix are incorporated to assist the penetration of blood vessels. Obstruction of the blood supply formation has been reported to perturb the healing process.

2.1.5.2.5 Mineralisation and Resorption of Cartilaginous Callus

The penultimate stage of the healing process entails the resorption of cartilaginous callus that is replaced by callus chondrocyte, whereby their proliferation results in a hard bony callus. The calcification mechanism entails the build-up of calcium granules located within mitochondria, which are released into the extracellular matrix and proceed to precipitate with phosphate to form mineral deposits. As this stage of the fracture healing process advances, the mechanical stability of the defect site is enhanced.

2.1.5.2.6 Bone Remodelling

The final stage of the healing process ensures that pre-facture mechanical strength is restored, which could take years to accomplish. For this to occur, the bony callus is further resorbed by osteoclasts, and lamellar bone structure is formed by osteoblastic activity. Concurrent with this period, the marrow space is re-established, and pre-injury vascular flow is restored.

2.1.6 Failure to Heal

Despite the healing capabilities of bone tissue, there are instances, whether due to genetic or external factors, when it fails to heal; examples of such are given in the following

section (section **2.2**). In particular instances, an extrinsic stimulus is needed to induce bone regeneration. This can be in the form of a structure that adjoins both ends of the defect sites and provides structural support for the mediators of healing to perform their respective duties: essentially a scaffold for the cells. Such a structure will need to be biologically safe and not toxic to cells. A more desirable structure would need to be conducive to the healing process, and fortunately, there are synthetic materials that can perform said feat. In addition, the scaffold should mimic the lost bone tissue with respect to geometry and mechanical strength.

In summary, the skeleton is an extraordinary organ that has the capacity to pre-empt against deleterious defects by remodelling on a frequent basis. The skeleton can also heal itself when defects arise, provided the underpinning process is unperturbed. However, in particular cases, surgical treatments are needed to rejuvenate the healing process, such as bone graft substitutes. Bone graft substitutes (BGS) belong to the cross-disciplinary research field of tissue engineering: the extrinsic approach of replacing missing biological tissue. In bone graft substitution, the process entails the use of either a natural or synthetic substrate to replace missing or damaged bone tissue. The remainder of the chapter will describe the need for BGS and the materials that can be used; and the concerted endeavour to develop the ideal BGS using calcium phosphate ceramics.

2.2 Clinical need for BGS

In 2014, Trauma and Orthopaedics was ranked as the surgical speciality with the second highest activity in the U.K. (1.2 million procedures), surpassed only by ‘General Surgery’ (1.3 million procedures), in which the latter is a broad collection of unclassed procedures [76]. Bone transplantation is second to only blood transfusion [77]. Thus, there are both medical, as well as economical motivations, for developing treatments for said activity, of which bone graft substitute should be considered. The number of procedures is expected to rise, which are driven by populations living longer, as well as lifestyle choices. Examples of where BGS are needed include trauma, joint replacement surgery, spinal surgery and bone tumour resection [78].

2.2.1 Trauma

Each year in the USA there are an estimated 700,000 vertebral fractures, 280,000 hip fractures and 250,000 wrist fractures that cost $10 billion to treat [79]. However, in 5% of all fractures and 20% of high-impact fractures, healing is either delayed or does not occur [80]; the latter is clinically referred to as non-union fracture. In such instances, the intervention of surgical means is required to facilitate bone healing, of which BGS is one of limited treatment options. Open reduction and fixation of fractures with dynamic screws and plates is one means of attaining stability in order for bone to heal. However, this approach can lead to periosteum impairment, which is a key source of osteoprogenitor cells necessary for bone restoration [81]. The demand for BGS is emphasised by the fact there are around four million procedures involving BGS performed globally per year, and an expected increase in fracture-caused death or disability [78, 82-84]. Previous clinical studies have demonstrated that risk factors with higher odds of fracture include obesity, excessive alcohol consumption, smoking and psychological stress [85-88].

2.2.2 Joint Replacement Surgery

Joint replacement surgery (JRS) was the most common surgical admission procedure performed in the UK in 2013/2014 [76], and is expected to rise due to risks associated with lifestyle choices. The surgery is used to treat joints where the articulating component between two bones has been extensively damaged beyond self-repair. JRS include total and partial hip, knee and shoulder replacements. The use of synthetic materials, such as polished stainless steel, can provide many years of mobility to the patient before loosening. It has been shown that Ancient Egyptians had implanted iron prosthesis for knee joint replacement as early as 600 BC [89]. Unfortunately, these materials are associated with a relatively high rate of implant loosening, which require a revision surgery, thereby subjecting patients to further surgical-associated risks. The loosening of implants is thought to arise from particulate wear debris that initiate an immunological response resulting in osteolysis via osteoclast activity [78]. There is ongoing research into improving both material selection and surgical procedures to mitigate implant loosening. For example, using ceramic-on-ceramic articulations instead of metal-on-metal considerably reduces the revision rate over a ten-year period [90].

2.2.3 Spinal Surgery

Back pain is a debilitating disorder for both patient and civilisation, with an estimated cost exceeding £1.5 billion to the UK economy. If the pain is skeletal-related, including non-union fractures, then surgical intervention is once more used to alleviate pain. Over 500,000 bone graft autotransplants for spinal surgery are performed annually in the USA alone [78].

2.2.4 Bone Tumour Surgery

Although primary bone tumour (i.e. tumour originating from the bone) is uncommon, they are difficult to identify, and excision thereof often leaves large skeletal defects. Bone tumours particularly affect children and adolescents, and therefore an effective treatment is required to avoid long-term, chronic health problems. Further to this, bone cancer incident rates were found to increase in 0-39 year olds from 1982 to 2002 [91]; and for the over 40 different bone cancers recorded by the World Health Organisation, a link between old age and some of the cancers was established [92]. Bone cancer aetiology is poor, with putative causes include radium contamination from water, wherein bone interprets the element as calcium and the subsequent irradiation therefrom [93]; consequence of over-weight [94]; and the fact that bone is a common metastatic cancer site [95].

As this section demonstrates, there are multiple clinical needs for BGS. Indeed, prevention is better than cure, but as mentioned, some have unknown aetiology, and others such as ageing cannot be prevented. Hence, treatment is inevitable. Fortunately, there are numerous BGS options available, and selection of an ideal graft relies on several factors. BGS can be synthetic, in which bespoke grafts can be fabricated to meet specific needs, provided that the fabricated part meets the requirement for an ideal BGS.

2.3 Designing Bone Grafts

2.3.1 Requirements for Bone Grafts

The purpose of using bone grafts is to restore missing bone, and thus lost function. For a material to be considered suitable for grafting, certain biological and physical criteria need to be matched.

2.3.1.1 Biological Properties

For a synthetic material to be considered in any tissue engineering application, it must be biologically safe, in which elements released therefrom must not result in an adverse reaction, such as inflammation and septic rejection; all the while performing its intended application. If a material is biologically safe then it is categorised as biocompatible [96], which can be further divided into three aptly-named different sub-categories: bioinert, bioactive and bioresorbable [97]. Materials that do not elicit an adverse reaction are classed as bioinert, which include aluminium oxide and zirconium oxide [96]. Materials that are biocompatible and elicit a favourable reaction are termed bioactive. Such responses include inducing bonding between bone and material, or the recruitment of bone cells. The last sub-group contains materials that are either resorbed or degraded in the body, and the products are safely excreted thereafter. Resorption refers to materials that are absorbed into circulation by cells, namely osteoclasts, whereas degradation pertains to those materials that are removed from the body through natural breakdown, such as structural or chemical. Thus, bioresorption can be either cell-mediated, chemically-mediated or physically-mediated.

The ideal BGS should be bioactive and bioresorbable. Upon implantation, the material should initiate a bioactive response that results in bone regeneration, whilst simultaneously bioresorbed at a rate matching the regeneration process [98]. This means the material must be osteoconductive, where bone cells are recruited for new bone growth; osteoinductive, wherein the implant is conducive in stem cell differentiation into osteoblasts and osteocytes; and osseointegrative to allow integration with the surrounding tissues [99].

2.3.1.2 Physical Properties

The ideal bone graft with its bioactive properties should provide sufficient physical support for bone regeneration to take place. This entails a structural support for cells to adhere onto the implant; dynamically maintaining the mechanical properties that allow continued function (e.g. mobility) by closely mimicking characteristics of the missing bone throughout resorption (e.g. compressive strength, elastic modulus and fracture

toughness); and mimicking bone porosity with regards to pore size, total porosity and interconnectivity.

Porosity, particularly interconnected porosity, facilitate the migration and proliferation of cells and nutrients throughout the implant, as well as vascularisation [100]. As stated in section **2.1.5.2.4**, facilitating blood supply formation prevents healing complications, which can be achieved by incorporating porosity. Furthermore, a porous architecture enhances the mechanical interlocking at the interface between implant and the adjoining tissue resulting in greater implant stability [101]. Hence, incorporating porosity would be beneficial in clinical applications where implant loosening is encountered (section **2.2.2**). In addition, the distribution of porosity can be used to tailor the rate of degradation.

Pore size requirements are bimodal, consisting of micropores (< 5 μm) and macropores (> 100 μm) [102]. Both microporosity and macroporosity are important for attaining osteoconductivity [103]. However, the pore size requirements are inconclusive, as, for example, studies have surmised macropores greater than 400 μm are necessary for bone formation [104, 105]. With regards to the total porosity volume, numerous studies have verified that higher porosity leads to improved osteogenesis. This is likely to be as a consequence of a larger surface area that increases the rate of ion exchange and other bone-inducing factors. If the porosity is interconnected then it is considered more advantageous as it provides a continuous spatial connection for bone growth to proceed [100].

Porosity and mechanical properties are mutually exclusive in ceramics, and hence the mechanical strength of an implant should be considered when pursuing high porosity. The principle mechanical property used to characterise the strength of an implant is the compressive strength, which for cancellous bone ranges from 2 to 45 MPa, and from 90 to 230 MPa for cortical bone [106, 107]. Indeed, the strength of bone varies from patient to patient, and between different bone sites (section **2.1**). Furthermore, the extent to which porosity can be increased without being detrimental to mechanical properties depends on the nature of the material and the fabrication technique used.

In summary, the ideal bone graft substitute should promote bone regeneration and simultaneously degrade or resorbed to preclude the need for a second surgery; and therewithal providing sufficient mechanical strength and interconnected porosity.

2.3.2 Natural Bone Graft Substitutes

The gold standard in BGS is autotransplantation, whereby osseous matter is harvested from one bone site to the defect site within the same individual. Autologous bone is osteoconductive, osteoinductive and osteogenic due to, respectively, the presence of bone chips, growth factors and cells [108]. Further advantages of autologous bone are their excellent success rate, histocompatibility and low risk of disease transmission.

Autologous bone can either be cancellous or cortical, with the former reported to be easily re-vascularised and rapidly incorporated into the recipient site [109]. A cancellous graft is suitable for non-load-bearing application, however it does not deliver substantial structural support immediately, requiring six to twelve months to achieve similar strengths to a cortical graft following implantation; hence a cortical graft is preferred for load-bearing applications [109]. Accordingly, cancellous grafts are recommended for bone defect sites of under 6 cm that do not require immediate structural integrity [110]. Autologous cancellous bone is commonly harvested from the iliac crest since a large supply of bone can be extracted.

Autologous cortical bone can be grafted from the iliac crest, ribs and fibula, and are ideal for segmental defects greater than 6 cm. Cortical grafts can be extracted with or without their vascular segments, with pedicles thereof recommended for defects greater than 12 cm [111]. Although cortical grafts can achieve immediate structural support, they possess little or no osteoinductive properties and are mostly osteoconductive, with surviving osteoblasts providing osteogenic capabilities [110].

The main disadvantage of autologous bone is their limited quantity and the donor site morbidity. Quantities are further limited in individuals who have bone diseases that lower the quality of available bone, such as in osteoporosis or arthritis. For these reasons, alternatives to the gold standard were pursued.

Allograft is another common BGS approach, and was used in 35% of all bone transplantation in the United States [112]. In allotransplantation, the graft is obtained from a donor or cadaver, and thus safety is a concern with regards to histocompatibility and the risk of disease transmission. The benefits of allograft over autograft bones are no donor site morbidity to the patient and increased graft availability, although quantities are still limited. The disadvantages in comparison to autografts include limited osteoinduction that results from the processing and sterilisation of allografts [113].

2.3.3 Synthetic Bone Graft Substitutes

In 1994, the use of synthetic bone graft substitutes in orthopaedic procedure surpassed that of auto- and allografts in the United States [114]. A wide range of synthetic materials have been researched as replacement to autografts. These include metals, plastics, glass and ceramics, each with their respective strengths and weaknesses.

2.3.3.1 Metallic Alloy-based Implants

Metals were the first widely adopted orthopaedic material-of-choice in the last century, in which metallic alloys attained a wider application as implants than pure metals due to their enhanced mechanical properties and good biocompatibility. The first alloy developed for implantation in humans was "Sherman Vanadium Steel" [115], with stainless steel alloys introduced in the 1920s [116]. Stainless steel alloys are reliable with regards to fatigue resistance, however, studies discovered that fatigue properties decreased when subjected to corrosive media, such as the biological milieu, leading to increased implant failure [116]. Such alloys have poor pitting and crevice corrosion resistance due to the chromium carbide forming on the grain boundaries that induces crack initiation on the surface [117]. Furthermore, there are cytotoxicity concerns with the alloying elements used in stainless steels, particularly nickel which has been reported to induce localised tumour formation [118-120].

Later, cobalt and titanium alloys were introduced for their higher mechanical properties and biocompatibility. Cobalt alloys were first used in the 1940s as medical implants having demonstrated great corrosion resistance and excellent mechanical properties for aircraft applications. Of interest is the cobalt-chromium-molybdenum alloy that demonstrated high biocompatibility, which was attributed to its high corrosion resistance that limits ion release. As such, cobalt-based alloys succeeded stainless steel implants in certain clinical applications. However, both cobalt and chromium were later classified as highly toxic elements, and were found to be problematic in long-term implants, due to the release of ions as a result of metal-on-metal contact. The alloys have a high density (9.8 gm/cm^3), are expensive, and require a costly fabrication processes that further limit their application [117].

Similar to cobalt alloys, titanium alloys were also used in aerospace application before employed as dental implants in the 1950s. Of interest is Ti6Al4V (titanium-aluminium-vanadium alloy), which has a relatively low density (approximately 4.5 gm/cm^3) yet high strength, and hence, a superior specific strength; a low elastic modulus that minimises the effects of stress shielding; displays excellent corrosion and biocompatibility, with both *in vitro* and *in vivo* analyses demonstrating titanium's safety; and, where both stainless steel and cobalt-alloys lacked in, osseointegration [117]. However, concerns have arisen due to the use of aluminium and vanadium as alloying elements due to their deleterious effect within the body. Aluminium is a growth inhibitor to bone and a possible cause of Alzheimer's, whereas vanadium is toxic to cells [121-123]. Furthermore, Ti-alloys are also costly and are difficult to forge, compared to other biomaterials.

The two main concerns with metallic implants, which are osseointegration and ion release, can be obviated with the use of ceramic coating. As will be detailed in the following section (section **2.3.4**), calcium phosphates (CaP) form a strong bond with the surrounding bone tissue, and provides a barrier that mitigates metallic ion release. Plasma spray coating is a commercially-available technique that can be used to coat metallic substrates, but others are also being researched, such as the sol-gel and pyrosol methods. However, CaP decomposition, coating delamination and incurring costs are problems encountered when coating metal-based implants. Other problems associated with metallic implants include interference with magnetic resonance imaging procedures, which is a widely used diagnostic technique [124-126].

In conclusion, despite possessing excellent mechanical properties, metal-based implants are limited by the release of metal ions into the body, a high elastic modulus that is counterproductive for long-term application, and a lack of bioactivity. It is worth remarking that osseointegration in metals (e.g. titanium and tantalum) is only achieved where a passive ceramic oxide layer is formed (e.g. TiO_2 and Ta_2O_5), and it is this oxide layer that is conducive to the spontaneous nucleation of apatitic crystals. Moreover, the formation of oxide layers in metals, such as Co- and Ti-alloys, helps to minimise ion release. The human body only possesses metal ions but no metallic structure. Thus, it can be reasoned that ceramic materials are more suitable for the physiological milieu as well as providing a favourable surface for osteogenesis.

2.3.3.2 Polymer-based Implants

As stated previously, bone is composed of both ceramic and polymers. As such, the use of polymers has been explored as potential BGS. Polymers can be classed either as natural or synthetic polymers, of which both degradable and non-degradable forms exist. Development of polymers synthesised from glycolic acid and other α-hydroxy acids for industrial application were abandoned because of the resulting polymers' long-term instability. However, this instability was found to be attractive for medical applications as it resulted in biodegradation, which can be accomplished by synthesising polymers that have hydrolytically unstable linkages formed between monomers. Said linkages can be cleaved in the presence of an aqueous media, and can be as rapid as 1 to 2 months for polylactide-co-glycolide (PLGA), to over two years for polycaprolactone (PCL) [127, 128]. Thus, polymers provide a broad degradation range that can be personalised to specific tissue repair rates. Polymers can further be tailored by varying molecular weight, crystallinity and morphology, which again can be tuned towards desirable mechanical properties and rate of degradation [127, 128].

In addition to possessing desirable bioresorbable properties, polymers are relatively inexpensive to manufacture, compared to ceramics and metals, and can be processed by a wide variety of fabrication techniques. However, the drawbacks of polymers are their inherently poor mechanical properties for load-bearing usage, and lack of osteoconductivity. For example, *in vivo* results demonstrated near-complete degradation of PLGA, with new bone generated bridging the defect site. However, no bone-implant intimate contact was observed, and hence the authors concluded that the substrate behaved as a 'tissue spacer' [129]. The failure to bond to the surrounding tissue may be more problematic in load-bearing application where the prevalence of implant loosening is greater. However, both the mechanical properties and osteoconductivity drawbacks can be addressed by compositing the polymers. For example, PCL, a widely-researched BGS polymer, possess compressive strength typical of most polymers at below 1 MPa [130-133]. A remarkable strength of 47 MPa was recently achieved when PCL was composited with hydroxyapatite, in addition to imparting HA's osteoconductive properties [134]. However, this will need to be investigated *in vivo*, as rapid strength losses can occur as a result of degradation even with an initially high strength [135]. Moreover, and similar to metallic implants, degradation of the polymer products induces a local acidic change to the physiological milieu that can also have adverse effects on the

surrounding tissues. For example, previous work has shown PCL to induce inflammation and apoptosis [136, 137].

2.3.3.3 Bioactive-Glass

Bioactive -glasses (BG) are a group of synthetic glasses with unique bone-bonding characteristics. The first bioactive-glasses were based on a four-component network of silica (SiO_2), sodium oxide (Na_2O), calcium oxide (CaO) and phosphate (P_2O_5) [138], and have been extensively used in clinical applications in the form of particulates and solids [114]. The bioactivity of BG can be favourably tailored by varying the glass composition.

In vitro studies have shown that bioactive-glasses induce osteogenesis by stimulating the growth and proliferation of osteoblasts, as well as stimulating multipotent bone marrow cells [139, 140]. The chemical mechanism of bioactive-glass reaction is initiated after contact with body fluids, and subsequently, rapid ion exchange occurs between the extracellular fluids (ECF) that results in the dissolution of Si, Na, Ca and P ions. A silicon-rich layer forms through polycondensation of the hydrated silica groups, after which calcium and phosphates precipitate therein from the ECF [141, 142]. The newly-formed calcium phosphate layer provides a template for the formation of new bone by attracting extracellular proteins, and subsequently the cellular mechanism ensues. Sodium ions also play a role in the exchange between the implant and ECF [114]. The coating or incorporation of BG with metals and polymers have been thoroughly researched, as typical bio-metals and bio-polymers do not possess the aforementioned elements [139, 143, 144].

The action of BG enhances osteoblast activity, which in turn allows the defect site to proceed with bone remodelling. *In vivo* studies demonstrated the significant new bone formation and high local bone turnover achieved with bioactive-glass. In comparison to the control group (i.e. free of bioactive glass), in which new bone formation peaked at two weeks and decreased thereafter, fracture sites filled with bioactive glass microspheres continued to promote new bone formation; by the eighth week after operation, twice as much bone had formed than the control group [114].

As mentioned, the composition of bioactive-glasses can be modified, with doping of the aforementioned silica-based composition with copper, strontium or zinc promoting

angiogenesis. Traditional bioactive-glasses, including the widely-researched Bioglass®, exhibit poor mechanical properties, with strengths comparable to cancellous bone, and hence not suited for load-bearing application. Ceramifying the BG can obviate this issue, as demonstrated by Roohani-Esfahani et al. (2016) [145], whereby a scaffold with a porosity and compressive strength of 60 vol% and 139 MPa, respectively, was achieved using a proprietary glass-ceramic. In addition to possessing compressive strength comparable to cortical bone, *in vitro* and *in vivo* results revealed enhanced expression of osteogenic-related genes, and no adverse effects when implanted. However, one drawback of glass-ceramics is that the bioresorptioon is sacrificed [146]. Thus, further research is needed to balance high strength with resorbability.

2.3.3.4 Ceramics

Ceramics are brittle in nature, with poor tensile and fracture toughness properties. However, their excellent biological properties and no cytotoxicity cannot be disregarded, and for those reasons, there is ardent interest in producing BGS using ceramics [147]. There are a number of ceramics that display bioresorbable characteristics with excellent osseointegration, which is in contrast to metals. As mentioned, bioresorbability precludes the need for a second surgery, thereby halving surgery-associated risks. The advantages of ceramics over polymers are that intimate bonding between implant and tissue can be achieved, superior strength, and the degraded products do not induce inflammation [136]. Furthermore, the ceramic hydroxyapatite ($Ca_{10}(PO_4)_6(OH)_2$) (HA) has been demonstrated to induce bone regeneration in its synthetic form [148]. HA belongs to a sub-group of non-toxic ceramics referred to as calcium phosphates (CaP), which possess excellent bioactivity and varying rates of bioresorbability. Other ceramics are also biocompatible and have been clinically used as orthopaedic implants, such as zirconium oxide and aluminium oxide. These oxides generally have mechanical properties greater than CaP, however, they are not bioactive. Thus, one aim of CaP is to match the mechanical properties of alumina and zirconia without loss of bioactivity. As calcium phosphates are the focal materials researched in this project, they are given their own section in this chapter.

2.3.4 Calcium phosphates

Calcium phosphate ceramics are among the most widely utilised bioactive materials for dental and orthopaedic applications. They have been used in the form of granules, cements and porous scaffolds, as well as coatings for metallic implants [149]. This is due to their compositional resemblance to biological apatite that may allow the ceramics to be osteoconductive, osteoinductive and resorbable [150, 151]. Examples of CaP include tetracalcium phosphate, α- and β-tricalcium phosphate (TCP), and hydroxyapatite. Each CaP has unique mechanical and biological characteristics, and combination of the two, referred to as biphasic calcium phosphates (BCP), are implemented to tailor scaffold properties. For instance, HA can be combined with TCP, where the extent of dissolution depends on the HA-to-TCP ratio [152]. An additional attractive feature of CaP is their ability to form a strong bond with the surrounding tissue, which consequently yields a strong interaction between implant and bone (**Fig. 2-10** and **Fig. 2-11**). This is achieved by their ability to elicit a cellular event from the host akin to that of natural bone, which include osteoclasts and osteogenic cells. Moreover, elements with a positive mechanical or biological effect can be ionically substituted into the CaP lattice to achieve the desired property, and hence extending their versatility.

Stoichiometric HA belongs to a general group of ceramics known as apatites, represented by the formula:

$$\mathbf{Me_{10}(XO_4)_6Y_2}$$

Where Me is a divalent cation, XO_4 is a trivalent anion and Y can be a monovalent anion [153]. The chemical formula for hydroxyapatite is $Ca_{10}(PO_4)_6(OH)_2$, which is the double chemical formula as a result of two formula units found in the unit cell of HA. There are two known polymorphs of hydroxyapatite: monoclinic and hexagonal. The former polymorph, which occurs in the monoclinic space group $P2_1/b$, is easily destabilised in the presence of contaminants. For that reason, the hexagonal form, with a space group of $P6_3/m$, is more prevalently encountered in biological apatites [50].

The lattice parameters of the hexagonal structures are: a = 9.418 Å, c = 6.884 Å (ICD PDF No. 9-432). It contains crystallographically two cation sites, Ca(I) and Ca(II), and two separate anionic sites occupied by phosphate and hydroxyl group. There are four Ca(I) present in the unit cell, which are bonded to nine oxygen atoms. There are also six

Ca(II) present, which are surrounded by seven oxygen atoms, with the oxygen atoms of the hydroxyl group situated either above or below the cationic site [50].

The structure of bone apatite is different from stoichiometric hydroxyapatite that is typically synthesised in the laboratory. The former contains non-apatitic carbonate and hydrogen phosphate groups, substituted into the Y_2 and XO_4 group, respectively. These non-apatitic components are structurally and physically unstable, and are also reactive. The reactive nature provides particular physiochemical, biological, and chemical features important for the formation and dissolution of the apatite crystals within the physiological milieu. The non-apatitic substitutions decrease the crystal size, which results in an increase to the surface area compared to stoichiometric HA [154]. In addition, bone apatite contains traces of elements including magnesium, copper, zinc, fluoride and potassium [155]. **Fig. 2-9** provides examples of where cationic and anionic doping could occur.

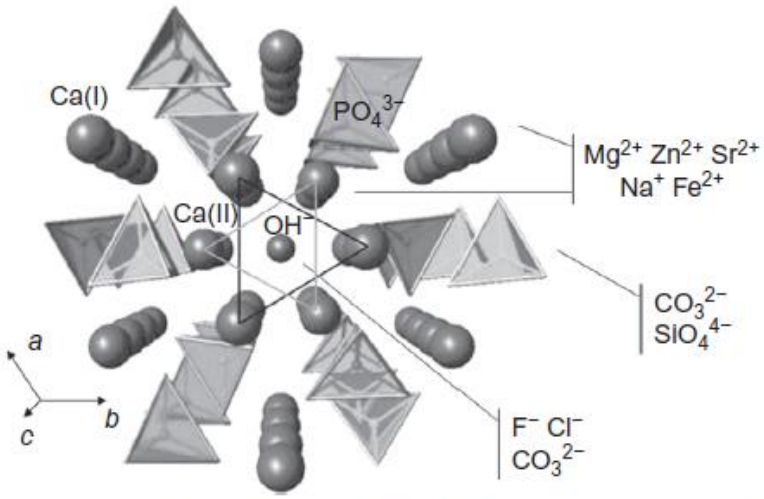

Fig. 2-9. *Schematic depicting the structural unit of hydroxyapatite, taken from the perspective along the c-axis of the hydroxyl channel environment. The figure illustrates the positioning of the two calcium sites, the phosphate and hydroxyl group, and in relation to one another. The schematic also provides examples of where possible ionic doping could occur [50].*

Similarly, TCP has been extensively researched as granules, scaffolds and surface coatings. TCP exists as different polymorphs, which affects the rate of resorption [156], however, these materials are generally mechanically weaker than HA. A comparison of the compressive strengths between HA- and TCP-honeycomb extruded scaffolds is the

subject of **Chapter 5**. The difference in the properties of hydroxyapatite and β-TCP are enumerated in **Table 2-3**. The properties, including solubility, thermal stability and mechanical properties, of calcium phosphate are a function of their crystal structure. The bioresorpability of CaP is governed by their solubility [157-161]. The stability of CaP was also verified by computer simulations [162]. Previous work has revealed that the inclusion of the hydroxyl group yields a greater atomic order, and thus more stable [159, 163, 164]. Consequently, the increase in stability decreases the bioactivity and osteoclastic resorption thereof [160]. This could explain why hydroxyapatite has a lower rate of bioactivity than β-TCP, as the latter does not have a hydroxyl group within its lattice. Another study has shown that the biphasic composition of β-TCP and HA yields higher bioactivity with increasing content of β-TCP [157]. Another factor are the lattice constants of the material. Moreover, the properties of CaPs may be influenced by their respective lattice constants. Investigations into the effect of magnesium-substituted β-TCP revealed that doped calcium phosphate was more stable than in its pure form; which was a reflection of a decrease in its lattice constants, and thereby resulted in a lower solubility [165, 166]. Conversely, ionic substitution of HA that leads to the expansion of crystal lattice increased its solubility [167]. Other studies have shown that a decrease in lattice constants produces CaP with greater mechanical properties [168, 169]. As previously, mentioned the Ca/P ratio also affects bioactivity, with a ratio of 1.5 reported to be more soluble than 1.67, and values below of 1.0 are not recommended because of their high solubility [24]. Royer et al. (1993) also demonstrated that the Ca/P ratio impacts the flexural strength of CaP; with optimal flexural strength observed between 1.60 and 1.66, with ratios outside this range exhibiting lower flexural strength [170]. A peak in strength at Ca/P ratio of approximately 1.67 has also been documented, with an exponential decrease in strength at higher ratios [171]. Crystal defects have also been reported in β-TCP and inferred to contribute to its bioactivity [172]. Other factors that also influence bioactivity include the surface charge and the capacity of the binding sites available for, for example, protein binding [173-179]. Therefore, the fundamental properties of calcium phosphates has an effect on their biological and mechanical properties. Comparing HA and β-TCP, the most frequently researched CaPs, the former possesses a higher Ca/P ratio, shorter lattice constants and a hydroxyl group, which all contribute to its relatively slower rate of bioactivity.

2.3.4.1 Stability in physiological systems

Calcium phosphate resorption is both cell- and dissolution-mediated [180]. The formation and dissolution of CaP is affected by the particle morphology and crystallinity thereof. Some CaP are insoluble in water with most being barely soluble in water. However, CaP solubility can vary with pH, temperature and the composition of the surrounding body fluid. CaP dissolutions occurs as a result of the exchange at the liquid-solid interface between implant and extracellular fluid, for all CaP. Calcium, phosphate and other ionic impurities, are transferred from the solid to the aqueous liquid phase through surface hydration of calcium and phosphate species. Equally, ionic transfer occurs from the liquid to the solid phase, wherein apatite nanocrystals form on the surface of the biomaterial [153]; in the presence of proteins, the *de novo* surface can contain both mineral and organic compounds. The dissolution is affected by the degree of crystallinity, with low crystallinity results in faster resorption [181]. Moreover, increasing the surface area via porosity can accelerate the ion exchange, and thus enhance resorption.

In vitro studies revealed that the surrounding proteins play a role in the ionic exchange mechanism. Their interaction with CaP is again dependent on particle size, composition and texture, but also on the proteins' features [182, 183]. Proteins can support or inhibit calcium phosphate nucleation and growth. For example, phosphorylated proteins were found to nucleate and grow calcium phosphate crystals [184]. In addition, proteins can adsorb onto the CaP substrate, and their adherence can either obstruct or facilitate the nucleation sites of CaP, thereby indirectly affecting apatite deposition. Biological tests had discovered bone cells, such as osteoblasts, adhere to the surface of the CaP substrate, in order to initiate the differentiation phase. Proteins are once again involved in this process, where integrin proteins form an adhesion between cell and substrate. The osteoblasts then secrete the relevant molecules for cell differentiation to take place [153].

Several parameters of calcium phosphates influence cellular activity [185]. The substrate's surface affects cell interaction, with both surface charge and topography contributing to cellular activity. Cells have been reported to sense and use topography as guidance for mineral deposition by varying the rate of proteins secreted by osteoblasts.

Table 2-3. *The formula, Ca/P ratio, crystal structure, symmetry, lattice constants, density solubility and stability of hydroxyapatite (HA), α- and β-tricalcium phosphate (TCP) and tetracalcium phosphate (TTCP). (*could not be precipitated from aqueous solutions) [158, 186].*

CaP	**Formula**	**Ca/P ratio**	**Crystal Structure**	**Symmetry**	**Lattice Paramters (Å)**	**Density (g/cm^3)**	**Solubility at 25 °C (-log(K_{sp}))**	**pH stability range in aqueous at 25 °C**
HA	$Ca_{10}(PO_4)_6(OH)_2$	1.67	Hexagonal	$P6_3/m$	a = b= 9.43 c= 6.87	3.16	116.8	9.5-12
β-TCP	$Ca_3(PO_4)_2$	1.5	Rhombohedral	R3c	a= b=10.43 c= 37.39	3.07	28.9	*
α-TCP	$Ca_3(PO_4)_2$	1.5	Monoclinic	$P2_1/a$	a= 12.88 b= 27.28 c = 15.21 β = 126.20°	2.86	25.5	*
TTCP	$Ca_4P_2O_9$	2.0	Monoclinic	$P2_1$	a = 7.023 b= 11.986 c= 9.473 β = 90.9	3.05	38-44	*

Similarly, surface charge has also been evinced to improve osteoblast behaviour, however, such advantage is short-lived as similar osteoblastic activities were eventually observed irrespective of surface charge [183].

Indeed, the surface topography will vary as dissolution progresses, due to the variation in free calcium and phosphate. Hence, the cellular activity is temporal-dependent. Furthermore, as the biomaterial contributes to the free calcium and phosphate, the composition of CaP (e.g. Ca/P ration) also impacts cellular activity, via the mechanism described above (section **2.1**). The solubility, and other properties, can be controlled through ionic substitution. The HA lattice includes several exchangeable sites that accommodate both anionic and cationic substitution [187]. Of interest are magnesium and silicon substitution that promote angiogenesis, and strontium for enhanced osteogenesis. An example of bone integrating to a silicon-doped hydroxyapatite implant are presented in **Fig. 2-10** and **Fig. 2-11**.

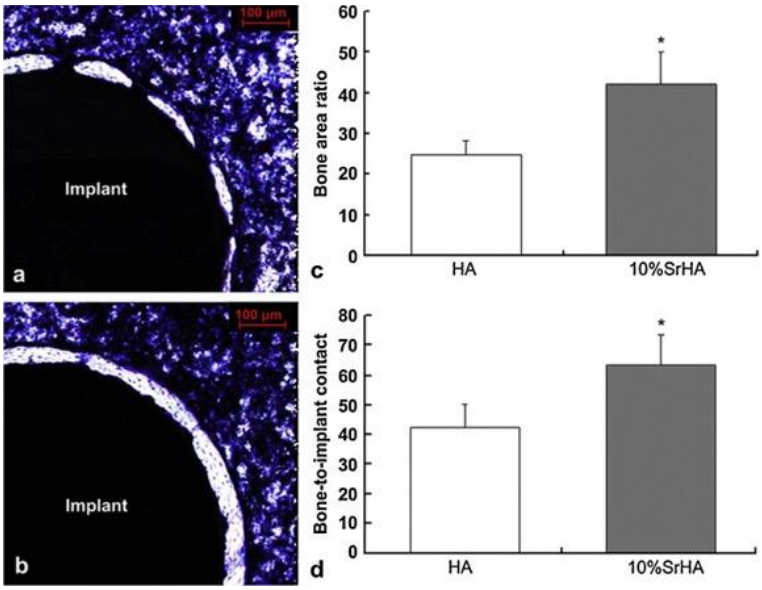

Fig. 2-10. *Enhanced bone formation due to HA substituted with 10 wt% strontium. The figure demonstrated toluidine blue-stained photographs of the proximal tibiae with* ***(a)*** *HA and* ***(b)*** *10 wt% Sr-HA implant three months post implantation [188].*

Furthermore, dopants can increase HA solubility by distorting the PO_4 tetrahedra [189]. For example, a charge imbalance created by the replacement of PO_4 for SiO_4 increases the electronegativity of the HA surface, which has been linked to increased surface adhesion. Furthermore, and as mentioned above (section **2.3.3.3**), silicon

dissolution promotes a silicon-rich layer that propagates bone bonding thereafter. For tricalcium phosphate, an *in vivo* study found that dissolution was the predominant degradation route [190], and hence the process is phase-dependent for calcium phosphates. The process is also dependent on the size of fragments, whereby dissolution is favoured in larger fragments [191].

Cell-mediated CaP resorption is driven by macrophage osteoclast activity. The process is similar to that observed for natural mineral resorption (section **2.1.2.1**), wherein a sealing zone is formed on the substrate, and hydrogen ions and lysing enzymes are secreted [192]. Furthermore, the osteoclast activity can be inhibited when the release of Ca^{2+} exceeds a certain threshold [153], and thus the initial calcium composition of the CaP affects the rate of material degradation. In addition to calcium ions, dopants can affect the rate of resorption. For example, fluoride and zinc have been revealed to inhibit osteoclast behaviour. Conversely, the incorporation of carbonates can accelerate osteoclast resorption. Once more, surface energy and topography are known to influence osteoclast adherence, with a rougher surface enhances adherence thereof [153].

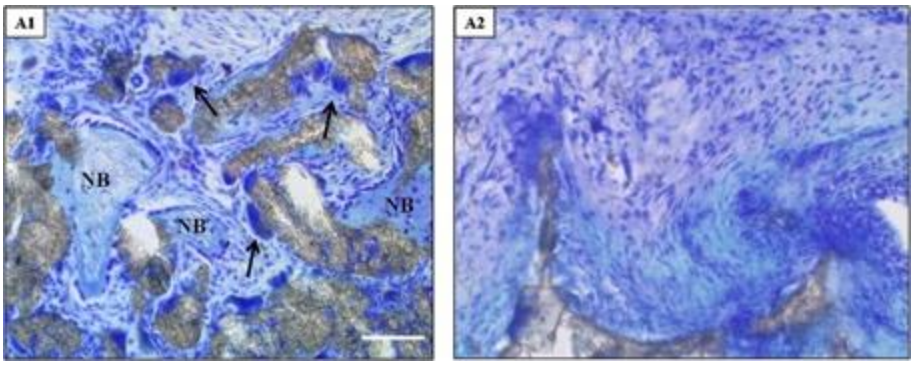

Fig. 2-11. *More histological evidence demonstrating new bone formation (delineated as NB) due to hydroxyapatite scaffolds. The researchers also reported the process was mediated by osteoblasts and osteoclasts (black arrows) [148].*

In addition to the surface, the bulk morphology influences bioactivity, namely the previously discussed porosity. It was surmised that osteoinductivity of CaP scaffolds may be due to the entrapment and concentration of growth factors, which are directly involved in osteoblast differentiation, by the combination of both micro- and macro-porosity.[187, 193].

In summary, calcium phosphates possess exceptional biological responses, thus making them a unique sub-group of ceramics for orthopaedic applications. Their necessity is further highlighted by their use as the reinforcing phase in polymeric scaffolds and coatings for metallic implants, aimed at both imparting desirable mechanical and biological properties. CaP can also be used as cements, granules and scaffolds, hence further demonstrating their utility as BGS. Moreover, CaP can be favourably tuned by ionic substitution to vary their biological and mechanical properties. As mentioned, different bone sites exhibit varying strengths and healing rates, and hence the ability to tailor both is desirable.

To review, the ideal bone graft should be (i) resorbable, (ii) osteoinductive and osteoconductive, and (iii) mechanically strong. It is the latter point that has restricted CaP usage for load-bearing application. Although, dense HA can be fabricated to possess compressive strengths several folds greater than cortical bone, the strength decreases significantly when pores are introduced. Consequently, fabrication of porous CaP scaffolds typically results in compressive strengths significantly lower than what is required for weight-bearing. A few factors have already been mentioned that can be researched to improve this, such as the versatility of HA to be ionically-substituted. However, scaffold strength is also a function of the fabrication technique employed, and thus consideration should be given thereto. Recently, techniques capable of achieving structured porosity have demonstrated promising compressive strength values. The following section explores the conventional fabrication techniques used, as well as *state of the art* techniques.

2.4 Porous Scaffold Fabrication Techniques

Porosity is a key component for attaining the ideal bone graft substitute, and there are a variety of fabrication techniques used to generate porous calcium phosphate scaffolds. Osteoconductive properties of CaP are partly attributed to scaffolds exhibiting macro-pores of above 100 μm in size, with a total interconnected porosity of at least 60 vol%. These requirements correspond to that of cellular ceramics [187, 194]. Examples of cellular ceramic fabrication techniques that are either widely researched for BGS, or of interest to this work are described in this section.

Fig. 2-12 delineates the processing steps involved in conventional ceramic fabrication techniques. The steps involved include mixing of the raw materials, which typically consist of a ceramic, organic additives and solvents. This is followed by the fabrication step that shapes the admixture of raw materials into a scaffold, and may include the incorporation of pores therein. The final stage is a sequence of heat treatments used to remove the organic additives and solvents, as well as sintering the ceramic particles to achieve permanence.

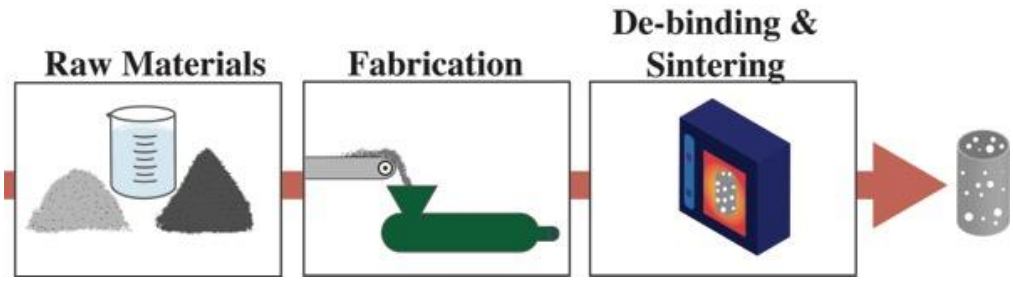

Fig. 2-12. Schematic depicting the general processes involved in fabricating a porous scaffold.

2.4.1 Gel Casting

Gel casting is a near-net porous forming technique that has been widely researched as a CaP fabrication route [195, 196]. The process entails the *in situ* polymerisation and gelation of organic additives that are subsequently thermally degraded once dried. The gelation of the additives results in rapid casting, and an interconnected porous structure with typically spherical pores. Although the technique is rapid and simple, CaP with low compressive strengths have been attained thus far (below 20 MPa [197, 198]), which make it unsuitable for load-bearing application.

2.4.2 Sacrificial Technique - Foam Replication

The foam replication method revolves around using a foam-like material, typically polyurethane sponge, that is dipped into a ceramic slurry [199]. The slurry comprises CaP powder, organic additives and a solvent. The CaP slurry adheres to the foam template to form a green body that is then dried, de-bound and subsequently sintered to generate a porous scaffold. The porosity and scaffold geometry are controlled by the foam-like

material, hence tailoring scaffold features using this technique can be achieved by varying the foam template. For example, if pore sizes of 500 μm are needed, then a polymer template with comparable pore sizes is selected.

This technique is relatively simple, inexpensive and requires minimal components. The pores attained are highly interconnected, and varying pore sizes can be generated, albeit with a stochastic orientation. Scaffolds fabricated by this method are mechanically weak, as **Table 2-4** demonstrates. It has been surmised that the stochastic porosity and the high polymer content are the cause of the poor mechanical properties. The extraction of polymer can lead to residual stresses within the scaffold. Additionally, the extraction of polymer results in hollow struts, which are mechanically weak [187].

Table 2-4. *Examples of porosity, pore sizes and compressive strengths of scaffolds fabricated via the foam replication technique. Despite the techniques popularity, it produces scaffolds with weak compressive strengths. Note porous titanium scaffolds were fabricated using this approach with considerably low mechanical strengths.*

Group	Material	Porosity (vol%)	Pore Sizes (μm)	Compressive Strength (MPa)
Lett **[200]**	HA	50	200	0.85
Tripathi **[201]**	HA	~70	100-300	1.3
Swain **[202]**	HA	56	50-125	0.85
Wang **[203]**	BCP*	77.1	200-700	1.18
Lee **[204]**	Titanium	~70	Undisclosed	18

*Biphasic calcium phosphate

2.4.3 Sacrificial Technique – Porogens

Another sacrificial technique is the use of porogens, also referred to as pore formers, wherein additives are used to generate the pore phase. In this approach, the porogens are dispersed within a ceramic slurry, and the extraction thereof, whether through thermal or solvent extraction, generates the pores. This approach can in its simplest form be combined with dense ceramic fabrication processes, for example powder compaction techniques, to generate porous structures. In addition, porogens have been utilised in

conjunction with other porous fabrication techniques, such as freeze-casting [205] and additive manufacturing [206], to further tailor the pore morphology, including pore sizes and interconnectivity. Examples of were porogens have been used are tabulated in **Table 2-5**. Drawbacks of using porogens is the lack of control with regards to their dispersibility, as some have been known to agglomerate resulting in unwanted pore sizes. Moreover, the possibility of imparting residual stresses is of concern.

Table 2-5. *Examples of porogen use in hydroxyapatite fabrication. Porogens are used to alter the pore architecture of scaffolds, and have been incorporated in various fabrication techniques.*

Group	Technique	Porogen Agent	Comments
Liu **[207]**	Cold Pressing	PVB*	Impart desirable pore sizes to an otherwise dense ceramic fabrication technique.
Liu **[208]**	Slip Casting	PVB*	Impart desirable pore sizes to an otherwise dense ceramic fabrication technique.
Dash **[209]**	Gel Casting	Naphthalene	Used naphthalene to further tailor pore morphology
Zuo **[205]**	Freeze Casting	PMMA**	Experimented with PMMA of varying particle sizes
Koh **[210]**	Ceramic Extrusion	Carbon Black	Impart desirable pore sizes to an otherwise dense ceramic fabrication technique.

*Poly vinyl butryal

**Poly(methyl methacrylate)

2.4.4 Gas Foaming

Gas foaming was developed to avoid using large polymer quantity and toxic solvents. The process entails the pressurised use of an inert gas, such as nitrogen, to generate gas bubbles within a polymer mould. The advantages of this technique include high macro-pore sizes generated and high porosity values. However, due to the lack of control over

the formation of the gas, it is difficult to control the pore architecture of the scaffolds. Consequently, forming interconnected porosity, and controlling pore diameter is a challenge [211, 212].

2.4.5 Freeze-casting

Freeze-casting involves the sublimation of a CaP slurry to generate porosity. In this technique, the solvent, which acts as a temporary binder, is first frozen to compact the ceramic particles and forms distinct frozen phases. Upon sublimation, the frozen phases are removed thus generating pores. The advantages of the technique include periodic porosity, interconnectivity and high compressive strengths [213]. However, the disadvantages of freeze-casting include limited porosity geometry and limited macro-pore sizes. Furthermore, concerns have been raised whether the technique can be industrially scaled, and if large-sized scaffolds can be generated [214].

2.4.6 Injection moulding

Hydroxyapatite has been fabricated using ceramic injection moulding (CIM) [215, 216]. CIM is widely used in numerous continuous manufacturing applications, including metals, glass and elastomers. The process involves injecting heated ceramic particles enveloped by thermoplastic polymers into a mould, after which the green body is allowed to cool down. The advantages of CIM are complex shapes can be fashioned; varying porous architecture, including graded porosity can be formed; and industrially scalable with a high degree of accuracy [217, 218]. Currently, porosity of less than 40 vol% has been achieved, with an elastic modulus of approximately 2 GPa [216], which make scaffolds fashioned by CIM unsuitable for load-bearing applications (trabecular: 6.9 GPa; cortex: 25 GPa [219]).

2.4.7 Solid Freeform Fabrication

Solid freeform fabrication (SFF) are considered to be the *state of the art* for fabricating materials, including metals, glass and polymers. There are several SFF techniques that use different means to form three-dimensional, porous structures in an additive manner;

the commonality being the use of a computer-aided design for generating structures layer-by layer. This allows for complex geometries to be obtained, with a relatively high spatial resolution. SFF approaches include the use of a laser to sinter CaP powders layer-by-layer [220], or an inkjet print-head that deposits inks that bind adjacent CaP powders to form green bodies [221].

Of particular interest is robocasting, or also referred to as direct ink writing. The technique is a modified version of ceramic extrusion, whereby a ceramic paste is extruded through a computer-numerically-controlled nozzle. The paste is deposited layer-by-layer and can achieve relatively high spatial resolution. This technique has been demonstrated to attain high compressive strengths for HA [222], as well as bioactive-glass [145], that are comparable to cortical bone. However, like other SFF techniques, robocasting is still in its infancy, and more work is needed to address existing issues, such as cost, fabrication of large-sized scaffolds and industrial scalability [105, 214].

2.4.8 Summary of Fabrication Techniques

To summarise, there are several techniques that can be used to fabricate calcium phosphate scaffolds with desirable porosity. In all of the aforementioned techniques, the process starts with CaP raw powders that are then shaped and sintered to attain permanence. Furthermore, all of the techniques use polymers in varying capacities, such as binders, pore formers, or foam templates. However, as mentioned, polymers can have a detrimental effect on the final scaffold. Indeed, polymers are needed for most fabrication techniques, however, minimising polymer content will facilitate downstream processes. One fabrication technique that has not been thoroughly explored is ceramic honeycomb extrusion. Using this method, interconnected pores are generated by physical means, thereby minimising the need for polymers and chemistry knowledge. In addition, the interconnected pores can be achieved in a controlled manner and tailored with respect to size and morphology. The following section will present the rationale for using ceramic honeycomb extrusion for fabricating bone graft substitutes.

2.4.9 Processing Parameters

2.4.9.1 The effect of the Raw Ceramic Powder on the Finished Product

The fabrication process of most bioscaffolds commences with the raw ceramic powder, and the processing parameters applied thereto affects the final scaffold properties. A powder consists of particles with a relatively large surface area per weight, which confers the advantage of easily being sintered when subjected to high temperatures; forming a single, large coalesced body [223]. The selection criteria for powders depend on the final properties of the finished article desired. For most research, the goal is to achieve a high-strength scaffold comparable to that of natural bone, and for that the particle morphology and chemical purity of the powder are important. For powder morphology, spheroidal particles are favoured as they are likely to attain a higher sintered density than acicular morphologies [224, 225], with a previous study further demonstrating the incorporation of the latter into a spheroidal particulate system decreases the mechanical properties as a direct result [226]. It is worth noting that acicular have the potential to achieve a high sintering density, but this requires a technique capable to orienting the particles in a manner that improves particle contact [227].

Another particle property to consider is the particle size distribution. Similar to morphology, the goal is to achieve a particle size distribution that can maximise particle packing. A powder consisting of unimodal particle size results in over 30% voids spaces, and hence is not considered ideal for packing [228, 229]. Spath et al. (2015) have circumvented this problem by adding 25 wt% relatively finer particles, which resulted in a higher particle packing, and consequently, improved the mechanical strength of their HA scaffolds by 55% compared to the strength of single particle fraction [230]. Cunningham et al. (2009) examined two powders and reported a higher solid loading with their HA slurry when the powder exhibited a wider particle size distribution [231]. Kaviani and Zamanian (2015) revealed that the incorporation of nano-sized HA particles into micron-sized HA particle, resulted in freeze-casted scaffolds with higher mechanical strength [232].

Regarding the particle size themselves, this will depend on the fabrication technique. For example, Zamanian et al. (2013) investigated the effects of raw powders with particle sizes of 1.69 and 3. 9 μm on freeze-casted scaffolds, and discovered that the latter yielded scaffolds with higher compressive strengths, across sintering temperatures

ranging from 1250 to 1350 °C; with increases ranging from 37.5% to ~250% [233]. Michna et al. (2005) demonstrated that by increasing the particle size via calcination from nano to micron-sized a higher hydroxyapatite solid loading could be achieved during slip formulation [234]. The same was observed by Ryabenkova et al. (2017) when they compared two different powders that had particle sizes below 100 nm: they found the finer powder (cross-sectional area of 182 nm^2) exhibited a ten-fold increase in initial viscosity compared to the relatively coarser powder (cross-sectional area of 410 nm^2), thereby resulting in a lower solids loading [235].

Furthermore, the starting powder purity will also need to be considered, as this is correlated to thermal stability [236] and mechanical properties [237]. Stoichiometric HA possess a calcium-to-phosphate (Ca/P) ration of 1.67, and, for example, reducing the ratio results in HA powder with higher tendency to transform into tricalcium phosphate [238, 239]. Prior studies have demonstrated that a stoichiometric hydroxyapatite powder exhibits higher mechanical properties over a non-stoichiometric hydroxyapatite powder [237]. Chaudhry et al. (2011) demonstrated that the Ca/P ratio of HA powders effects their propensity to decompose into tricalcium phosphate. A Ca/P ratio of 1.39 was found to decompose into TCP at 950 °C, whereas no sign of secondary phases where observed at 750 and 850 °C by XRD. In contrast, their HA powder with a Ca/P ratio of 1.42 displayed no evidence of TCP at 1000 °C; furthermore, they revealed the higher Ca/P resulted in scaffolds with smaller grain sizes [240].

However, Merry et al. (1998) found no significant difference in flexural strength between stoichiometric and non-stoichiometric HA [241], whereas Raynaud et al. (2002) evidenced a higher flexural strength with HA with a Ca/P ratio of 1.65 compared to the stoichiometric 1.67 [242]. Mostafa (2005) reported that a powder possessing Ca/P ratio of 1.58 achieved a sintering density of ~ 90% and a compressive strength of 87 MPa; whereas a powder with a ratio of 1.67 achieved a maximum sintering density and compressive strength of ~75% and 58 MPa, respectively [243]. These studies suggest that there are other factors to consider alongside the Ca/P ratio. The presence of hydrogen phosphate in the starting raw material is indicative of calcium-deficient hydroxyapatite, and has been noted to expedited phase decomposition during sintering [244-246].

In summary, the particle properties will need to be considered holistically with regards to both particle morphology and purity. Thus, characterising the powder using

scanning electron microscopy to determine morphology; surface area analysis to determine surface area; particle size analysis to determine particle size and distribution; as well as x-ray diffraction and vibrational spectroscopy will be needed to determine the phase purity thereof. Such characterisations will elucidate the nature of the raw ceramic, and help identify possible traits that can be modified to maximise the mechanical properties of the scaffold.

2.4.9.2 Solids Loading Depends on the Fabrication Technique

Most fabrication techniques entail the use of organic additives to plasticise the hydroxyapatite, and thereby allowing it to be shaped. Thus, there is a limit to the maximum amount of hydroxyapatite within the admixture, and this is frequently referred to as solids loading. However, a balance is needed between achieving a high solids loading, which minimises defect occurrence and article shrinkage; with the organic additives to allow the HA to be shaped [228]. With all other factors being equal, previous studies have demonstrated that a higher solids loading yields higher compressive strengths, but at the expense of porosity [213, 247-249]. The maximum solids loading that can be achieved will indeed depend on the fabrication techniques working viscosity, the solvent's hydrogen-bonding abilities, and any other additives used [223]. Solids loading used for fabricating porous CaP scaffolds vary greatly, from as low as 5 vol% [250] to 60 vol% [251], but generally the values are between 30-55 vol% [209, 252-257].

2.4.9.3 Removal of the Organic Additives

The organic additives employed to achieve a workable HA material will need to be removed to obviate the formation of defects in the finished product. If a solvent is incorporated then drying thereof will be required. Depending on the solvent this can be achieved at room temperature [239, 258, 259], or oven-dried at, for example at 70 °C [260] or 110 °C [200]. The duration can vary from three days [261] to as short as one hour [260], with a drying duration of $\leq$24 hours numerously used [239, 258, 262-264].

Where a polymer is incorporated, then extraction thereof will be required. Of the available methods, the thermal approach is most frequently utilised, whereby high temperatures are used to burn-out the organic additives [229]. Here, process

considerations include the temperature of burnout, the dwell time and at the heating rate. The temperature at which to extract the polymer will depend on the degradation temperature thereof, which thermal gravimetric analysis could be used to help elucidate. Investigating the literature revealed that the temperature of extraction varied from 250 to 900 °C [265, 266], however two former studies foregone a dedicated debinding stage [267, 268], and a multi-stage temperature approach has been previously incorporated [269-271]. Hitherto heating rates varied from 0.3 to 15 °C/min [261, 272], however the latter is seldom used with numerous researchers opting for a rate of 3 °C/min or below [255, 265, 270, 273-275]. Regarding the dwell time, this ranged from 0.5 [265] to 20 [276] hours, with a dwell time of 4 hours or less most frequently selected [255, 269, 275, 277]. The dwell time is a function of additive content and the thickness of the green-body. For instance, producing a large green-body will require more time for additive extraction due to the distance the binder travels therein [229]. In summary, a range of thermal parameters have been previously used, and verily TGA and other thermal techniques will be needed, for example dilatometry and differential scanning calorimetry, to facilitate the decision making.

2.4.9.4 Achieving Permanence of the Hydroxyapatite Scaffold

The process of sintering is needed to produce a single, coalesced body from a particulate system. Previous studies have achieved this with temperatures as low as 600 °C [201, 278]. Different dwell periods and heating rates have also been used, ranging from 1 to 10 hours [201, 279, 280], and 1 to 10 °C/min [278, 281], respectively. Indeed the sintering parameters will depend on the processing stages proceeding the sintering stage, such as the purity of the raw powder, and size of article to be sintered. Previous studies have suggested that higher sintering temperatures (above 1000 °C) results leads to better biological properties, such as osteocalcin, bone sialoprotein, and osteonectin protein production; and cell proliferation is higher too; whereas Type I collagen production was comparable between both sintering temperatures [282, 283]. However, at elevated temperatures the problem of phase transformation is encountered, which has been previously reported to occur at a temperature as low as 700 °C [284], but occurring more frequently at temperatures above 1100 °C [209, 239, 281]. As previously stated, the phase purity of the raw powder affects the phase stability of the ceramic at elevated

temperatures, with other studies sintering until 1300 °C or above without evidence of phase decomposition [213, 232, 247, 285].

2.4.9.5 Chemical Structural Analyses for Determining Phase Purity

It is evident that the phase composition of hydroxyapatite requires monitoring, particularly when subjected to high temperatures when it is susceptible to phase transformation. Determining phase composition could be achieved through different methods. Although thermal analyses provide an intimation [286-288], particularly when scanning for events over a wide temperature range, physicochemical characterisation techniques are better suited thereto. Two of the most frequently used physicochemical techniques used to determine phase purity are XRD and FTIR.

XRD is employed to confirm the phase composition of HA because it is able to provide a unique pattern thereof with respect to its crystal structure. **Fig. 2-13** presents an XRD pattern of bone apatite (a), nano-sized crystals, crystalline HA (b) and a highly crystallised HA (c). The figure illustrates a highly crystallised HA has peaks at approximately 26, 28.5°, 29.5°, 32°, 32.5°, 33°, 34.5°, 35.5°, 39.5° and 40°. Thus, a pattern conforming thereto confirms the presence of HA. To further illustrate this point, **Fig. 2-14** presents examples of commonly secondary phases found in sintered HA: β-Tricalcium phosphate (a), α-tricalcium phosphate (b) and tetracalcium phosphate (c) XRD patterns.

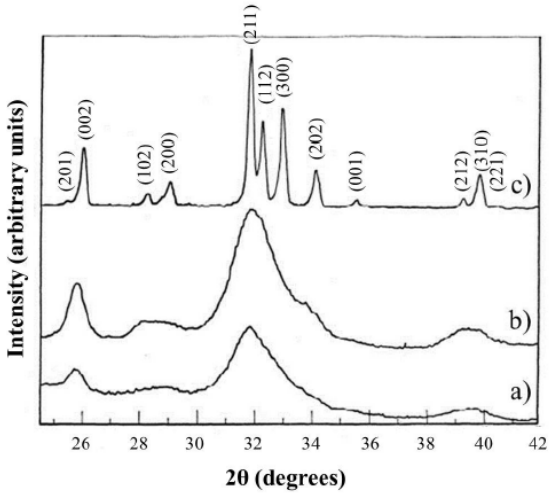

Fig. 2-13. *XRD pattern of bone apatite (a), nano-sized crystal HA (b) and a highly crystallised HA (c) [289].*

As the figure illustrates, the CaP display an XRD pattern distinct from HA. For example, β-TCP possesses a single intense peak at 31° not observed in HA (**Fig. 2-14** (**a**)); α-TCP exhibits a main peak at 30.7° that is not displayed by HA (**Fig. 2-14** (**b**)); and TTCP has an intense peak at 30° that is also not observed in the XRD pattern of HA (**Fig. 2-14** (**c**)).

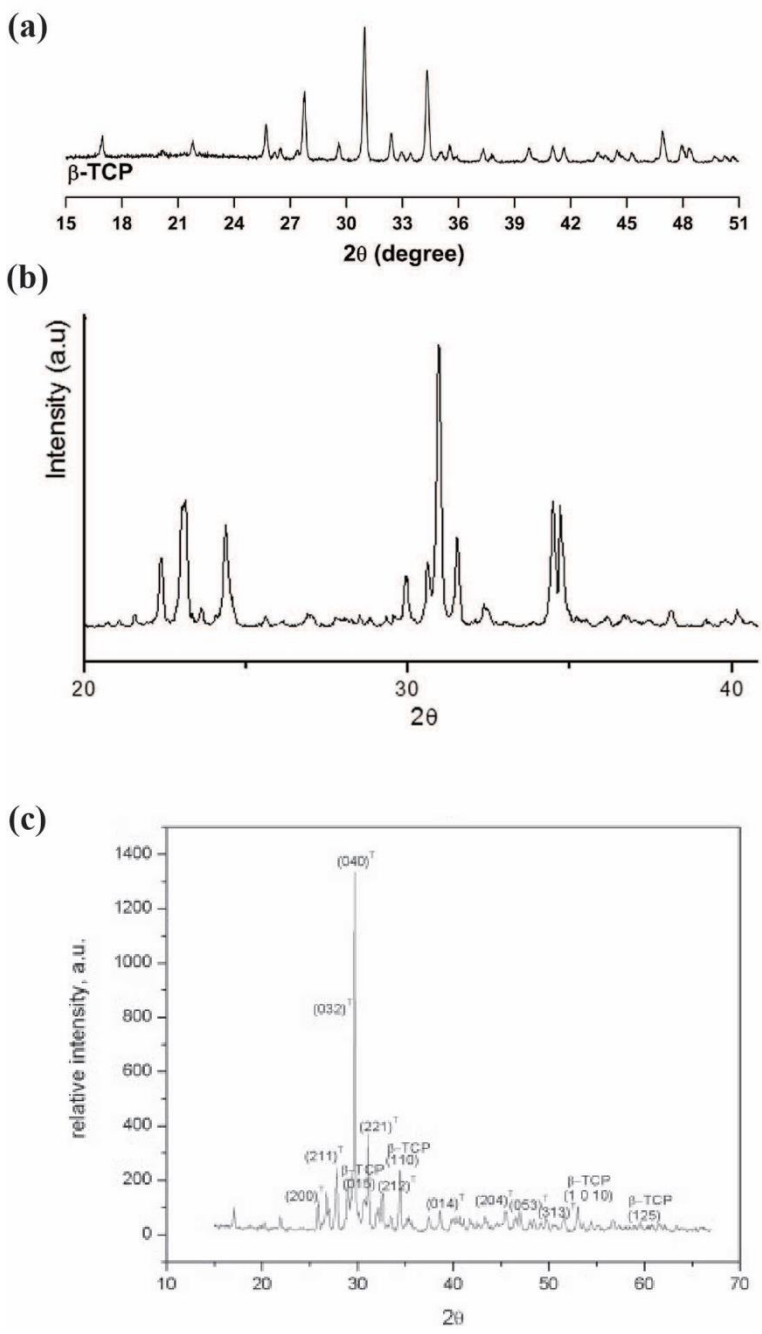

Fig. 2-14*. Representative XRD Pattern of β-Tricalcium phosphate (a) [290], α-tricalcium phosphate (b) [291] and tetracalcium phosphate (c) [292]. The figure illustrates the similarity and differences in peak position and relative intensity of said calcium phosphates to HA.*

There are, however, examples of peak proximation, and in some cases an overlap, and for that reason a second physicochemical technique could facilitate in verifying the phase composition of the analysed material.

A second technique that is widely used in the literature is FTIR. This is a vibrational spectroscopic technique that is relatively simple, yields reproducible data and only requires small amounts (micrograms) of sample for analysis [293]. FTIR elucidates the functional group present in the sample, which for stoichiometric hydroxyapatite are the phosphate and hydroxyl bands. An example of a hydroxyapatite spectrum is presented in **Fig. 2-15**, with a frequency ranging from 4000 to 500 cm^{-1}, or a wavelength ranging from 2.5 to 20 microns. The figure illustrates a solitary peak at approximately 3570 cm^{-1}, which pertains to the hydroxyl stretching mode group. The remainder of the troughs are found at frequencies below 1500 cm^{-1}: 1090 and1040 cm^{-1} troughs are the triply degenerate v_3 antisymmetric phosphate stretching mode; 960 cm^{-1} band is the v_1 nondegenerate phosphate symmetric stretching mode; 630 cm^{-1} is the hydroxyl libration mode vibrating; and 601 and 561 cm^{-1} are assigned to the triply degenerate v_4 phosphate bending mode [294-304]. Carbonate groups may also exist in HA between 1650 and 1300 cm^{-1}; the presence thereof reveals a non-stoichiometric HA [299]. Hydrogen phosphate is another possible contaminant found in HA, which has a vibrational mode at approximately 866 cm^{-1} [246], which is characteristic of calcium deficient HA [244, 245]. Furthermore, the disappearance of the hydroxyl bands at ~3570 [305-307] and ~630 cm^{-1} [306, 307] that is associated with dehydration, is indicative of a phase transformation to an anhydrous calcium phosphate, possibly β-TCP. Another previously encountered bands include at ~ 1120 [308-311] and ~ 945 cm^{-1} [307, 309, 312], which have also been ascribed to β-TCP, and verified by XRD [308-310] and EDX [309]. Regarding TTCP and α-TCP, a broad band between 1200 to 950 cm^{-1} has previously been attributed thereto [298, 313]. Hence, FTIR is a valuable characterising technique for determining stoichiometric HA.

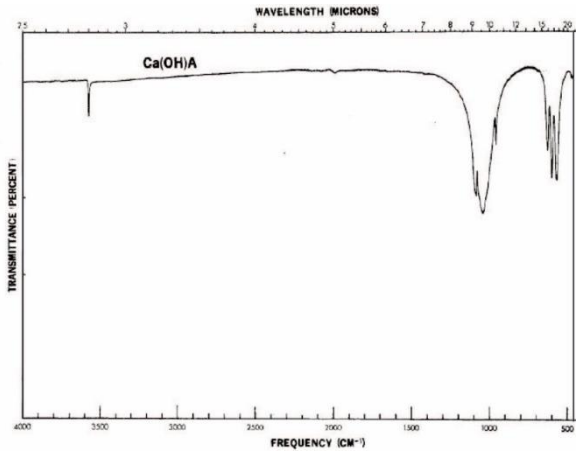

Fig. 2-15. *A representative FTIR trace of hydroxyapatite adapted from [294]. The figure illustrates the frequency positions of the bands pertaining to hydroxyapatite.*

2.5 The Case for Ceramic Honeycomb Extrusion

Extrusion is a widely used near-net fabrication technique for industrial production of metals, polymers, glass and ceramics with a constant cross-sectional geometry. The technique is favoured for its simplicity, low capital and running costs, and can be integrated with other technologies, such as a mixer to streamline the process of paste formulation and shaping [314]. **Table 2-6** presents the shaping parameters of extrusion as well as two others commonly used for ceramics. It can be seen that extrusion provides a compromise between the other two shaping techniques, whereby industrially-medium sized articles with quite complex geometries and high green densities can be obtained; at a high productivity rate, whilst requiring low plant complexity and production costs. For this reason, extrusion is favoured for the fabrication of bricks, ceramic pipes, heat regenerator application, and catalytic supports for catalytic converters. In the latter two they are favoured as they are said to generate high strength and a high level of porosity [315, 316], and thus it was hypothesised that these properties could be translated to bioceramic fabrication.

Table 2-6. *Table presenting the shaping parameters of extrusion and two others that are commonly used: dry pressing and slip casting. Adapted from ref. [314].*

	Dry Pressing	Extruding	Slip Casting
Avg. solvent content before shaping	5 wt%	17 wt%	28 wt%
Avg. solvent content after shaping	5 wt%	17 wt%	18 wt%
Duration of shaping process	Low	Medium	High
Shaping energy consumption	High	Medium	Low
Green Density	High	Medium-High	Low
Green Deformability	Low	Medium	High
Shrinkage after firing	Low	Medium	High
Drying energy consumption	Low	High	High
Geometry of shaped article	Simple	Quite complex	Complex
Article size	Small	Medium	Large
Article thickness	Constant	Variable	High variable
Productivity	Very high	High	Low
Automation level	High	High	Low
Plant complexity	Medium	Low	High
Specific production costs	Medium	Low	High

2.5.1 Aspects of Ceramic extrusion

A schematic outlining the steps involved in ceramic extrusion is presented in **Fig. 2-16**. Having formulated an extrudable ceramic paste, the ceramic extrusion process consists of loading a ceramic paste into a barrel and then passing it through a shaped orifice, known as the extrusion die. From here, the shaped body is then cut into the desired length that will be dried and subsequently sintered. Hence, there are two aspects to the extrusion

process: the extruder and the ceramic paste. A brief introduction into the extrusion facets is provided below, and more will be detailed in **Chapter 4**.

2.5.1.1 Extruder

The extruder consists of a propulsion system, the barrel and the honeycomb die. The propulsion system can either be piston or auger (screw) driven, and each possesses advantages and disadvantages [314]. The piston extruder is more suitable for a laboratory-scaled extrusion, when compared to an auger extruder, for the following reasons:

- Smaller material batches are required;
- Lower moisture content is needed because less plasticity is required;
- Easier to actuate the propulsion system;
- Lower contamination rates;
- Easier to clean.

The main disadvantage of piston extrusion is the reduced throughput rate, as time is needed for loading the ceramic paste in-between extrusions, as well as de-airing the new paste. However, this is less of a concern for laboratory-scale settings. As such, piston extrusion was employed for this research project.

The barrel is where the ceramic paste is contained prior to extrusion, and has the die attached at one end. The extrusion die is the part of the system that provides the green body with the uniform cross-sectional shape. The die can range from a simply cylindrical orifice for fabricating ceramic rods, to a honeycomb die for fabricating a porous green body.

2.5.1.2 Ceramic Paste

The ceramic paste, or ceramic body, consists of ceramic particles suspended within a polymeric gel. It is the gel that imparts plasticity and hence allows the ceramic paste to flow through the extruder. A simple ceramic paste comprises ceramic powder, binder and water; although additional organic additives can be used to facilitate extrusion, such as lubricants and plasticisers. However, every additional component complicates the

extraction process, as the non-ceramic components need to be removed, and each one will have its own extraction conditions that will need to be accommodated [223]. The ultimate goal of formulating a ceramic paste, as in most fabrication techniques, is to achieve a body with a high ceramic content, which will reduce cracking during downstream processes.

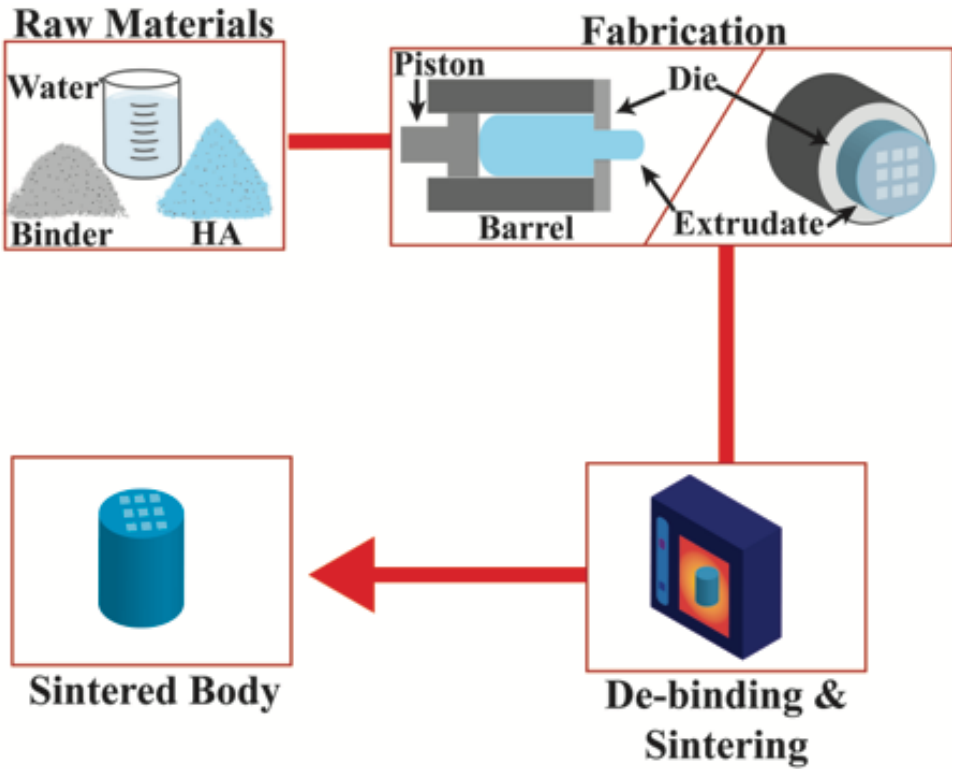

***Fig. 2-16**. Schematic depicting the stages in the extrusion process.*

2.5.2 The Case for Structured Porosity

Compressive strength is used as an indicator of mechanical performance for CaP scaffolds, as it is the principle form of stress load-bearing-bones are subjected to [317]. A scaffold with aligned pores (**Fig. 2-17**) is purported to achieve higher mechanical strengths than scaffolds with stochastic pores (**Figure 2-18**) because of the orientation of the struts. Stochastic-oriented struts are subjected to various mechanical stresses under axial loading due to their random orientation [105, 194, 318]. This was recently verified using X-ray tomography [319]. For example, in a stochastic porous architecture under compressive loading (e.g. foams), the structure is strong in some regions and weak in

others, and it is the weak that reduces the overall strength. These weak regions are due to struts oriented perpendicularly to the load that will exhibit flexural stress, which ceramics are known to have a lower tolerance for than compressive stress, thereby resulting in early failure. For an aligned porous structure, subjecting compressive load thereto results in the struts exhibiting only compressive stress. Indeed, and just as cortical bones are, such scaffolds are anisotropic, where applying the load perpendicular to the aligned struts would result in flexural stresses to the struts, and hence lower strength compared to parallel compressive loading. The anisotropic mechanical properties of extruded scaffolds are examined in **Chapter 5** and **Chapter 6**.

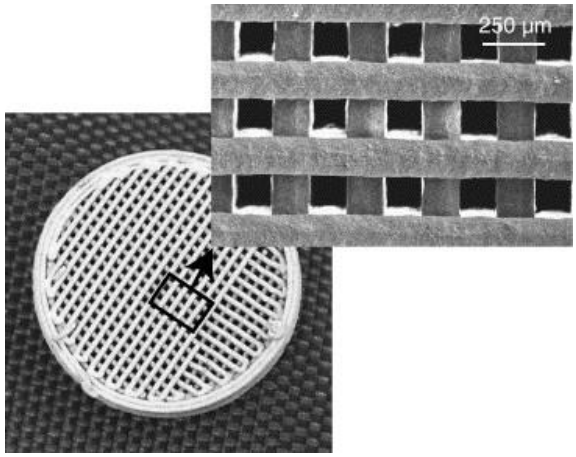

Fig. 2-17. *An example of a scaffold with structured porosity, prepared by robocasting [320].*

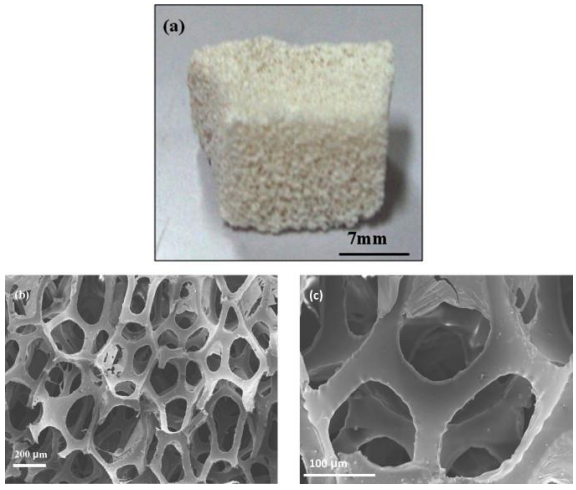

Figure 2-18. *Figure illustrating an example of a stochastic porous structure, fabricated via the polymer sponge replication method [201].*

Perusal of the literature reveals that techniques capable of fabricating aligned porous scaffolds yield remarkable compressive strengths, which are presented in **Table 2-7**. Such techniques include freeze-casting and robocasting; however, honeycomb extrusion would require less expertise, lower capital and running costs, and is capable of achieving large-sized scaffolds for large segmental defects. For example, varying the porosity in freeze-casting would require knowledge of solvent freezing kinetics, whereas in extrusion this can be easily accomplished by changing the die (e.g. from square-shaped pores to hexagonal-shaped). Furthermore, additional steps are required in freeze-casting compared to extrusion, such as freezing and sublimation, which makes the process considerably slower than extrusion[1]. On the other hand, robocasting is fast, which is beneficial in both research and industrial settings; and can generate complex structures, provided they can be modelled using a computer-aided design software. However, considerable expertise is required, from knowledge of generating computer-aided design models to maintaining the electrical components of the instrument; such expertise may hinder the realisation of robocasting if not available. Nonetheless, these techniques illustrate the potential of incorporating structured porosity for attaining high-strength scaffolds, and by comparison, honeycomb extrusion is already a well-established technique. Lastly, the low production costings of extrusion will be of particular interest to countries with rising healthcare expenses.

Table 2-7. *Physical properties of fabrication techniques that are capable of forming aligned pores.*

Technique	Material	Macro-pore size (µm)	Porosity (vol%)	Compressive strength (MPa)
Ceramic co-extrusion [210]	HA	270	27	240
Freeze-casting [213]	HA	< 600	47	145
Robocasting [222]	HA	~300	~50	140
Robocasting [145]	Sr-HT glass	~900	~60	139

[1] For example, using water as a solvent requires cooling to – 80 °C, and at a generously fast rate of 5 °C min^{-1}, will take 20 mins. This is in contrast to extrusion where a green body can be generated in less than 30 s.

2.6 Summary of the literature review

A rise in bone trauma prevalence that require extensive reconstructive surgery has seen the field of bone graft substitution becoming increasingly important for the treatment of bone defects. As mentioned, bones are important for mobility and regulating other organs due to their ability to store calcium ions and produce red blood cells. Although metals were originally used as substitutes, a concerted effort has focused on using ceramics that are bioactive. Calcium phosphates are capable of inducing bone-growth by exploiting bone's inherent ability to self-heal, and the potential to obviate the need for a second surgery.

The literature has shown that porous calcium phosphate scaffolds exhibit poor mechanical strengths. However, recent work has illustrated that fabricating an aligned porous architecture can yield strengths comparable to cortical bone. Ceramic honeycomb extrusion was identified as a technique capable of generating aligned pores. Extrusion offers many advantages compared to other techniques, namely low costings, rapid processing and low skills required to operate.

Despite its advantages, the literature has revealed that ceramic honeycomb extrusion has not been thoroughly explored for fabricating bone graft substitutes. Thus, there lies the potential for novelty in this field. The current project investigated the viability of honeycomb extrusion for achieving high-strength scaffolds, with the aim of understanding the relationship between processing parameters and raw material selection, to the quality of the final product.

Chapter 3: Characterisation

3.1 Physical Characterisation

Physical characterisations were primarily applied to the raw materials. Powders are available in different morphologies and sizes, hence characterisation thereof with respect to physical properties are needed to understand their effect on subsequent processing stages. The aim herein was to understand which physical attributes were a prefigure towards fabricating a scaffold with desirable properties. Physical characterisation was also employed to determine paste density and the bulk porosity of sectioned scaffolds; the former was performed to compare the paste density to the theoretical results.

3.1.1 Particle Size analysis

Particle size analysis was performed using the Mastersizer 3000™ from Malvern, UK, in wet-mode. A photograph of the instrument is provided in **Fig. 3-1**. The parameters and measurements were performed by the Mastersizer 3000 software (provided by the manufacturer with the instrument), where the following parameters were set:

Number of measurements per run: 5;

Background measurement: 1 minute;

Laser obscuration: 10-20%, as recommended by the manufacturer;

Stirrer speed: 3000 rpm, reduced to 2000 rpm during live readings;

Ultrasound: 70%.

Table 3-1 presents the refractive indices used for the different materials, as well as the absorption indices. For the latter, an absorption index of 0.01 was used for translucent powder; 0.1 for white powder; and 1 for pale coloured powders.

Table 3-1. *Refractive and absorption indices of the samples analysed.*

Materials	Refractive index	Absorption index
As-received HA	1.65 [321]	0.1
Calcined HA	1.65 [321]	1
Y-HA	1.65	1
β-TCP	1.62 [322]	0.1
Bioglass®	1.59 [323]	0.01
Canasite	1.54[324]	0.01

A clean 600 ml beaker was filled with 500 ml of distilled water and placed on the apparatus stage. The instrument was then initialised and following a one minute gap, the background measurement was performed. If contamination was detected during the background measurement, then the run would be stopped and the system would be cleaned before resuming. Once satisfied with the background measurement the samples were loaded incrementally using a laboratory spatula, until an obscuration level of ~ 15% was attained; which was within the 10-20 % range recommended by the manufacturer for wet-mode. Ultrasound was applied to the system for 2-3 minutes, before commencing measurement following a one minute resting period to prevent air bubbles generated by the ultrasound from being recorded. After the measurements, the system was subjected to another round of ultrasound, before a second measurement was taken. If the results were inconsistent with the first measurement, then another round of ultrasound and recording was performed. This continued until consecutive consistent data were obtained, which was indicative of successful soft agglomeration breakdown by the ultrasound. This strategy was adopted to ensure the recordings obtained were not those of soft agglomerates. Results were only accepted if the residual weight of the data was below 1.00, as recommended by the manufacturer.

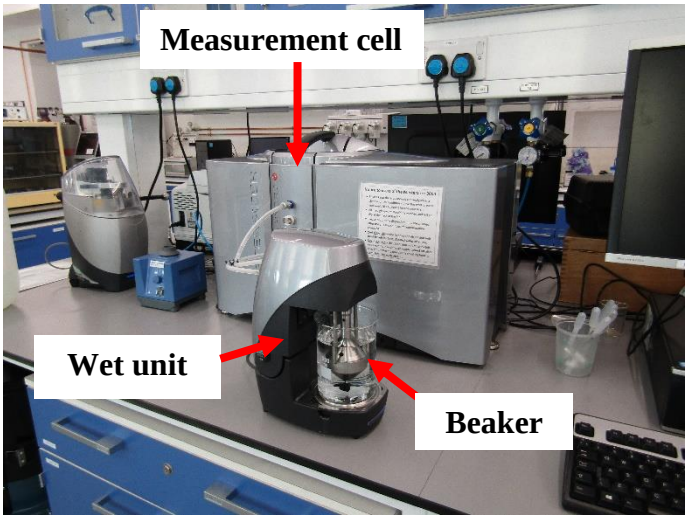

Fig. 3-1. *Particle size analysis set up, which was used in wet-mode.*

3.1.2 Density measurements

A gas helium pycnometer (Accupyc II 1340, Micromeritics, UK) was utilised for powder density, paste density and scaffold bulk porosity measurements. The software, 1340 Accupyc, was used to set the parameters and control the instrument.

Powder density: As recommended by the manufacturer, between ½ and ¾ of the crucible was filled with the powder to be analysed. Loading of the powder was performed on a scale and the mass was recorded. The crucible was then inserted into the chamber of the apparatus.

Paste density: Paste density was empirically measured to validate the theoretical paste density, and thus as a means to quantify the final paste composition. The high shear-energy mixer generates excessive heat, causing the distilled water to evaporate in some instances, and thus resulting in possible variation to the water content, which needed to be verified. In addition, as measurements were performed in triplicates, the analysis also serves as a means of determining paste homogeneity with respect to composition, hence samples were taken from different sites of the formulated paste. **Table 3-2** represents a calculation example of a paste composition in both mass and volume percentage:

Table 3-2. *Example of paste composition presented as both mass and volume.*

Component	Composition (g)	Density (g/cm^3)	Volume (cm^3)
Hydroxyapatite	241	3.22	74.8
Methycellulose	17.9	1.34	13.4
Distilled water	90	1	90
Total	**348.9**		**178.2**

To calculate paste density in **Table 3-2**, the hydroxyapatite and methycellulose densities were empirically determined by the pycnometer, and the theoretical density for distilled water at ambient temperature was used. The mass of the individual components was then divided by their respective densities to obtain the volume, which was then summated. The total mass was then divided by the total volume to determine paste density.

The protocol was similar to the powder protocol, except the equilibrium pressure was increased as the system failed to equilibrate within the instrument's limit (1000 seconds); this could be as a result of the paste samples absorbing the helium slowly. The parameters can be found in **Table 3-3**.

Bulk Porosity: Adjustments were made to accommodate the relatively small size of the scaffolds. The weight of the scaffolds was once again measured on a scale, and subsequently placed into the crucible, along with a stainless steel rod with a height of 4.5 mm and diameter of 10 mm, which was used to compress the helium. Although not required, this was done because nearly filling the crucible results in greater measurement sensitivity [325]. Furthermore, the approach was consulted with the manufacturer, who confirmed the approach was common practice. The volume of the rod, which was pre-determined by the pycnometer, was then subtracted from scaffold measurements. Thereafter, the new volume was used to calculate the density of the porous scaffold. The following equation was used to determine the bulk porosity **P**:

$$P = \left(1 - \frac{\rho_a}{\rho_t}\right) \times 100$$

Where ρ_a is the apparent density, whereby the volume was measured by a vernier caliper (**Fig. 3-2**); and ρ_t is the true density, whereby the volume was determined by the pycnometer.

Using the steel rod resulted in an increase in air pressure, which caused the scaffold to ricochet within the crucible. To accommodate for this, the purge and reading pressures were reduced to prevent cracking of the scaffolds. The parameters can be found in **Table 3-3**.

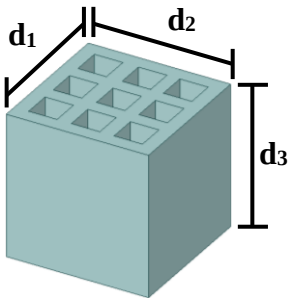

Fig. 3-2. *CAD model depicting the dimensions measured to obtain the apparent density of scaffolds.*

Table 3-3. *The helium pycnometer parameters for the different sample types.*

Analysis type	Number of Purges	Purge fill pressure (psig)	Number of cycles	Cycle fill pressure (psig)	Equilibrium rate (psig/min)
Powder	20	12	20	12	0.0050
Paste	20	12	20	12	0.5000
Bulk porosity	5	5	8	8	0.0050

3.1.3 Surface Area

Surface area was performed using the 3Flex from Micromeritics, UK., which utilises the Brunauer-Emmett-Teller (BET) theory. BET uses physical adsorption to measure the surface area of powders using a set gas. At their liquefaction temperature, the molecules of the gas will adsorb onto the surface of the sample. As the pressure of the gas rises, so does the number of adsorbed molecules on the surface until a monoloyer of molecules is formed. The quantity adsorbed is then used to quantify the surface area.

The experiment procedure for surface area analysis can be divided into two steps. An initial sample preparation step was performed, which was followed by the analysis itself. For sample preparation, first, the mass of the 12 mm diameter glass tubes (**Fig. 3-3**), followed by mass of the tube with sample, were recorded. A glass funnel and drink straws were utilised to aid the deposition of the powder to the base of the glass tube, with the purpose of minimising powder adherence to the inner side walls of the tubes, and thus minimising data error.

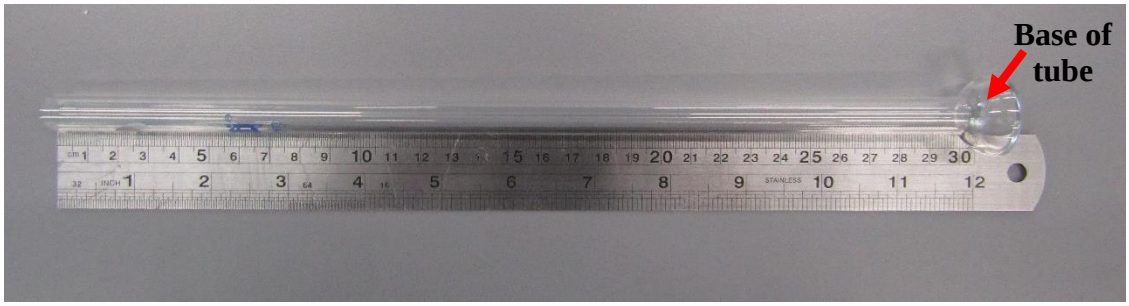

Fig. 3-3. *Image of a glass tube. The powdered samples had to be inserted in a way to ensure the powder reached the base of the tube without adhering to the side walls.*

The tubes were attached to the sample degas system (VacPrep 061) thereafter, where the samples were vacuumed and heated for 4-5 hours, at 0.1 mbar and 300 °C, respectively. This was performed to remove unwanted particles and moisture from the surface of the powder that may interfere with the measurement. Following this, the samples were gassed for 30 seconds, before removing the tubes from the system. The final step was to attach the tubes to the 3Flex instrument before commencing the test. **Fig. 3-4** is a photograph depicting the degasser and the surface area analyser itself.

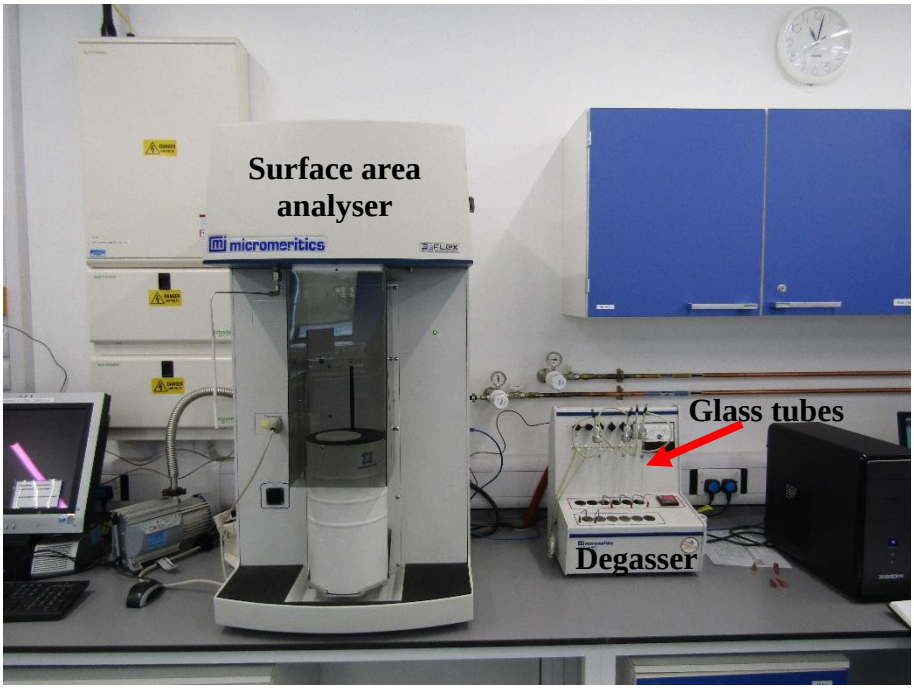

Fig. 3-4. *Surface area analyser setup, portraying the degasser, which was used to remove contaminants and moisture; and the surface area analyser itself.*

A multipoint BET analysis, with relative pressures of between 0.05 and 0.4 was performed. Evaluation of the results were performed and the results were inspected for evidence of experimental errors. The BET surface area data was only accepted if the Y-intercept was positive; the BET C value (BET constant) was between 5 to 300; and the correlation coefficient of the regression line was 0.999 or greater; if the test was applied correctly, the data reduction plot will be linear. All the aforementioned parameters were in accordance with the manufacturer's guidelines [318]. An example of such a plot is illustrated in **Fig. 3-5**. Each sample analysis was repeated a further two times.

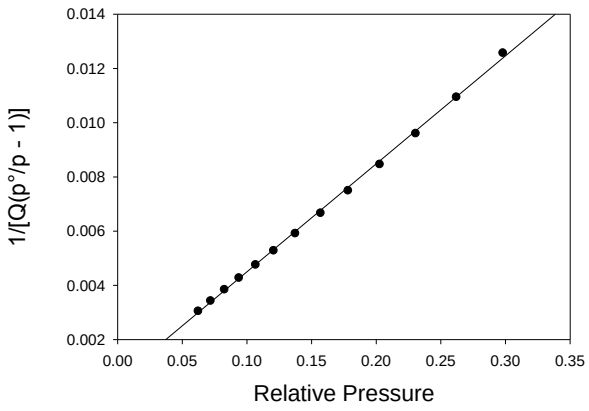

Fig. 3-5. *Example of a BET transform plot (data reduction method). The plot is that of the as-received hydroxyapatite powder used in* ***Chapter 5****.*

3.2 Chemical Structural Characterisation

The chemical structure of ceramics and glass are key determinants in the materials' biological and mechanical properties. Hence chemical analyses were employed to elucidate the chemical structure thereof, particularly as the materials are subjected to heat and other procedures that could result in phase transformation. All chemical analyses were carried in powder form. For measuring the chemical structure of sintered samples, segments of the extrudate were sectioned off using a slow saw (IsoMet™ Low speed, Buehler, UK), then crushed with a percussion mortar, and ground using a pestle and mortar, in order to obtain fine powders for analysis.

3.2.1 X-ray Diffraction (XRD)

XRD techniques can be used to identify the phases present in samples, from the raw material to the final product. In XRD, X-rays are generated and targeted towards the sample. These incident x-rays are scattered upon striking crystal planes towards a detector, which records the incident angle and the intensity thereof. Depending on the crystal structure, the X-rays are scattered accordingly to generate an X-ray spectra that is used to identify the material.

XRD was performed using the Siemens D5000 Powder Diffractometer (Munich, Germany), with a voltage and amplitude of 35 kV and 30 mA, respectively. The desired powder was loaded onto the sample holder as illustrated below. A microscope glass slide was used to ensure that the powder was levelled to avoid erroneous XRD patterns. The sample holder was also tilted at approximately 45 ° to ensure that the powder was stable. Subsequently, the holder (**Fig. 3-6**) was inserted into the instrument where analysis ensued. Each sample analysis was repeated at least once.

The XRD Wizard software was used to set the parameters of the instrument, and the information was transferred to XRD Commander, which was the software used to initialise the instrument, as well as commence analysis. The following conditions were opted for XRD analysis:

Scan Type: Locked Couple

Scan Mode: Continuous Scan

Parameters:

Start (°):	20	Time per Step (s):	2
Stop (°):	70	Divergence Slit:	2
Step size:	0.03	Antiscattering slit	2
Number of Steps:	1667		

Data analysis was performed using PDF-4 software (ICDD, USA) for confirmation. All the powder diffraction files (PDF) listed in the forthcoming results chapters were obtained from this software.

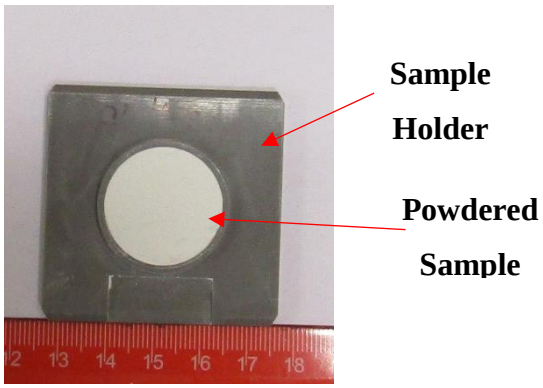

Fig. 3-6. *Photograph of the sample holder containing a powdered sample ready for XRD analysis.*

3.2.2 Fourier-Transformation Infrared Spectroscopy (FTIR)

FTIR spectroscopy is a form of vibrational spectroscopy that determines chemical structure based on the vibrations of the atoms of a molecule. When infrared radiation is passed through a sample, the energy is absorbed by the molecules, and is transferred into kinetic energy. Provided there is a net change in dipole moment of the molecules, the energy results in a change in amplitude of molecular vibration. Different bonds will

absorb infrared radiation at different frequencies, which is then used to identify the overall chemical structure thereof.

FTIR analysis was performed using the Frontier from Perkin Elmer, USA, and operated using the Spectrum software, which was provided by the manufacturer. First, the powder samples were mixed with potassium bromide (KBr)[2] at a ratio of 2:200 mg using an agate pestle and mortar. Once sufficiently mixed and the admixture appeared homogenous, the samples were pressed into a disc using a 10 mm stainless steel pellet die; the force was first applied at 1 ton for 1 minute, and then increased to 10 tons for a further one minute. Samples (**Error! Reference source not found.**) were then inserted nto the sample holder, which was then transferred to the instrument. The instrument's lid was closed to minimise external interference.

A total of four background measurements were taken, which were subtracted from sample measurements. The following settings were chosen for all FTIR measurements: wavenumber range from 4000 to 400 cm^{-1}; resolution of 4 cm^{-1}; and a total of four scans per run.

3.2.3 X-Ray Fluorescence (XRF)

XRF analysis was used to determine the elements present in the raw glass powders. Unlike the calcium phosphate, the synthesised glass powder underwent a vigorous processing step, and the technique was used to determine if the glass powder was contaminated as a result.

XRF analysis was performed using Panalytical's Zetium (Almelo, Netherlands), and its accompanying software (Super Q Launcher). Powder samples were placed in the 37 mm plastic sample cups, which were supported using Mylar™ film. The samples were subsequently placed in the instrument, and analysis ensued, which was performed under helium. The same software was used for sample analysis.

[2] The potassium bromide disc approach was used to expand the scanning range to below 600 cm^{-1} for this particular instrument. Potassium bromide was used to form the disc as it has a transmittance of 100% in the range of 4000-400 cm^{-1}, which was needed to identify the functional groups present in hydroxyapatite and β-tricalcium phosphate.

3.3 Thermal Characterisation

A crucial step in the fabrication process is the firing of the extrudate. The process is preceded by drying and de-binding; all of which require delicate thermal treatments to prevent premature failure. Hence, the thermal behaviour of the different raw materials needed to be clarified in order to optimise the thermal processing stages.

4.4.1 Dilatometer

Pushrod dilatometry is a method for determining dimensional changes as a function of time or temperature. The instrument was employed to elucidate the shrinkage behaviour of the starting materials when subjected to elevated temperatures and to ensure sintering temperatures used will densify the ceramics.

Pellets of 10 mm diameter and approximately 1.5 mm in thickness were fabricated using a pellet die and press. The pellets were pressed at 0.6 tons, and subsequently transferred to a rectangular alumina crucible for safe transportation. Stainless steel tweezers were used to insert the pellets into the sample holder of the dilatometer (402 C, Netzsch, Germany). The pushrod of the dilatometer was activated, and brought into contact with the pellet at its centre. The force applied by the pushrod to the pellet was set to 30 cN, which was sufficient to hold the pellet and sensitive enough to record linear shrinkage, without fracturing the pellet. Once this was achieved, the furnace was closed.

The parameters were controlled using the Proteus® software. The temperature parameters of the analysis were: a heating and cooling rate of 5 and 10 K/min, respectively; and a starting temperature of 25 °C.

To ensure that the pellets will not react with the alumina sample holder and pushrod at elevated temperatures, separate pellets were first sintered in alumina crucibles using a muffle furnace, at the designated temperatures. Pellets were subsequently inspected to ensure no reaction had taken place. As a result, the maximum sintering temperature for the samples were set to either 1350 or 1400 °C.

4.4.2 Differential Scanning Calorimetry (DSC)

DSC is a thermal analysis technique that looks at how a material's heat capacity is changed by temperature, where a sample of a known mass is heated and its heat capacity is tracked as changes in heat flow. DSC allows the detection of phase transformation in calcium phosphate, as well as other glass thermal events, such as crystallisation, glass transition, and melting.

Before commencing DSC (404 C Peguses, Netzsch, Germany) analysis, the protective gas flow, argon gas, was set to a rate of 90 ml/min for thirty minutes in order to rid the system of humidity or reaction products. An 80 µl alumina crucible was placed on a scale and the measurement was tared, where thereafter the powdered sample was deposited into the crucible via a micro stainless steel spatula. The typical weight for ceramic samples was 37 mg, which is within the recommended weight supplied by the manufacturer (30-40 mg). Once the sample was weighed, the crucible was transferred to the DSC sample holder, and the furnace was closed thereafter. An empty alumina crucible was used as reference, and the experiments were performed using a purge gas flow of 50 ml/min. Air was used as both the purge and analysis gas during measurements.

The Proteus® software provided by Netzsch was used again to control the experiment. The heating and cooling rate were set to 5 and 10 K/min, respectively, with a start and end temperatures of 25 and 1400 °C, respectively.

4.4.3 Thermal Gravimetric Analysis (TGA)

TGA analysis was performed to determine the change in sample mass as a function of temperature, using the Pyris TGA 1 from Perkin Elmer, UK. The instrument was used primarily for determining a suitable binder burnout temperature profile, as the instrument had a maximum analysis temperature of 1000 °C.

Again, a similar protocol to that of the DSC was used, except for the purge gas was either air or nitrogen, depending on the experiment; the flow rate thereof was set to 100 ml/min, and samples weighed between 20-30 mg. The Pyris software was used for controlling and analysing the data.

4.4.4 Simultaneous Thermal Analysis (STA)

The STA was performed using the SDT-Q600 from TA Instrument, USA, which allows for simultaneous DSC and TGA analysis. Unlike the Pyris TGA 1, temperatures of above 1000 °C could be used for analysis, which was useful for analysing glass samples.

The sample protocol was similar to that of the aforementioned DSC protocol, except for the purge gas was either air or nitrogen, depending on the experiment, and the flow rate thereof was set to 100 ml/min. Furthermore, the control and analyses software were Q600 and Thermal Advantage, respectively.

3.4 Microscopy

Microscopy was used to provide qualitative analysis of the samples. Post-test microscopy analysis were performed using ImageJ from National Institute of Health, USA.

3.4.1 Optical microscopy

Optical microscopy was employed to examine the physical properties of the sectioned scaffold, with respect to cell length and strut thickness. Optical images were taken using Motic®'s BA310Met-T microscope, fitted with Moticam 3 attachable digital C-mount camera, and calibration and images were taken using the Motic Images Plus software.

4.4.5 Scanning Electron Microscopy (SEM)

SEM analysis was performed to examine sample microstructure. The technique uses a beam of high-energy electrons that are focused towards the sample. The electrons interact with the material's atoms and the scattered electrons are collected to image the surface.

All of the samples that were analysed were non-conductive, and thus were coated with gold, using a gold sputter (SC 500A, Emscope, USA). Specimens were adhered to aluminium stubs (Agar Scientific, UK) via either a carbon adhesive and/or a silver conductive paste (Acheson Silver DAG, Agar Scientific, UK) (**Fig. 3-7**). In the case of powdered specimens, an air gun was used to level the specimen and to avoid charging of the images.

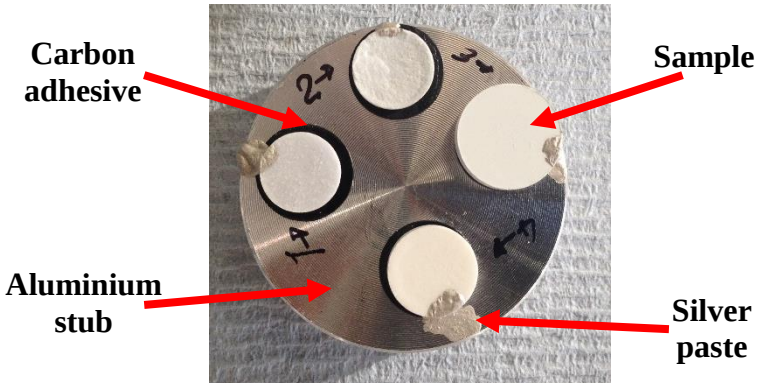

Fig. 3-7. *Example of SEM sample mounting prior to gold coating, and the use of carbon adhesive or silver paste to adhere the sample to the aluminium stub.*

Sputtering was performed under rough vacuum (0.1-0.05 torr) and argon gas, and the deposition current and coating time were set to 15mA and 3 minutes, respectively. Once coated, the samples were transferred to the SEM (Inspect F50, FEI, Netherlands), where the SEM was used in secondary electron mode to provide images of the sample. The working distance was set to approximately 10 mm. The spot size and voltage were 3 and 5 kV, respectively, and were consistent throughout the research.

Energy Dispersive X-ray Spectroscopy (EDS) (X-MAXN 80T, Oxford Instruments) was employed to provide elemental analysis of specimens. For EDS mapping, the measurements were taken at a resolution of 256; acquisition time of 50 or greater; energy range of 20 keV; number of channels was set to 2048; a process time of 4 was opted for; and a pixel dwell time of 20 µs.

3.5 Rheology

Rheological analysis has been proven to be a good indicator of ceramic paste extrudability, and can be measured using instruments called rheometers. The sample is loaded onto a rheometer and is then subjected to a well-controlled shear rate or shear stress. The ratio between shear stress (τ) and shear rate ($\dot{\gamma}$) gives the viscosity (η):

$$\eta = \frac{\tau}{\dot{\gamma}} \qquad \textbf{(3.1)}$$

With the units being pascal second (Pa.s), pascal (Pa) and reciprocal second (s^{-1}) for the viscosity, shear stress and shear rate, respectively. There are different rheometers and each are able to perform viscosity measurements through different modes. For extrusion, a paste should exhibit shear-thinning properties, which both a capillary and rotational rheometer are capable of characterising.

A capillary rheometer (CR) is similar to extrusion in that the material is forced through a given die by a piston. An illustration thereof is provided in **Fig. 3-8**. The instrument works by either controlling the shear rate or the shear stress of the instrument. All rheological analysis using the capillary rheometer were performed using the former mode. The shear rate ($\dot{\gamma}$) is a function of piston speed, and bore and die internal diameter. The following equation relates the parameters:

$$\dot{\boldsymbol{\gamma}} = \frac{\mathbf{8} \times \boldsymbol{D^2} \times \boldsymbol{s}}{\boldsymbol{d^3}} \qquad \textbf{(3.2)}$$

Where D is bore internal diameter; s is piston speed; and d is die internal diameter. The shear stress (τ) is calculated as:

$$\boldsymbol{\tau} = \frac{\Delta \boldsymbol{p}}{\mathbf{2}(\boldsymbol{L}/\boldsymbol{r})} \qquad \textbf{(3.3)}$$

Where L is the capillary die length; r is the die radius; and Δp is the difference in pressure between the barrel and atmospheric pressure. Essentially, the user sets the shear rate range, and the instrument calculates the speed of the piston that corresponds to the set shear rates. As the material flows through the capillary rheometer, a pressure transducer situated in the bore measures the pressure developed during a test. The pressure measured is then used to determine the shear stress of the material under the set shear rate, using **equation (3.3)**.

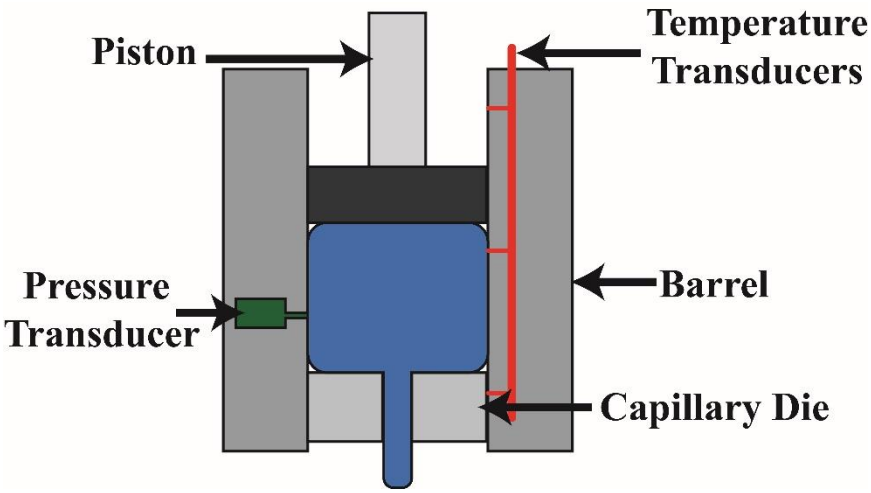

Fig. 3-8. *Schematic depicting a capillary rheometer and its components. Using this method, the material of interest is forced through a capillary die via a piston. The speed of the piston equates to the shear rate, and a pressure transducer is used to obtain the resultant pressure from the pre-determined piston speed, and subsequently used to obtain the shear stress. The ratio of shear stress to shear rate gives the viscosity. The temperature can also be altered to provide a temperature-controlled analysis, in order to understand the effect of temperature on viscosity.*

Where CR uses pressure-driven flow (Poiseuille flow), rotational rheometers (RR) achieve shearing via drag flow (Couette flow). In RR, samples are placed between parallel plates (**Fig. 3-9**) and are subjected to torsional shearing. The shear rate is calculated by dividing the velocity of the parallel plates by the distance between plates:

$$\dot{\gamma} = \frac{v}{h} \qquad \textbf{(3.4)}$$

where v is the angular velocity, and h is the height of the sample measured (i.e. gap between the parallel plates). For a standard viscosity measurement, the gap is fixed and the angular velocity of the plate increases, and the shear rate increases accordingly. The force applied is measured by a transducer, and takes the cross-sectional area of the sample into account to give the shear stress.

The benefits of RR over CR are better sensitivity, and small sample sizes are required. In addition, RR can be used in oscillatory (dynamic) mode to determine viscoelastic properties of materials. In this mode, the rheometer applies a sinusoidal force that progressively increases in either amplitude (i.e. force) or frequency (i.e. speed). From

this, viscoelastic properties such as the storage (i.e. elastic) and loss (i.e. viscous) moduli can be determined. The storage modulus (G') can be used to determine the stiffness of the ceramic paste, and is derived as:

$$G' = \frac{2hM_0 Cos\delta}{\pi r^4 \phi_0} \quad \textbf{(3.5)}$$

Where M_0 is the torque amplitude; ϕ_0 is the angular amplitude of oscillation; δ is the phase angle, which represents the time dependent behaviour of the strain to the sinusoidal stress applied; r is the radius of the parallel plate geometry; and h is the gap height. The G' was used to provide information regarding the shear modulus and plasticity of ceramic pastes. The former is akin to the elastic modulus, but as the RR applies a torsional force rather than an axial force, it is the shear stiffness that was measured. The storage modulus was used to correlate the ceramic paste to the quality of the extrudates.

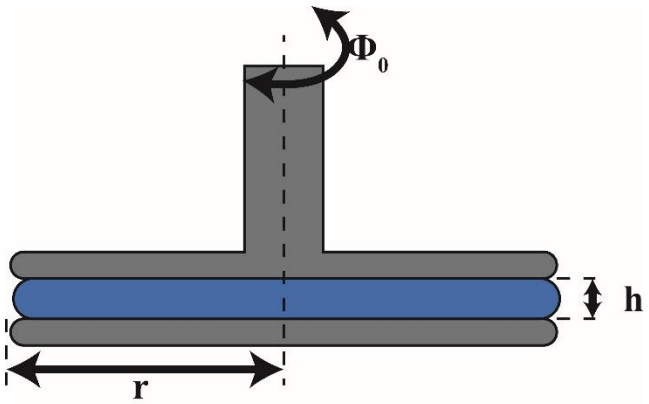

Fig. 3-9. *Schematic depicting a rotational rheometer with parallel plates (ϕ – angular amplitude of oscillation; h is the sample gap height; r is the radius of the parallel plate). The parallel plates are coloured as grey, with blue representing a sample. Using this rheological approach, a sample is placed between two plates; typically, the lower plate is stationary, and the upper plate rotates. The viscosity in rotational rheometry is a function of the ration between the velocity of the plate and the geometric gap height (h).*

4.4.6 Capillary Rheometer Procedure

Rheological measurements of the pastes were performed using the Rosand RH200 15 mm twin bore capillary rheometer (Malvern Instrument, UK), and the experimental procedure was selected using the Flowmaster™ software. A tungsten carbide die with a diameter, length and angle of 1 mm, 16 mm and 180 °, respectively, was used. Before each measurement, the samples were kneaded by hand and loaded into the barrel at ambient temperature, where thereafter manual compaction was performed using the piston of the instrument. Once the samples were loaded to a reference point (95-110 mm), the analysis was commenced. A pre-test compression of 0.5 MPa was incorporated into the test procedure for reproducibility. In the event a test was performed under controlled temperature, the sample was left in the bore for 15 minutes to ensure the sample was homogeneously heated.

4.4.7 Rotational rheometer Procedure

To compliment the capillary rheometry analysis, a rotational rheometer was employed in oscillatory mode, which is also referred to as dynamic mechanical analysis (DMA), to elucidate the mechanical behaviour of pastes. Tests were performed using the rotational rheometer (MCR 302, Anton Paar GmbH, Germany), which was equipped with an 8 mm parallel plate geometry, and controlled using the Rheoplus software. Prior to analysis, the warm up protocol was performed, as recommended by the manufacturer. A trimming size of 1.025 mm was selected, and samples were trimmed using a plastic spatula. Following sample trimming, the rheometer reached the gap size, which was set to 1 mm, and analysis ensued. Once a test run was finished, the Peltier surface and geometry were cleaned using distilled water, and then dried before commencing the next run.

4.4.8 Extrusion measurements

The MOOG SmarTEST ONE controller, which was used to actuate the extruder's piston, was also used to record the force feedback as a function of piston distance travel, and thus produce the force-displacement curves. The recording was commenced once the loaded paste underwent compaction and vacuuming. Sampling was performed at a recording frequency of 100 Hz.

3.6 Mechanical Characterisation

Mechanical analysis was performed to measure the maximum compressive strength of the sintered scaffolds, which in the literature is used as the benchmark for a scaffold's mechanical properties. Tests were performed using the Roell Z050 from Zwick, UK, and operated by the testXpert II software. Compressive strength was used as the benchmark mechanical test. The testing was performed using a 20 kN load cell (Xforce K, Zwick; 0.5% resolution). Two cylindrical cone boron nitride toolings were adhered to the platens of the instrument via a double-sided adhesive, which were employed to ensure that the platens will not be damaged by the samples. Once this was done, a spirit level was used to ensure that the setup was level, and using the software, the new distance between the toolings was referenced and set to zero. **Fig. 3-10** illustrates the setup for the mechanical testing, and **Fig. 3-11** is a closer image demonstrating the position of the scaffold between the conical boron nitride toolings.

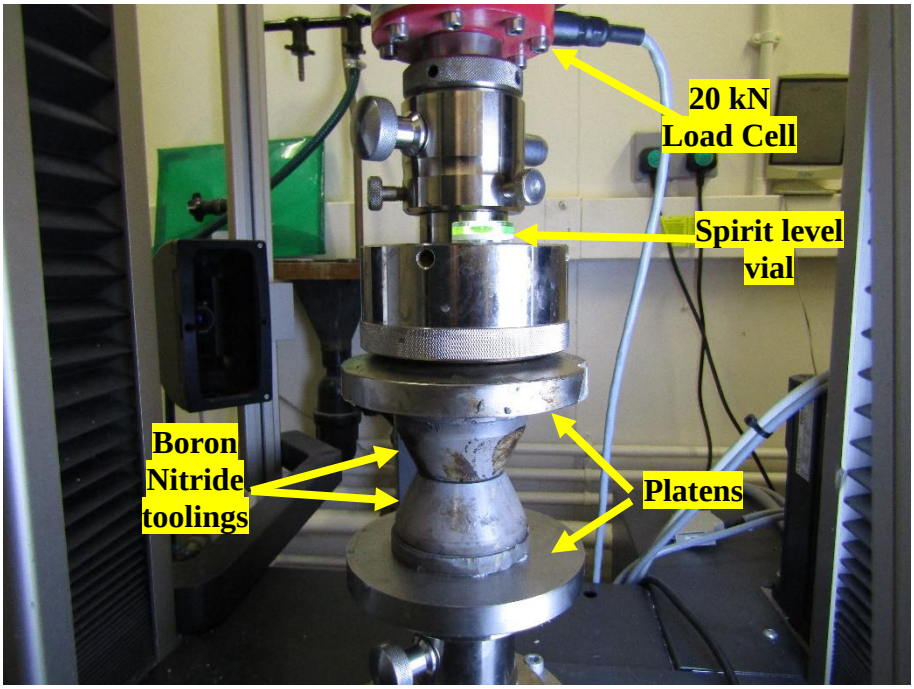

Fig. 3-10. *Mechanical test setup.*

Due to the different shrinkage behaviour exhibited by the samples, and to incorporate a level consistency, all mechanical analysis was performed on 3 x 3 sectioned

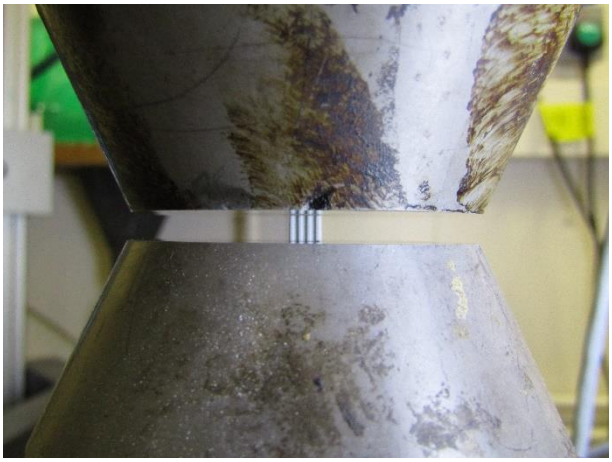

Fig. 3-11. *Photograph of the mechanical setup, illustrating the conical boron nitride toolings used. The figure demonstrates the typical position of the upper and lower tooling to the scaffold before commencing the test, and the central position of the scaffold.*

cubes, and a minimum of eight samples were used for each material. The samples' apparent test surface area were measured using a digital Vernier caliper (**Fig. 3-12**), and the information was entered into the software. The sample was then placed in the centre of the bottom tooling (**Fig. 3-11**), and the top tooling was manually brought closer to expedite the test. Prior to testing, a pre-test of 5 kN at 1 mm/min was used, which was incorporated to improve the contact between the tooling and sample before the actual test.

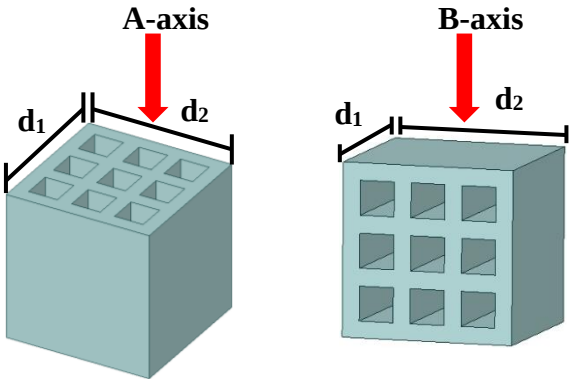

Fig. 3-12. *CAD model illustrating which dimensions were used for the area in order to determine the compressive stress.*

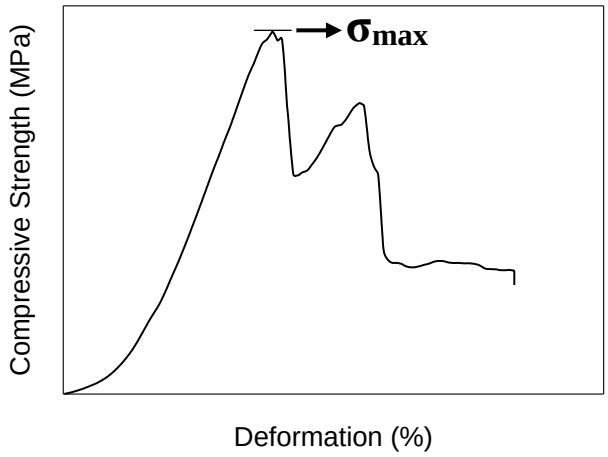

Fig. 3-13. *Stress-deformation curve to illustrate how the maximum compressive strength (σ_{max}) was determined. The curve is that of a BG2 sample sintered at 1300 ^{o}C.*

A stroke rate of 1 mm/min was also used for the main test. Sample analysis was concluded following a brittle fracture, as determined by a sharp decrease in compressive strength, which an example thereof can be observed in **Fig. 3-13**. The maximum stress was determined as the maximum strength exhibited by the first fracture was recorded. The surface of the toolings were wiped cleaned thereafter, before the start of the next test. Where possible, remnants of the fractured scaffolds were collected and used for post-compression SEM analysis.

3.7 Statistical Analysis

Graphpad prism (v7, Graphpad, USA) was used for both t test and one-way analysis of variance (ANOVA) statistical analyses. Unless otherwise stated, the statistical significance is given by $P< 0.05$. Prior to this, a D'Agostino-Pearson omnibus normality test was performed, as well as an F test to determine variance. If the data was not normally distributed and of equal variance, then a non-parametric test was performed.

Chapter 4: Fabrication Process

The chapter herein details the fabrication process, and guides the reader through the rationale for parameter selection. The processing stages are (i) mixing, (ii) extrusion and (iii) thermal treatment. Moreover, this section details the screening used to determine which binder to use, as the subsequent chapters will be centred on the ceramics. The extrusion section will detail the extruder setup and the empirically-determined extrusion parameters. The chapter concludes with the de-binding protocol used throughout the project, which again were empirically determined.

4.1 Binder Selection & Mixing

The purpose of the binder is to temporarily bind the ceramic particles, and to impart green strength until the particulate system can be sintered. Accordingly, the green strength forms part of the desirable characteristics for binders, with other characteristics being easy burn-out, a solvent with compatible polarity, and low cost.

Binders typically comprise 4 – 6 mass% of the admixture. They can either be organic, for example starch, or inorganic, such as sodium silicate [223]. Inorganic binders have a high degradation point and leave residues, which can be undesirable where the formulator requires complete extraction of binder. There are processes where the inorganic residues are not detrimental, and indeed processes were the residue adds to the properties: for example organometallic binders where inorganic residues facilitate densification [223]. Furthermore, binders can be categorised as aqueous or non-aqueous, wherein the former is soluble in water. This is desirable, as in contrast to other solvents, water is cheap and non-toxic.

Perusal of the literature revealed that most extrusion work was performed using organic binder, which included polyvinyl alcohol, ethylene vinyl acetate and cellulose ether derivatives. The benefit of using organics are easy burn-out, availability and wide range of viscosity grades [223]. Due to the availability of distilled water and the desire to work with non-toxic binders, it was decided that aqueous organic binders would be utilised for the plasticisation of the ceramic bodies.

A common organic additive brand used in ceramic processing are the Methocel™ range, developed by Dow Chemical. Methocel™ (MC) is a binder with other additive properties, such as lubricity, non-ionic thickening and wetting properties when mixed with distilled water. Previous studies have successfully fabricated honeycomb extrudates solely with MC as the additive [326, 327].

MC are cellulose-derived ethers that are classed as polysaccharides and industrial gums [328]. **Table 4-1** lists examples of other water-soluble binders commonly used in ceramic fabrication. Although cellulose ethers are commonly used, in the interest of prudence, a total of three binders were screened. Binders with a higher green strength than the MC used (Methocel™ F4M, Dow Chemicals) were sought after. Preliminary extrusion trials using this grade resulted in shearing that reduced the viscosity of extrudates to the extent that deformation occurred thereto when handled. Typically, a positive correlation exists between viscosity and green body strength; both properties increase with increasing molecular weight [329-331]. As such, carboxymethylcellulose (CMC) and guar gum (GG) were selected (Sigma Aldrich, Germany) for their high viscosities. This was based on the data obtained from **Table 4-1**, which illustrates that both binders possessed relatively high viscosities.

***Table 4-1**. Examples of water-soluble binders [229]. The table illustrates the variety of viscosities available, of which high viscosity grades were desirable for extrusion.*

	Viscosity Grade				
Binder	**V. low**	**Low**	**Medium**	**High**	**V. High**
Gum Arabic					
Poly(vinylpyrrolidone)					
Poly(vinyl alcohol)					
Polyethylene oxide					
Starch					
Methylcellulose					
Carboxymethlycellulose					
Hydroxypropylmethylcellylose					
Xantham gum					
Locust bean gum					
Gum karaya					
Guar gum					

Fig. 4-1 are SEM images of all three polymeric binders, where it was determined that each binder exhibited a distinct morphology. In their as-received states, MC and CMC appear to comprise both linear and branched polymers; whereas, the GG powder consists of smaller particle sizes that are branched to a higher extent.

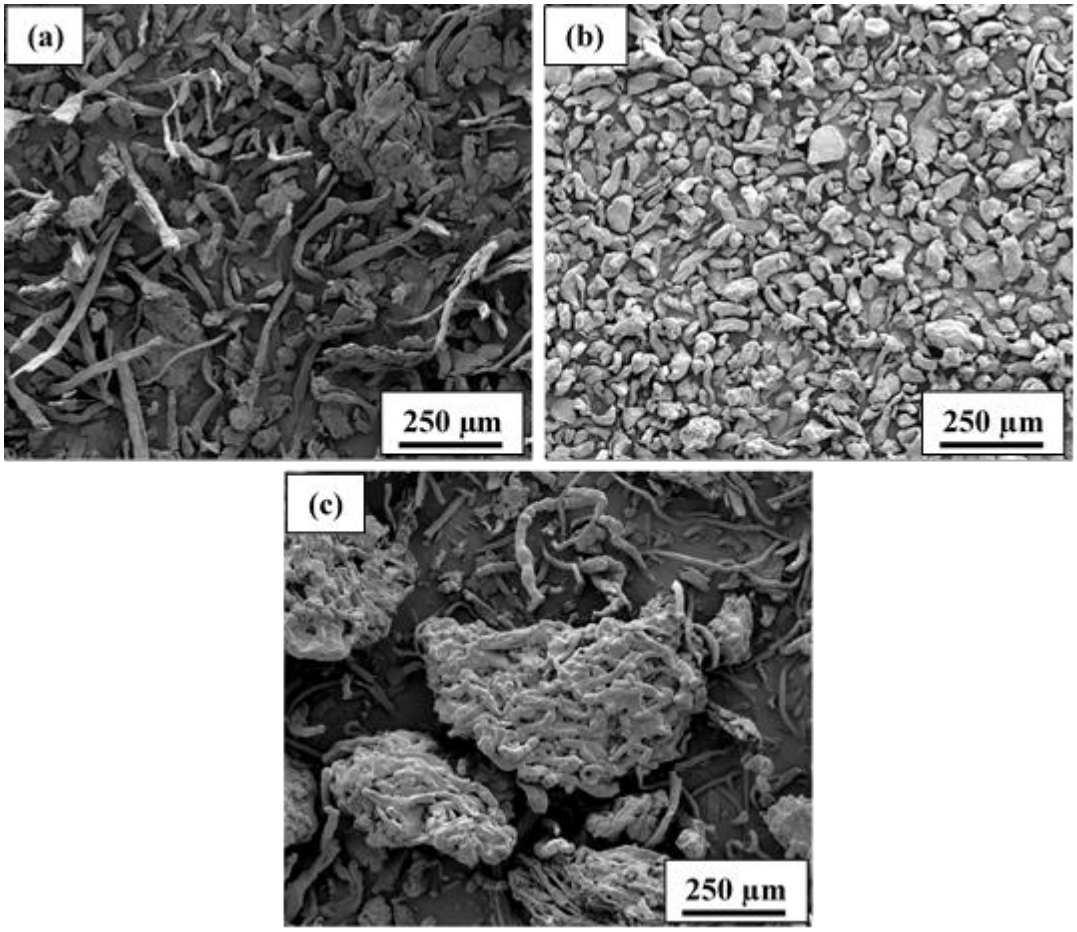

Fig. 4-1. *Scanning electron microscopy (in secondary electron mode) micrographs of* ***(a)*** *Methocel™,* ***(b)*** *guar gum and* ***(c)*** *carboxymethyl cellulose. GG exhibited a distinct morphology from MC and CMC.*

4.1.1 Paste formulation

Paste formulation is a complex procedure. In addition to composition selection, the processing parameters are equally wide-varied, as they include mixing speed, mixing time, temperature and humidity control, and mixing technique. During paste formulation, the binder and water combine to form a gel whereby the inorganic particulates are suspended within. Although the constituents of the paste were limited to three ingredients:

ceramic, binder and distilled water; difficulties still arose, which will be discussed in this chapter.

4.1.1.1 Trials to Optimise Mixing Strategy

The aim of formulating a ceramic paste is to achieve an extrudable paste whilst minimising the non-ceramic components. One aspect was to determine whether the mixing order influenced the ceramic paste. Mixing was performed in polypropylene containers, which comprised a cup and lid that were compatible with the high-shear-energy mixer (Speedmixer™ DAC 300 FVZ, Synergy Devices, UK) utilised. The mixing instrument was a blade-less mixer that minimised contamination and the generation of air pockets.

It was discovered that mixing the dry components first (i.e. the ceramic and binder powders) resulted in an increase in ceramic solids loading. This was because mixing the binder and water first caused the binder to gelate, which increased the viscosity of the system, and thereby made it difficult for the ceramic powders to penetrate and be suspended therein. Hence, the dry components were first added and mixed prior to the addition of distilled water. **Fig. 4-2 (a)**, is a representative image of a paste exhibiting phase separation, where the binder formed a ceramic-free gel; which would yield poor extrudates due to the inconsistent viscosities produced due to the different phases. By mixing the dry components first, it ensured a homogenous distribution of ceramic and binder, and the subsequent addition of water resulted in a homogenous coating of the ceramic particles by the binder. Indeed, increasing the mixing duration or shear speed may have eventually homogenised the paste, however, prolonged mixing or greater speeds caused partial evaporation, and attempts to compensate for the water loss thereafter proved difficult. The addition of water was performed incrementally until a clay-like paste was formulated. Excessive amounts of water, as **Fig. 4-2 (b)** portrays, results in a cream-like formulation that are unsuitable for ceramic extrusion. Hence the incremental addition approach.

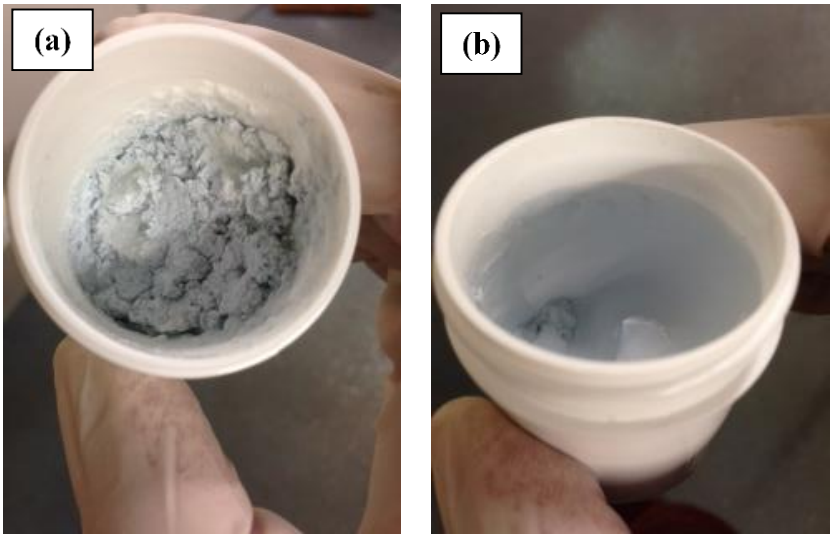

Fig. 4-2. *Images depicting examples of poorly formulated pastes.* ***(a)*** *is an example of binder phase separation, which would be difficult to extrude as the different phases of the paste would possess different viscosities, and hence under a constant extrusion force, the different phases would flow at different rates and yield poor extrudates; and* ***(b)*** *is a cream-like paste unsuitable for extrusion, which would seep through the honeycomb die when poured into the vertical extruder.*

4.1.1.2 Trials to Optimise Composition Ratio

Determining the ideal mixing order was necessary to ensure efficient binder coverage of the particles. The next step was to determine the maximum ceramic particles that could be suspended. The higher the ceramic proportion the more desirable the formulation is, as it would alleviate the difficulties during the thermal treatment steps (as discussed in **section 4.3**). However, inadequate amounts of organic additives resulted in miniature globules forming (**Fig. 4-3 (a)**). Subsequent addition of water resulted in progressively larger globules forming (**Fig. 4-3 (b & c)**), until a single, coalesced paste was formed (**Fig. 4-3 (d & e)**). By increasing the water content, the viscosity of the admixture was reduced, thereby allowing adjacent globules to coalesce. However, excessive amounts of water resulted in a slurry with a cream-like consistency (**Fig. 4-2 (b)**), which would not be feasible for extrusion as it would seep through the honeycomb die when poured into the vertical extruder. The transition from a solvent-deficient to a solvent-excessive admixture was highly sensitive, requiring incremental additions of 0.5 – 1 mass% of water to prevent extreme transitions. Once this was understood, formulating a coalesced ceramic paste using MC, CMC and GG were achieved. The next step was to rheologically characterise the different pastes and determine their suitability for extrusion.

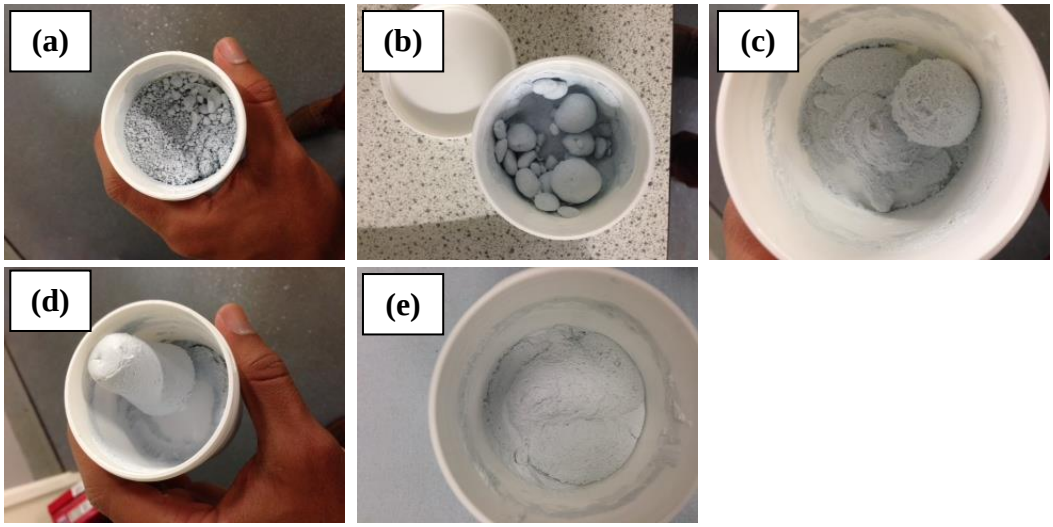

Fig. 4-3. *Examples of the effects of inorganic-organic ratios on the paste morphology. The presence of globules (**a-c**) were indicative of a poorly coalesced paste and unsuitable for extrusion; whereas (**d** & **e**) are examples of coalesced pastes suitable for extrusion.*

4.1.2 Rheological Properties of the Ceramic Pastes

Ceramic pastes are required to possess shear-thinning properties. Shear-thinning is where initially the paste does not flow when subjected to low forces, but with increasing shear rates (which is proportional to shear stresses) the paste will eventually flow; until the stress is removed when it will behave once again like a solid. This type of property is suited for extrusion as when the pressure is applied the ceramic paste will flow through the die, resulting in a given shape; and once the pressure is removed, said shape is maintained and resists collapsing.

Shear-thinning can be determined using rheometers. The rheometers are programmed to apply an increasing shear rate to the sample, and the resultant viscosity behaviour is measured. There were two rheometers used in this project: capillary and rotational.

4.1.2.1 Capillary Rheometry

For ceramic extrusion, the admixture of inorganic and organic components should exhibit shear-thinning properties [332]. Rheological analysis of MC, CMC and GG pastes all

demonstrated shear-thinning properties. As illustrated in **Fig. 4-4**, all possessed a relatively high shear viscosity that decreased exponentially with increasing shear rate, until reaching the shear-infinite region, where further increases in shear rates had no effect on the viscosity.

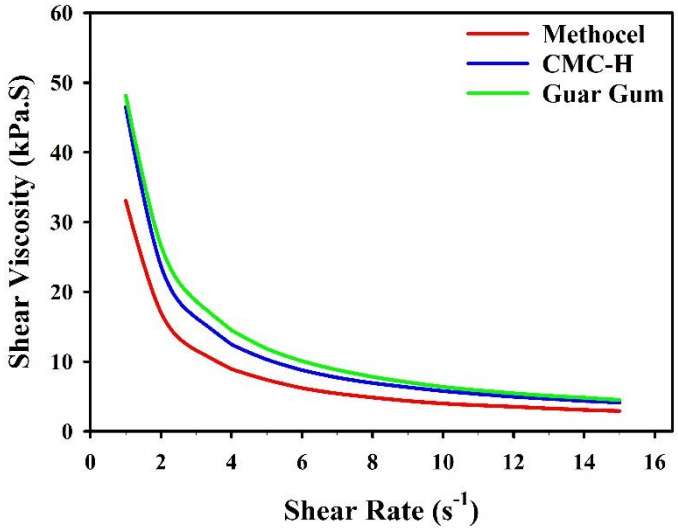

Fig. 4-4. *Flow properties of MC, CMC and GG, as measured by a capillary rheometer. All binders exhibited shear-thinning behaviour. Capillary rheometry was used to verify the shear-thinning nature of the formulated pastes using different binders (n = 1).*

Further analyses revealed that all three binders were capable of displaying shear-thinning properties at different shear rates, temperatures and solid loadings, as displayed in **Fig. 4-5 (a)**, **(b)** and **(c)**, respectively. Changes were seen in the viscosity when the solids loading and temperature were varied. **Fig. 4-5 (b)** demonstrates the increase in shear viscosity with increasing solids loading, at a given shear rate range; whereas, **Fig. 4-5 (c)** demonstrates the increase in viscosity with increasing temperature. In the latter, the difference in viscosity between pastes at ambient temperature and pastes measured at 40 °C was indiscernible, however, the difference was much more pronounced at 50 °C. In the case of MC, several attempts were made to measure the shear viscosity at 60 °C, but the paste could not be made to flow. Indeed, by increasing the temperature one would expect the paste to age and harden, however, the probable cause is likely to be the thermal gelation that MC undergoes at approximately 60 °C [333]. In a solution, thermal gelation occurs when the bonds in the polymer crosslink and convert the solution to a solid gel [334], consequently solidifying the structure. Coupled with a ceramic suspension, the

material stiffened to such an extent that it could not be effectively extruded by the capillary rheometer. Therefore, it was concluded that processing should not exceed 50 °C. This further highlights a benefit of using GG, as it is a non-thermally gelling polysaccharide [335]. In fact, GG has been demonstrated to effectively increase the thermal stability of other polysaccharides [335]. Nevertheless, capillary rheology revealed that the speed of extrusion, temperature and solid loading were not an issue for attaining shear-thinning characteristics, and hence suitable for extruding at room temperature.

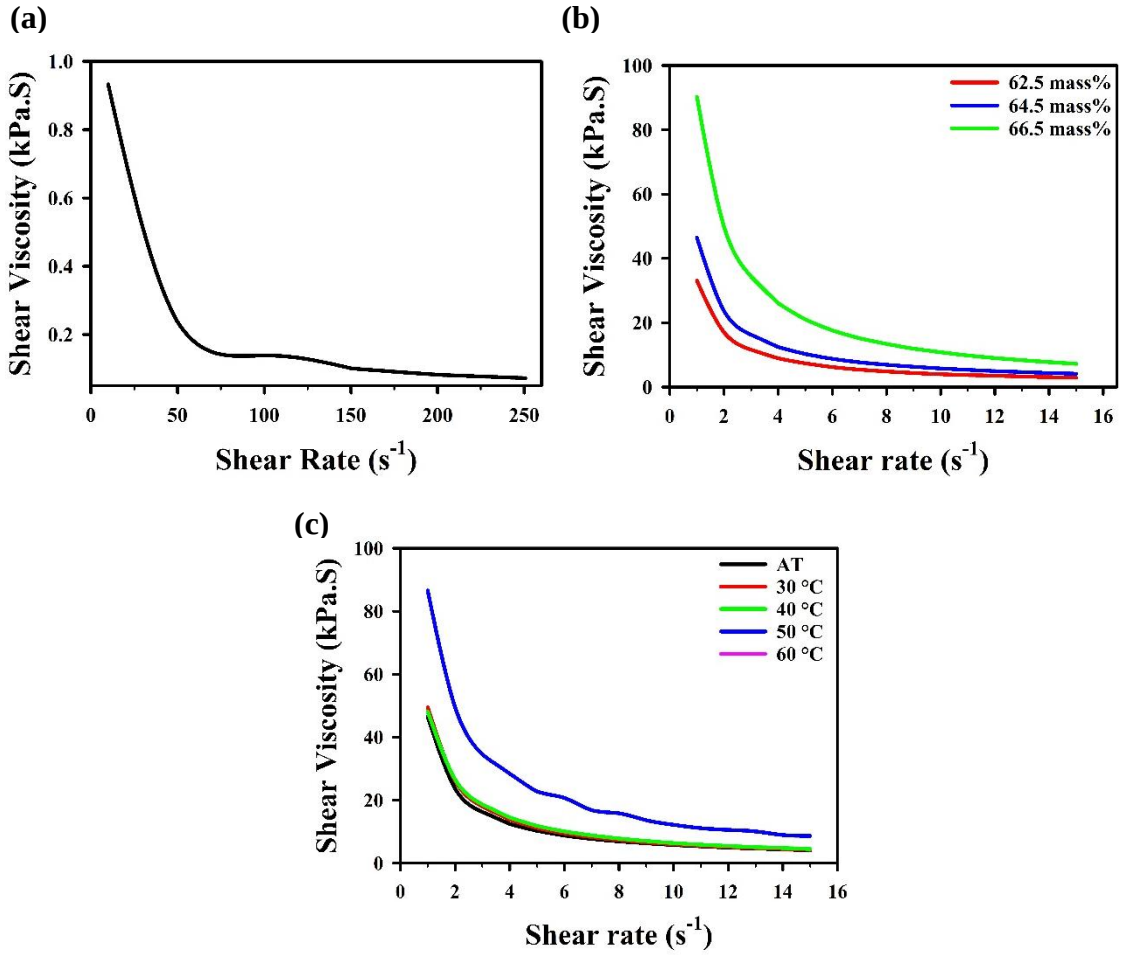

***Fig. 4-5**. Examples of how at varying shear rate **(a)**, solids loading **(b)** and temperatures **(c)**, the pastes were able to maintaing shear-thinning capabilities. Methocel™ was chosen as an example (n = 1).*

4.1.2.2 Rotational Rheometry: Dynamic Mechanical Analysis

Predicting paste properties for extrusion are traditionally performed using capillary rheometry. To compliment the rheological data obtained from the capillary rheometer, a rotational rheometer in dynamic mechanical analysis (DMA) mode was utilised to elucidate further information regarding the rheological properties of the paste. Rotational rheometers have higher sensitivity than capillary rheometers, and can quantify events that would otherwise need to be extrapolated using data obtained from the latter. DMA has conventionally been performed using mechanical testing machines. However, these require considerably larger sample sizes, and have a lower resolution compared to rotational rheometers. Furthermore, they do not provide shearing stresses, but rather normal forces. Thus, rotational rheometry offers several advantages over conventional methods for measuring DMA. To the author's best knowledge, the use of rotational rheometers in DMA mode for characterising pastes for extrusion has not been previously attempted.

DMA was principally employed to obtain the shear modulus and yield stress of pastes, which pertain to the stiffness of the pastes, as well as to qualify the plastic regions thereof. Similar experiments, such as varying solids loading (**Fig. 4-6 (a))** and temperature **Fig. 4-6 (c))** were again conducted, and the results concurred with the capillary rheometer's findings. For simplicity, the curves were plotted as shear stress-strain curves[3]. Increasing the solids loading of the pastes was found to increase the stiffness, and decrease the plasticity region. Using the stress-strain curve in **Fig. 4-6 (a)** as an example, at a solid loading of 62.5 wt%, ceramic pastes displayed an initial stiff behaviour (elastic region), succeeded by plastic behaviour. As the ceramic content was increased by increments of 2 wt%, increases in the paste stiffness were observed, and as well as decrease to the plasticity; until a solid loading of 68.8 wt%, where the pastes exhibited a limited plastic behaviour. This was expected, as an increase in ceramic content requires more binder coverage to obviate particle-particle contact. **Fig. 4-6 (b)** is a plot of the shear modulus as a function of solids loading, whereby it can be observed that the relationship is a growing exponential at the measured solids loading range. The data obtained is akin to that of Liu and Chou (2000) [336], where it was demonstrated that

[3] Typically shear modulus-stress curves are plotted, however, they are not easily interpreted by those unfamiliar with rheology.

steep increases in viscosity where an indication of the solids loading approaching the state of maximum packing.

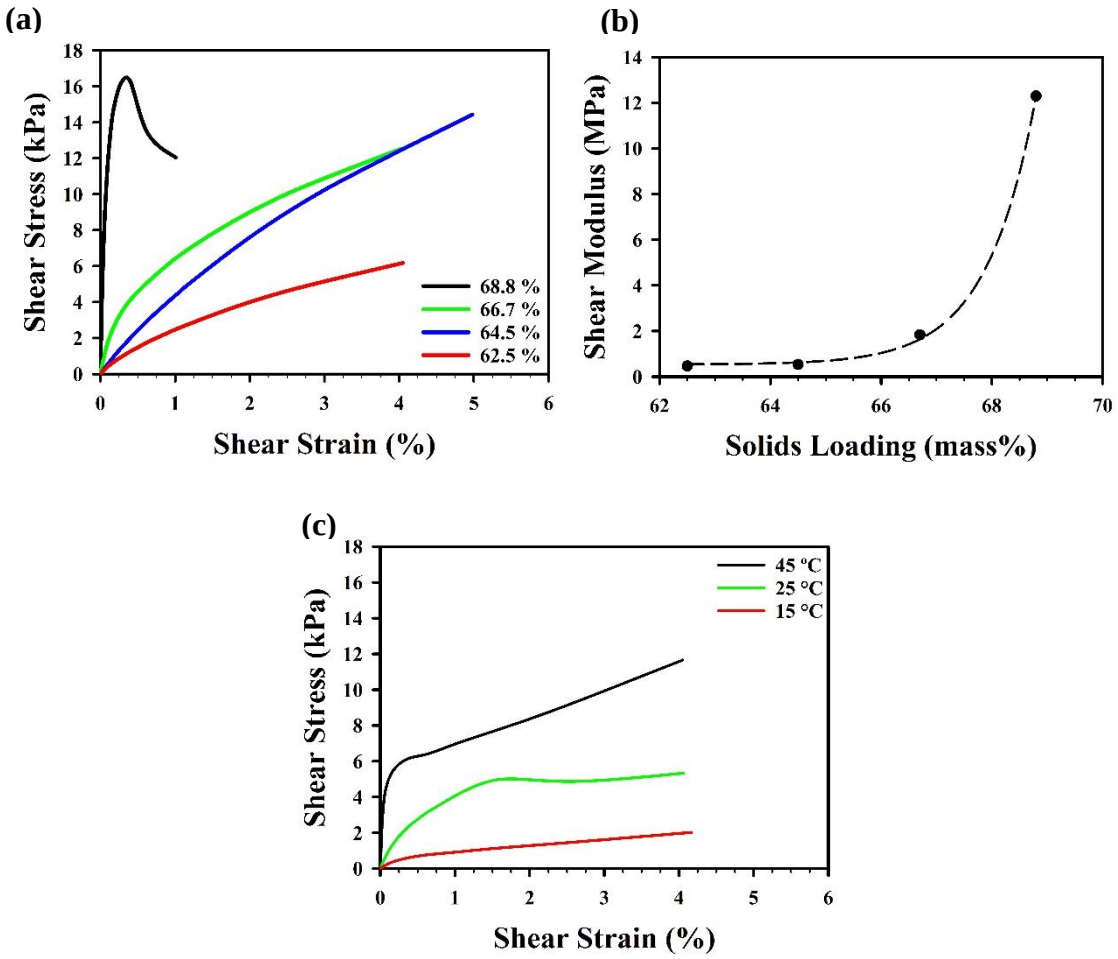

Fig. 4-6. *Torsional Dynamic Mechanical Analysis (DMA) of the pastes at varying solids loading* ***(a)*** *and Peltier plate temperature* ***(c)****. Plot* ***(b)*** *is the shear modulus as a function of solids loading (n=1).*

These preliminary rheological characterisations were performed to provide an insight into the rheological properties of the chosen binders. Capillary rheometry highlighted that paste flow remained shear-thinning, irrespective of binder, solids loading, shear rates and temperatures. DMA, on the other hand, demonstrated that paste mechanical properties varied, such as yield stress and shear modulus; in some instances, the difference was over an order of a magnitude. Therefore, depending on the desired extrusion outcome, pastes can be tailored to the desired stiffness by varying the solid loading, or controlling the extrusion temperature. Once extrusion has been performed, only then can it be understood what the desirable mechanical properties are.

4.1.3 Thermal Properties of Binders

Once the binder has been used to impart plasticity to the ceramic particulates, it will then need to be removed from the admixture before sintering of the ceramic can occur. Thermally degrading the polymeric binder is one means of achieving said task, whereby the admixture is subjected to sufficient heat that results in the degradation of the binder, and thus its extraction from the admixture. The ideal binder should be removed before sintering of the ceramic occurs, as to not impede the densification thereof. **Fig. 4-7** is a dilatometry curve of three different types of hydroxyapatites that were examined, which is used to exemplify that different HA raw materials exhibit different shrinkage. Despite subjected to the same heating parameters, all possessed varying sintering behaviours, which were ascribed to the difference in particle and chemical properties of the starting material. In this illustration, the sintering onset ranged from 510 °C (HA3) to 1050 °C (HA2). In light of this information, a binder that completely degrades by 500 °C would be ideal, as it can accommodate a wide range of hydroxyapatite materials.

Thermogravimetric analysis (TGA) was employed to determine the thermal properties of the binders, and the results are presented in **Fig. 4-8**. The salient feature that the analysis demonstrate was that only MC and GG underwent complete degradation, whereas approximately 10 mass% of the CMC remained at 1000 °C (**Fig. 4-8 (a)**). As mentioned, CMC possess a higher molecular weight than MC, and hence a higher burnout temperature was expected. However, the same would be true of GG, which is also a high-molecular weight binder. The CMC analysed was a high viscosity grade, and thus the test was repeated on a CMC with a lower molecular weight[4]. However, the lower viscosity grade also did not completely degrade within the instruments temperature limit (1020 °C).

[4] Also purchased from Sigma Aldrich

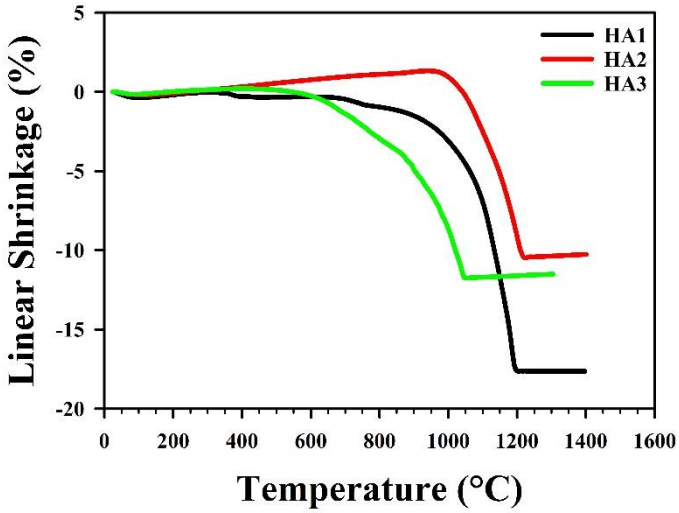

Fig. 4-7. *Examples of sintering profiles of three different hydroxyapatite samples[5]. As different hydroxyapatites possess different sintering profiles, the degradation behaviour of a binder will need to be determined to ensure that it is compatible with the ceramic (n=1).*

Alternative to the molecular weight, it could be deduced that the chemical composition of CMC was the cause of the increase in thermal stability, as CMC is known to be mixed with sodium monochloroacetate [337], and thus may contain inorganic functional groups that necessitates a relatively high degradation temperature. As a result of its high thermal stability, it was decided that CMC as a binder will be precluded from further studies.

Another noticeable feature was the multi-modal degradation observed in all samples, which is an indication that the polymers have a heterogeneous structure [338]. It can be observed that the first MC degradation step occurred at approximately 250 °C, whereby ~ 80% of the polymer was degraded; followed by a second degradation step commencing at approximately 370 °C, where the remainder of the polymer was degraded; complete binder degradation had occurred by 490 °C. Similarly, the first GG degradation had occurred from the start of the test until 125 °C, whereby 9 mass% of the binder was degraded; the second degradation step occurred between 235 to 315 °C, in which approximately a further 48 mass% loss was observed; the third degradation step occurred

[5] HA3 is the same hydroxyapatite material referred to as C-HA in **Chapter 7**. HA1 and HA2 are hydroxyapatite batches that were initially used for this project, but were then discontinued by Plasma Biotal. The inclusion of this figure is to illustrate the variance in sintering properties with different hydroxyapatites.

between 320 and 460 °C, where a further 32% mass loss was observed; the final degradation step that led to complete degradation occurred at 465 °C until 510 °C.

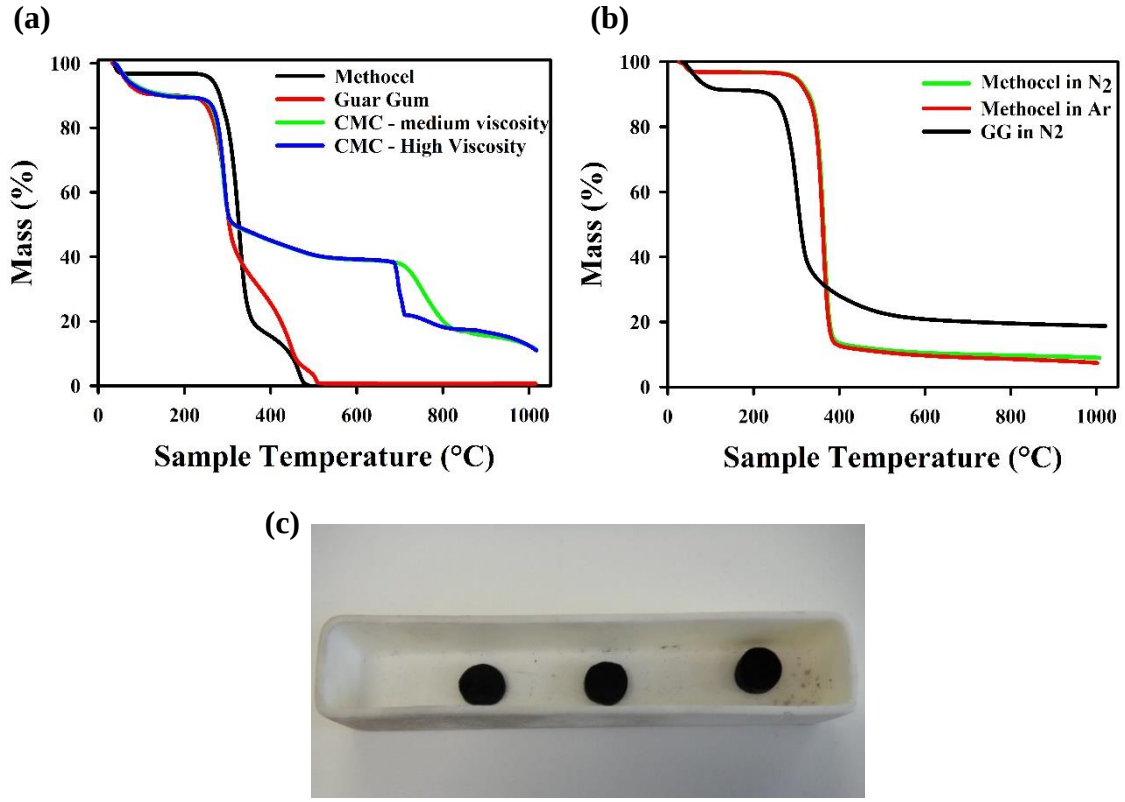

Fig. 4-8. *TGA of* ***(a)*** *Methocel™, guar gum and two variants of carboxymethyl cellulose in air;* ***(b)*** *Methocel™ and guar gum under inert atmosphere; and* ***(c)*** *an example of discoid pellets de-bound under nitrogen atmosphere. The experiments revealed on MC and GG completely degraded in the presence of air, but not under inert gases (n = 1).*

MC and GG were also examined under inert gas (**Fig. 4-8 (b)**), where it was discovered that incomplete degradation had occurred. The data demonstrate that MC does not completely degrade under both nitrogen and argon atmosphere; and similarly, GG does not completely degrade under nitrogen atmosphere. Approximately 10% and 25% of binder mass remained for MC and GG, respectively. **Fig. 4-8 (c)** portrays discoid HA pellets fabricated using GG that were heated to 500 °C under nitrogen atmosphere. The figure highlights the char residue coating the pellets, which account for the incomplete degradation observed in **Fig. 4-8 (b)**. Therefore, it was concluded that an oxidising atmosphere was needed to eliminate the carbonaceous coating and achieve complete degradation.

4.2 Extrusion

Following binder screening, the next step was to investigate the additives' performance for honeycomb extrusion, and correlate the results to the preceding analysis. This section begins by describing the extrusion kit used for fabricating the extrudates, followed by examining the effect of extrusion speed on extrudate quality.

4.2.1 Extruder Design

Extrusion was performed using a stainless-steel extruder that was designed *in-house*. The actuation of the piston was controlled by a servo-hydraulic press (Schenk 250). Initially, the extruder comprised a barrel, a piston and a honeycomb die, as illustrated in **Fig. 4-9**. An aluminium support was designed to allow visual access to the extrudate, as well as cutting thereof.

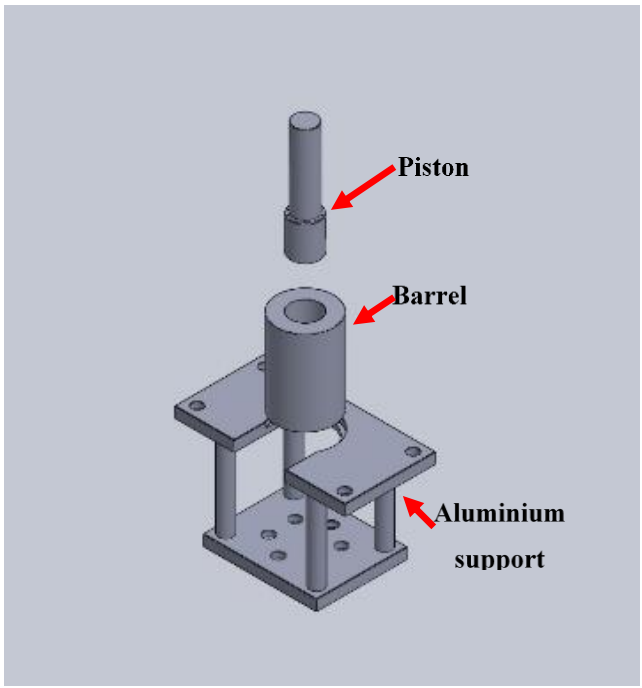

Fig. 4-9. *CAD model of the initial extruder setup.*

4.2.1.1 Die Design

A 60 mm die was designed and manufactured for the fabrication process. A computder-aided design (CAD) model of the honeycomb die is illustrated in **Fig. 4-10**. The die

comprised feed holes with a diameter of 1.2 mm, with a distance of 1.52 mm apart; the channels were 10 mm in length; and the pins that defined the pore shape were 10 mm in length, a width of ~ 1 mm, and a gap of ~0.6 mm between adjacent pins. The die was attached to the barrel by a combination of die flanges and a ring. 8 mm screws were used as fasteners (**Fig. 4-11**).

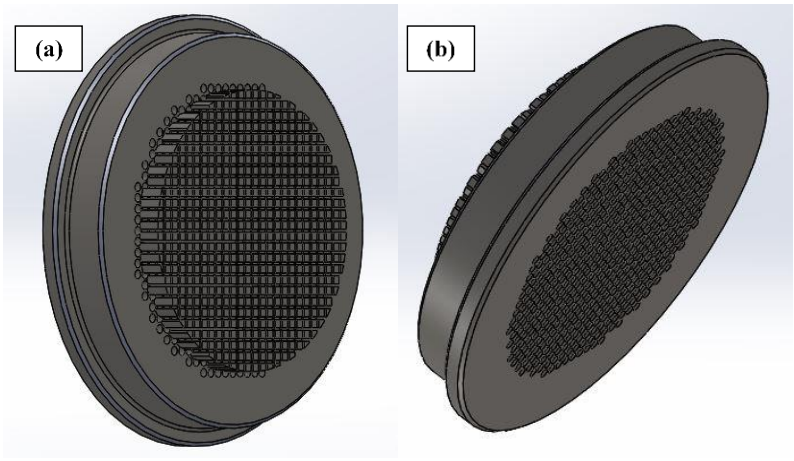

Fig. 4-10. *CAD rendering of the honeycomb die.*

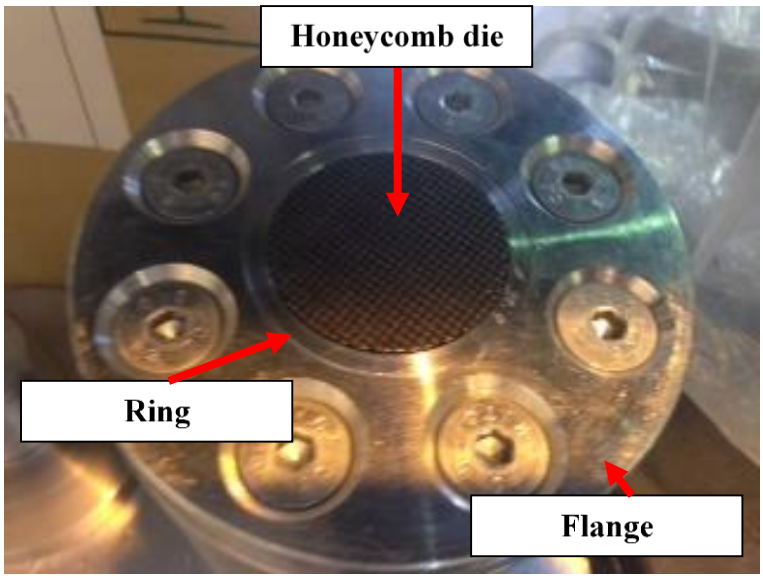

Fig. 4-11. *Image of the die, ring and flange setup.*

4.2.1.2 Compression and Vacuum Plates

The initial setup was too inconsistent in producing successful extrudates. The extrudates presented with typical extrusion defects, such as delamination. Many attempts were made

to see if the paste formulation could be varied to improve the quality of the extrudate, however, this proved unsuccessful. It was then decided that the extruder setup required additional components.

The revised approach was to incorporate a compression plate to the extruder. This allowed for a pre-extrusion step of evenly flattening the paste, in order to ensure equal pressure is applied across the cross-sectional area of the paste during the extrusion run. In addition, a vacuuming element was incorporated to remove trapped air that may have been introduced, for example, during kneading. The new designs accommodated O-rings to ensure a seal was formed during vacuuming (**Fig. 4-12**).

The pre-extrusion step entailed compressing pastes against the compression platen (**Fig. 4-12 (a)**). This compaction was performed manually by lowering the piston until forces of between 40-50 kN were reached. Subsequently, a diaphragm pump was switched on for 30 seconds to de-air the content of the extruder. A 6-mm polytetrafluoroethylene tube was used to connect the pump to the vacuum plate via the vacuum inlet.

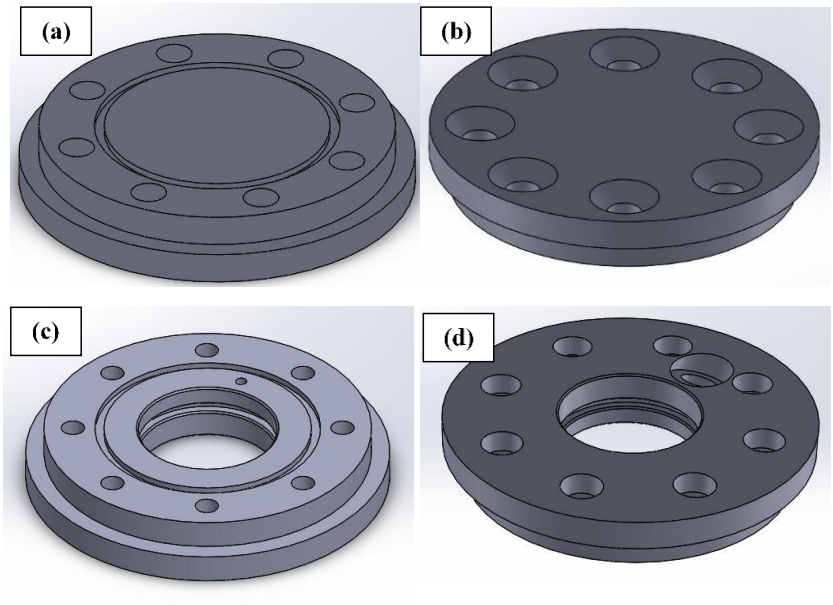

Fig. 4-12. *CAD models of the compression plate* ***(a)*** *top and* ***(b)*** *bottom view, and the vacuum plate* ***(c)*** *top and* ***(d)*** *bottom view; which were used to ensure the paste was levelled prior to extrusion, and remove air pockets within the paste, respectively.*

Following the pre-extrusion step, the compression plate was removed and replaced with the die, and extrusion ensued. The revised approach was successful in

improving the consistency of extrudate quality, by removing air pockets, as well as ensuring the paste was evenly levelled before forced through the die. **Fig. 4-13** depicts the levelled surface of the extrudate following the aforementioned pre-extrusion procedure.

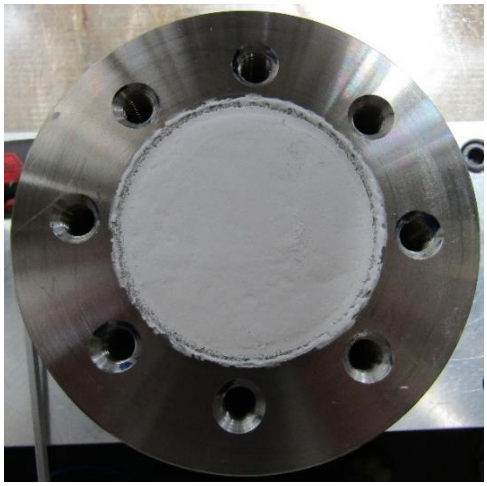

Fig. 4-13. *Image of the compressed paste before extrusion. A levelled paste before extrusion ensured the pastes entered the die uniformly.*

4.2.2 Extrusion Speed

The speed of extrusion was found to influence the quality of the extrudate. At lower speeds (1-100 mm/s), the extrudate had a tendency to warp, as illustrated in **Fig. 4-14**. The degree of warpage was decreased with increasing speeds. In the end, a speed of 250 mm/s was settled for after trialling at speeds ranging from 1 to 600 mm/s. Warpage during extrusion could have occurred due to improper die alignment [229], however, careful alignment and measurement was used to ensure this was not the case.

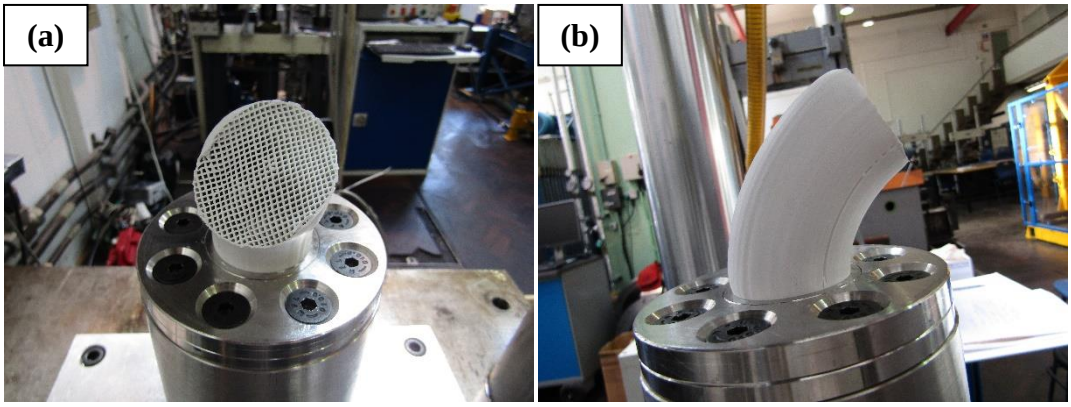

Fig. 4-14*. Examples of two warped extrudates. Such deformation resulted in small cracking during thermal treatments. These extrudates were of HA and Methocel™.*

4.2.3 Ideal Extrudable Paste Formulation

As discussed in **section 4.1**, pastes with varying properties can be formulated. However, following extrusion trials, it was evident that not all formulations produced an extrudable paste. Furthermore, variations were observed between MC and GG, where the ideal paste formulation of the former required a higher stiffness, which was achieved by increasing the solids loading. Using DMA, failed pastes (pastes that extruded but were too soft), and pastes resulting in successful extrudates were compared; characterisation was performed on pastes once mixed. DMA revealed that GG pastes with a shear modulus of ~0.4 MPa produced successful extrudates (**Fig. 4-15**). On the contrary, MC pastes of comparable modulus resulted in soft extrudates (**Fig. 4-16**). It is plausible that MC pastes were affected by the shearing of the extruder to a greater extent than those formulated with GG. The paste composition of said pastes are enumerated in **Table 4-2**.

Table 4-2. *Paste composition of the extrudates portrayed in* ***Fig. 4-16*** *and* ***Fig. 4-15****.*

Binder	**Constituents (vol%)**		
	HA	Binder	Distilled water
Methocel™	38.3	7.8	54.0
Guar Gum	34.4	5.7	59.9

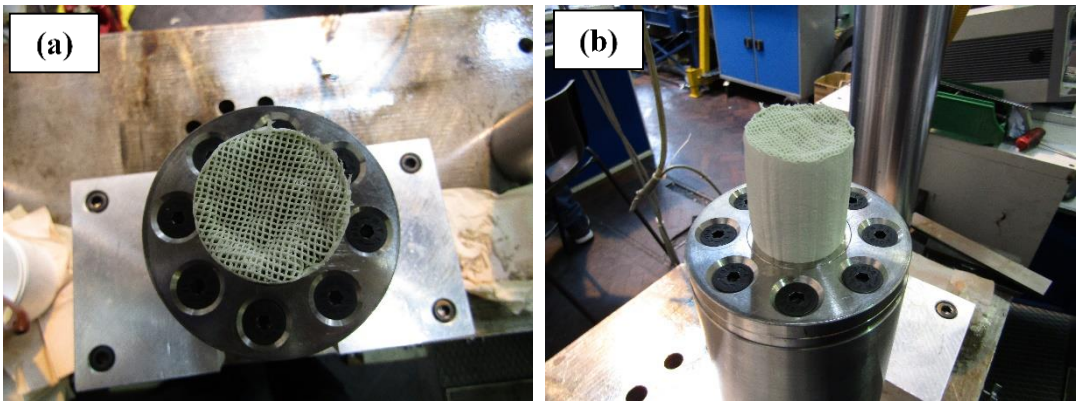

Fig. 4-15. *Images of an ideal extrudate, from* ***(a)*** *top-down view and* ***(b)*** *isometric view. Delamination, small tears, flow warpage, or other deformations were not observed. This particular extrudate was formulated using HA and guar gum.*

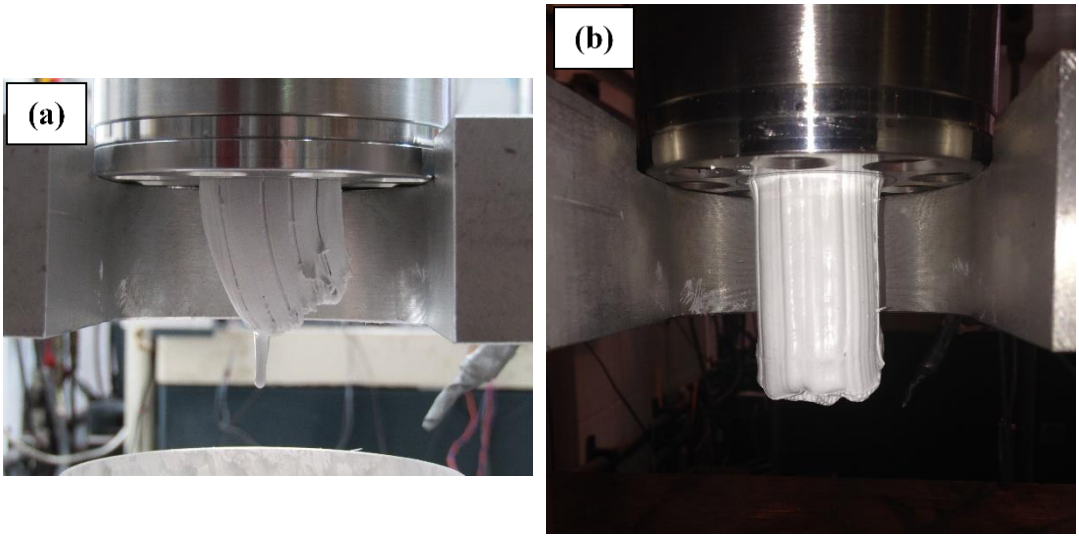

Fig. 4-16. *Examples of extrudates with a low shear modulus. These pastes were difficult to handle due to their softness.*

For successful MC extrudates, the shear modulus needed to be in mega-pascal region before extrusion, rather than the sub-mega pascal range. These values ranged from 5-30 MPa, depending on paste composition and ceramic raw material. It is uncertain as to the cause of the discrepancy between the two binders. Without an in-depth analysis between the two to understand the chemical composition and chemical structure thereof, and how said properties affect the rheology (e.g. storage modulus, loss modulus, yield stress), a complete conclusion cannot be drawn. It is possible that the manufacturer of MC tailored the proprietary formulation to be loaded with a high ceramic content, as a high ceramic loading will minimise the shrinkage during firing. As a result, the higher demand for solids loading increased the shear modulus, as outlined in **Fig. 4-6**. This value of shear stiffness was able to be extruded using the current setup, but could be impractical for other extrusion-based fabrication techniques that operate at lower pressures, such as robocasting.

Additional differences were observed between MC and GG pastes by DMA. GG pastes presented with a wide plasticity region, whereas MC demonstrated no appreciable plasticity. Moreover, *in-situ* extrusion recordings revealed an indiscernible difference between the maximum extrusion force (**Fig. 4-17**), despite the difference in solids loading and DMA properties; albeit a difference in extrusion behaviour was descried following peak extrusion force. The maximum solids loading achieved with GG was 34.4 vol%,

whereas MC pastes were able to achieve 42.0 vol%. For this reason, MC was regarded as more favourable, and was the primary binder for this project.

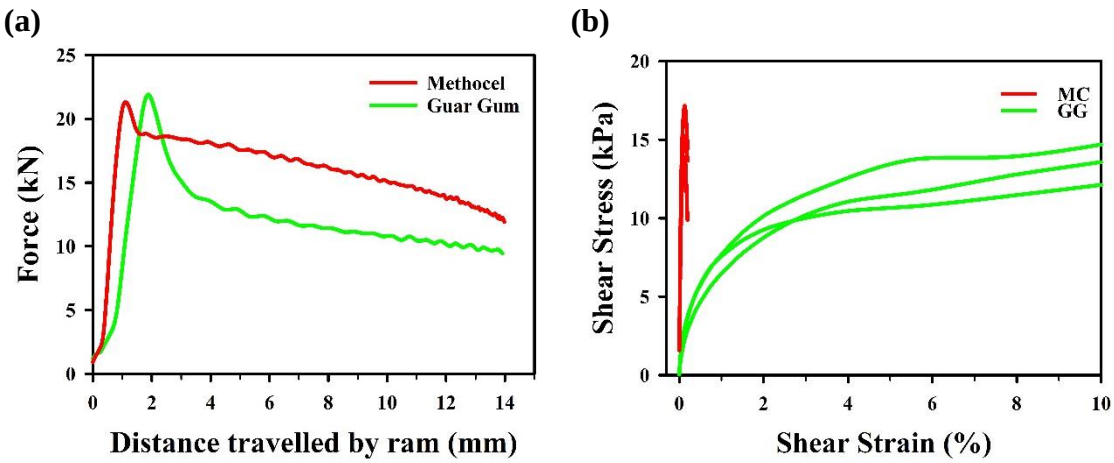

Fig. 4-17. *Figure to illustrate the difference between Methocel and guar gum pastes during* ***(a)*** *extrusion (n=1) and* ***(b)*** *DMA tests (n=3). The data demonstrates that pastes with higher shear modulus detected by DMA manifested in pastes with a steeper gradient in the force-distance data observed during extrusion.*

In summary: extrusion was performed following compaction and de-airing of the pastes; a speed of 250 mm/s was discovered to mitigate warping of the pastes; and DMA analysis revealed that successful MC and GG extrudates required a shear modulus within the mega pascal and sub-mega pascal range, respectively. The disparities in DMA characteristics highlight the versatility of extrusion in accommodating pastes with varying rheological properties.

4.3 Thermal Treatment

The final stage of the fabrication process will be to achieve permanence through densification. Prior to this, drying and thermal de-binding are required to extract the organic components on the extrudate. Accordingly, this section of the chapter describes the drying and de-binding that the extrudates were subjected to.

4.3.1 Drying

The green bodies were composed of 25 – 35 mass% water, which makes the drying a critical step. Drying is a complex process that involves evaporation, fluid flow through permeable pores, and shrinkage. The former two induce macroscopic stresses (e.g. due to capillary forces) that lead to cracking. Fast evaporation results in high macroscopic stresses and hence large differential strains. Furthermore, drying may lead to "binder migration", whereby the solvent carries dissolved binder as it evaporates. This too may cause macroscopic stresses.

Preliminary trials in drying the extrudates in a furnace at temperatures as high as 100 °C, down to 50 °C, for 24 hours at 5 °C/min resulted in the formation of cracks, of which some only became evident during subsequent thermal stages. It was concluded that these temperature ranges resulted in fast, detrimental drying. The best results were seen when extrudates were dried at room temperature. This was performed by placing the extrudates in a container for 24-48 hours prior to binder extraction.

4.3.2 Thermal De-binding

Similar to drying, excessive pressure can be produced from inside the green body during de-binding. Binder composition ranged between 4 – 6 wt%, which is significantly less than that of water, but nonetheless incorrect handling can lead to cracking. De-binding of the extrudate was performed thermally. TGA was once again performed on successfully-extruded pastes to elucidate changes in binder degradation within the admixture. It is known that in the presence of inorganic powder, the degradation shifts to higher temperature, as the binder is adsorbed onto the surface of the particles. Hence, higher energy is needed to counteract this adherence [223]. Moreover, TGA of pastes provided a quantitative means of determining the paste composition. The solvent and binder exhibited discrete temperature ranges for their respective extraction, and thus mass changes during these discrete ranges equated thereto. The final mass remained after the analysis equated to the ceramic solid loading. The TGA values correlated to the theoretical amount, despite the partial evaporation observed during mixing, and thus reaffirmed that the theoretical value could be accepted.

Fig. 4-18 is an example of a TGA trace depicting pastes formulated using MC and GG. As can be observed, the initial mass loss was due to the water evaporation. The bimodal degradation observed in the raw MC powder was once more observed in the admixture, but the multimodal degradation observed in GG was less pronounced in pastes thereof. It can also be observed that the second MC degradation step occurred at a later temperature, and completely degraded by 750 °C. This was likely due to the extraction of binder that adhered on particles.

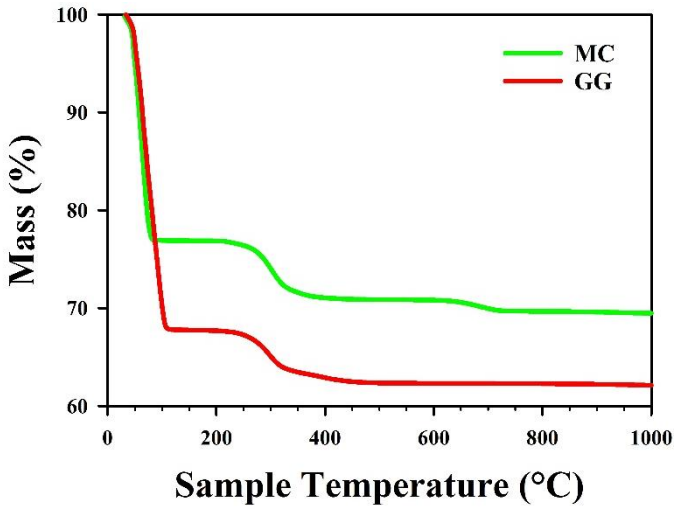

Fig. 4-18. *Examples of a TGA trace of pastes formulated using Methocel™ and guar gum. TGA analysis of the pastes revealed the binders to degrade at higher temperatures, in contrast to the as-received binder powder (n=1).*

At 500 °C, an imperceptible amount of GG remained (**Fig. 4-18**). This was confirmed by SEM micrographs (**Fig. 4-19 (b))**, where it was revealed that the binder remained on the particle surface at 500 °C. Attempts to analyse samples de-bound above this temperature were unsuccessful, as samples were too weak due to insufficient green strength, and crumbled during sample preparation. However, SEM analysis of sintered scaffolds did not present with noticeable MC or GG residue, thereby indicating binder extraction occurred above 500 °C. **Fig. 4-19 (a)** is included to highlight the difference in paste morphology at 400 and 500 °C, where the adhered binder can be seen to start degrading in the latter.

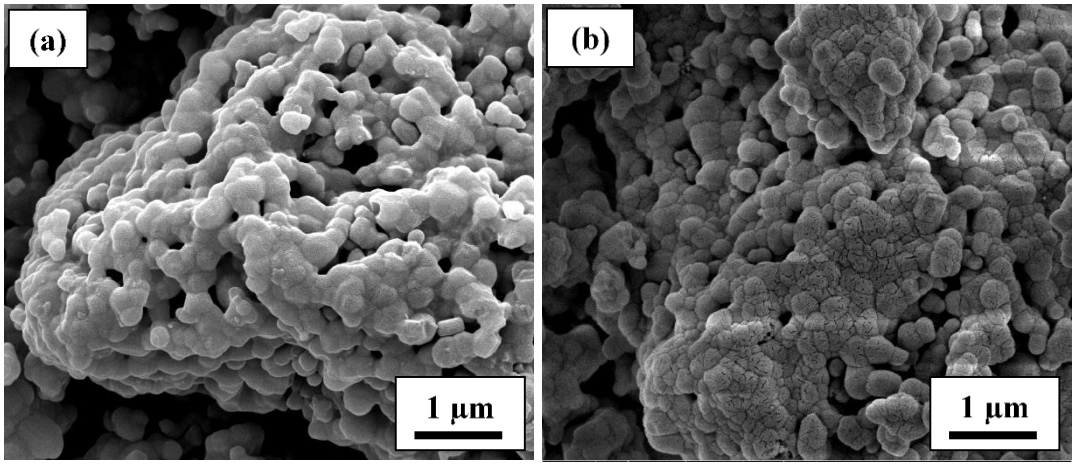

Fig. 4-19. *Scanning electron microscopy (in secondary electron mode) micrographs of a sectioned part of a hydroxyapatite extrudate formulated using guar gum subjected to temperatures of* ***(a)*** *400 and* ***(b)*** *500 °C. The micrographs revealed that guar gum remained adhered at said temperatures.*

De-binding and sintering had to be performed in two separate muffle furnaces, due to the acerbic nature of the binders and laboratory restrictions. Based on paste TGA, the extrudates were thermally de-bound in air at a maximum temperature of 400 °C, where the majority of the binder was eliminated. Extrudates were placed on an alumina crucible and inserted inside a muffle furnace situated inside a fume hood. However, the furnace could only reach temperatures of 1100 °C, which was below sintering range. Thus, the extrudates were transferred to a different muffle furnace capable of reaching higher temperatures once de-bound at 400 °C. De-binding at 400 °C was opted for as a small amount of binder was left to impart enough strength to prevent the structure from collapsing during the transfer.

The heating rate at which to thermally de-bind the extrudates was empirically determined. Initially, a heating rate of 5 °C/ min was trialled, but as **Fig. 4-20** illustrates, this resulted in cracks forming, which were later exacerbated by sintering. De-binding at 3 °C/min was an improvement, however, cracks formed on extrudates after sintering. The ideal heating rate was 1 °C/min, where improvements to the integrity of the structure were observed. The results suggest a rate above 1 °C/min was excessively fast and initiated cracking. The same was true for both extrudates formulated using MC and GG.

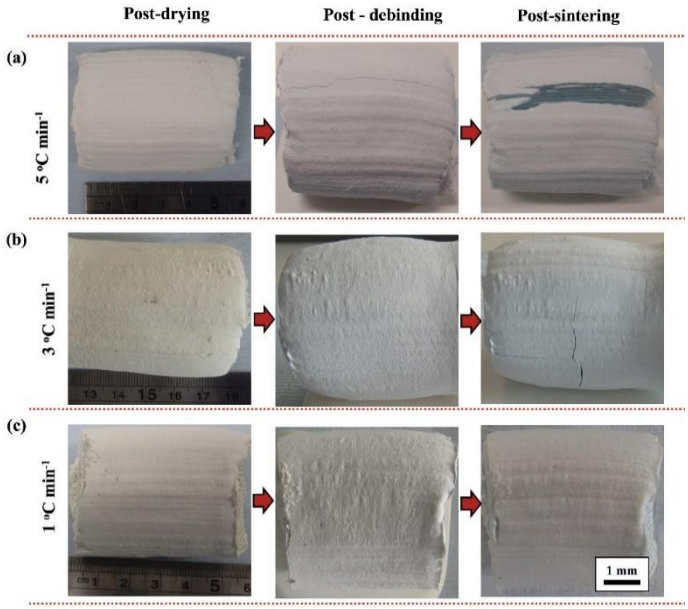

Fig. 4-20. *Images of guar gum-formulated extrudates that were subjected to different heating rates. The figure illustrates that 1 °C/min resulted in crack-free extrudates, whereas higher heating rates of 3 and 5 °C/min during de-binding resulted in cracks.*

As a result, a ramp rate of 1 °C/min was used with the following de-binding protocol:

- Heat to 200 °C for 1 h;
- Heat to 300 °C for 1 h;
- Heat to 400 °C for 3 h;
- Cool down to room temperature at 5 °C/min.

Fig. 4-21 are front images of the extrudate depicted in **Fig. 4-20 (c)**, used to illustrate the effects of the slow heating rate on the extrudates. After sintering, a small number of struts fractured, but this was superficial.

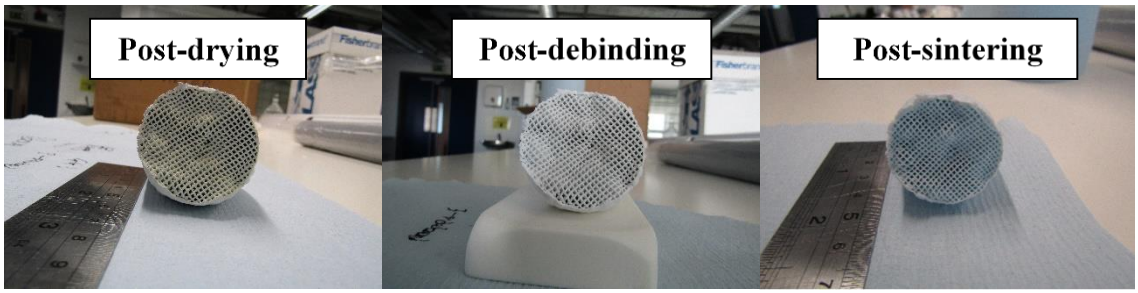

Fig. 4-21. *Front images of the extrudate from* ***Fig. 16 (c)*** *at different stages of the heating cycle.*

4.3.3 Sintering

Following drying and de-binding, the final thermal treatment was sintering, which is an irreversible process whereby a particulate system is transformed into a single, coalesced body. The transformation increases the system's density, eliminating voids and in the process, enhances the strength. In conventional sintering, which is used herein, the driving force for this densification is a reduction in free energy, which is achieved by decreasing the surface area.

Sintering parameters were determined by dilatometry analysis, and fabricating discoid pellets. The latter was opted for the hybrid materials that contained glass (**Chapter 7**), as the material would have reacted with the dilatometer's sample holder and pushord and thus, damaged the instrument. Indeed, dilatometry was preferred where possible as it provided a more comprehensive detail of the sintering characteristics of materials (**Fig. 4-7**). As detailed in the subsequent results chapters, sintering analyses revealed that all samples except for one were densified by 1200 °C (**Canasite, Chapter 7**). Accordingly, it was established that sintering of the biomaterials were to be performed in air at either 1200, 1250 or 1300 °C. Moreover, these temperature values were widely used by other researchers (**section 2.4.9.4**), which allowed for comparison of, for example, mechanical properties. Sintering was performed at nominal heating and cooling rates of 5 and 2.5 °C/min, respectively, unless otherwise stated. An example of a sintered extrudate is illustrated in **Error! Reference source not found.**.

4.4 Summary of Chapter

The chapter herein highlights the steps involved in the fabrication of the scaffolds, and the rationale for the parameters chosen. Furthermore, the chapter illustrates the feasibility of fabricating extrudates using simply a binder and distilled water. Distinct polymeric binders were also successfully fabricated into honeycomb extrudates, emphasising the versatility of the technique to accommodate different rheological properties. The extrudates were then subjected to a slow thermal treatment in order to mitigate the occurrence of defects. Key findings determined during the optimisation procedure were:

- An ideal mixing strategy for the order of mixing, and preventing partial evaporation of water. The order of mixing established was the mixing of the

ceramic powder and binder first, followed by incremental addition of distilled water;

- High extrusion speeds minimised the paste flow warpage, with an extrusion speed of 250 mm/s found to produce warpage-free extrudates;
- DMA analysis revealed paste stiffness in the order of 10^{-1} MPa for guar gum pastes, and 10^{1} MPa for Methocel™ were suitable for extrusion;
- Methocel™ was the most suitable for this research, as it can thermally degrade at 500 °C, which was a temperature prior to hydroxyapatite particle sintering. Furthermore, a higher solids loading was achieved with Methocel™ (38.3 vol%) compared to guar gum (34.4 vol%);
- A slow de-binding rate of 1 °C/ min minimised defect formation during de-binding and sintering.

The chapter was centred on binders and their effects on extrusion. The following chapters will primarily focus on the effects of the raw ceramic powders using Methocel™ as the binder, the extrusion parameters determined, and the thermal treatments determined herein.

Chapter 5: Fabricating Calcium Phosphate Porous Scaffolds via Extrusion

In the previous chapter, the effects of the binder and the extrusion parameters were detailed. The present chapter is first of three that centres on the raw ceramic powder, beginning with two most widely used calcium phosphates: Hydroxyapatite and β-tricalcium phospate; and their effect on scaffold properties. The two materials were subjected to similar processing steps, except for sintering of the β-TCP scaffolds that was performed only at 1200 °C to prevent the anticipated phase transformation. Included in this work are characterisation of the starting powders, the formulated pastes and of the densified scaffolds. The purpose of this preliminary study was to gain an understanding into the effects of the starting powder on the final product fabricated via ceramic honeycomb extrusion.

5.1 Introduction

Hydroxyapatite (HA) and β-Tricalcium phosphate (β-TCP) are the most studied and surgically used calcium phosphates due to their advantageous properties [339]. For this reason, both were chosen for the initial study of fabricating calcium phosphate via honeycomb extrusion. HA, $Ca_{10}(PO_4)_6(OH)_2$, and β-TCP, $Ca_3(PO_4)_2$, vary in their chemical composition, where HA has a hydroxyl group incorporated into its crystal lattice and β-TCP does not. Broadly speaking, HA scaffolds possess the higher strength, but also exhibit significantly lower bioresorpability, which is unsuitable for some bone grafting applications [340, 341]. This is believed to be as a consequence of the difference in chemical composition of said materials. Indeed, other factors contribute towards the properties of the scaffold, such as the particle properties and phase purity of the samples.

As previously mentioned, the use of ceramic extrusion for the fabrication of β-TCP and HA remains relatively unexplored. This chapter explores the potential of ceramic honeycomb extrusion for the fabrication of both HA and β-TCP scaffolds. The characterisation of the raw materials, and their effects on paste formulation and scaffold properties, are detailed below.

5.2 Experimental Procedure

5.2.1 Raw Materials

Commercially available hydroxyapatite (Purum grade, Sigma Aldrich, U.K.) and β-Tricalcium phosphate (batch 340S, Plasma Biotal, U.K.) were used for this study. The Methocel™ binder was as mentioned in **Chapter 4**. Distilled water was used as the solvent.

5.2.2 Method

The mixing, extrusion, and de-binding processes employed for this study were as detailed in **Chapter 4**. A one-step sintering strategy was used for densifying the extrudates, whereby samples were sintered to the designated temperature at a heating rate of 5 °C/min, with a dwell time of either three or five hours, and a cooling rate of 2.5 °C/min. The characterization techniques used are all documented in **Chapter 3**.

5.3 Results

5.3.1 Raw Powder

The effects of the raw powder on CaP scaffolds have been well documented. Suffice it to say, as the raw powders are the starting point of the fabrication process, their characterisation is needed to understand the effects on subsequent processing stages. For example, ceramic particles are available in a myriad of morphologies, and hence it is imperative that their properties are elucidated.

5.3.1.1 Physical Properties of the Raw Powders

SEM analysis was employed to examine the morphology of the β-TCP and HA raw powders used, whereby stark differences were discovered. The β-TCP powder comprised a mixture of equiaxed, nano- and micron-sized particles, which were near-spherical in shape, as illustrated in **Fig. 5-1**.

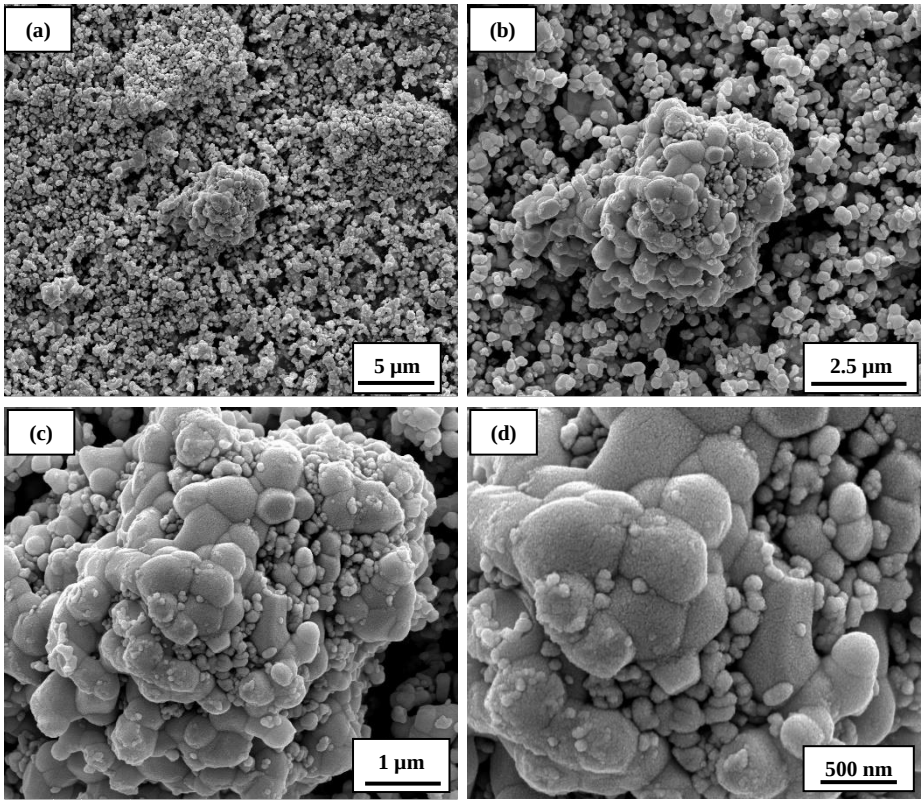

Fig. 5-1. *Scanning electron microscopy (in secondary electron mode) micrographs of the TCP starting powder at different magnifications.*

On the other hand, the HA raw powder consisted of nano-sized primary particles that formed near-spherical agglomerates, as delineated in **Fig. 5-2**. Higher magnification SEM analysis (**Fig. 5-2 (d)**) placed the size of the primary particles at below 10 µm.

The starting CaP powders were also analysed for their density, surface area and particle size distribution, and the results are enumerated in **Table 5-1**. The β-TCP powder exhibited a higher density and a wider particle size distribution, but a markedly lower surface area than that of the HA powder; both of which were statistically significant. The table clearly demonstrates that the β-TCP particles were larger. The β-TCP particle size distribution was found to range from 0.5 to 40 µm, whereas the HA powder ranged from 0.1 to 13 µm. The HA powder was then subjected to vigorous comminution options available to the instrument (stirrer speed and ultrasound), but to no avail.

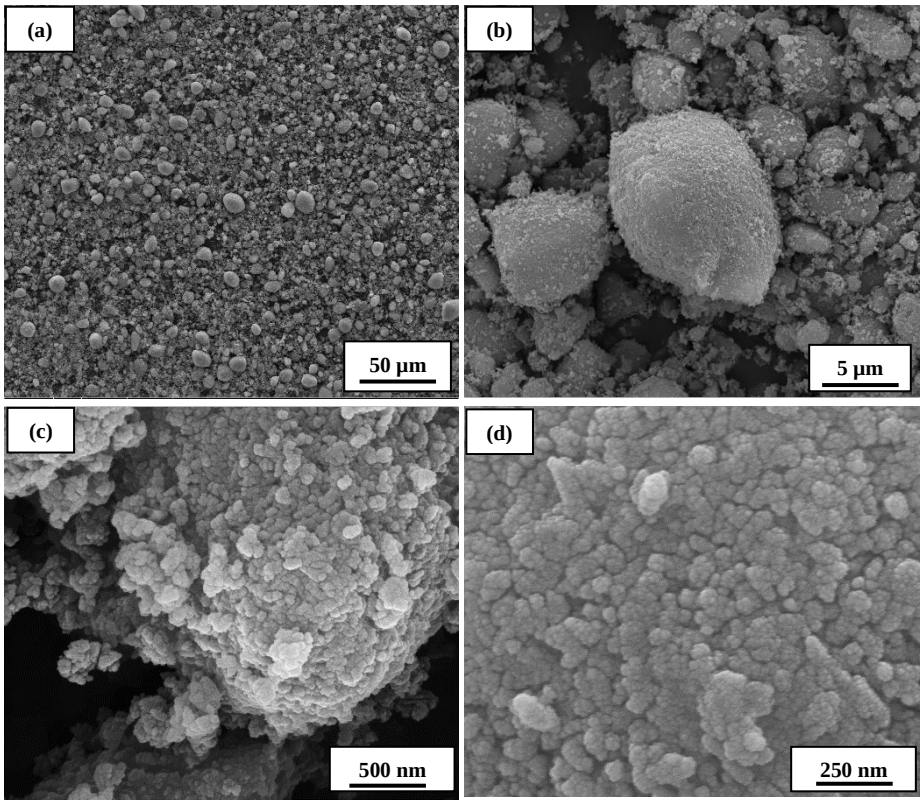

Fig. 5-2. *Scanning electron microscopy (in secondary electron mode) micrographs of the HA starting powder at different magnifications. The particle sizes appeared to be markedly smaller than that of β-TCP.*

Table 5-1. *Physical properties of the β-TCP and HA powders. The density was measured using a helium pycnometer (n = 3), BET using a BET surface analyser (n = 3)) and the particle size distribution using a particle size analyser (n = 5). All plus/minus signs represent the standard deviation.*

Sample	**Density[a] (g/cm^3)**	**BET (m^2/g)[a]**	**Particle Size Analysis (µm)[a]**		
			D_{10}	D_{50}	D_{90}
β-TCP	3.11 ± 0.01	8.97 ± 2.9	1.36 ± 0.17	3.65 ± 0.26	13.6 ± 1.41
HA	2.90 ± 0.04	107.91 ± 6.1	0.45 ± 0.04	2.49 ± 0.02	7.57 ± 0.17

[a] An unpaired t-test was performed to determine the statistical significance. A significance was found between the β-TCP and HA density and BET data ($p < 0.05$).

5.3.1.2 XRD and FTIR Analyses of the Raw Powders

XRD and FTIR analyses were also performed on the starting calcium phosphate material, and the results are portrayed in **Fig. 5-3** and **Fig. 5-4**, respectively. XRD analysis of the β-TCP powder confirmed the presence of β-TCP phases (PDF: 04-001-7104), with a trace HA phase (PDF: 01-089-4405), as highlighted by the red asterisk in **Fig. 5-3 (a)**. The starting powder was confirmed as HA (PDF: 01-089-4405), and no secondary phases were detected. In contrast to the β-TCP pattern, the HA powder presented with a poorly defined XRD pattern that had broader peaks and lower peak intensities.

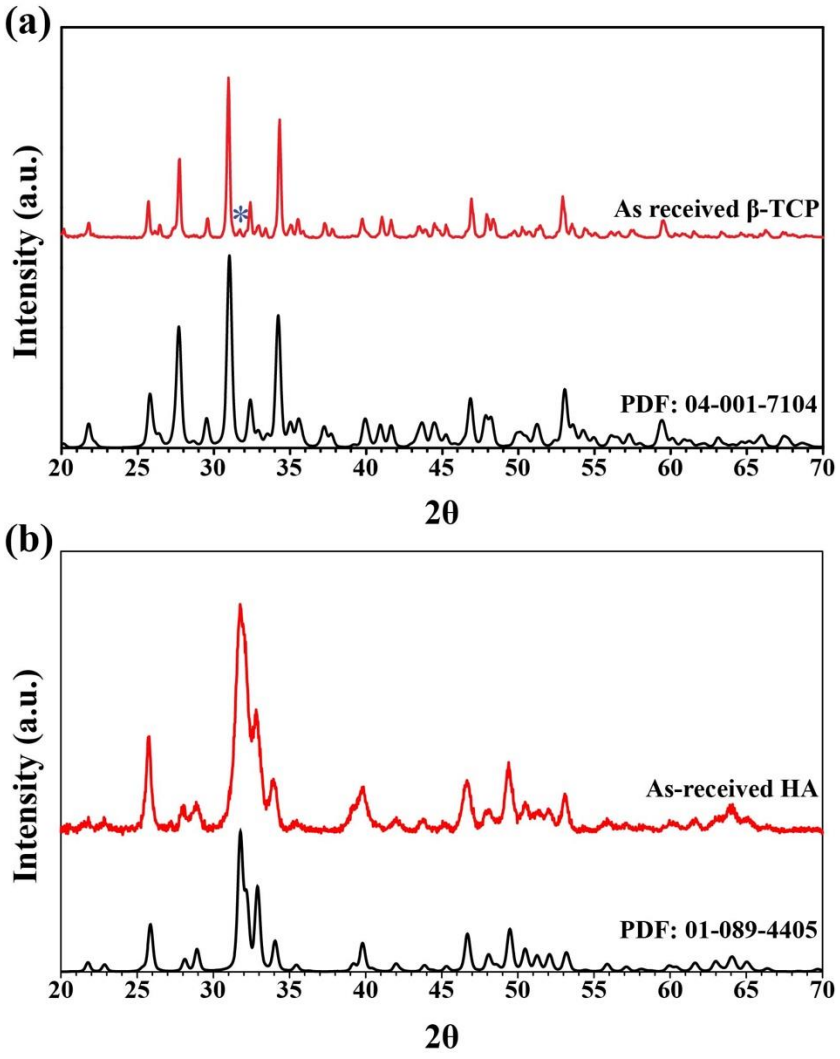

Fig. 5-3. *XRD pattern of the* ***(a)*** *β-TCP and* ***(b)*** *HA starting powder. The blue asterisk indicates an HA secondary phase in β-TCP. No additional peaks were found in HA, as confirmed by the included powder diffraction file.*

Examining the β-TCP powder via FTIR analysis (**Fig. 5-4 (a)**) revealed characteristic β-TCP phosphate bands at 1120, 1100, 1045, 972, 945, 605 and 553 cm^{-1}. An additional peak at 3570 cm^{-1} was also identified, which pertains to a hydroxyl group, thereby corroborating with the XRD data in the trace presence of a HA phase. FTIR analysis of the HA starting powder (**Fig. 5-4 (b)**) revealed characteristic HA phosphate peaks at 1089, 1038, 962, 875, 603 and 567 cm^{-1}. Again, analysis of the raw powder presented with an ill-defined spectrum. Furthermore, the hydroxyl group at 630 cm^{-1} was not detected, and the peak indicative thereof at 3570 cm^{-1} was minute.

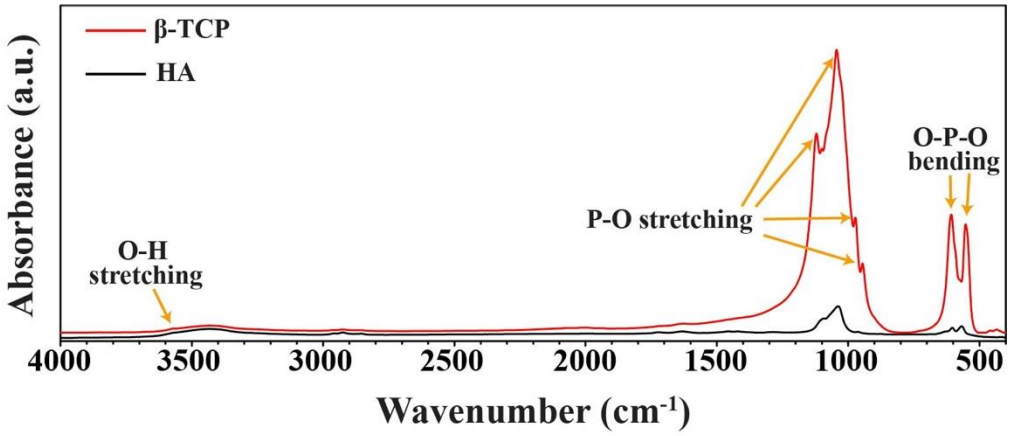

Fig. 5-4. *FTIR spectra of the as-received β-TCP and HA. Both samples presented with a hydroxyl group at 3570 cm^{-1}, indicating that the as-received β-TCP was not phase pure. Additionally, HA possessed an ill-defined spectrum in respect to β-TCP.*

5.3.1.3 Thermal Properties of the Raw Powders

Thermal analyses were employed to determine a suitable sintering temperature for the starting calcium phosphate powders. Sintering is required for densification of a particulate ceramic compact. Dilatometry analysis can elucidate sintering characteristics, such as the onset of sintering, and hence, was employed to determine temperature points that can be used to form dense CaP scaffolds.

Fig. 5-5 depicts the dilatometry and differential scanning calorimetry (DSC) analyses of the as received β-TCP powder. The β-TCP material underwent an initial shrinkage, which was attributed to sample dehydration, and thereafter proceeded to expand by 2% from ~ 100 °C to 950 °C, and subsequently began to sinter (highlighted by

the vertical red line). From the onset of sintering, the shrinkage proceeded until ~1220 °C, where a minute decrease in the rate of shrinkage was observed until ~1260 °C. A transient and sharp expansion of 1% ensued, which was followed by a gradual expansion until the end of the test. **Fig. 5-5** also displays a DSC curve were an endothermic trough reaction occurred at approximately 1220 °C.

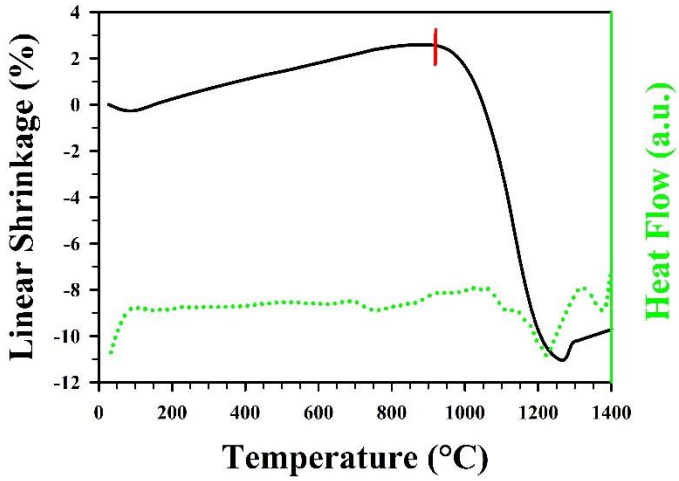

***Fig. 5-5**. Dilatometer (solid line) and Differential Scanning Calorimetry (dotted green line) curves of the TCP starting powder. The solid red line highlights the sintering onset. The transient expansion observed in the dilatometry at ~1220 °C is believed to be due to phase transformation, which corresponded to an endothermic event in the DSC.*

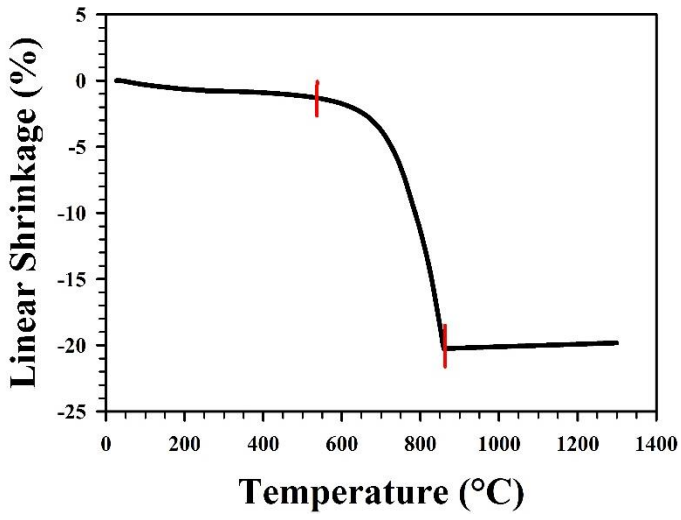

***Fig. 5-6.** Dilatometer curve of the HA starting material. The solid red lines are used to highlight the onset and end point of sintering. Compared to β-TCP, HA had a lower sintering onset, and a greater maximum linear shrinkage.*

Fig. 5-6 delineates the HA powder dilatometry results. The material presented with linear shrinkage from the outset, with an initial but gradual shrinkage of approximately 1% until ~ 650 °C, where the rate of shrinkage markedly increased until ~ 850 °C. During this temperature range, the HA material exhibited shrinkage of ~ 20%, resulting in a total shrinkage of approximately 21%. At 850 °C, the material underwent no further shrinkage until the end of the analysis. The data did not present with phase transition characteristics, and therefore, inferred that temperatures of up to 1300 °C will produce a phase-pure sample.

5.3.1.4 Summary of β-TCP and HA Raw Materials

In summary, the calcium phosphate starting material were characterised to determine their particle characteristics, purity and thermal properties. Particle analyses revealed distinct morphologies, with the β-TCP powder comprising of both nano and micron-sized particles; whereas HA was comprised of nano particles that had a high tendency to form micron-sized agglomerates. Chemical analyses revealed that both the β-TCP and HA starting materials were nonstoichiometric. Finally, thermal analyses demonstrated the relatively lower sintering onset and endpoint of HA, as well as the noticeably higher total shrinkage. Moreover, dilatometry and DSC analysis revealed a thermal event occurs in β-TCP at approximately 1220 °C.

5.3.2 Paste Properties

The calcium phosphate powders were mixed with Methocel™ and distilled water to form a plasticised ceramic paste, and their respective compositions are displayed in **Table 5-2**. An arbitrary ratio of ceramic powder-to-binder 10:1 was used. The ratio was successful for formulating a paste using β-TCP, however, a HA paste could not be formed. After several attempts, it was found that more distilled water was required for forming a paste using the HA, thereby resulting in a paste with a lower ceramic solid loading.

Table 5-2. *The contents and mass% of the β-TCP and HA pastes.*

Material	Paste composition (mass%)		
	Ceramic	Binder	Distilled Water
β-TCP	62.2	6.2	31.5
HA	57	6	36

The pastes were loaded into the barrel of the extruder and then extruded. The average forces required for extruding the β-TCP and HA pastes through the honeycomb die were 19.31 ± 3.05 and 44.01 ± 4.0 kN, respectively. Therefore, the force required to extrude the HA was more than double of that required for the β-TCP paste.

5.3.2.1 Rheological analysis: DMA

Dynamic mechanical analysis (DMA) was also conducted on the two calcium phosphate pastes that were formed, and the results are displayed in **Fig. 5-7** in the form of a shear stress-strain curve. The elastic moduli of β-TCP and HA pastes were 10.2 ± 1.5 MPa and 25.8 ± 2.9 MPa (n=3), respectively. Furthermore, the HA paste was also found to have a lower plasticity region, as indicated by the plastic region following the elastic region illustrated in **Fig. 5-7**.

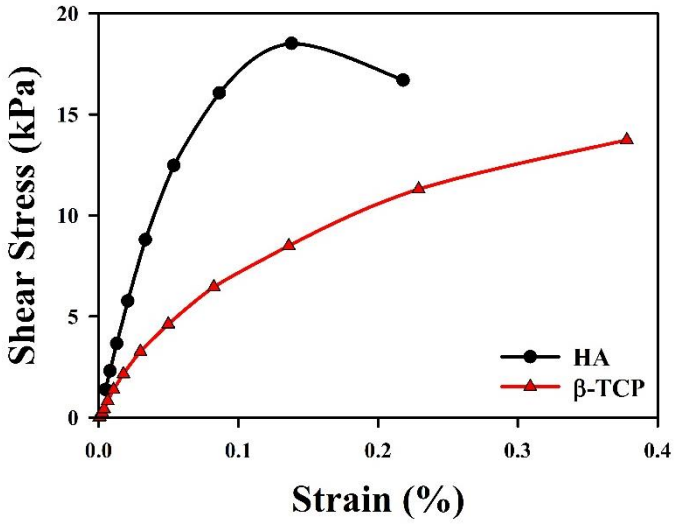

Fig. 5-7. *Plot of the dynamic mechanical analysis performed on β-TCP and HA pastes. Formulation of the latter resulted in stiffer pastes, with a smaller yield stress. (n=1)*

5.3.3 Scaffold properties

Following extrusion, the extrudates were dried, de-bound and then sintered. Both sets of extrudates were subjected to the same drying and de-binding protocol detailed in **Chapter 4**. In order to avoid phase transformation, the β-TCP extrudates were only sintered at 1200 °C, whereas the HA extrudates were sintered at 1200, 1250 and 1300 °C. After sintering, the β-TCP remained white, whereas the HA extrudates transformed from a white particulate structure to a blue densified structure. **Fig. 5-8** are optical microscopy images that demonstrate the cell and strut structure of β-TCP and HA.

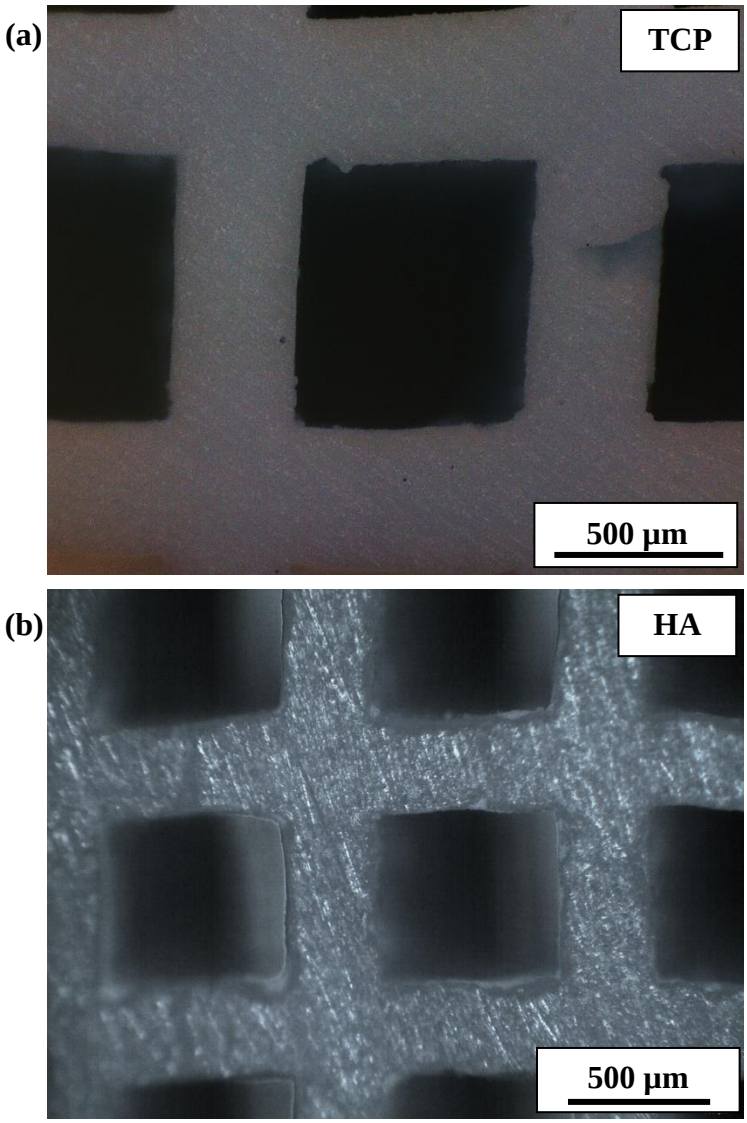

Fig. 5-8. *Optical microscope images depicting the cell and strut structure of the* ***(a)*** *β-TCP and* ***(b)*** *HA scaffolds. Both scaffolds maintained a symmetrically square cell shape.*

As illustrated, symmetrically square cell shapes were fabricated using both materials. Optical microscopy was used to measure the cell and strut dimensions. Sintering the β-TCP at 1200 °C resulted in cell lengths of approximately 750 µm, and strut widths of approximately 400 µm. The HA cell length and strut width were approximately 650 and 360 µm, with no significant changes to the sizes as the sintering temperature was raised. Thus, the HA scaffolds underwent a higher degree of shrinkage following sintering than β-TCP. This corresponded well with the dilatometry data in **Fig. 5-5** and **Fig. 5-6**, which suggested that HA possessed a higher degree of shrinkage.

5.3.3.1 XRD and FTIR analyses of HA and β-TCP Scaffolds

Chemical analyses were performed to determine the effects of the previous processing steps, on the scaffolds, particularly sintering. For these analyses, parts of the extrudate were sectioned off, and crushed and ground into powders using percussion and pestle mortars, respectively. Analysing in powder form allowed for a more homogenous analysis of the scaffolds, rather than just the superficial chemical structure.

5.3.3.1.1 XRD

XRD was employed to determine the phase purity of the calcium phosphate scaffolds, and the corresponding results are portrayed in **Fig. 5-9**. The XRD pattern of the sintered β-TCP powder (**Fig. 5-9 (a)**) was confirmed as phase pure β-TCP (PDF: 04-001-7104). The trace hydroxyapatite peak at 31.5^{o} that was detected in the as-received powder was absent (**Fig. 5-3 (a)**).

The XRD pattern of all three sintering temperatures used for the HA scaffolds are portrayed in (**Fig. 5-9 (b)**). By sintering the raw material at 1200 °C, an improvement to peak crystallinity was observed, as evidenced by the sharper peaks. Increasing the sintering temperature to 1300 °C resulted in a noticeable increase in peak intensity, albeit an unremarkable difference was observed when between 1200 and 1250 °C. However, small peaks of tetracalcium phosphate (TTCP) ($Ca_4(PO_4)O$) were detected in the samples sintered at 1300 °C that were not previously evinced (PDF: 00-025-1137).

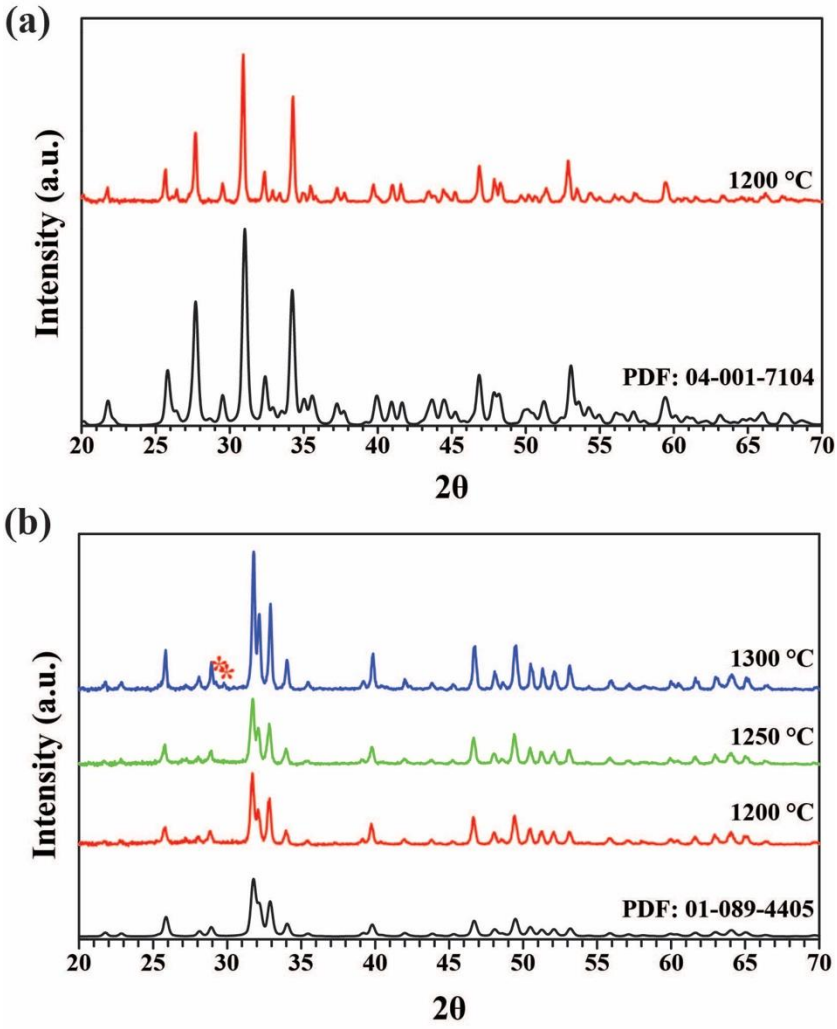

Fig. 5-9. *XRD pattern of the* ***(a)*** *β-TCP, which was phase pure, and* ***(b)*** *HA scaffolds sintered at the respective temperatures. The red asterisks highlight peaks pertaining to tetracalcium phosphate, which were only observed at 1300 °C, hence indicating scaffolds thereof were not phase pure.*

5.3.3.1.2 FTIR

FTIR analysis was also performed on the sintered samples, and the results are depicted in **Fig. 5-10**. The β-TCP sample sintered at 1200 °C consisted of the same phosphate groups observed in the as-received powder, however, the hydroxyl group pertaining to HA at 3570 cm^{-1} was no longer present (**Fig. 5-10 (a)**). Furthermore, the peak at 1045 cm^{-1} divided into two, as can be seen in **Fig. 5-10 (a)**.

According to the FTIR data, sintering of the HA scaffolds resulted in several chemical restructurings of the material. First, the emergence of a minute peak at 945 cm^{-1} pertaining to a β-TCP phosphate group appeared, which became more evident by 1300

°C. Furthermore, the trace hydroxyl group at 3570 cm^{-1} was also more evident in samples sintered at 1200 and 1250 °C when compared to the as-received powder. Despite the hydroxyl group's noticeable appearance at 3570 cm^{-1}, the OH^- group characteristically found in stoichiometric HA at 630 cm^{-1} remained absent. Moreover, peak shifting to higher wavenumbers was observed in the large intensity peak, from 1038 to 1045 cm^{-1}. Lastly, with increasing temperature, the peaks can be seen to narrow and decrease in intensity, which indicated an increase in crystallinity with increasing temperature.

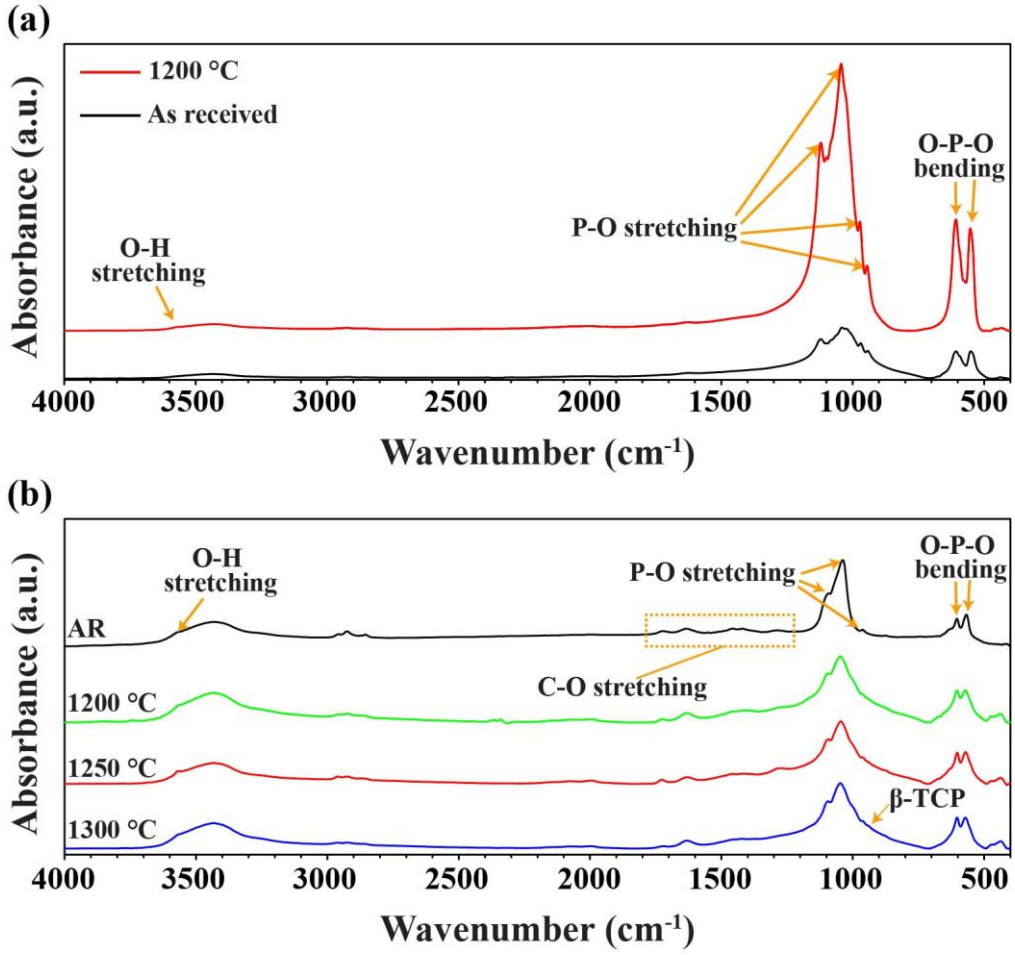

Fig. 5-10. *FTIR spectra of the* ***(a)*** *β-TCP and* ***(b)*** *HA sintered samples. A phase pure β-TCP was obtained when sintered at 1200 °C, as the hydroxyl band at 3570 cm^{-1} was not detected thereat; whereas the HA presented with an additional phosphate band (denoted as β-TCP) when sintered. (AR – as received).*

5.3.3.2 Physical Properties of Scaffolds

The scaffolds' resultant bulk porosity and maximum compressive strength were investigated, and the measurements are recorded in **Table 5-3** and **Table 5-4**. As **Table**

5-3 delineates, sintering the β-TCP at 1200 °C led to a bulk porosity of 53.6 vol%. The β-TCP scaffolds were examined to determine their compressive strength. As the β-TCP extrudates were only sintered to one temperature, this provided the opportunity to examine the compressive strength thereof both parallel and perpendicular to the cell direction. Applying the load parallel to the cell (i.e. A-axis) resulted in an average maximum compressive strength of 23.6 ± 5.7 MPa; whereas examining the scaffolds in the perpendicular direction (i.e. B-axis), resulted in a compressive strength of 7.4 ± 1.8 MPa. Thus, β-TCP scaffolds fabricated by ceramic honeycomb extrusion displayed anisotropic mechanical strengths.

Table 5-3. *β-TCP bulk porosity (n = 3) and compressive strength (n = 8) sintered at 1200 °C. The '±' represents the standard deviation. The scaffolds were found to be weaker when tested in the B-axis (perpendicular to cell alignment).*

Sintering Temperature (°C)	Dwell Time (h)	Bulk Porosity (vol%)	Compressive Strength (MPa)[a]
1200	3	53.6 ± 1.7	A- 23.6 ± 5.7
			B- 7.4 ± 1.8

[a] A statistical significance was determined using an unpaired t-test (***; $p < 0.05$)

The HA scaffolds were sintered at various temperatures and dwell times, and the results are depicted in **Table 5-4**. It was observed that increasing the sintering temperature resulted in strengthening of the mechanical properties. When sintered with a dwell time of three hours, the compressive strength increased by 109% between 1200 and 1250 °C, and by34% between 1250 and 1300 °C. Whereas with a dwell time of five hours, an increase of 130% was observed between 1200 and 1250 °C, and 50% between 1250 and 1300 °C. Thus, both exhibited a greater increase between 1200 and 1250 °C, than between 1250 and 1300 °C. A one-way Anova test revealed a significant difference between all three data sets: increase in strength between sintering at 1200 and 1250 °C ($p < 0.001$), and also between 1250 and 1300 °C ($p < 0.05$), where found to be significant. With a dwell time of five hours, a significant difference was observed between the values sintered at 1200 °C, to those sintered at 1250 ($p < 0.01$) and 1300 °C ($p < 0.0001$); however between 1250 and 1300 °C the data was found to be statistically invariable. A non-parametric, unpaired t-test was performed to determine whether the difference between the dwell times at each of the sintering temperatures, revealed only a significant

difference was observed between the values obtained at 1200 °C ($p < 0.05$). This suggests that increasing the dwell time produces less variation in data. Regarding the bulk porosity, although a general trend appeared, in that increasing the sintering temperature resulted in a decrease in thereof, one-way Anova tests revealed a statistically significant decrease only between values sintered at 1200°C to the other two sintering temperatures, for both dwell times ($p < 0.05$); the bulk porosity values between 1250 and 1300 °C were found not to be statistically significant. A non-parametric, unpaired t-test revealed the data between dwell times at each sintering temperature to be statistically invariable.

Table 5-4. *HA bulk porosity, as determined by the helium pycnometer method (n = 3; plus/minus sign indicates the standard deviation), and maximum compressive strength in the A-axis, at varying sintering temperatures and dwell times (n = >8; '±' indicates the standard deviation). The statistical analyses are reported in the paragraph above.*

Sintering Temperature (°C)	Dwell Time (h)	Bulk Porosity (vol%)	Compressive Strength (MPa)
1200	3	48.1 ± 3.9	10.6 ± 2.3
	5	50.9 ± 5.3	8.5 ± 1.2
1250	3	37.9 ± 1.2	22.2 ± 5.0
	5	40.2 ± 2.3	19.6 ± 6.3
1300	3	35.2 ± 3.2	29.8 ± 8.6
	5	32.5 ± 0.1	29.4 ± 8.9

5.3.3.3 Microstructural Properties of HA and β-TCP Scaffolds

Following the compression tests, fragmented samples were examined using an SEM to explicate the relationship between the microstructure and compressive strength, as well as to examine the grain morphology.

5.3.3.3.1 Fracture Surface

SEM analysis was also conducted to further elucidate the effects of the processing procedure on the microstructure. SEM micrographs at the fracture site of the samples were taken, and the results are displayed in **Fig. 5-11** and **Fig. 5-12**.

SEM analysis elucidated the fracture behaviour of the β-TCP samples when loading was subjected in different directions. In the A-axis, the scaffolds were found to principally fracture at the midpoint of the struts, as illustrated by **Fig. 5-11 (a)**. It was

observed that the propagation of the main crack was parallel to the load direction. In contrast, no principle crack was observed when the load was applied perpendicular to the cells. Instead, struts that were perpendicular to the loading direction collapsed on top of each other. The results are illustrated in **Fig. 5-11 (b)**, where it was discovered that the perpendicular struts remained whole but with recesses of where the parallel struts were previously adjoined. The recesses suggested the dislodgement of the parallel struts. With regards to the mode of fracture, higher magnifications revealed that both inter- and transgranular fractures were detected in both loading axes, as illustrated in **Fig. 5-11 (c & d)**. In addition, SEM images revealed the scaffolds exhibited both nano- and micron-sized pores.

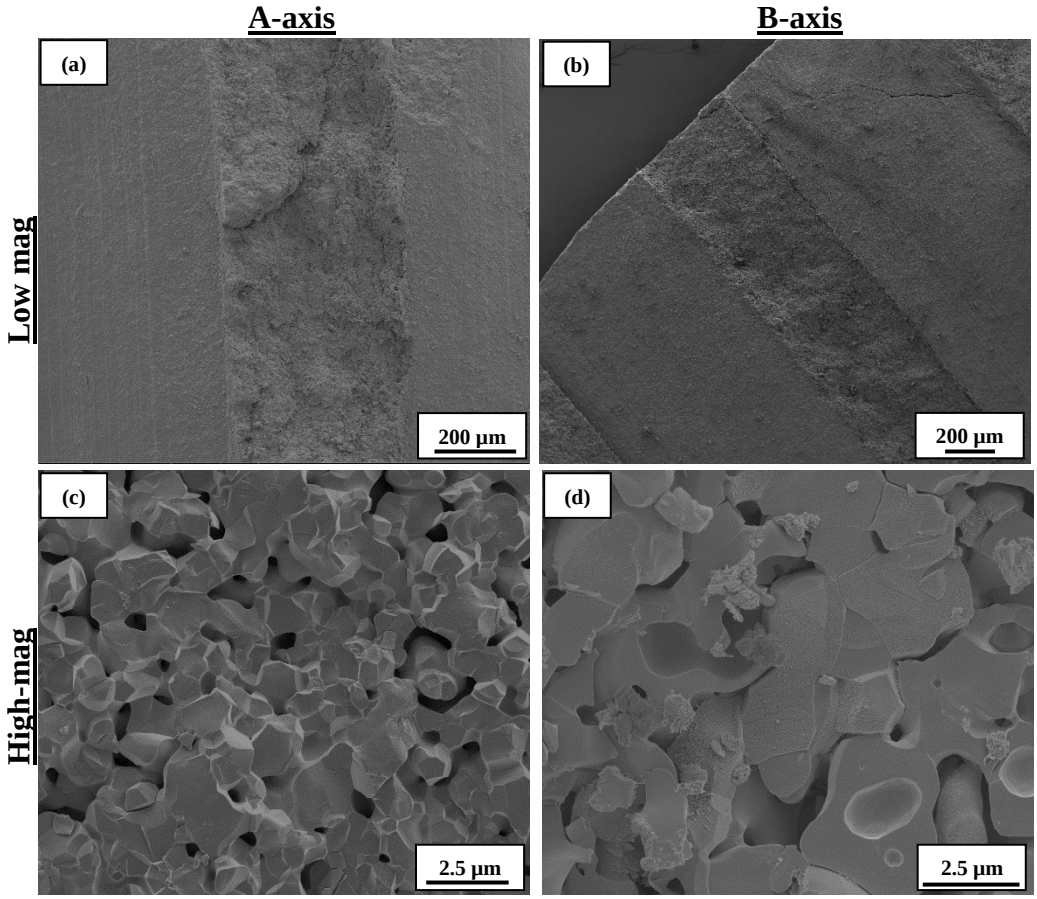

Fig. 5-11. *Scanning electron microscopy (in secondary electron mode) micrographs of the β-TCP fractured surfaces, representative of samples subjected to loading in the A-axis* ***(a & c)*** *and the B-axis* ***(b & d)****. The micrographs illustrate the different fracturing behaviour occurred when the scaffolds were subjected to different compression loading axis. In the A-axis, struts were found to fracture longitudinally at the midpoint* ***(a)****; whereas when scaffolds were subjected to loading in the B-axis, the scaffolds were dislodged resulting in recesses* ***(b)****. Both presented with mix-mode fracturing at higher magnification.*

Fig. 5-12 are micrographs of the HA fracture sites. Similar to β-TCP, mix-mode fracturing was observed. Furthermore, SEM imaging revealed that the sintering temperatures selected resulted in complete densification of the HA scaffolds, where the presence of micro-pores were considerably more scarce. **Fig. 5-13** are SEM micrographs used to clearly highlight the difference in the level of porosity between hydroxyapatite and β-tricalcium phosphate scaffold microstructure at the fracture sites.

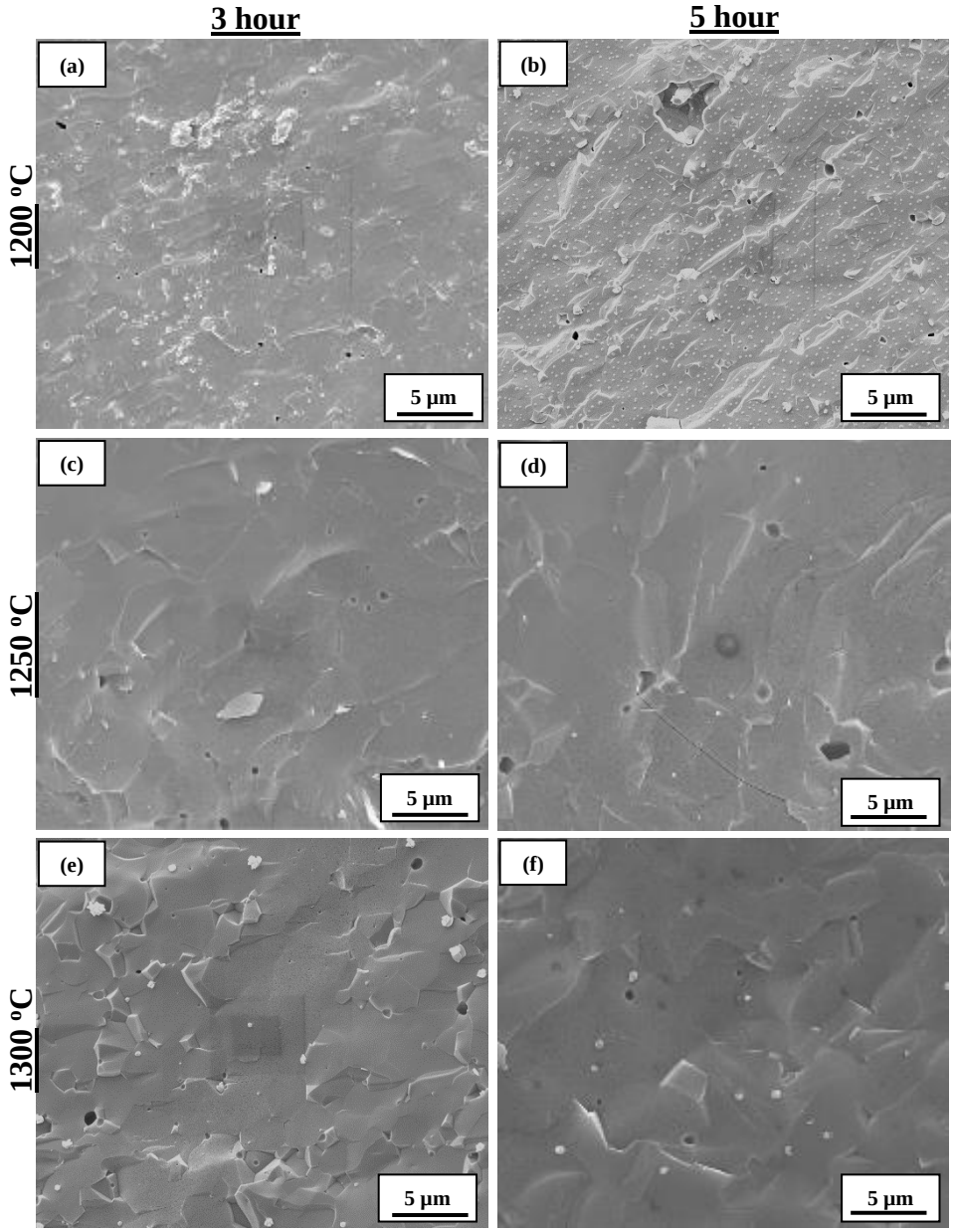

Fig. 5-12. *Scanning electron microscopy (in secondary electron mode) micrographs of the fractured HA sites when compression loaded in the A-axis. Compared to β-TCP, HA had undergone significant densification, thereby resulting in scarce micro-porosity.*

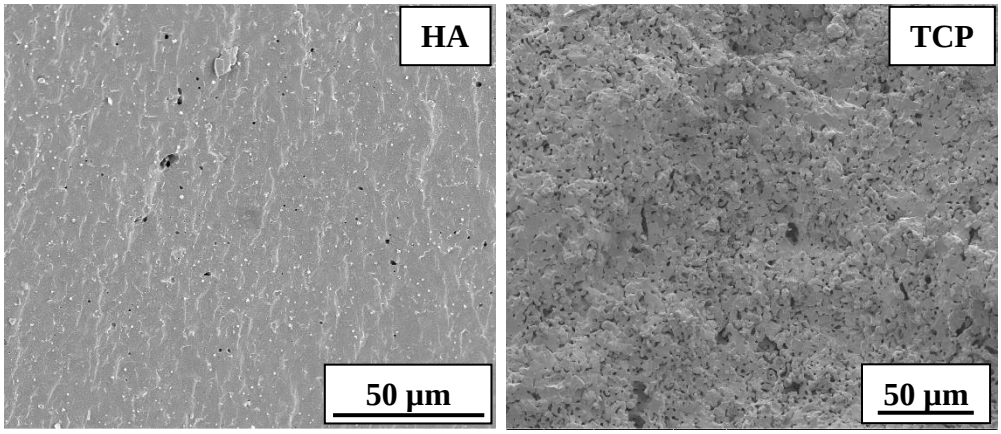

Fig. 5-13. *Scanning electron microscopy (in secondary electron mode) micrographs of the calcium phosphate fracture sites sintered at 1200 ^{o}C, when compression tested in the A-axis. The figure is used to highlight the difference in the level of porosity, which were seldom observed in HA.*

5.3.3.3.2 Grain Morphology of HA and β-TCP Scaffolds

Imaging of the calcium phosphate grains were also examined, and the results are outlined in **Fig. 5-14** and **Fig. 5-15**. The micrographs revealed that the β-TCP exhibited grain sizes of less than 5 µm, including grains that underwent abnormal growth. Moreover, mix-mode cracks (**Fig. 5-14 (a)**) and intergranular porosity (**Fig. 5-14 (b)**) were observed on the surface. Such features were found in both A- and B-axis samples.

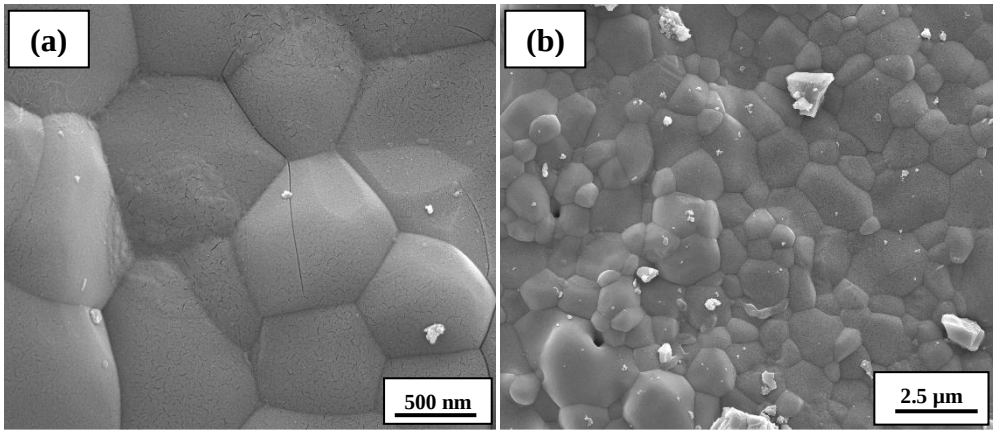

Fig. 5-14. *Scanning electron microscopy (in secondary electron mode) micrographs of the β-TCP surface, depicting the grain morphology of the sample. Note the lack of secondary grain structures, which were observed in the HA grains (**Fig. 5-15**). Furthermore, micro-cracks were observed on the β-TCP grains, which were not observed in HA.*

Fig. 5-15 are micrographs portraying the grain morphology of the HA samples. The micrographs revealed sintering at 1200 °C produced similar grain sizes to that of its β-TCP counterpart, and grew in size with increasing sintering temperature. Moreover, increasing the sintering temperature resulted in an increasing presence of abnormal grain growth. In contrast to the β-TCP microstructure, no micro-cracks or micro-porosity were observed in or around the HA grains. However, the presence of secondary grains were observed, and their prevalence grew with increasing temperature. At higher magnifications, the secondary structures were revealed to comprise of a cluster of nano-sized grains that emanated from the grain boundaries.

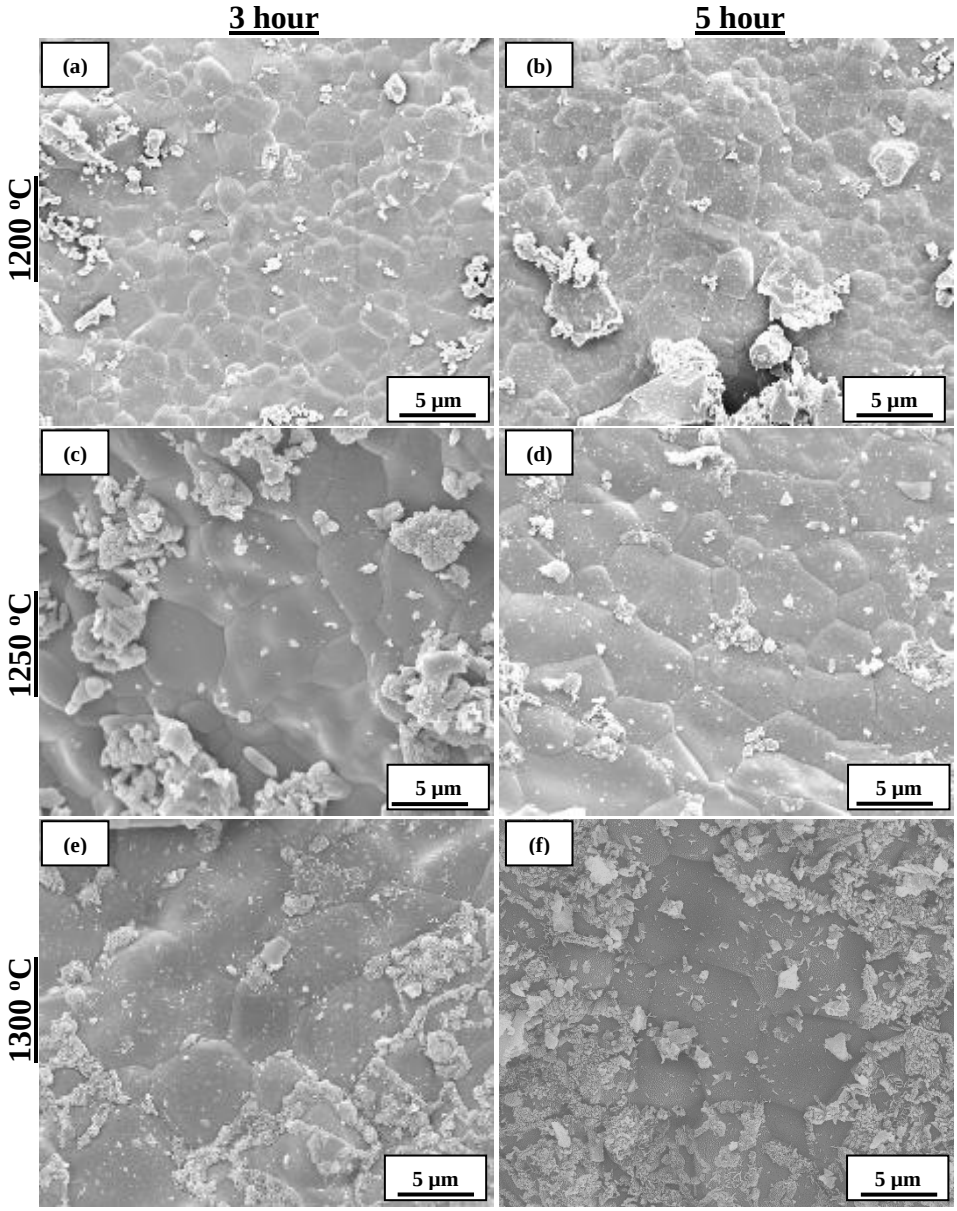

Fig. 5-15. *Scanning electron microscopy (in secondary electron mode) micrographs depicting the HA scaffold surface at varying sintering profiles. These images*

demonstrate the secondary grain structures emanating from the grain boundaries, with further growth thereof observed with increasing sintering temperature. The secondary grain structures are believed to pertain to secondary calcium phosphate phases.

The width of the HA grains at different sintering temperature and dwell times were measured using the ImageJ software, and the results are portrayed in **Fig. 5-16 (a)**. The grain sizes at a dwell time of three hours were 2.2 ± 0.7, 4.8 ± 1.6 and 7.3 ± 2.2 µm at 1200, 1250 and 1300 °C, respectively; which corresponded to an increase of 118% and 52%, respectively. A one-way ANOVA test revealed such increases in grain sizes to be statistically significant ($p < 0.001$). For a dwell time of five hours, the grain sizes 2.7 ± 1.2, 6.6 ± 2.2 and 9.4 ± 2.5 µm at 1200, 1250 and 1300 °C, respectively; which was an increase of 144% and 42%, respectively. A one-way ANOVA once more revealed that the grain size increased with sintering temperature ($p < 0.0001$). Regarding the effect of dwell time, a parametric, unpaired t-tests revealed a significant difference at 1250 and 1300 °C ($p < 0.05$), but not at 1200 °C. Therefore, the analysis revealed that increasing the sintering temperature can significantly increase the grain size, and that increasing the dwell time to five from three can also significantly affect the grain sizes at 1250 and 1300 °C. An Arrhenius plot (**Fig. 5-16 (b)**) was derived from plotting the grain sizes as a function of holding time, which allowed the activation energy of grain growth across all three sintering temperatures to be calculated. The activation energies for the HA scaffolds at dwell times of three and five hours were determined from the slope of the line of best fit, which were 53.4 and 59.1 kcal/mol, respectively. These values are comparable to what has been previously reported for HA [342, 343].

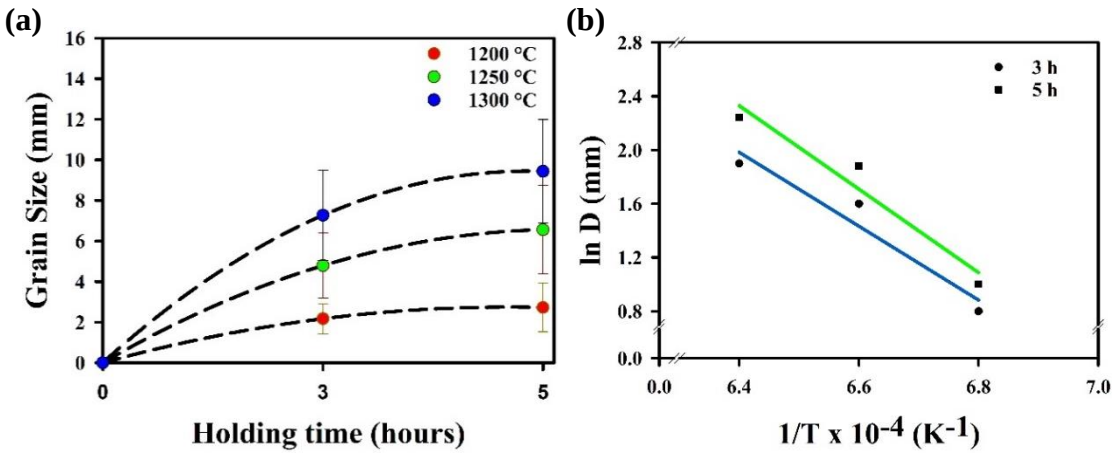

Fig. 5-16. *Plots outlining the **(a)** grain sizes and **(b)** corresponding Arrhenius results of the HA scaffolds. Increasing the sintering temperature increased the grain size, whereas the holding time produced an insignificant difference thereto. (n = 20; error bars represent the standard deviation).*

5.3.3.3.3 EDS analysis

Energy dispersive spectroscopy (EDS) was utilised to provide an elemental map of the β-TCP microstructure. EDS analysis of the HA samples will be discussed in **Chapter 7**.

EDS mapping was performed to elucidate the elemental distribution of grains, and **Fig. 5-17** illustrates an EDS map that typified the results. The results illuminated the homogenous distribution of phosphor throughout the microstructure whereas, calcium and oxygen detection were scarce at the grain boundaries, with the latter's scarcity more noticeable. Furthermore, oxygen-deficient areas were observed to be congruent with grain boundaries. EDS mapping was also used to compare the elemental composition of crack-free sites to that of sites exhibiting cracks, however, the difference in elemental distribution was unremarkable. Hence, a correlation between elemental distribution and crack propagation could not be deduced using EDS analysis.

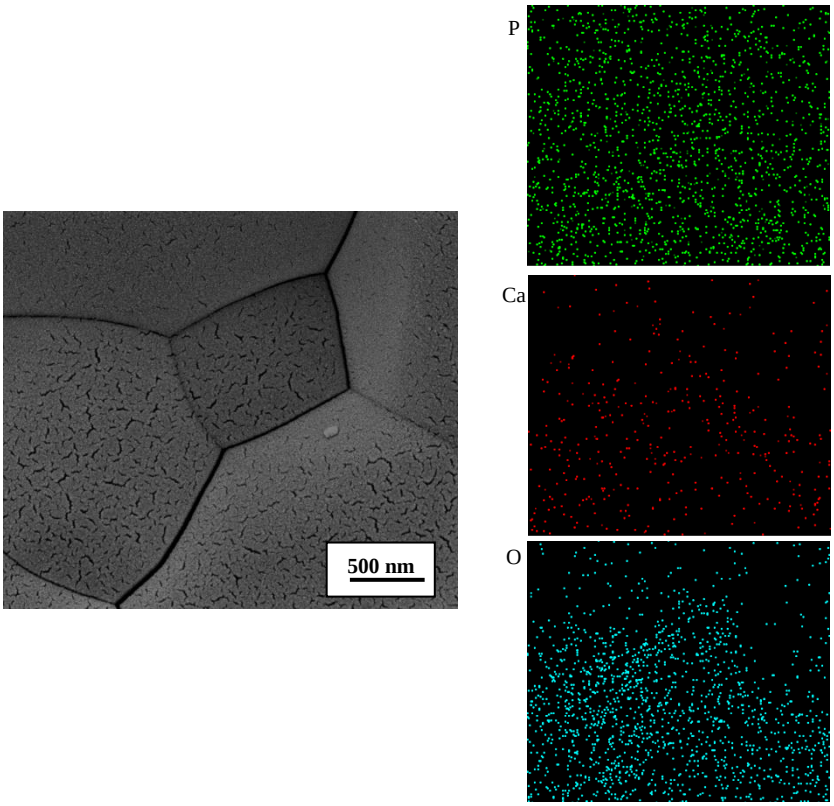

Fig. 5-17. *A representative EDS map of a fracture found in β-tricalcium phosphate scaffold. The analysis revealed the presence of calcium, phosphorus and oxygen within the β-TCP grains.*

5.4 Summary of Scaffold Properties

Characterisation of the raw powders revealed nonstoichiometric starting materials with distinct particle morphologies. The HA powders consisted of nano-sized primary particles that had a tendency to agglomerate, whereas β-TCP comprised a mixture of nano- and micro-sized particles. The difference in particle properties resulted in β-TCP attaining a paste with a higher solids loading, whereas the HA required more distilled water in order to formulate an extrudable paste.

Scaffolds of β-TCP and HA were successfully fabricated, where it was ascertained that β-TCP possessed both a higher bulk porosity and compressive strength. A comparable compressive strength was achieved with the HA scaffolds when sintered at 1300 °C, however, this was at the expense of the bulk porosity. In addition, the compressive strength of β-TCP scaffolds perpendicular to cell alignment was investigated, where it was discovered that the scaffolds displayed heterogeneous mechanical properties. The chemical analyses of the scaffolds showed stoichiometric β-TCP scaffolds, whereas the HA scaffolds were composed of trace amounts of other CaP phases.

Finally, SEM analysis elucidated the effects of the processing parameters on the scaffolds' microstructure, where the presence of secondary phases on HA were evinced. Moreover, it was observed that the HA samples densified to such an extent that no micro-pores were observed. In contrast, β-TCP comprised said pores and was free of secondary structures. A difference in fracture mechanism was observed between β-TCP scaffolds subjected to compressive loads in the A- and B-axis.

5.5 Discussion

5.5.1 The Effects of the Raw material on the Extrusion Process

The calcium phosphate materials used to fabricate the scaffolds have produced contradictory results to previous work [242, 344-346]. These previous studies have found that β-TCP is mechanically weaker than HA. However, the unexpectedly higher compressive strengths thereof could be understood by comparing the differences between the β-TCP and HA powder morphology and the phase purity of the sintered scaffold.

Several studies have demonstrated the benefits of using nano-sized particles to enhance the mechanical strengths of calcium phosphate scaffolds [232, 347]. The main contribution of nano-sized particles to the scaffold strength is their tendency to form smaller grain sizes, as smaller grain sizes are known to attenuate crack propagation, which is known as the Hall-Petch relation [348]. Furthermore, the benefits of smaller grain sizes are also realised during biological studies [193]. Hence, one would expect that the hydroxyapatite used for this study would yield the higher mechanical strength [349-352].

5.5.1.1 Confirming the Nature of the Raw Powders

5.5.1.1.1 Physical Properties

Scanning electron microscopy inferred that the HA powder may have comprised of nano-sized particles, and particle size analysis revealed a bimodal distribution of nano- and micro-sized particles. However, it was the BET and XRD analysis that confirmed the sizes to be in the nano region. The BET value of 107.91 m^2/g is in the nano-region for particles [353], and as mentioned below, an ill-defined XRD pattern is indicative of nano-sized particles. This prompted the use of higher SEM magnification which began to reveal the presence of nano-sized primary particles. In contrast, the β-TCP powder, which comprised of both nano- and micro-sized particles, produced a well-defined XRD pattern, and possessed a surface area value that was considerably lower. Thus, it was concluded that the HA powder was nano in size and that inter-molecular forces resulted in the strong tendency of the nano primary particles to agglomerate; hence why the particle size analyser detected micro-sized particles. Moreover, higher SEM magnification revealed that the micro-sized β-TCP particles were comprised of nano-sized grains, which suggest that the manufacturer calcined the powder to achieve this bimodal particle size. The significantly lower surface further suggests that the particles are coalesced together rather than weakly bonded. Bimodal particle size distribution are favoured in powder metallurgy as they lead to a higher packing density, in which the smaller particles fill the voids between the larger particles, thereby increasing the density of the green and sintered body [332].

One benefit of using the current powders was that both were comprised of near-spherical shapes, which are beneficial for formulating a ceramic paste, as spherical particles are known to have the highest packing density [223]. The more particles that can

be suspended in the polymer gel, the less shrinkage is to be expected during densification, and consequently resulting in less defects.

5.5.1.1.2 Chemical Properties

Chemical analyses of the powder revealed that both β-TCP and HA were nonstoichiometric in nature. The HA powder did not display crystal phases or functional groups pertaining to other calcium phosphates, however, and in contrast to the β-TCP data, both the XRD pattern and FTIR spectra were poorly defined, which is suggestive of nano-sized particles [342, 354]. Furthermore, the HA powder lacked one of the two hydroxyl group bands typical in stoichiometric HA, which was the librational and stretching of OH^- band at ~ 631 cm^{-1} [298, 302, 355-357], as observed in the FTIR spectrum in **Fig. 5-4 (b)**.

Following the clarification of powder morphology and chemical purity, it was possible to correlate the results of the subsequent processing steps thereto, starting with the paste formulation.

5.5.1.2 The Effects of the Raw Powder on Paste Properties

Extrudable pastes were successfully formulated, using only Methocel™ and distilled water to impart plasticity. The first notable difference between the CaP powders was that a higher solid loading was achieved with the β-TCP powder than the HA powders. Attempts to increase the HA solids loading resulted in the paste globules discussed in **Chapter 4**, and thus required more distilled water to achieve a coalesced paste. It was believed that the higher surface area of the HA particles necessitated the need for more binder coverage, thereby decreasing the ceramic-to-non-ceramic ratio of the paste.

However, despite attaining an extrudable paste, DMA and extrusion data revealed the CaP pastes to exhibit different flow characteristics. The DMA measurements demonstrated that the HA paste in comparison to the β-TCP paste exhibited a limited plasticity region, as well as an approximately 2.5-fold increase in both the extrusion force and shear stiffness. This could be due to the agglomeration characteristics of the HA powder, which may have prevented the complete coverage of the primary particles by the binder and solvent, as illustrated in **Fig. *5-18***. One function of the binder was to form a

lubricating layer between the ceramic particles, thus facilitating particle flow during extrusion. However, the binder may have only coated the agglomerates, and hence, the primary particles were forced to slide past one another to flow in the direction of the extrusion, thereby resulting in the markedly higher extrusion forces [229, 358]. The benefit of reducing the extrusion force from an industrial perspective include reducing the running costs of the process.

Agglomeration is a dynamic process, in which re-agglomeration can occur following de-agglomeration. Despite the vigorous attempts to de-agglomerate the powder using the high-energy shear mixer, future studies will require an alternative approach. It is possible that re-agglomeration occurred once mixing ceased, or perhaps when the distilled water was introduced. The current mixing strategy utilised culminated in the HA powder requiring a markedly higher force to extrude. As for the β-TCP paste, despite achieving a higher solid loading, it can be inferred that more of the primary particles were coated by the binder, which allowed them to easily flow during extrusion flow; hence, a lower extrusion force was needed [223].

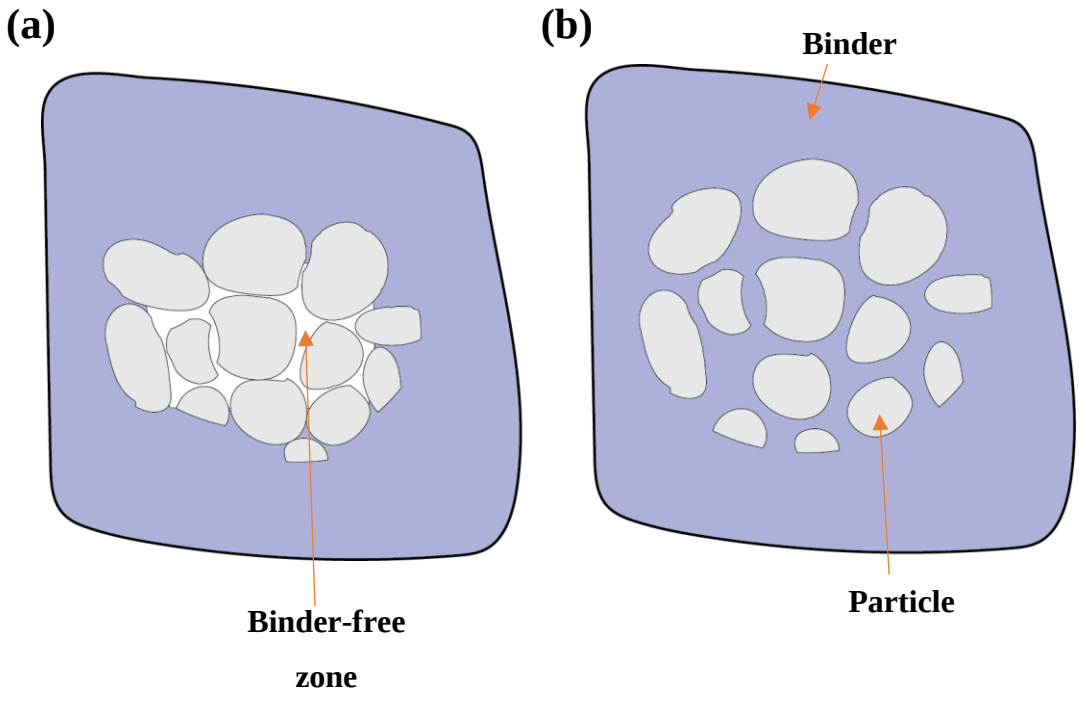

Fig. 5-18. Diagram portraying the difficulties in coating agglomerated ceramic particles with a binder. The image on the right depicts the ideal scenario, where all of the individual primary particles are dispersed and coated by the binder gel. The image on the left depicts the difficulty in a binder penetrating an agglomerate. An insufficient binder coating of the hydroxyapatite primary particles resulted in particle-particle contact during extrusion, and demanded a higher extrusion force.

Therefore, using nano-particles with the current mixing strategy may require additional processing treatments to achieve flow characteristics seen with the β-TCP pastes. The first problem that will need to be addressed is the high surface area that demands more binder coverage to lubricate the system. The second issue is the high tendency of the particles to agglomerate, which is again a consequence of high surface area.

5.5.1.3 The Effects of the Raw Powder on Scaffold Properties

Following extrusion, the calcium phosphate samples were subjected to a slow procedure of drying and thermal de-binding in order to eliminate the non-ceramic components from the extrudate. Upon removal from the furnace, a noticeable change in colour occurred in the HA extrudates between de-binding and sintering, whereby the extrudate displayed a blue appearance, having previously been white. This behaviour is common when upon sintering of HA [350, 359-361], and is attributed to manganese contamination during synthesis, and the oxidation thereof [360].

Prior to sintering, thermal analyses were performed to determine suitable sintering temperature ranges to utilise for densifying the HA powders. Most researchers use a sintering temperature in the range of 1100-1300 °C. Dilatometry analysis of HA revealed that the samples would be densified by then, however, with β-TCP it was less obvious, which in contrast to HA, did not present with a clear sintering endpoint. β-TCP sintering was limited by the phase transformation into α-TCP: the mechanically weaker polymorph of β-TCP. Phase decomposition of β-TCP into α-TCP has been previously reported in the range of 1125 to 1280 °C [157, 362]. The variation in results is believed to be due to the differences in, for example, particle properties [363] and powder purity [364]. The phase transformation is accompanied by a volume expansion, as **Fig. 5-5** portrays, which creates mechanical stresses that initiate micro-cracks within the material [344, 364, 365]. Therefore, to avoid the phase transformation, all of the β-TCP scaffolds were only sintered at 1200 °C. The dilatometry results of the hydroxyapatite powder did not present with phase transformation characteristics. As a result, HA scaffolds were sintered at 1200, 1250 and 1300 °C (**Fig. 6-9**).

5.5.1.3.1 Chemical Structure

Chemical analyses of the as-received β-TCP powder revealed trace amounts of hydroxyapatite, however, after sintering the scaffolds at 1200 °C, evidence thereof, or any other CaP phase, were not detected. The loss of HA phase can be attributed to the liberation of the OH^- that occurs at high temperatures. The peak splitting at 1045 cm^{-1} may have been as a result of the chemical restructuring that occurred, caused by the liberation of the hydroxyl group; a weak hydrogen bond is known to form between the phosphate and hydroxyl function groups [303].

In contrast, the HA scaffolds exhibited additional CaP phases when sintered, despite not displaying any impurities in the starting powder. The HA partially decomposed into β-TCP, as well as TTCP, which are common products of HA decomposition [366]. The sintering temperature of HA was limited to 1300 °C, as previous studies have demonstrated that temperature above this value result in thermally-induced phase transformation of HA. This form of phase transformation may have occurred at lower temperatures in the present study because of the HA raw powder, as nano-sized ceramic particles have been reported to enhance the sintering process. This was corroborated by the dilatometry measurements as the HA material exhibited a considerably higher shrinkage, which inferred the raw powder was susceptible to enhanced densification [227]. Nano particles possess a greater surface area that requires less energy to coalesce the adjacent particles. Hence, the phase transformation observed could be attributed to the particle size, which reduced the temperature threshold for the decomposition event to occur.

In addition, the temperature threshold may have been reduced because the HA powder used herein was nonstoichiometric. The FTIR spectra of the HA powder revealed the absence of the hydroxyl group at 630 cm^{-1}, and thus expediting the decomposition process. Previous studies have demonstrated that sintering HA in the presence of moisture precludes dehydroxylation, and hence, concluded that the availability of the hydroxyl group is key to preventing HA decomposition [367]. Thus, the expedited decomposition of HA can be partly attributed to the nonstoichiometric characteristics of the raw powder.

The chemical analyses of both β-TCP and HA infer that the former is favoured at higher temperatures due to dehydroxylation. As a result, β-TCP scaffolds were phase pure, whereas, the HA scaffolds consisted of anhydrous CaP impurities. From the

chemical analyses, it can be concluded that sintering of the HA scaffolds resulted in the following decomposition equation:

$$Ca_{10}(PO_4)_6(OH)_2 \rightarrow 2\ \beta\text{-}Ca_3(PO_4)_2 + Ca_4(PO_4)_2O + H_2O$$

5.5.1.3.2 Physical and Mechanical Properties

As previously mentioned, HA normally exhibits the higher mechanical properties of the two. The results obtained in this study contradict the aforementioned general consensus regarding HA and β-TCP mechanical strength. Examining the one comparative compressive strength data at 1200 ºC, the β-TCP obtained a value twice that of HA, albeit displaying similar bulk porosity values. Additionally, the latter's microstructure was visually more dense, hence, given the reciprocal relationship between strength and porosity, one would expect the HA scaffolds to possess a higher strength.

The contradictory results can be partly ascribed to the decomposition of the HA scaffold following sintering. Previous studies have discovered that the decomposition of HA into β-TCP results in a decrease in compressive strength. Both β-TCP and TTCP have a larger crystal lattice volume and a dissimilar thermal expansion to HA crystals. Thus, their growth at the grain boundary produces internal pressures that makes the multi-phasic system susceptible to fracturing [366]. This could explain why inter-granular fractures were the predominant mode of fracturing, as observed by SEM. However, it should be noted that previous work have surmised the presence of the secondary phases can improve the mechanical properties of HA scaffolds through obstructing crack propagation, and deflecting the crack into the grain body where more energy is required for propagation [354, 368]. The studies concluded that the interfacial bonding formed between the primary and secondary phases affect crack propagation. Hence, the presence of secondary phases may not necessarily be detrimental to the mechanical strength provided the interfacial bond is not weaker than that found in a phase pure system. This may explain why a decrease in compressive strength was not observed with increasing temperature, despite the notable increase in the secondary phase: with increasing temperature, a stronger interfacial bond may have formed between the primary and secondary phases.

Other determinants of mechanical strength include the porous architecture of the scaffold. SEM imaging of both β-TCP and HA scaffolds revealed that the former

consisted of micro-pores, whereas the latter lacked said features. Voids in HA scaffolds were observed; however, they were believed to be due to fragmentation of the scaffold following compression loading. It is possible that the micro-pores were a source of crack obstruction that led to the former possessing a higher compressive strength. The influence of micro-pores on crack propagation is inconclusive, with previous experimental and simulation studies highlighting their crack obstructing capabilities [369-371]. As for this study, it is believed that upon reaching a micro-pore, rather than travelling around the edge of the pore, the crack was enticed to enter the pore due to the stress concentration surrounding the pore, but did not have enough energy to reconvene past the pore (**Fig. 5-19**). In addition, as the pores formed exclusively on the grain boundaries, their presence could have alleviated the stresses formed in between the grains as they began to compress against one another [371]. This could also explain why the mechanical properties of HA scaffolds increased in line with sintering temperature, as adjacent grains began to envelop one another and thus, reducing the level of grain boundaries therein. In a previous study, grain boundaries have been found to be mechanically the weakest link in HA samples [352].

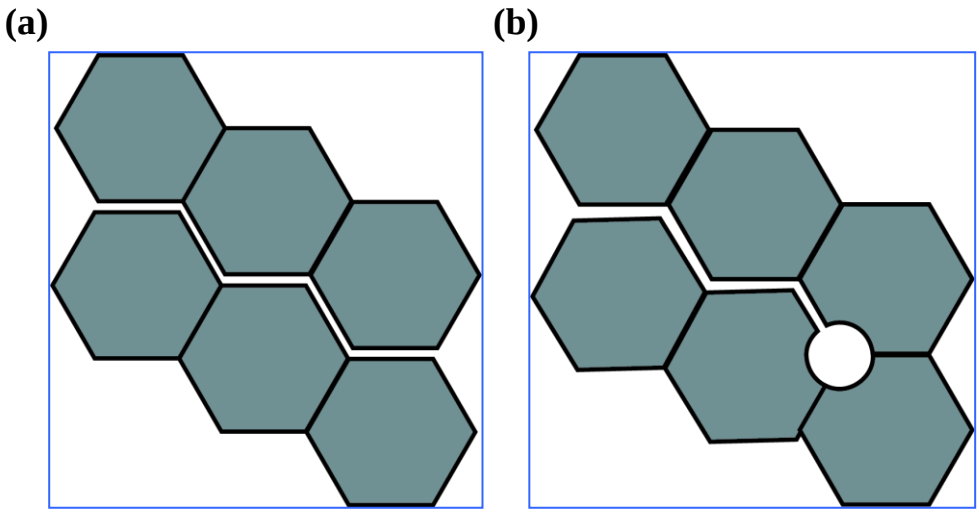

Fig. 5-19. *Illustration depicting the benefits of intergranular micro-pores. The image on the left depicts an unimpeded micro-crack, whereas the image on the right portrays a micro-crack impeded by a micro-pore. It was believed that the micro-pores' crack-hindering properties were partly responsible for the β-tricalcium phosphate scaffolds possessing a higher compressive strength than hydroxyapatite.*

5.5.1.4 The role of sintering temperature and dwell time on HA Scaffolds

Increasing the sintering temperature resulted in an increase in grain size, the presence of abnormal grain growth and secondary phases; all of which are known to affect the mechanical properties of scaffolds. Except for the latter, all are known to adversely affect the mechanical strength. However, as this was not observed, it is possible that the main determinant of mechanical strength was the densification of the scaffold, as the trend observed coincided with the general consensus in its effect on mechanical properties. As such, the detrimental effects of the undesirable microstructural features were not significant enough to overcome the level of densification. However, the increase in compressive strength between 1250 and 1300 °C in comparison to that achieved by the same temperature margin of 1200 and 1250 °C, was notably lower, and thus it is possible that the deleterious effects of the undesirable microstructural features may have begun to affect the scaffolds. Furthermore, the compressive strength variation widened with increasing temperature, which again, may have been as a result of the growing prominence of said microstructural features resulting in heterogeneous variations between samples. Although the compressive strength increased through further densification of the HA scaffolds, the highest value obtained was still comparable to that of the β-TCP scaffold sintered at 1200 °C.

It is feasible that the undesirable microstructural features may have been restricted to the surface, as **Fig. 5-20** illustrates. In this figure, the sub-fracture microstructure of a HA sample is depicted, and portrays a lack of secondary phases growing below the surface. The figure conveys HA grains with free of secondary phases originating from the grain boundary. If the unwanted features were only superficial, then it could explain why their deleterious effect on mechanical strength were not observed. It could also explain why the secondary phases were not detected by the XRD when sintered at 1200 and 1250 °C, as the instrument has a detection limit of 5%.

With respect to varying dwell times, no difference was observed across all temperatures. The HA material examined in this chapter was susceptible to enhanced sintering, thus a dwell time of three hours was more than sufficient to avoid incomplete densification, and extending the dwell time to five hours only prolonged the effects of enhanced densification.

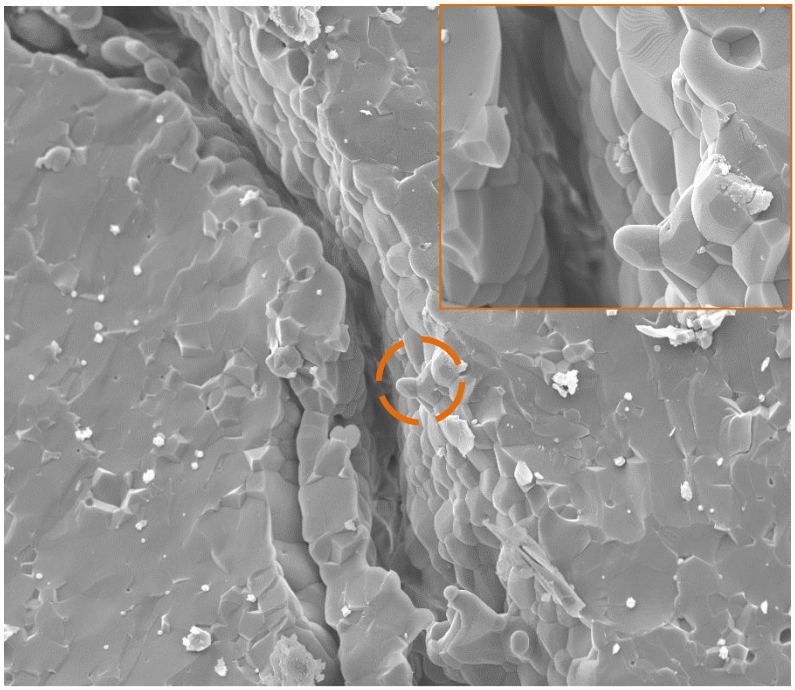

Fig. 5-20. SEM (secondary electron mode) micrograph of a surface crack observed in a HA scaffold sample. The inset is a higher magnification image of the circled region. The figure highlights the lack of secondary grain growth at the grain boundaries below the surface.

In summary, raw material physical and microstructural analyses elucidated the influence of the starting powder on the final CaP scaffold. Sintering at 1200 ^{o}C produced β-TCP scaffolds that displayed compressive strengths double that of HA, and despite further densification of HA scaffolds by increasing the sintering temperature, the status quo was not achieved. Nonetheless, raising the sintering temperature was successful in increasing the compressive strength of the HA scaffolds. The study herein showed that raising the temperature produced both favourable and unfavourable factors that influence mechanical strength. It was believed that the main determinant of mechanical strength was believed to be densification, which took precedence over other factors. The unfavourable microstructural features may have had an effect on the compressive strength of HA, however, this was not enough to overcome the positive effect produced by the increase in densification. Further studies will need to be performed to confirm these theories, as well determining the effect of micro-porosity on mechanical strength.

5.5.2 Comparison of Compressive Strength to Other Work

Traditional methods of fabricating β-TCP have struggled to fabricate a scaffold suitable for non-load-bearing application, with values either at the low end of cancellous bone (2-12 MPa) or below. One advantage of their approach is that they possessed high porosity, which favours rapid osseointegration (**Section 2.4.4**). The current state of the art has shifted towards Solid freeform (SFF) methods because of the advantages they offer, including control over the porosity with high resolution. As **Table 5-5** delineates, SFF techniques are an improvement on traditional methods with respect to compressive strength; however, this has come at the expense of the porosity.

The compressive strength of β-TCP fabricated in this study is an improvement on many of the previous methods with regards to strength. Honeycomb structures are known for their high strength, however, their mechanical properties are anisotropic [194, 318]. The same is true for the β-TCP fabricated by ceramic extrusion, with one direction (parallel) exhibiting higher strength than another (perpendicular). The difference can be attributed to the forms of stress(es) the struts are subjected to, whereby compression loading in the parallel plane results in compressive stresses, but perpendicular loading results in additional flexural stresses to the struts. Nevertheless, the weaker loading plane displayed a mean compressive strength comparable or better to previous methods.

Table 5-5. Examples of compressive strength and porosity values of β-TCP scaffolds fabricated via different techniques. The table demonstrates that the honeycomb extruded-scaffolds displayed comparatively remarkable strengths.

Method	Compressive Strength (MPa)	Porosity (%)	Ref.
Extrusion	A-23.6 ± 5.7	53.6 ± 1.7	Present Study
	B- 7.4 ± 1.8	-	Present Study
SLS	3.7 +/- 0.27	56.04	[220]
Template Casting Method	2.9 +/- 0.67	82.49	[372]
3D inkjet	6 +/- 1.5	-	[373]
Robocasting	10-20	45	[275]
3D inkjet	10.95 +/- 1.28	49.4	[374]
SLA	12	60	[375]
Freeze casting	0.9	50	[376]

The compressive strength of the HA scaffolds fabricated during this study were an improvement in comparison to traditional fabrication methods, as ***Table 5-6*** lists. HA scaffolds fabricated via robocasting are also enumerated in ***Table 5-6***, where it can be seen to possess remarkable compressive strengths. In addition, the freeze casting approach also accomplished remarkable compressive values. **Table 5-6** again demonstrates an inverse correlation between compressive strengths and porosity. The table also demonstrates that techniques capable of achieving structured porosity produce scaffolds with greater strengths, as discussed in section **2.5.2**.

Table 5-6*. Examples of compressive strength and porosity values of HA scaffolds fabricated via different techniques. The table demonstrates that the honeycomb extruded-scaffolds possessed relatively moderate compressive strengths.*

Method	Compressive Strength (MPa)	Porosity (vol%)	Ref.
Extrusion	29.8 ± 8.6	35.2 ± 3.2	Present Study
Foam Replication	0.51±0.14	91±2.4	[377]
Polymeric sponge infiltration	1.3	70	[201]
Sacrificial Template	9	35	[378]
SLS	8	61	[345]
Freeze casting	145	47	[213]
Freeze casting	28.0 ± 4.2	37.4	[379]
Robocasting*	302.3 ± 54.6	N/A	[222]
Robocasting*	~25	45	[344]

*****Pore sizes were 270 µm

* Pore size were ~ 250 µm

Table 5-6 also presents two examples of were research groups reported different compressive strengths using the same fabrication method (freeze casting and robocasting). In all four cases the particle properties were not characterised, and hence it was difficult to attribute the cause of the mechanical strength discrepancy thereto. Nonetheless, it demonstrates that different processing strategies with the same technique yield different strengths, hence the need for optimising the processing steps in order to enhance the mechanical strengths for each fabrication technique. The next chapter is

centred on optimising the commercial HA powder to enhance the mechanical strength of HA scaffolds.

5.6 Summary of Chapter

In this preliminary study, the difference in particle properties affected downstream processes, including the packing density, where a higher solid loading was achieved with the β-TCP powder. The resultant compressive strengths of β-TCP (23.6 ± 5.7 MPa) and HA (10.6 ± 2.3 MPa) scaffolds processed at 1200 °C were contradictory, as the HA should have possessed the greater strength. In addition, ceramic extrusion was successful in imparting macro-pores with sizes (> 600 μm) that exceeded the requirement for suitable bone grafting. However, the enhanced compressive strength came at the expense of bulk porosity, with β-TCP and HA possessing values of 53.6 ± 1.7 and 35.2 ± 3.2 vol%, respectively; which were lower in comparison to those fabricated via traditional routes. The improvement in compressive strength is believed to be due to the structured porous architecture that was fabricated using extrusion, and the results add further credence to the importance of periodic porosity for attaining high mechanical strengths.

The study further inferred the need for additional processing steps when using nano ceramic particles. Hydroxyapatite, which is inherently stronger than β-tricalcium phosphate, resulted in scaffolds that were weaker than that of the latter. It was deduced that the undesirable properties of agglomeration, which were ostensibly overcome by the processing route, were the cause of the contradictory outcome. The β-TCP results were encouraging, and suggest that using raw HA powder with similar characteristics could yield scaffolds with improved compressive strength. Therefore, in the following chapter, it was decided that HA powder with comparable properties to the β-TCP will be used.

Chapter 6: Enhanced Compressive Strength through Raw Material Optimisation: The effects of Pre-Calcination

In light of the previous chapter's findings, a new HA raw powder with desirable characteristic was sought-after. The β-TCP powder supplier (Plasma Biotal) also stocked HA powder, and with similar powder characteristics. However, the £200/Kg exc. VAT price was unwelcoming. A more cost-effective approach was utilised, whereby the commercial HA powder from the previous chapter (costing £12/Kg exc. VAT) was pre-processed. SEM imaging of the β-TCP powder inferred the supplier calcined the powder to obtain the near-spherical, bimodal-sized particle distribution, and hence this approach was adopted for the nano-sized, heavily agglomerated HA powder. As this chapter will detail, pre-calcining the powder led to a ceramic paste with a higher solid loading and ultimately HA scaffolds with remarkably higher compressive strengths. In addition, the chapter also simultaneously details the investigation of the effects of doping hydroxyapatite to resolve its inherent degradation behaviour at elevated temperatures. The chapter herein adopts a similar sequential investigation to that of the previous chapter, in which the physical, chemical and thermal properties of the powder and scaffold were analysed.

6.1 Introduction

The rationale for investigating the effects of hydroxyapatite comprised of nano-sized particles were based on the previous research [232, 347] that ascribed the size to both improved mechanical and biological properties. In the previous chapter, a contradictory set of results were obtained. On the one hand, ceramic extrusion produced β-TCP

scaffolds that were at the high-end of the compressive strength range, with respect to others' work, as enumerated in **Table *5-5***; but it produced HA scaffolds with comparatively mediocre strength. The difference was attributed to the raw material, where the HA material was susceptible to both agglomeration and enhanced densification in the temperature range chosen, whereby the effects thereof caused undesirable microstructural features. However, the results of the β-TCP scaffolds, and in concert with other studies that also opted for periodic porosity, provided the motivation to examine the effects of particle morphology on ceramic extrusion, and to adopt a new strategy to address the aforementioned unfavourable properties of the as-received HA powder.

As discovered in the previous chapter, the β-TCP raw powder was not susceptible to neither agglomeration nor enhanced densification. SEM micrographs alluded to the possibility that the manufacturer incorporated a heat treatment during the synthesis thereof, as evidenced by the diffusion of the grains, which were once nano particles that coalesced to form larger micro-sized primary particles. In the field of advanced ceramics, the process, known as 'calcination', is a common approach in treating the powder to a high temperature to modify its properties [229]; the process is distinct from sintering, where in the latter the aim is to achieve a dense, monolith structure. Broadly speaking, calcination is performed at a lower temperature than sintering, whereby enough heat energy is supplied to the system to allow adjacent particles to coalesce, but not to attain complete densification of the whole system.

Calcination of hydroxyapatite has been previously investigated, with a myriad of benefits discovered. For example, in comparison to a nano powder, whether synthesized or purchased, the benefits included increases to crystallinity, a decrease in total shrinkage, reduction in grain growth and improved packing were demonstrated [285, 380, 381]. If these benefits could be reproduced in this study then it is expected to result in HA scaffolds with greater compressive strengths.

Aside from altering the raw powder's morphology, calcination has been utilized to extract HA from natural bone [381, 382], induce phase transformation into other calcium phosphates [383, 384], eliminate volatile elements [385, 386], and to incorporate desirable ions into the HA lattice for an improved performances [182, 387]. Verily, HA has been ionically substituted with a plethora of ions [387-389], which is made possible because the apatite lattice is easily accepting of elements that have an ionic radii similar to that of the calcium ions [165, 390]. The incorporation of substitutional ions are of

considerable interest because they can modify the characteristics of the crystal lattice. Of interest for this study are ionic substitution that can improve the mechanical strengths of HA, and address the flaws discovered in the as-received HA powder examined in the preceding chapter, such as enhanced densification and phase decomposition [391]. Particular attention has been given to substituting with titanium oxide, aluminium oxide, magnesium oxide and silicon oxide, which were selected based on their favourable biological properties independent of hydroxyapatite, however all have been found to expedite HA decomposition [224, 308, 392-394].

The incorporation of yttria (Y_2O_3) into HA for the fabrication of scaffolds is a subject of recent interest. This is unsurprising given the addition of Y_2O_3 has enhanced the mechanical properties of ceramics [395], particularly zirconia, where the addition thereto has expanded the ceramic's acceptance in dental and orthopaedic application by resulting in a toughened bioceramic [396, 397]. In addition, yttria was found to improve the mechanical properties of bioactive glass, including the compressive strength [398]. Further to this, previous work had established that the addition of 10 mol% yttria to hydroxyapatite increased the electrical conductivity of the material [399], which is presumed to be beneficial for orthopaedic implants [400] as bone is piezoelectric[6] [401]. Moreover, yttria-substituted hydroxyapatite has been demonstrated to enhance osteoblast adhesion on implants, which is a prerequisite for successful scaffold anchorage [400, 402]. However, Zhang et al. (2010) noted that the concentration and culture time in *in vitro* experiments can convert the effects of yttria from toxicity to activity [403], but were not able to determine a trend in concentration to the effects. Indeed this dose-dependent characteristic is true of many ions used in commercial implants [147].

The addition of 10 w/w% yttria has been revealed to retard HA decomposition [393]. It was postulated that yttrium possess a stronger interstitial bond to oxygen in comparison with calcium [404], and hence, prevents the cascade of events associated with the dehydroxylation of HA that may lead to a decrease in mechanical properties [405].

The chapter herein aims to investigate two calcination effects: one, are the effects of calcination that was intended to alter the particle morphology of the as-received hydroxyapatite powder examined in the previous study; and two, the effects of ionic

[6] Electrical activity has been reported to enhance bone cell activity.

substitution calcination, with the incorporation of yttrium into said powder with 10 w/w% yttria. The ultimate aim of both calcination routes was to achieve a compressive strength comparable to cortical bone, which is in accordance with the aims of this project (**1.1**). A second motivation for the ionic substitution-calcination was to elucidate the challenges that may be encountered, if any, when using ceramic honeycomb extrusion for the fabrication of composite systems.

6.2 Experimental Procedure

6.2.1 Raw Materials

The chapter examines three different starting hydroxyapatite powders. The as-received commercial hydroxyapatite (Purum grade, Sigma Aldrich) from the previous chapter was used again, and is denoted in the chapter as AR-HA.; the calcination thereof, which is denoted as C-HA; and the ionic substitution calcination thereof with yttria (Reacton®, Alfa Aesar), which is denoted as Y-HA.

6.2.2 Calcination

Calcination of the as-received HA powder were performed in a muffle furnace. Initial experimentation of calcination used 5 g of the as-received powder poured into a 10 ml alumina crucible to calcine at different temperatures, using a heating and cooling rate of 5 °C/min, and a dwell time of five hours. This was sufficient to yield enough powder to perform preliminary experiments on the powders.

For the fabrication process itself, the as-received powder was poured into a 150 ml alumina crucible and then calcined at 5 °C/min for five hours, which yielded a coalesced powder (**Fig. 6-1**). As a result, the powder was then poured into a polypropylene cup and subjected to high-shear energy mixer for 5 minutes at 800 rpm, to break up the weak agglomerates.

For the fabrication of ion-substituted hydroxyapatite, 10 w/w% of yttria was added to the as-received powder and calcined using the aforementioned heating parameters. The resultant powder was also weakly coalesced, and thus subjected to the same shearing protocol.

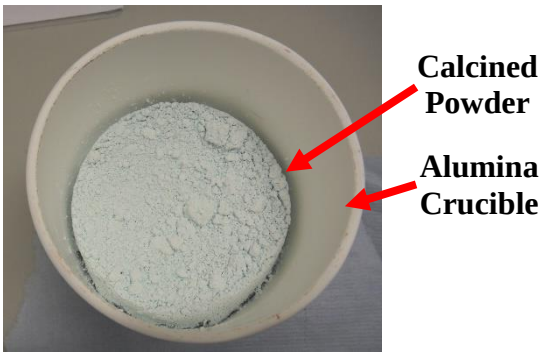

Fig. 6-1. *Image of the post-calcined powder, forming a weakly coalesced structure. The powder in the image was calcined at 1000 °C, and the figure demonstrates the pale blue colourisation observed at said temperature.*

Prior to the fabrication process, pellets of the calcined samples were fashioned to ensure a solid structure can be achieved from the new material. The pellets were formed using a 10 mm die and pressed at 0.5 tons for one minute, and subsequently sintered at 1200 °C in a muffle furnace. A vernier calliper was used to measure the diametric length of the sintered pellets.

6.2.3 Fabrication Process

The fabrication process was as detailed in **Chapter 4**. Briefly, extrudable pastes were formulated using the as-received powder, C-HA powder, and the Y-HA powder; the final paste compositions are discussed in section **6.3.5**. Said pastes were extruded and subjected to the drying and de-binding protocol described in **Chapter 4**. The sintering temperatures investigated in this study were 1200 and 1250 °C, with a dwell time of 8 hours, and a heating and cooling rate of 5 and 2.5 °C/min, respectively. Once sintered, the extrudates were sectioned into cubes, and characterisation ensued thereafter.

6.2.4 Characterisation

All of the characterisation methods used herein are detailed in **Chapter 3**. In addition the number of micro-pores of scaffolds were determined from SEM micrographs. This was

obtained using ImageJ software (National Institute of Health, USA). Quadrants of 100 μm^2 were drawn on the SEM images and the number of micro-pores therein were counted.

6.3 Results

In this chapter, the effects of two forms of calcination were examined. An initial screening process was performed using SEM analysis to identify a calcination temperature to use for the fabrication of scaffolds, and consequently, characterisation thereof. Physical, chemical and thermal analyses were performed to elucidate the effects of calcination.

6.3.1 Starting Powder

6.3.1.1 SEM Characterisation of the Calcined Powders

The first aim of the study was to determine a suitable calcination temperature. The AR-HA powder was calcined at temperatures between 400 to 1000 °C. SEM micrographs depicting the results following high-shearing are displayed in **Fig. 6-2**. It was ascertained that calcining at 1000 °C produced distinct results from the other temperatures (**Fig. 6-2 (e)**), particularly to the as-received powder. The once nano primary particles were found to bond with adjacent particles and thus forming larger particles comprised of grains; which are similar to that observed in the commercial β-TCP powder in the preceding chapter. Examining the interface of the bonded grains revealed no neck formations, which are a source of stress concentration. It is likely that subjecting the calcined powder to high-shear energy mixing may have broken the weakly bonded necks, as remnants thereof were observed. The samples calcined at 800 °C (**Fig. 6-2 (d)**) may also have exhibited a similar bonding behaviour but due to the difficulty of gold coating sub-micron particles, it was difficult to establish whether this was true. The Y-HA powder was also calcined at 1000 °C, and the results (**Fig. 6-2(f)**) were similar to that of the undoped calcined sample. Furthermore, a pale shade of blue was seen in both the powders calcined at 1000 °C (**Fig. 6-1**).

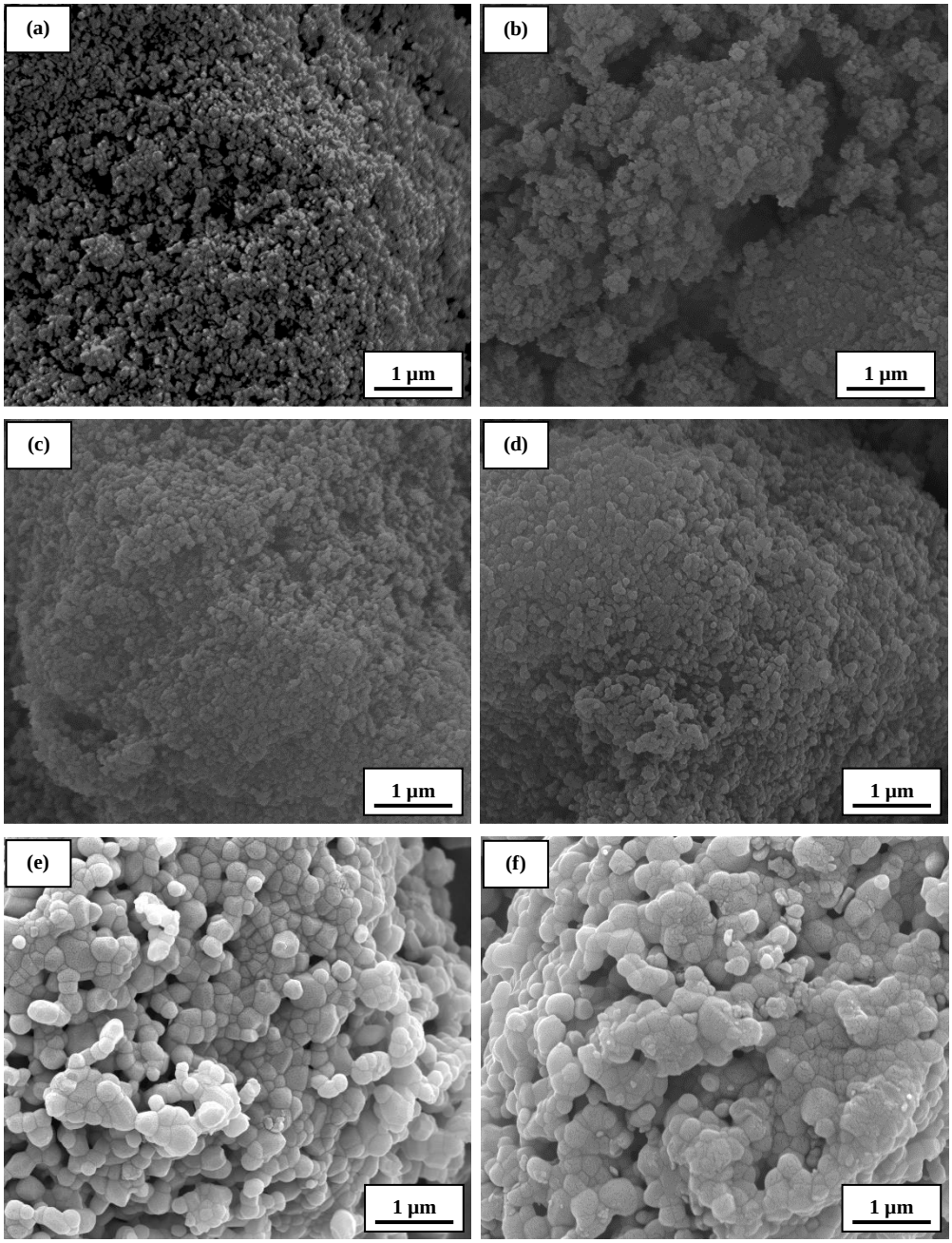

Fig. 6-2. *SEM (Secondary electron mode) micrographs of the as-received hydroxyapatite powder processed at different temperatures. The micrographs are of the as-received powder* ***(a)****, and those calcined at 400* ***(b)****, 600* ***(c)****, 800* ***(d)*** *and 1000 °C* ***(e)****. The micrograph at* ***(f)*** *is that of the as-received powder calcined with 10 wt% yttria at 1000 °C. The micrographs illustrate the increase in particle size with sintering temperature.*

Fig. 6-3 are lower magnification micrographs depicting the primary particles of both the C-HA and Y-HA powders. The Y-HA powders were found to consist of primary particles that were more angular in shape (**Fig. 6-3 (b)**) than the C-HA powder (**Fig. 6-3 (a)**).

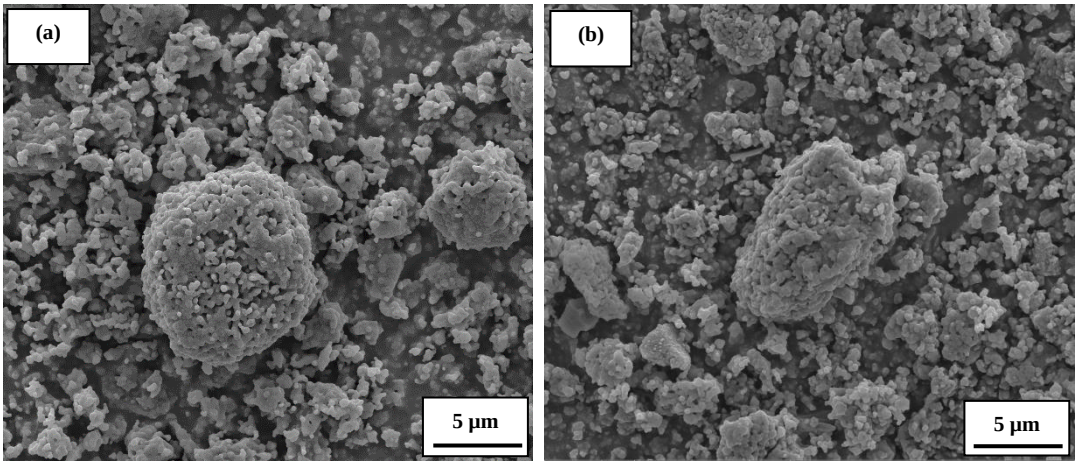

Fig. 6-3. *SEM (secondary electron mode) micrographs depicting representative post-calcination primary particles of* ***(a)*** *C-HA and* ***(b)*** *Y-HA powders. Note the more angular particle morphology of Y-HA.*

6.3.2 Chemical Structure of the Calcined Powders

XRD analysis of the calcined samples were also conducted, and the evolution of crystallinity is portrayed in **Fig. 6-4**. An increase in crystallinity was observed with increasing calcination temperature. In comparison to the as-received pattern, calcining at 1000 °C resulted in narrower peaks with a noticeable increase in peak intensity. No other calcium phosphate phases were observed in the probed calcination temperature range, including β-TCP or tetracalcium phosphate phases.

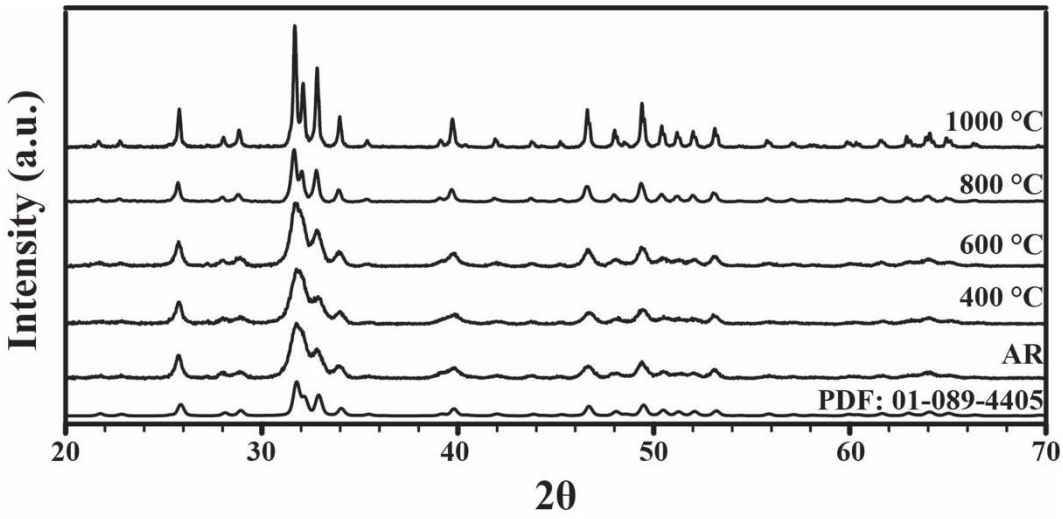

Fig. 6-4. *XRD pattern of the powders calcined at temperatures ranging from 400 to 1000 °C, with a diffraction pattern to illustrate the phases pertain to HA. The figure highlights the increase in crystallinity with increasing sintering temperature.*

XRD analysis of the Y-HA powder calcined at 1000 °C was too performed, and the results are outlined in **Fig. 6-5**. The figure includes the XRD pattern of the C-HA powder, which, as mentioned, was confirmed as phase pure HA (PDF: 01-089-4405). The addition of 10 wt% resulted in a biphasic material, composed of HA with a secondary yttria phase (PDF: 01-088-1040). The yttria phases are highlighted in **Fig. 6-5** by the red asterisks. In addition, a reduction in HA peak intensity was also observed, with respect to the C-HA powder.

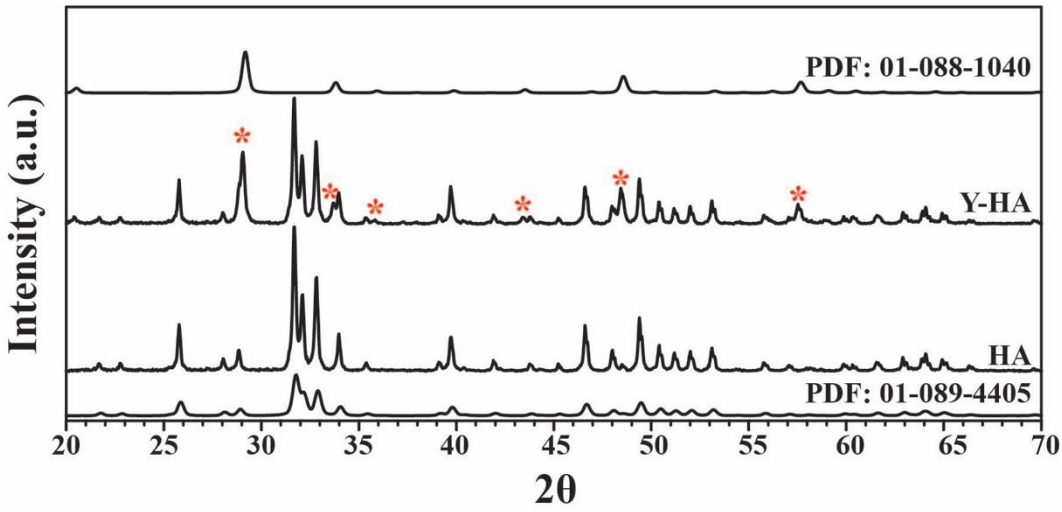

Fig. 6-5. *XRD pattern of the C-HA and the Y-HA powders calcined at 1000 °C. The Y-HA powder was found to be biphasic, consisting of both hydroxyapatite and yttria phases. The red asterisks highlight peaks pertaining to yttria. The powder diffraction files used to identify the peaks of both ceramics are included.*

In addition to XRD analysis, FTIR characterisation was performed, and the results are provided in **Fig. 6-6**. It was observed that the as-received powder displayed a poorly defined spectrum, whereas the C-HA and Y-HA samples delineated a spectrum with a marked improvement to the definition. Furthermore, the peaks pertaining to the OH^- group at 3570 and 630 cm^{-1}, which were absent in the as-received samples, were clearly apparent in the spectrum of the calcined samples.

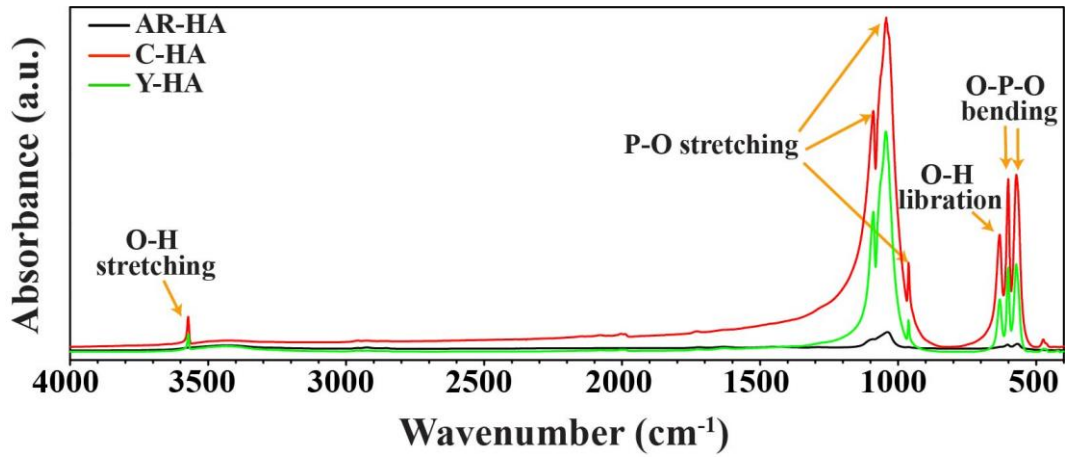

Fig. 6-6. *FTIR spectra of the different starting materials. As-received powder (AR-HA), undoped calcined powder (C-HA) and yttria-doped HA (Y-HA). Bands were more discernable in both calcined powders, than AR-HA. Furthermore, both C-HA and Y-HA possessed a hydroxyl group at 630 cm^{-1}, which was not observed in AR-HA.*

6.3.3 Physical Properties of the Calcined Powders

Particle size analysis was performed on the starting materials, and the results are displayed in **Fig. 6-7**. A distribution of 0.1 to 14.5 µm was determined for the as-received powder; 0.3 to 30 µm for the C-HA powder; and 0.45 to 18.7 µm for the Y-HA powder. Both calcined samples displayed a bimodal distribution, with the larger of the two peaks in the micron range, and the smaller peak in the sub-micron range; the C-HA peaks were detected at 0.6 and 5.9 µm, respectively; whereas the Y-HA peaks were found to be at 0.9 and 5.9 µm.

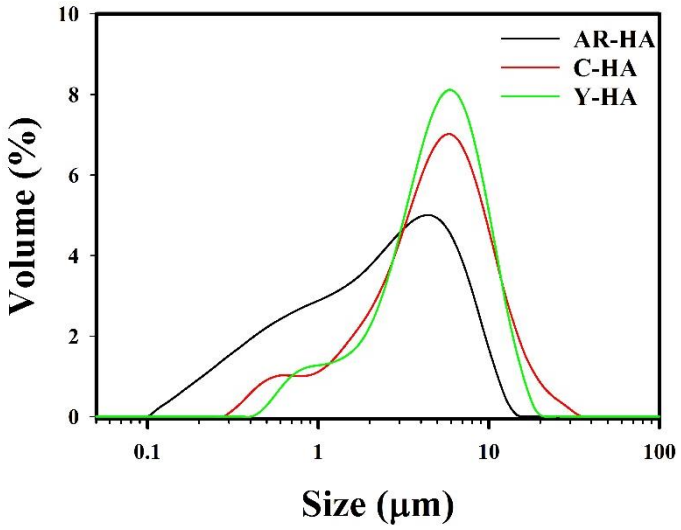

Fig. 6-7. *Particle size distribution of the different starting powders. The pre-calcined powders possessed higher particle sizes.*

Further particle analyses were performed, and the results are enumerated in **Table 6-1**. Calcining the as-received powder at 1000 °C resulted in a statistically significant increase in powder density, from 2.9 to 3.22 g/cm^3 (an increase of 11 %); the density was further increased to 3.25 g/cm^3 when the as-received powder was doped with yttria before calcination, which was an increase of 12%. The increase in density between C-HA and Y-HA was statistically invariable. BET surface analysis of the powders was also undertaken, whereby the surface areas of the C-HA and Y-HA powders were revealed as 4.95 and 5.88 m^2/g, respectively, which is a marked and statistically significant decrease from the 107.91 m^2/g detected for the AR-HA powder; this corresponded to a decrease of 95% for both C-HA and Y-HA powders. The difference between the C-HA and Y-HA were found to be statistically invariable once more. The d_{50} value obtained from the particle size analysis is also included in the table, where it can be observed that the calcined powders possessed similar values.

Table 6-1. *Table listing the results of the density (n = 3), BET surface area analysis (n = 3) and D_{50} value (n = 5) measurements of the starting materials. Pre-calcination yielded powders with a greater density, lower BET surface area and high D_{50} particle size. (the ± indicates the standard deviation).*

Sample	Density (g/cm^3)[a]	BET (m^2/g)[b]	D_{50} (µm)[a]
AR-HA	2.90 ± 0.04	107.91 ± 6.1	2.49 ± 0.02
C-HA	3.22 ± 0.01	4.95 ± 1.9	5.29 ± 0.06
Y-HA	3.25 ± 0.01	5.88 ± 1.8	5.52 ± 0.18

[a] A one-way ANOVA test revealed a significant difference in data between all three samples ($p < 0.05$).

[b] A one-way ANOVA test revealed a significant difference in density between the AR-HA and the calcined powders ($p < 0.0001$), but not between C-HA and Y-HA.

6.3.4 Thermal Properties

The final sets of analyses performed on the starting materials where to determine the thermal properties thereof. **Fig. 6-8** illustrates the dilatometry analysis performed on the

calcined powders. The dilatometry curve of the AR-HA powder from the previous chapter was included for comparison.

The AR-HA powder can be observed to commence shrinking from room temperature, where a slow and minute (1.5%) shrinkage occurred until ~ 600 °C. The majority of the shrinkage occurred between 600 and 865 °C, where a marked increase in shrinkage rate was observed; the shrinkage between the two temperatures was calculated as 19.5%, giving a total of 21 % linear shrinkage exhibited by the as-received HA powder. No further shrinkage was observed above 865 °C.

The dilatometry results of the C-HA powder revealed an initial, albeit minute shrinkage below 100 °C, which was followed by a small linear expansion up to 550 °C. Subsequently, the sample proceeded to shrink at a comparatively gradual rate until 1050 °C. Therefore, the onset and endpoint sintering temperature of this sample were determined as 550 and 1050 °C, respectively. The final linear shrinkage of the sample was approximately 12%, approximately half of the AR-HA powder's value.

The Y-HA sample also exhibited an initial, albeit minute linear shrinkage, which was succeeded by a linear expansion of approximately 2.5% from 100 to ~ 1050 °C. Here the sample proceeded to shrink until complete densification. The sintering onset and endpoint were determined as 1050 and 1250 °C, respectively, and the final linear shrinkage was approximately 9%.

To compliment the dilatometry analysis, the starting powders were pressed into discoid pellets using a 10 mm die, and sintered to 1200 °C, and their diametric values were measured. **Table 6-2** outlines the diametric shrinkage that the pelletised forms of the starting materials underwent. The measurements demonstrated that the AR-HA pellets underwent the largest shrinkage at 27.8%; followed by C-HA sample at 13.4%; and in concert with the dilatometry data, the Y-HA sample underwent the smallest shrinkage at 8.7%. A one-way ANOVA test revealed a statistical significance in shrinkage data between all samples, and hence, the addition of 10 wt% yttria was sufficient in significantly minimising the shrinkage of HA.

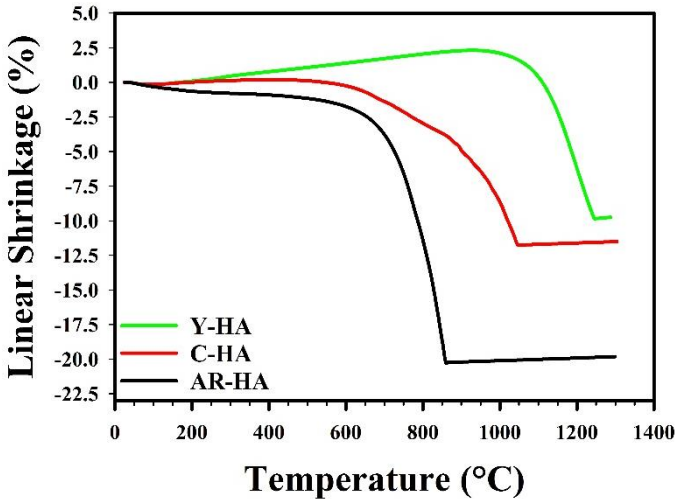

Fig. 6-8. *Dilatometry results of the starting powders. The pre-calcined powders possessed higher onset and endpoint sintering points, demonstrating the higher energy required for sintering thereof. Moreover, both exhibited notably smaller maximum shrinkages than the AR-HA powder, with Y-HA experiencing the least.*

Table 6-2. *Diametric shrinkage of the pelletised starting powders. The powders were pressed into 10 mm pellets using a hydraulic press and subsequently sintered at 1200 °C (n = 3; with the ± representing the standard deviation of the data).*

Sample	Diametric Shrinkage (%)[a]
AR-HA	27.8 ± 0.06
C-HA	13.4 ± 0.1
Y-HA	8.7 ± 0.0

[a] A one-way ANOVA test revealed the shrinkages were all statistically different ($p < 0.001$).

Differential Scanning Calorimetry (DSC) was also performed on all three starting materials, and the results are illustrated in **Fig. 6-9**. An endothermic trough at approximately 1310 °C were observed in the AR-HA and C-HA powders, but not in the Y-HA powder. The endothermic activity was believed to be that of a phase decomposition of hydroxyapatite, possibly into β-tricalcium phosphate or tetracalcium phosphate, and as a consequence, sintering was performed at 1200 and 1250 °C.

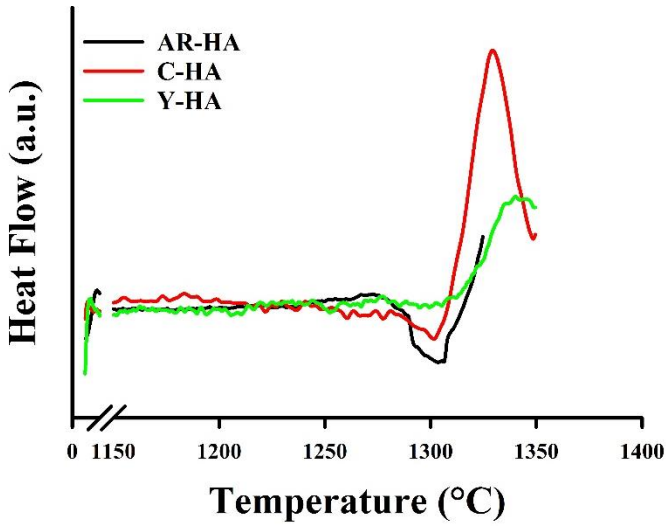

Fig. 6-9. *DSC analysis of the starting materials. Both AR-HA and C-HA presented with an endothermic trough at approximately 1300 °C, which was not observed in the Y-HA data (endothermic down).*

In summary, the as-received HA powder from the previous chapter was calcined at 1000 °C to produce near-spherical, micro-sized primary particles. Calcination of said powder resulted in increases to both powder density and particle size distribution, whereas the surface area considerably decreased. A more stoichiometric material was observed as a consequence of the calcination process, whereby improvements to the definition of XRD pattern and FTIR spectra were produced. Lastly, thermal analyses demonstrated an increase to the sintering onset and endpoint as a result of calcination, with a notable decrease in total shrinkage. The addition of yttria produced further changes to the physical, chemical and thermal properties of the calcined powder, with respect to the undoped calcined powder.

6.3.5 Paste Properties

All three HA materials were formulated into extrudable pastes with a similar stiffness using Methocel™ and distilled water. **Table 6-3** lists the solid loadings of the ceramic in terms of mass and volume percentage. It was ascertained that calcining the powders before formulating the pastes resulted in an increase in ceramic solid loading. An initial paste using the C-HA powder was formulated with a solid loading of 40.5 vol% (C-HA/1), however, upon extrusion it was realised that the paste was relatively soft, and difficult to handle (**Fig. 4-16**). Hence, a second paste was formulated using the same HA

material, whereby it was discovered that more of the ceramic powder can be suspended within the binder, and a solid loading of 42 vol% was obtained (C-HA/2). Formulating a ceramic paste with the Y-HA was also accomplished, where it was revealed that less of the powder can be packed into the binder, and hence a decrease in ceramic solid loadings was obtained. Further addition of Y-HA into the admixture were attempted but resulted in unextrudable pastes. The table also displays the density of the pastes. The results demonstrate that the paste density was correlated to the ceramic solid loading of the paste (i.e. increasing solids loading resulted in an increase in paste density).

Table 6-3. *Ceramic solid loadings and paste densities, as measured by a helium pycnometer of pastes formulated using the starting materials. A higher solid loadings was achievable with the pre-calcined powders.*

Sample	Solid loadings (mass%)	Solid loadings (vol%)	Paste density (g/cm^3)
AR-HA	58.7	33.7	1.66
C-HA/1	65.7	38.3	1.76
C-HA/2	69.1	42.0	1.96
Y-HA	65.6	38.1	1.82

The formulated pastes were then extruded using the extruder fitted with the honeycomb die. **Fig. 6-10** displays the extrusion plot of the results. The force required for the pastes to extrude in descending order was AR-HA paste > C-HA/2 > Y-HA > C-HA/1. The extrusion forces for the AR-HA, C-HA/2 and Y-HA, which were the pastes that were further investigated in this study, were 50.9 ± 7.9, 25.6 ± 4.6 and 22.4 ± 3.6, respectively. A one-way ANOVA test revealed the decrease between the AR-HA to both calcined pastes was significant ($n = >4$; $p< 0.05$), whereas the difference in extrusion force between C-HA/2 and Y-HA was not significant. As the figure also demonstrates, the AR-HA paste exhibited a pressure drop considerably larger than the other pastes, which was subsequently followed by a gradual decrease in extrusion force until the end of the run. In contrast, pastes formulated using C-HA and Y-HA powders exhibited a relatively small pressure drop, followed by a plateau. The behaviour is in accordance to

that observed in the previous chapter, whereby micron-sized particles resulted in lower extrusion forces (section **5.3.2**).

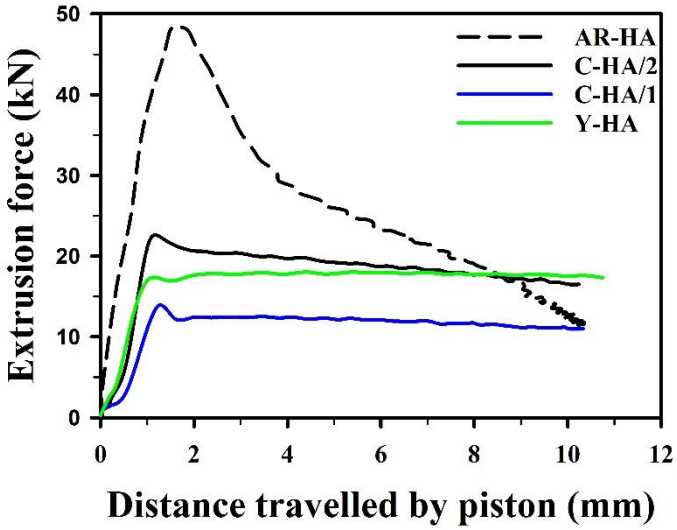

Fig. 6-10. *Extrusion plot representative of the starting materials extruded at a rate of 250 mm/s. C-HA and Y-HA pastes were better lubricated by the Methocel™ binder, and hence required a lower extrusion force than the AR-HA pastes.*

6.3.6 Scaffold Properties

The extruded samples were sintered at 1200 and 1250 °C, and sectioned into approximately 4.5 mm^3. As was previously noted, sintering resulted in a blue colour change, as demonstrated in **Fig. 6-11**, with the calcined samples exhibiting a paler blue colour.

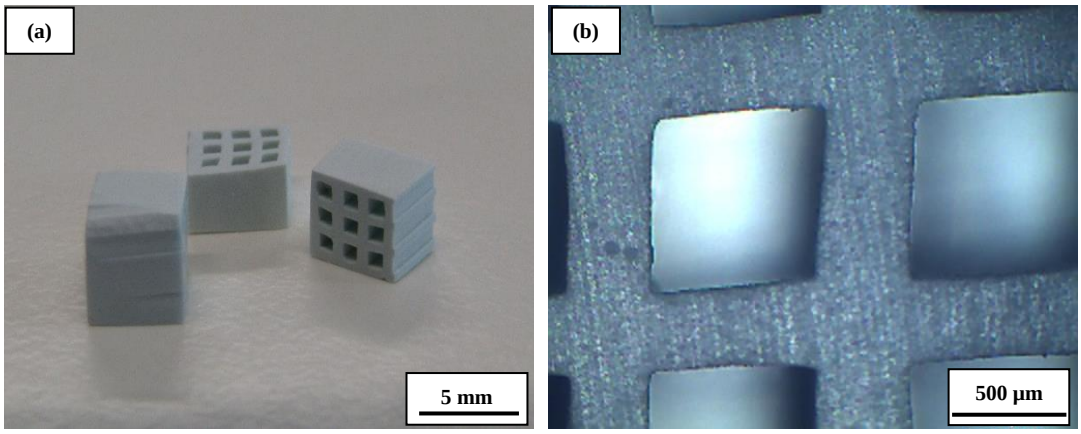

Fig. 6-11. *Images of the final scaffolds taken using* ***(a)*** *a digital camera and* ***(b)*** *an optical microscope. The images were taken of the C-HA/S scaffolds, and highlight the blue colourisation observed, in all scaffolds, when processed at 1200 and 1250 °C.*

6.3.6.1 Chemical Structure of Sintered HA Scaffolds

Fig. 6-12 illustrates the XRD pattern of the scaffolds sintered at 1200 and 1250 °C. Sintering further improved the crystallinity of all the samples, and the emergence of other calcium phosphate phases were not descried. The calcined powders maintained their relatively higher HA peak intensities over the scaffolds sintered using the as-received powder (AR-HA/S). The yttria peaks in the scaffolds fabricated using Y-HA powder (Y-HA/S) sintered at 1200 °C were found to decrease with respect to the HA peaks, and further decreases, albeit to a lesser extent, were detected at 1250 °C. Furthermore, the peak positions pertaining to hydroxyapatite in Y-HA/S were found to shift to higher angles compared to C-HA. It was further observed that the peaks in the scaffolds fabricated using the C-HA powder (C-HA/S) sintered at 1250 °C exhibited a lower intensity than at 1200 °C. The same behaviour was also observed in the as-received scaffolds but to a lesser extent.

FTIR analysis was again performed to verify the chemical structure of the samples, and the results are displayed in **Fig. 6-13**. Chemical structural differences between the uncalcined and calcined samples were once again observed. At 1200 °C, AR-HA/S exhibited a spectrum with an improved definition with respect to the starting powder, which is indicative of improved crystallinity within the sample. The phosphate bands at 962, 601 and 567 cm^{-1}, and the hydroxyl ion peak at 3570 cm^{-1}, were found to decrease in intensity. The phosphate bands between 1100 – 1000 cm^{-1} were found to split revealing an additional phosphate peak at 1023 cm^{-1}, which again is indicative of the material becoming more crystalline. However, the OH^- group at 630 cm^{-1} was still absent. In addition, albeit small, peaks were observed at 942 and 875 cm^{-1}; the latter could pertain to either a carbonate (CO_3^{2-}) or a hydrogen phosphate group (HPO_4^{2-}), which are commonly found in sintered HA materials, however, as no other peaks pertaining to either groups were found, the identity of the peak could not be discerned; the peak at 942 cm^{-1} pertains to a phosphate group belonging to β-tricalcium phosphate.

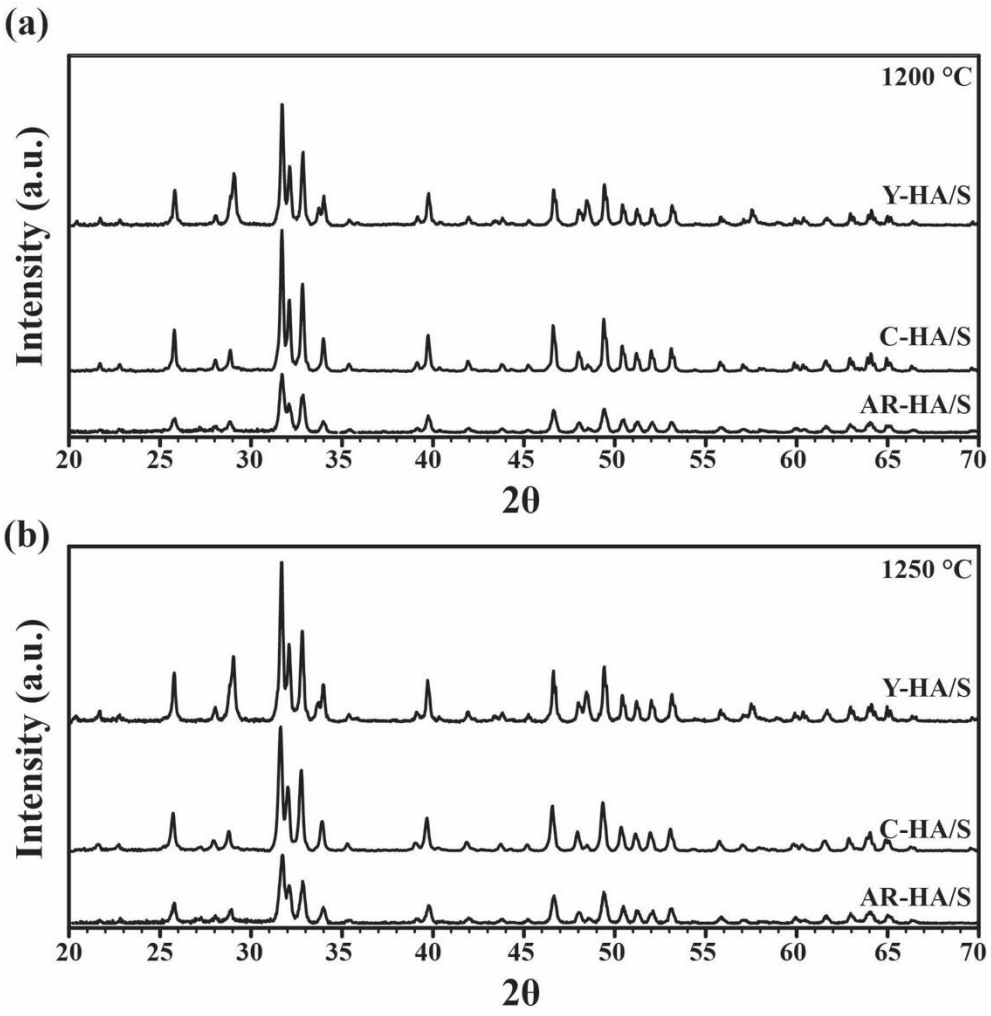

Fig. 6-12. *XRD patterns of the scaffolds sintered at* ***(a)*** *1200 and* ***(b)*** *1250 °C. The data highlights C-HA/S and Y-HA/S possessed peaks that were greater in intensities, as well as being narrower, compared to AR-HA/S. Furthermore, no secondary phases were detected in all samples by the X-ray diffractometer.*

Therefore, sintering HA scaffolds fabricated using the as-received powder at 1200 °C improved the crystallinity of HA phase, however, trace amounts of β-TCP, and the formation of either a carbonate or hydrogen phosphate group, were also detected. Both scaffolds fabricated using the calcined powders maintained their highly stoichiometric chemical structure over the as-received material at 1200 °C, as demarcated by the improved spectra definition, and the presence of both the stretching and bending hydroxyl ions (**Fig. 6-13**).

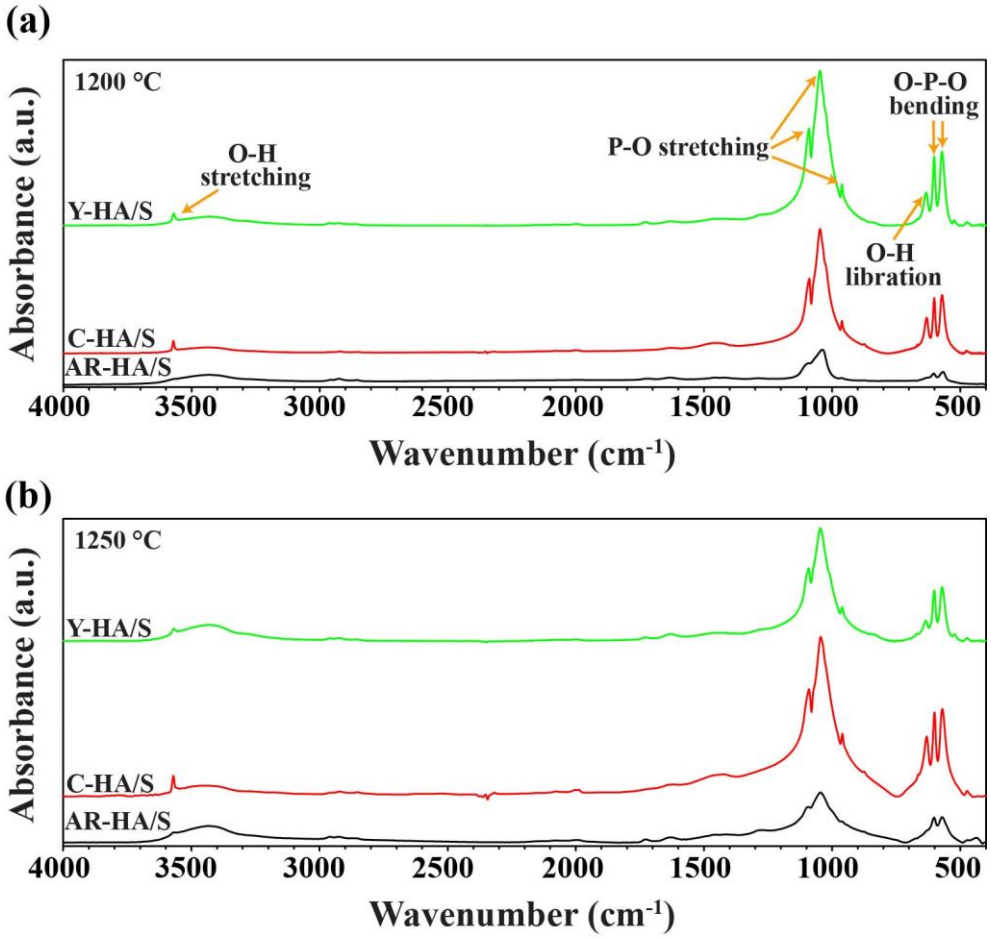

Fig. 6-13. *FTIR analyses of AR-HA/S, C-HA/S and Y-HA/S scaffolds sintered at* ***(a)****1200 and* ***(b)****1250 °C. The spectra revealed that AR-HA/S exhibited a band pertaining to β-TCP at 940 cm^{-1}, which was not observed in C-HA/S nor Y-HA/S. Furthermore, AR-HA/S continued to lack the OH^{-} at 630 cm^{-1}.*

Sintering of the calcined samples conduced chemical restructuring, and like AR-HA/S, the phosphate bands between 1100-1000 cm^{-1} had split, forming an additional peak at 1023 cm^{-1}. Moreover, both samples maintained their intense OH^{-} peak at 3570 cm^{-1}; and small peaks at 875 and 667 cm^{-1} were again visible in both calcined scaffolds at 1200 °C. Neither of the calcined scaffolds displayed bands pertaining to other calcium phosphate phases. Thus, it can be concluded that neither underwent a decompositional change to the same extent as the AR-HA/S.

Differences between the Y-HA and C-HA scaffold were also elucidated. The appearance of the new bands at 875 and 667 cm^{-1} were smaller in the Y-HA/S, and an additional peak was observed in Y-HA/S at ~ 500 cm^{-1}, which was not seen in C-HA material.

FTIR spectra of the scaffolds sintered at 1250 °C are depicted in **Fig. 6-13 (b)**. The spectrum for AR-HA/S depicts a curve with a similar definition to that of the starting powder. The hydroxyl group at 630 cm^{-1} remained absent, however, the other hydroxyl peak at 3570 cm^{-1}, as well as the phosphate peaks, can be seen to decrease in intensity; the unconfirmed peak at 875 cm^{-1} was again detected; and no additional peaks were descried.

Both calcined samples also exhibited a decrease in peak intensities. The presence of new, or the disappearance of existing peaks were not encountered. Although in general the bands were found to decrease as the sintering temperature was increased, the hydroxyl groups of the Y-HA/S were found to decrease to a larger extent than those belonging to the C-HA/S, consequently resulting in the C-HA/S possessing higher hydroxyl intensities at this temperature. This is in contrast to the FTIR data for the as-calcined samples (**Fig. 6-6**). The ratio of the hydroxyl bands at 3570 and 630 cm^{-1} to the largest phosphate peak at 1045 cm^{-1}, are presented in **Table 6-4**. It was determined that the phosphate-to-hydroxyl group ratio were higher in the Y-HA than C-HA following calcination, however, this was reversed when the samples were sintered at 1200 and 1250 °C. For the ratio between the phosphate peak and the hydroxyl band at 3570 cm^{-1}, the total decrease in ratio was found to be 84% and 69% for Y-HA and C-HA, respectively; whereas the decrease in ratio between the phosphate and the hydroxyl band at 630 cm^{-1} was found to be 64% and 36% for Y-HA and C-HA, respectively.

Table 6-4. *The ratio of band intensities between the phosphate at 1045 cm^{-1}, to that of the hydroxyl group at 3570 and 630 cm^{-1}, referred to as OH_1 and OH_2, respectively.*

	As-calcined		1200 °C		1250 °C	
	PO/OH_1	PO/OH_2	PO/OH_1	PO/OH_2	PO/OH_1	PO/OH_2
AR-HA	2.22	-	2.33	-	2.47	-
C-HA	7.88	2.74	2.79	2.03	2.47	1.74
Y-HA	8.84	3.82	1.77	1.59	1.42	1.36

6.3.6.2 Physical and Mechanical Properties of the Sintered HA Scaffolds

6.3.6.2.1 Bulk Porosity

The bulk porosity of the different HA scaffolds were measured, and the results are illustrated as bar graphs in **Fig. 6-14**. The AR-HA/S possessed bulk porosities of 46.2 ± 2.1 and 40 ±1.0% at 1200 and 1250 °C, respectively; the C-HA/S samples had bulk porosities of 52.1 ± 1.1 and 45 ± 1.1%, at 1200 and 1250 °C, respectively; and the Y-HA/S possessed bulk porosities of 52.5 ± 1.7 and 44.7 ± 1.2% at 1200 and 1250 °C, respectively. An unpaired t test between the sintering temperatures of each sample revealed the decrease in bulk porosity was significant; whereas a one-way ANOVA revealed that C-HA/S and Y-HA/S possessed significantly greater values than AR-HA/S.

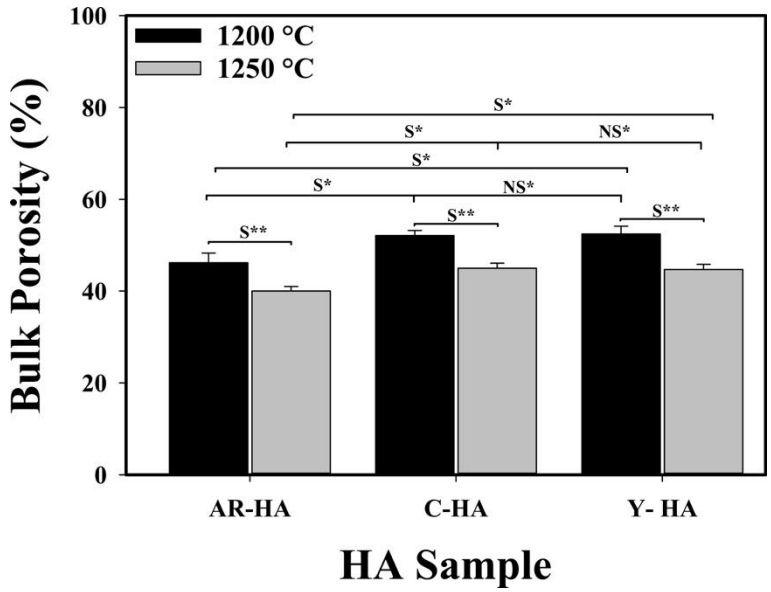

Fig. 6-14. *Bulk porosity measurements of the HA samples, as determined by a helium-pycnometer. The data demonstrates a decrease in scaffold bulk porosity when the temperature was increased from 1200 to 1250 °C (n = 3; error bars represent the standard deviation; S denotes a significant difference in data (p< 0.05), whereas NS is not significant; * denotes statistical analysis determined by a none-way ANOVA, whereas ** was determined by a t test).*

Optical microscopy was employed to estimate the cell length and strut thicknesses to further elucidate the effects of the starting powders on the physical properties of the different scaffold groups. In general, the mean cell lengths and strut thickness of the AR-HA/S were found to be ~ 650 and ~ 350 µm, respectively, upon sintering; C-HA/S

exhibited cell lengths and a strut thickness of ~ 750 and ~ 425 µm, respectively; and the Y-HA/S exhibited cell lengths and a strut thickness of ~ 800 and ~ 475 µm, respectively.

6.3.6.2.2 Compressive Strength

The scaffold groups were subjected to compression loading parallel to the open cell direction (A-axis direction), and the results of the compressive strengths are presented in **Fig. 6-15**. The AR-HA increased in strength as the temperature was increased, from 11.6 ± 1.1 to 20.4 ± 3.9 MPa, at 1200 and 1250 °C, respectively; this corresponded to an increase of 76%. At 1200 °C, the C- HA/S and Y-HA/S achieved maximum compressive strengths of 31.8 ± 5.2 and 27.9 ± 2.5 MPa, respectively. However, when sintered at 1250 °C, the maximum compressive strengths soared to 105.9 ± 12.2 and 127.3 ± 8.2 MPa, respectively, which corresponded to increases of 233% and 356%, respectively. A one-way Anova test revealed a significant difference between all three HA samples at 1250 °C, thereby revealing a significant difference between C-HA/S and Y-HA/S at 1250 °C. A one-way Anova test was also performed at 1200 °C, in which a significant difference was only observed between AR-HA/S, but not between C-HA/S and Y-HA/S. An unpaired, t-test was used to confirm that the increase in strength between 1200 and 1250 °C for each sample was significantly higher.

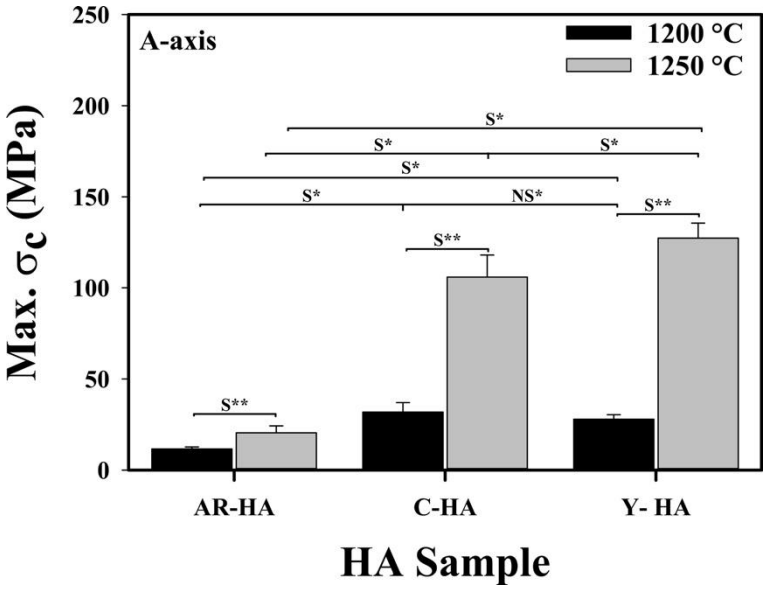

***Fig. 6-15**. Maximum compressive strengths of the HA samples loaded parallel to the direction of the cells. The data revealed that pre-calcining the powder resulted in*

scaffolds with higher compressive strength when sintered at both 1200 and 1250 °C. Furthermore, a dramatic increase in compressive strength for C-HA/S and Y-HA/S were observed when sintered at 1250 °C (n = >8; error bars represent the standard deviation; S denotes significantly different (p< 0.05), whereas NS indicates difference was not significance; both a one-way ANOVA (*) and t-test (**) were used to analyse the data).

Compression tests perpendicular to the cell direction (B-axis direction) were also performed for the calcined samples, and the results are portrayed in **Fig. 6-16**.The C-HA/S compressive strength increased from 7.5 ± 2.1 to 32.3 ± 2.3 MPa, at 1200 and 1250 °C, respectively, which is an increase of 331%. The Y-HA scaffolds maximum compressive strength also increased, from 8.6 ± 1.1 to 46.2 ± 2.8 MPa, at 1200 and 1250 °C, respectively, which is an increase of 437%. Again, it was determined that only the values at 1250 °C were statistically different, as determined by an unpaired t test.

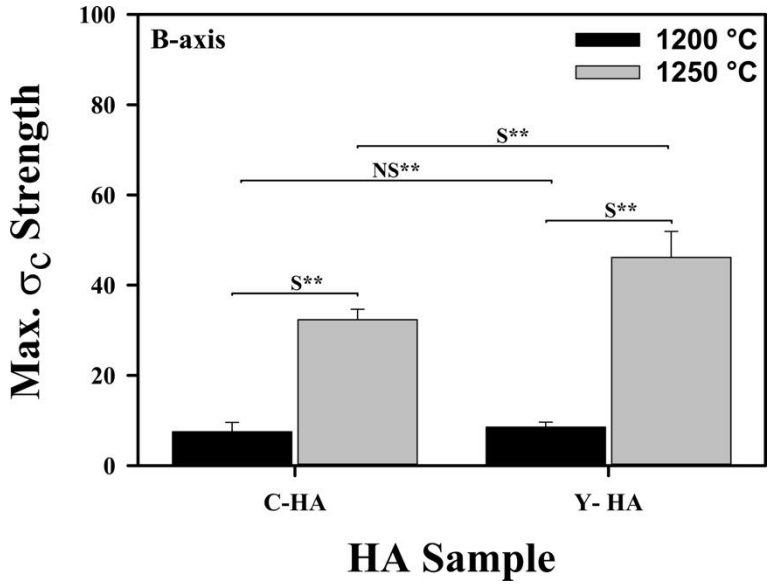

***Fig. 6-16**. Maximum compressive strength of C-HA/S and Y-HA/S samples loaded perpendicular to the direction of the cells. A significant increase in compressive strength of both samples was found when the sintering temperature was increased to 1250 °C. Moreover, the compressive strength results obtained in the B-axis at 1250 °C were greater than that obtained by scaffolds fabricated through traditional means, which are typically below 20 MPa (n = >8; error bars represent the standard deviation; a test was used to determine whether the difference in strength was (S) significantly different (p<0.05) or (NS) not significant different; an unpaired t-test was used).*

6.3.6.3 Microstructural Properties

6.3.6.3.1 Fracture Surface

The scaffolds loaded in the A-axis direction were found to fracture in a brittle manner, which is typical of ceramics. Fracturing of said scaffolds were observed at the midpoint of the cells, as denoted by the red dashes in **Fig. 6-17 (a).** **Fig. 6-17 (b)** is an SEM micrograph that delineates the remnants of the scaffolds, in which it can be clearly observed that the struts fractured halfway through the cell walls, and the cleavage traversed the length of the scaffold. Examining the microstructure of the fractured sample at sites where the struts failed (Site 1) and at where struts did not fail (Site 2) revealed that micro-cracks were exclusive to Site 1, inferring that the compressive load may not have been distributed homogenously across the solid phase of the scaffolds. Mix-mode, but principally intergranular, fracturing had occurred, as highlighted in **Fig. 6-17 (c)**. The fracture in the figure below can be seen to transform from an intergranular fracture to, albeit thinner, transgranular fracture.

Alternative fracture behaviour was observed when the scaffolds were subjected to compressive loading perpendicular to the cell alignment, as presented in **Fig. 6-18**. In contrast to the scaffolds that were subjected to compression loading in the A-axis, no audible sound accompanied the scaffold failure. When loading in the B-axis, the walls perpendicular to the load simply collapsed above one another. **Fig. 6-18 (b)** depicts a representative remnant of the scaffold post failure where it can be observed that struts parallel to the load were 'unhinged', leaving an intact perpendicular wall with a depressed fracture region where the perpendicular struts once merged (Site 1). SEM analysis elucidated that fracturing continued to be exclusive to Site 1, and again exhibited mix-mode fractures, but predominantly intergranular. **Fig. 6-19** is a high magnification SEM micrographs depicting the fracture sites of the studied samples. Sintering of the as-received samples at 1200 and 1250 °C resulted in a highly densified microstructure (**Fig. 6-19 (a & b)**), whereas the fracture site of the C-HA/S (**Fig. 6-19 (c & d)**) and of the Y-HA/S (**Fig. 6-19 (e & f)**) were noticeably more porous, and presented with small sintering necks; both these characteristics conferred the appearance of an unsintered scaffold at the microstructural level. The sintering necks observed in the calcined HA samples at 1200 °C grew when the temperature was raised to 1250 °C, and the growth was greater in the C-HA/S.

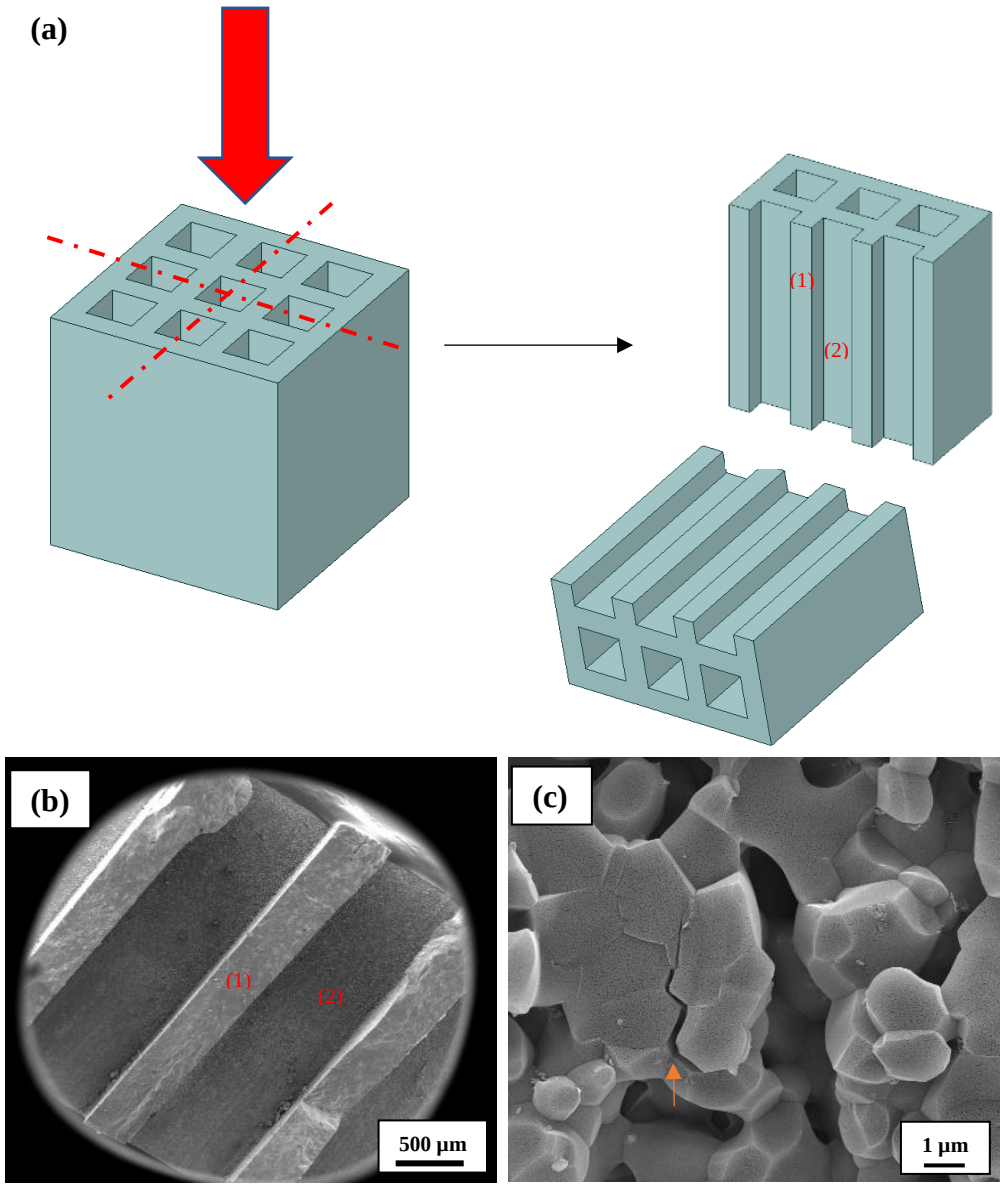

Fig. 6-17. *Fracture behaviour in the A-axis.* ***(a)*** *is a CAD schematic depicting the fracture results;* ***(b)*** *is a representative low magnification SEM image of the fracture site from C-HA/S sample; and* ***(c)*** *is a representative SEM image of the mix-mode fracture that was observed in the same C-HA/S. The micrograph is used to demonstrate the longitudinal fracture exhibited by the scaffolds when subjected to compressive loading parallel to cell alignment.*

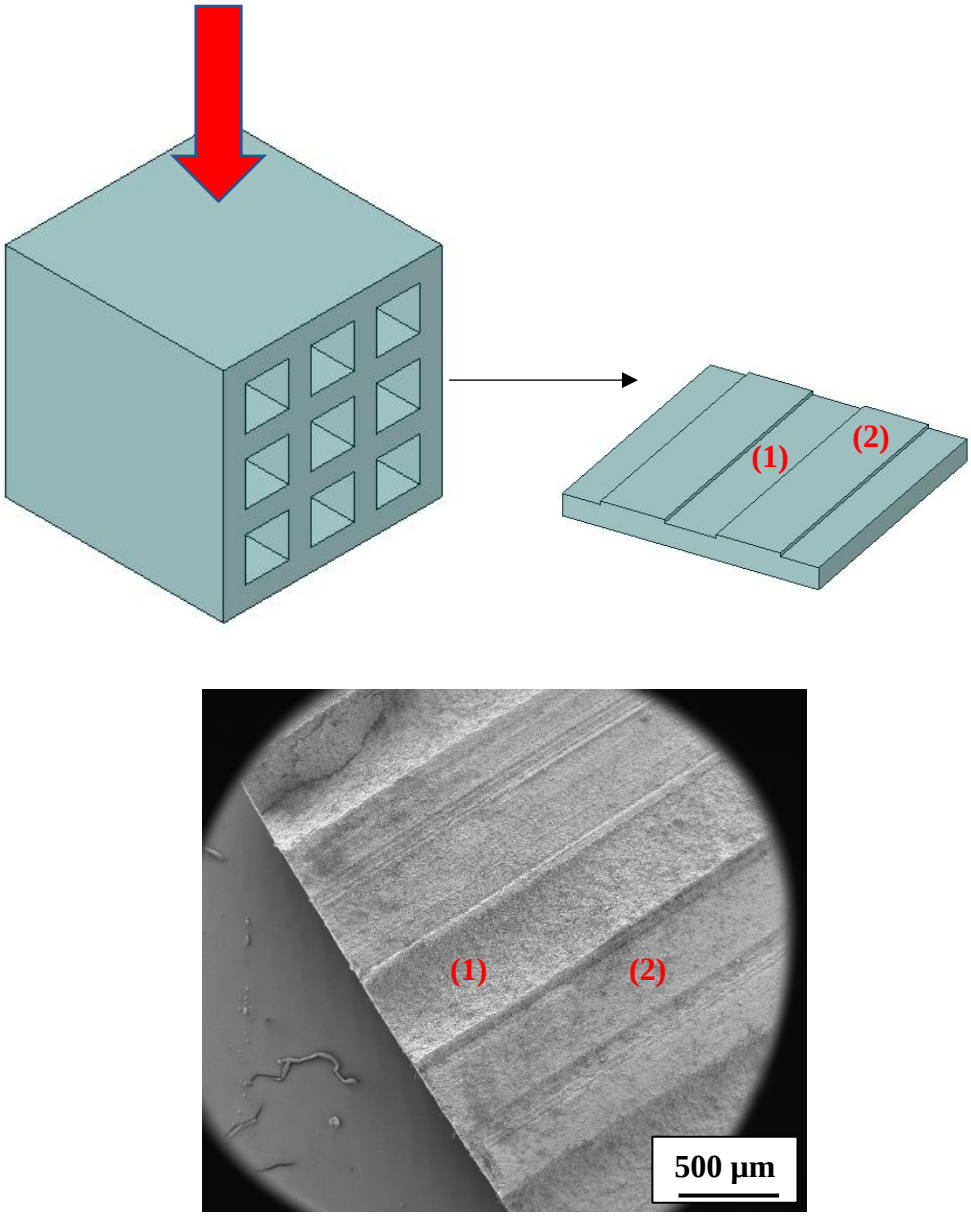

Fig. 6-18. *Fracture behaviour in the B-axis.* ***(a)*** *is a CAD schematic depicting the fracture results;* ***(b)*** *is a representative low magnification SEM image of the fracture site, where site (1) indicating where the parallel struts were once connected. Applying a compressive load perpendicular to the cell alignment resulted in the scaffolds exhibiting a different fracture mechanism; where a longitudinal fracture observed in the parallel axis (****Fig. 6-17****) was not descried. Alternatively, the parallel struts in-between the perpendicular struts dislodged, and hence presented the perpendicular struts with recess at site (1).*

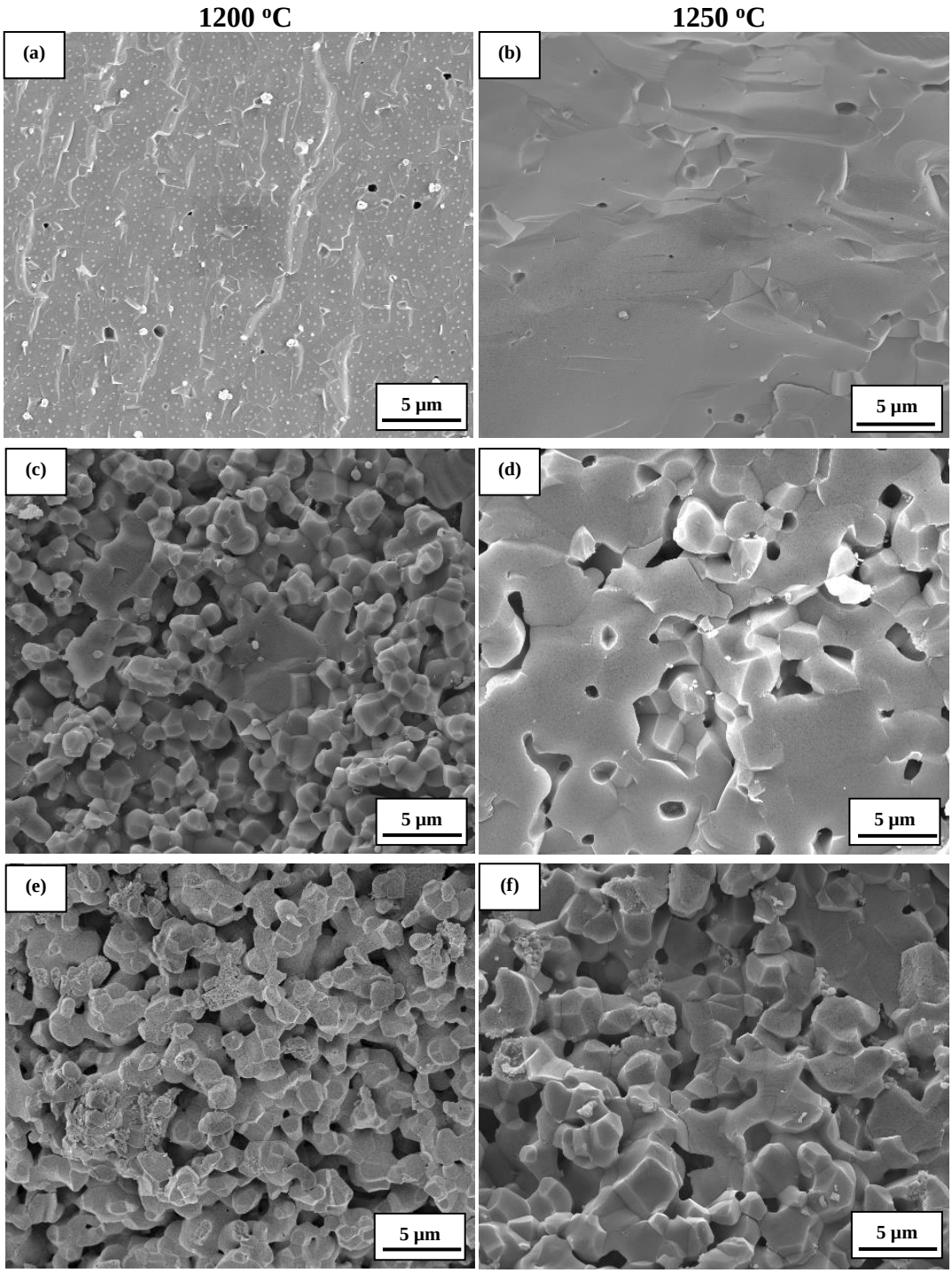

Fig. 6-19. *High magnification SEM (SE) micrographs depicting the fracture surface of the HA samples post compression testing (top row – AR-HA/S; middle row – C-HA/S; and bottom row – Y-HA/S). the micrographs demonstrate that AR-HA/S was more densified than C-HA/S and Y-HA/S.*

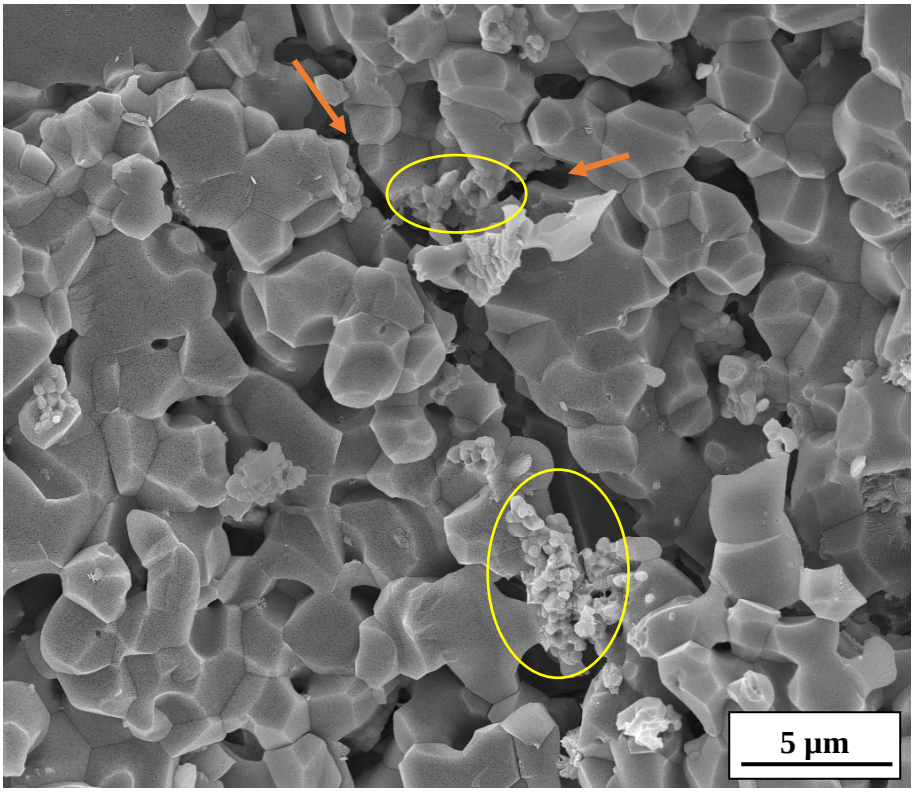

Fig. 6-20. *SEM (SE) micrograph depicting a representative 'yttria bridge', as highlighted by the yellow circles, found in Y-HA/S samples sintered at 1250 °C; the orange arrows are used to indicate crack pathways. These microstructural features were believed to possess crack-arresting properties.*

Further examination of the fracture surface in Y-HA/S samples revealed 'yttria bridges', as representatively delineated in **Fig. 6-20**. SEM analysis demonstrated that the yttria phase remained relatively intact when the surrounding HA matrix was fractured, and this spectacle was observed throughout the fracture surfaces of samples sintered at 1250 °C. EDS analysis confirmed that these microstructural features were indeed yttria phases, as illustrated in **Fig. 6-21**. The EDS micrograph illustrates the bridges to be heavily populated with yttrium ions, with respect to the surrounding microstructure. The 'yttria bridges' were revealed to consist of grains with sizes below 500 nm.

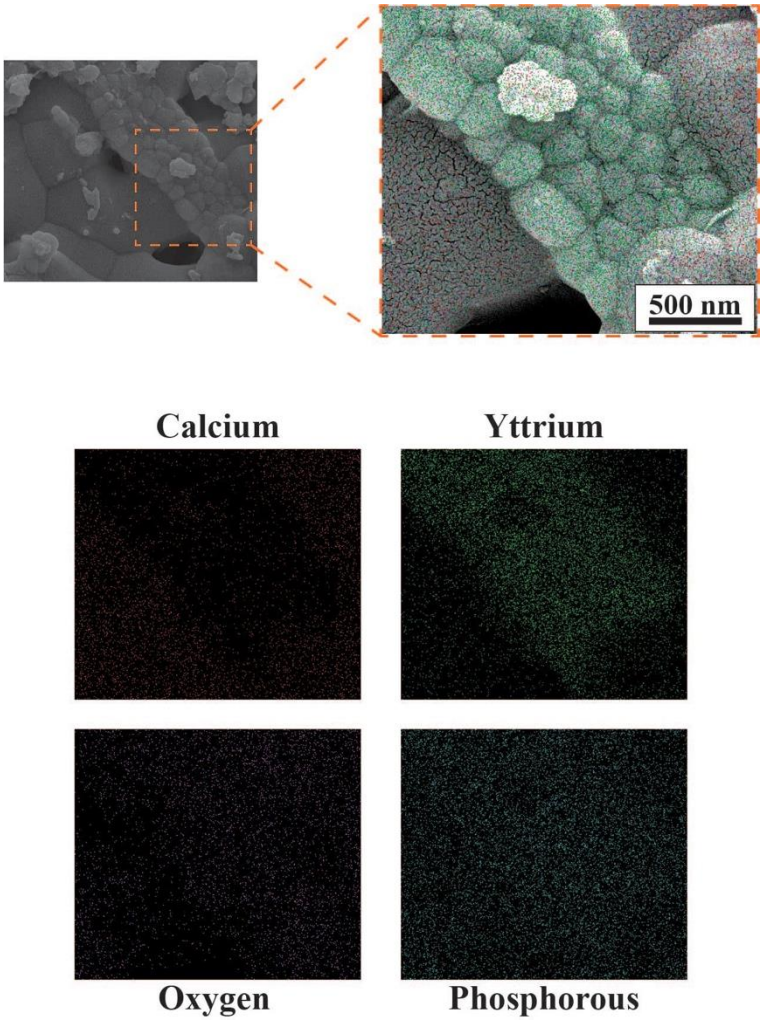

***Fig. 6-21**. EDS analysis of Y-HA/S portraying a representative 'yttria bridge'. The figure is used to qualitatively demonstrate the microstructural feature were indeed that of yttria. As illustrated, the 'yttria bridges' can be observed to be heavily populated with yttrium ions (green dots).*

For Y-HA scaffolds sintered at 1200 °C, such yttria bridges were found to have less crack arresting properties than samples sintered at 1250 °C, as illustrated by the cleaved clusters in **Fig. 6-22**. It was also observed that the yttria grain sizes were less than 100 nm. The interface between yttria and the hydroxyapatite at 1200 °C merits a mention: although no micro-cracks were observed at the interface, remnants of yttria corresponding to their grain size were detected.

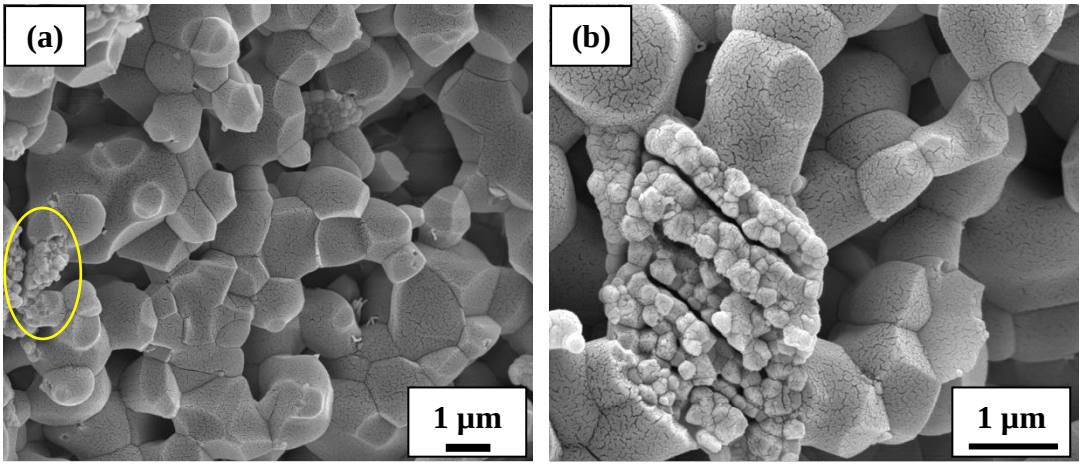

Fig. 6-22. *SEM (SE) micrographs representative of the 'yttria bridges' found in the Y-HA/S samples sintered at 1200 °C. Unlike when sintered at 1250 °C, the yttria bridges presented with fractures, and hence possessed less crack-arresting properties.*

6.3.6.3.2 Grain Morphology

SEM analysis was employed to elucidate the grain morphology of the different HA samples, which were taken from Site 2 (**Fig. 6-17**), and the results are illustrated in **Fig. 6-23**. Sintering of the as-received scaffolds presented with a grain morphology exhibiting bubble-like topography at 1200 °C, which subsided in the 1250 °C scaffolds. Secondary grain structures were also observed, emanating from the grain boundaries; at 1250 °C said structures development was considerably more extensive, which led to encroaching on the HA grain body with seldom visibility of the grain boundary. Furthermore, the microstructure presented with both normal and abnormal grain growth, with the normal grain sizes estimated as 2.4 ± 0.9 and 5.9 ± 1.5 µm, at 1200 and 1250 °C, respectively.

Calcination of the starting powders resulted in a different scaffold microstructure to that of the AR-HA/S (**Fig. 6-23 (c-f)**). The bubbles observed in the as-received microstructure were not apparent in either of the calcined samples. Moreover, the observed secondary grain structures formed to a considerably lesser extent, particularly at 1250 °C. Y-HA/S presented with a tertiary grain structure, which were ascribed to yttria phases. The scaffolds again comprised both normal and abnormal grain sizes, with the normal grain size estimated as 1.7 ± 0.4 and 3.2 ± 0.8 µm, at 1200 and 1250 °C, respectively, for the C-HA/S, corresponding to an increase of 88%; and 1.6 ± 0.3 and 3.5 ± 0.6 µm, at 1200 and 1250 °C, respectively, for the Y-HA/S, which was an increase of 119%. **Fig. 6-24** presents the estimated normal grain sizes.

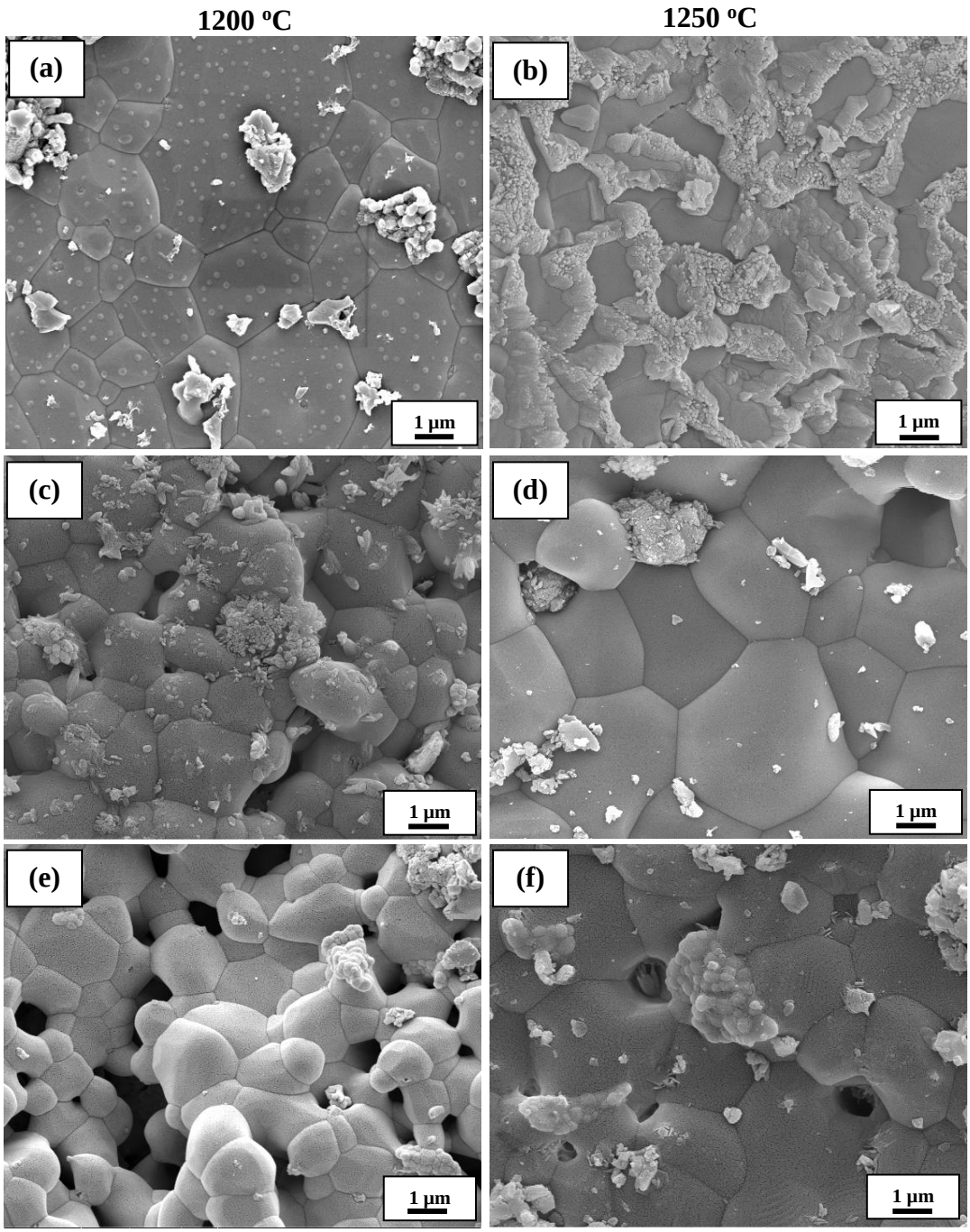

Fig. 6-23. *Representative SEM (SE) micrographs illustrating the grain morphology of the studies samples. Top row – AR-HA/S; middle row; C-HA/S; and bottom row – Y-HA/S. Micro-pores were observed in C-HA/S and Y-HA/S, but not in AR-HA/S. Moreover, the degree of secondary grain structures observed in AR-HA/S was greater than that of the other two samples.*

Another salient microstructural difference between the as-received and calcined samples was the level of densification. The calcined samples presented with sintering

neck formation between adjacent grains when sintered at 1200 °C, and grew significantly when processed at 1250 °C. As a result, the micro-porosity observed at 1200 °C

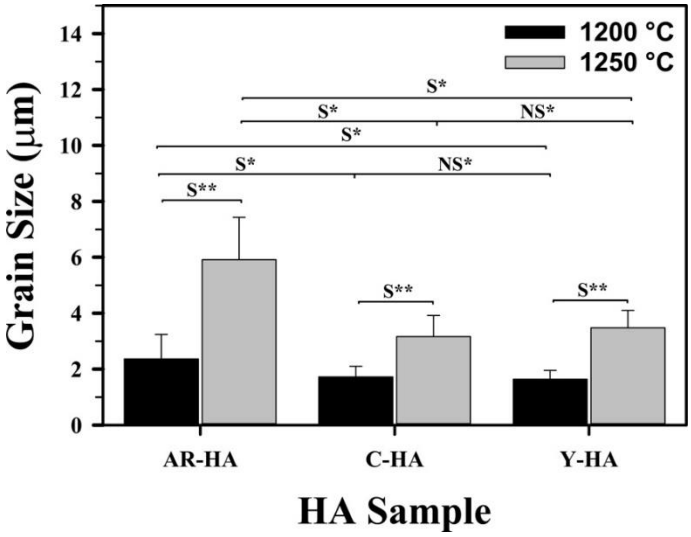

***Fig. 6-24**. Estimates of the normal grain sizes measured from SEM imaging. Increasing the sintering temperature resulted in larger grain sizes in all samples. (n = 20; the error bars represent the standard deviation of the data; S and NS denote whether the difference was significant or not significant, respectively; * denotes a one-way ANOVA was used, ** denotes a t-test was used).*

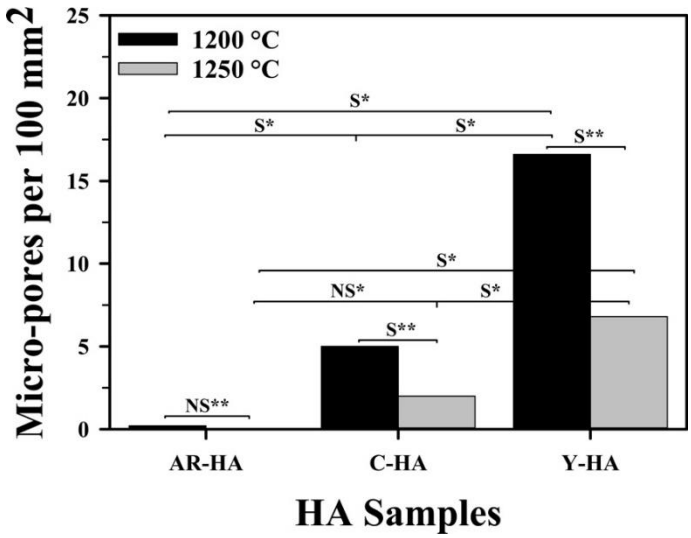

***Fig. 6-25.** Estimated number of micro-pores per 100 μm^2 measured in AR-HA, C-HA and Y-HA scaffolds when sintered at 1200 and 1250 °C. The data was obtained using ImageJ (**section 6.2.4**). The data highlights the increase in the number of micro-pores found in C-HA/S and Y-HA/S compared to the uncalcined AR-HA/S. In addition, increasing the sintering temperature considerably reduced the number of micro-pores. (n = 5 quadrants; error bars denote the standard deviation; S denotes statistically significant difference, NS denotes not significant; * analysis determined by one-way ANOVA test; ** indicates the analysis was determined by a t-test).*

diminished when scaffolds were processed at 1250 °C. The sizes of the micro-pores were found to be less than 2 μm in all samples. **Fig. 6-25** depicts the estimated micro-pore frequency measured per 100 μm^2 for all hydroxyapatite scaffolds. Y-HA/S displayed the greatest micro-porosity frequency at both sintering temperatures, with respect to the C-HA/S, which was significantly greater as determined by a one-way ANOVA test. The Y-HA/S micro-porosity measured at 1250 °C was approximately 6.8 per 100 μm^2, whereas for the C-HA/S at the lower sintering temperature of 1200 °C was approximately 5 per 100 μm^2.

6.3.6.3.3 Energy Dispersive Spectroscopy (EDS)

EDS analysis was performed on the hydroxyapatite grains for all samples, and was initially employed to elucidate the difference between the primary and secondary grain structures observed. The instrument was able to detect the elemental constituents of hydroxyapatite in all samples, which are calcium, oxygen and phosphorous; hydrogen is undetectable by the instrument. Initial EDS analysis revealed that the secondary grain structures exhibited a relatively high oxygen intensity, with respect to phosphorus (**Fig. 6-26 (a))**. In contrast, microstructural sites lacking in secondary grain structures presented with a relatively low oxygen intensity peak (**Fig. 6-26 (b)**). Examining the peak intensities of the main oxygen peak at 0.5 keV and phosphorus peak at 2.0 keV, revealed an oxygen-to-phosphorus ratio of 1.44 for **Fig. 6-26 (a)** and 0.89 for **Fig. 6-26 (b).**

EDS analysis was further performed on different sites on C-HA/S grain in order to determine the precise location of the oxygen discrepancy, and a representative image is portrayed in **Fig. 6-27**. Preliminary examination between the grain boundary (Site 1) and the grain body (Site 2) disclosed no discernible difference. However, narrowing the site examined at the grain boundary (Site 3) produced an EDS spectrum with oxygen intensities lesser than that of calcium and phosphorus, which is in contradiction to the other two sites; with an oxygen-to-phosphorus ratio of 1.24, 1.12 and 0.87 for Sites 1, 2 and 3, respectively. The peak intensity ratio between oxygen and calcium, at 3.7 keV, also decreased at Site 3; with values of 1.73, 1.12 and 0.93 for Sites 1, 2 and 3, respectively.

The aforementioned behaviour was further investigated by EDS mapping of the grain sites. As **Fig. 6-28** and **Fig. 6-29** attest to, oxygen-deficiency were observed only

on exposed HA grain boundaries (i.e. were secondary grains were absent (**Fig. 6-29**)), wherein the deficiency thereof was congruent to the grain boundary. The EDS mapping of calcium and phosphate presented with uniform distribution throughout the grain, with unremarkable characteristics.

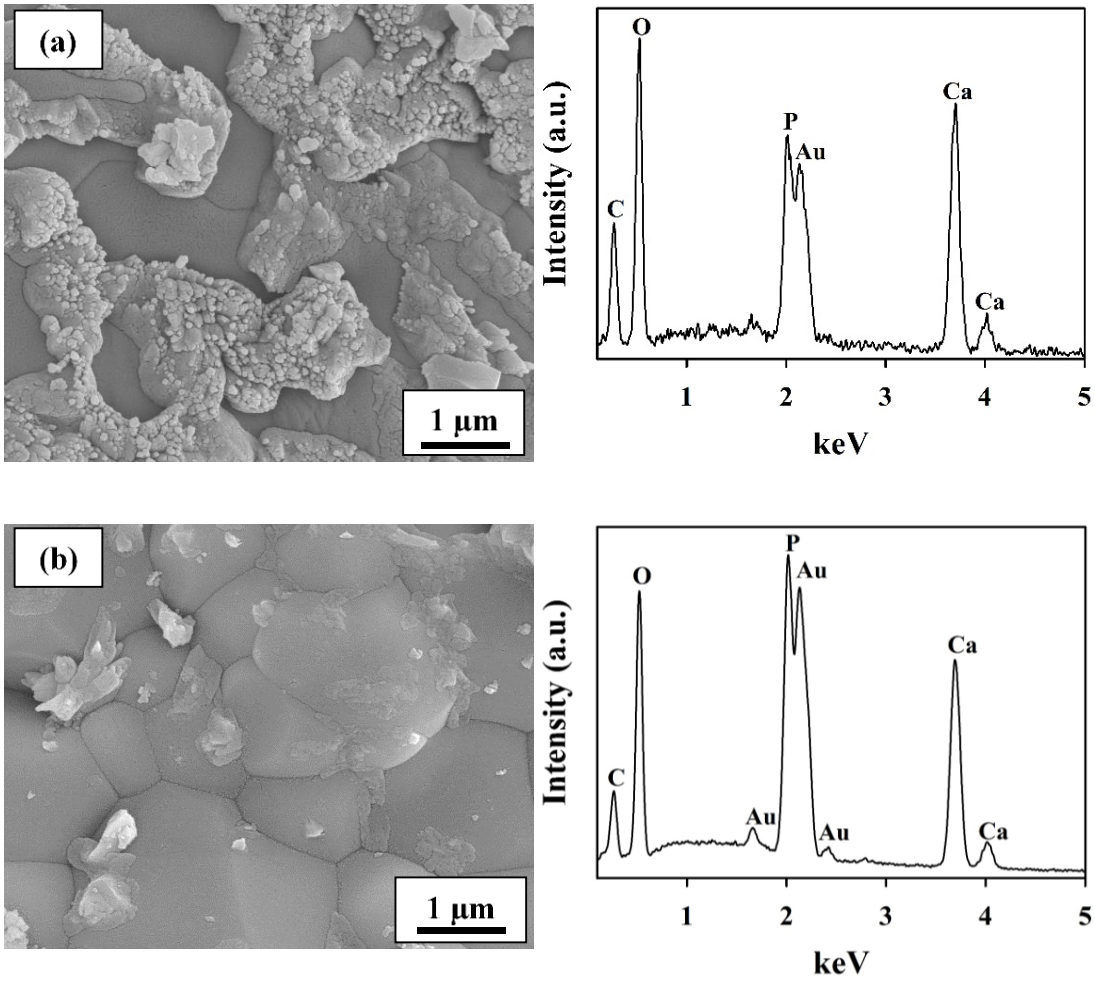

Fig. 6-26. *SEM (SE) micrographs representative of the grain morphology observed in the as-received 1250 °C* ***(a)****, and C-HA/S* ***(b)****; both micrographs are accompanied by their respective EDS spectra of sites. Note the difference in oxygen-phosphorus proportion between the two, with an O:P ratio of 1.44 for* ***(a)****, and a ratio of 0.89 for* ***(b)****.*

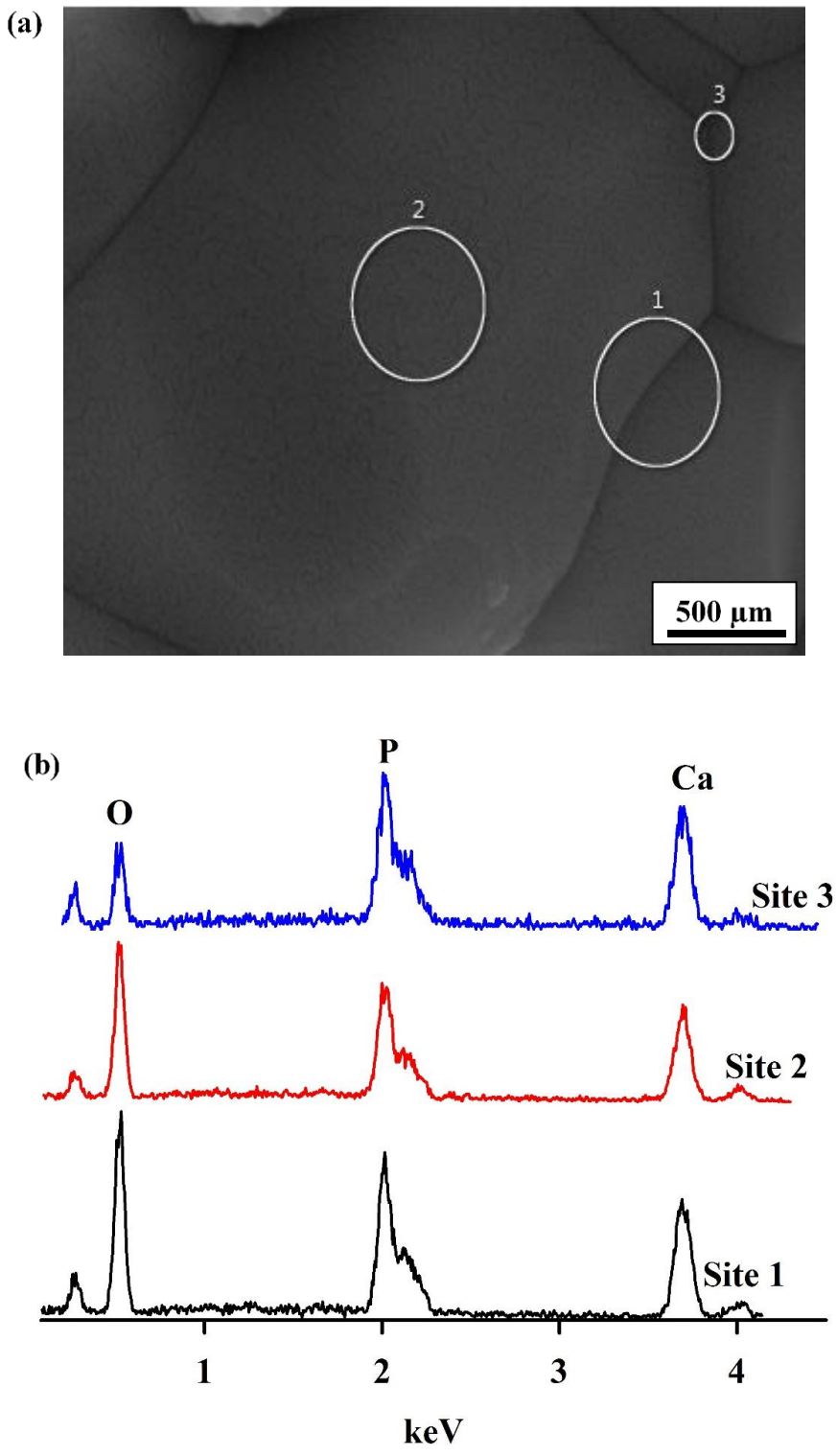

Fig. 6-27. *SEM (SE) micrograph of a C-HA/S grain sintered at 1250 °C that was analysed at three different sites* ***(a)****, and their corresponding spectra* ***(b)****. Site 3 produced an oxygen peak smaller than that of calcium and phosphorous ions, which was not observed in Site 1 or 2, inferring the grain boundary was oxygen deficient.*

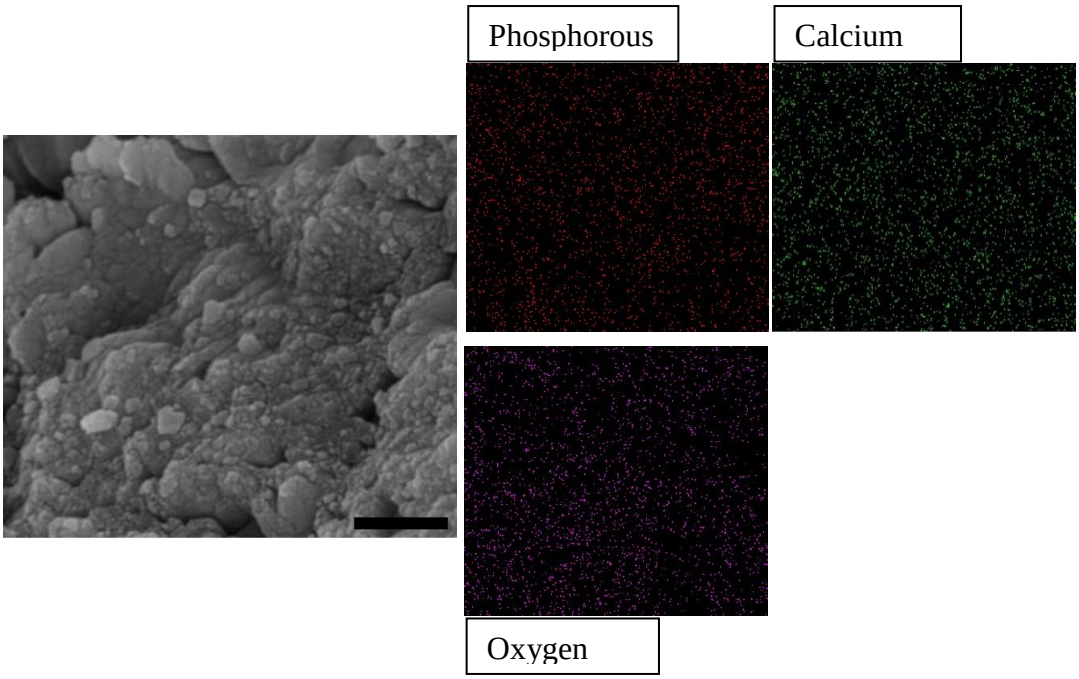

Fig. 6-28. *EDS mapping performed on the microstructure of an AR-HA/S sintered at 1250 °C (scale bar = 500 nm). The data reveals that all three elements were homogenously distributed across the hydroxyapatite grain. The oxygen-to-phosphorus ratio for this site was 1.42.*

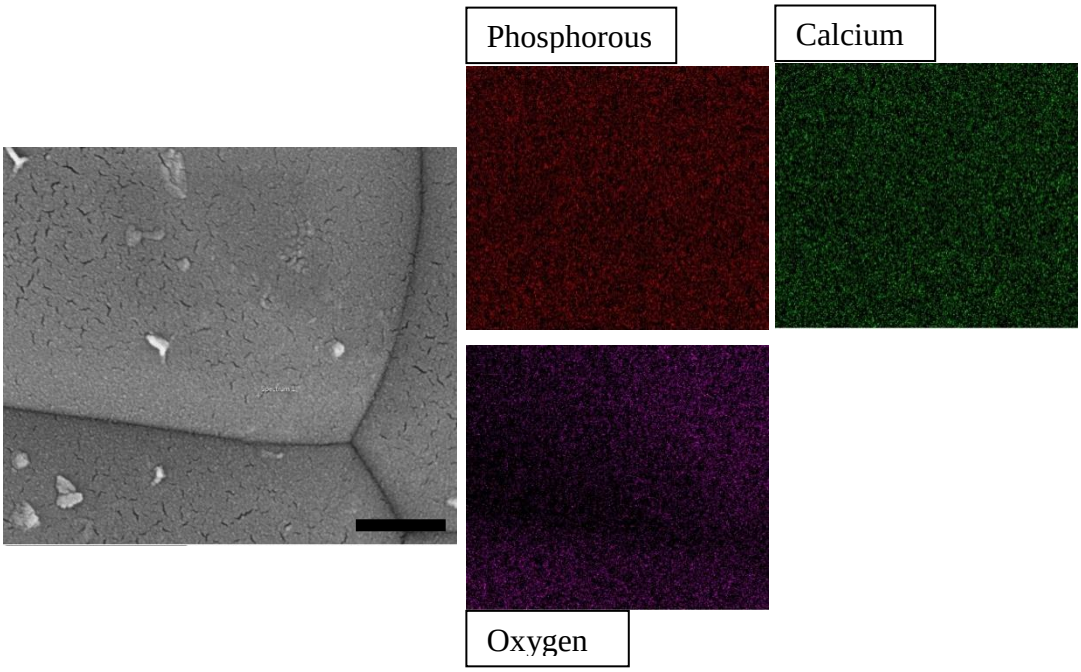

Fig. 6-29. *EDS mapping performed on the microstructure of C-HA/S sample sintered at 1250 °C. An oxygen-deficient area congruent to the hydroxyapatite grain boundary can be observed; conversely, phosphorous and calcium ions were homogenously distributed (scale bar = 500 nm). The oxygen-to-phosphorus ratio for this site was 0.63, which is again lower than that of sites where the grain boundary is impeded by the secondary structures emanating therefrom.*

EDS mapping was also conducted on Y-HA/S samples, and a representative image is illustrated in **Fig. 6-30**. In addition to displaying the presence of calcium, oxygen and phosphor, yttrium was detected. Thus, yttrium was either incorporated into the HA grain, or adsorbed onto the surface. With regards to the distribution of yttrium, EDS mapping revealed a homogenous distribution across the HA grain. Furthermore, oxygen-deficient regions previously observed in the C-HA/S were not evidenced at the grain boundary. A ratio between oxygen and phosphorus could not be determined, as the peaks for yttrium (Lα; 1.92) overlapped with the phosphorus (Kα; 2.01), and hence produced a phosphorus peak that was a combination of the two elements.

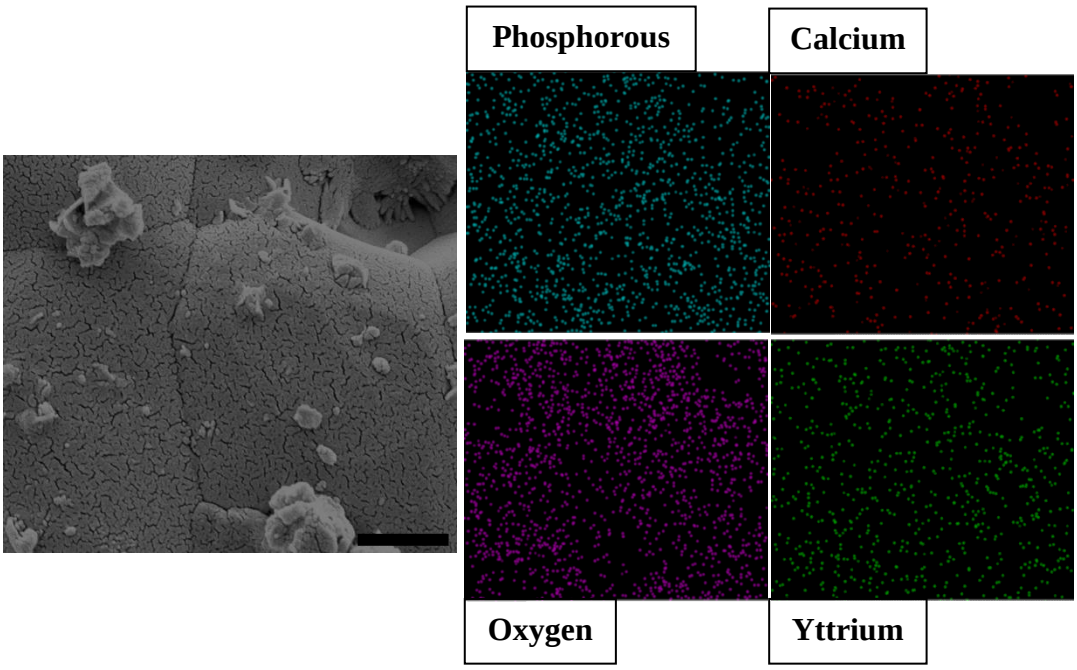

Fig. 6-30. *EDS mapping performed on a hydroxyapatite grain of Y-HA/S sample sintered at 1250 °C (scale bar = 1 µm). the figure clearly demonstrates that yttrium was detected in Y-HA/S, and that its distribution was uniform across the hydroxyapatite grain. Furthermore, a clear oxygen-deficient region was not descried, as observed in* ***Fig. 6-29****.*

6.4 Discussion

In this study, the effects of two pre-calcination approaches on an HA scaffold properties were examined. The effects were numerous, and conclusively beneficial to the aims of the project, amalgamating in a remarkable improvement to the compressive strength of extruded scaffolds; from 20.4 MPa for the AR-HA/S to 105.9 and 127.3 MPa for the C-

HA/S and Y-HA/S, respectively. The alterations due to calcination are outlined in **Table 6-5**, and will be discussed thereafter.

Table 6-5. *Summary of the calcination effects. The green and red arrows are used to denote increases and decreases, respectively, and blue arrows indicate no change.*

Particle Properties	Paste Properties	Scaffold Properties
↑ Particle size	↑ Packing Density	↑ Stoichiometry
↑ Powder density	↓ Extrusion force	↑ Thermal Stability
↓ Surface Area	↔ Stiffness*	↑ Bulk Porosity
↑ Powder morphology		↑ Compressive Strength
↑ Stoichiometry		↓ Grain Size
↑ Thermal Stability		↑ Micro-porosity

* As visually inspected

6.4.1 The Effects of Calcination on Powder Properties

The most noticeable change in particle properties as a result of calcination was to the particle morphology. The as-received hydroxyapatite powder's propensity to agglomerate into near-spherical agglomerates was exploited to form near-spherical primary particles. At 1000 °C, sufficient heat was supplied to provide the nano particles with energy for superficial diffusion to take place, thereby merging adjacent nano primary particles into coalesced micro-sized primary particles. Spherical particles have been demonstrated to attain the highest packing density in ceramic fabrication processes [332], and were successfully attained when powders were calcined at 1000 °C. Therefore, less organic constituents will need extracting from the extrudates, and thereby reducing chances of larger voids and inhomogeneous shrinkage that consequently result in the formation of defects [406-409]. In addition, the calcined powders consisted of particles with a wider size distribution, which again has been proven to augment particle packing [229, 332].

Furthermore, the addition of 10 wt% yttria resulted in HA particles that exhibited a more angular morphology. It is uncertain as to why this had transpired, however, it is clear the addition of yttria influenced the particle growth.

The substantial decrease in surface area was reflective of the changes to the primary particle size, which grew by a few orders of a magnitude in size. Previous studies into the effects of calcination revealed significant decreases to the surface area, however, the decreases observed in this study were one the highest found, as **Table 6-6** demonstrates. Indeed, parameters such as calcination temperature, dwell time and particle morphology, influence the final surface area produced.

Table 6-6. *The effect of calcination on hydroxyapatite surface area of other work. The percentage decrease in surface area following calcination recorded in the present study was amongst the highest found in the literature.*

Before calcination ($m^2 g^{-1}$)	**After Calcination ($m^2 g^{-1}$) (temperature in celsius)**	**Percentage decrease (%)**	**Ref**
107.9	4.95 (1200)	- 95.4	Present study
127	44 (550)	- 65.4	[410]
12.4	1.4 (800)	- 88.7	[411]
43.5	5 (1000)	- 88.5	[412]
43.5	0.97 (1200)	- 97.8	[412]
104	3 (1000)	- 97.1	[413]
8.4	0.8 (1000)	- 90.5	[414]

The marginal difference in surface area between the C-HA and Y-HA powders were attributed to the latter consisting of Y_2O_3 particles that were smaller than the HA particles, rather than attributing it to the incorporation of yttrium into the apatite lattice. The incorporation of ions thereto indeed influences lattice parameters that consequently affect particle size during calcination [415, 416]; however, the XRD analysis did not suggest the incorporation of yttrium into the HA. In both cases, the decrease in surface area would also improve particle packing density, as a decrease in surface area is expected

to attenuate agglomeration, and hence influence subsequent ceramic processing [227, 243]. All these effects on the particle morphology culminated in an increase in powder density as measured by the helium pycnometer, which provided the first insight into an improved packing behaviour. In the previous chapter, the density measurement was considered a prefigure for solid loadings during paste formulation. The Y-HA presented with a higher density than that of the C-HA, which was attributed to yttria's inherently higher density of 5.01 g/cm^3.

6.4.1.1 The Effect of Calcination on Chemical Properties

Further to the physical changes, calcination of the powder altered the chemical properties thereof. In both the C-HA and Y-HA powders, and with respect to the as-received powder, a transformation from non-stoichiometric to a stoichiometric HA was obtained, as evinced by the striking intensities of the FTIR and XRD patterns. **Fig. 6-4** highlighted the evolution of the AR-HA powder with increasing calcination temperature, from an ill-defined to a well-defined pattern. The evolution further confirmed the increase in particle size observed by the particle size analyser: the ill-defined pattern of the AR-HA powder was indicative of nano-size primary particles [342, 354] but transitioned to narrower peaks, which is associated with an increase to particle size [417].

The emergence of the hydroxyl group in C-HA and Y-HA was attributed to the re-hydroxylation process that the calcined powders underwent. Re-hydroxylation of hydroxyapatite can occur, so long as a critical temperature has not been exceeded [418]. Upon heating, the ceramic will undergo de-hydroxylation, which below a certain critical temperature the HA crystal structure is retained, thereby allowing HA to rehydrate during cooling. Thus, it can be deduced that calcining the as-received powder at 1000 °C resulted in re-hydroxylation of the HA lattice[7]. Typically, irreversible de-hydroxylation occurs over 1200 °C [418]. Hydroxyapatite lacking the hydroxyl group will be more susceptible

[7] Re-hydroxylation may explain why the starting β-TCP powder in **Chapter 6** had traces of hydroxyapatite. It was acknowledged that the β-TCP was calcined by the manufacturer, whereby the lattice may have accepted a hydroxyl group during calcination, thereby resulting in the presence of trace HA. Then when sintered at 1200 °C, the OH^- was liberated resulting in phase-pure β-TCP. Biphasic calcium phosphates are a subject of great interest, and the synthesis by 're-hydroxylation' through atmospheric moisture may provide a cheaper alternative.

to decomposition into anhydrous calcium phosphate phases [367]. The addition of yttria did not perturb the rehydration process; it is likely that calcining at 1000 °C did not induce ionic substitution of the admixture, and hence interfere with the OH^- group entering the HA lattice, despite the addition of 10 wt% Y_2O_3.

6.4.1.2 The Effects of Calcination on Thermal Properties

As was expected, the calcined powders possessed a more favourable thermal characteristic, which can be explained in two parts. First, the improved packing density equated to fewer voids, and hence particles required a shorter distance to travel for densification to occur. Second, the decrease in surface area inevitably required a greater energy for densification to commence, hence the increase to the sintering onset and endpoints. As for the Y-HA sample, it is uncertain as to why the material underwent a relatively noticeable linear expansion. Said observation in yttria-substituted ceramics have been attributed to phase transformation [419], and indeed expansion due to phase transformation was observed in the previous chapter with the transformation of β-TCP to α-TCP (**Fig. 5-5**); however, no HA phase transformation was confirmed for Y-HA. Other causes of dilatometric expansion have been ascribed to the removal of volatile and the formation of liquid phase [386]. Yttria has been demonstrated to dilatometrically expand up to 1550 °C [420], and it is plausible that the effects were conferred upon Y-HA. With regards to the increase in sintering onset and endpoint, it could be reasoned that this was due to yttria's relatively higher sintering properties.

A further possible explanation to the observed thermal expansion is the reorientation of the particles, which precedes the densification thereof, when heat is applied to a particulate system [229]. Hydroxyapatite [421] and biphasic calcium phosphate [422] have been demonstrated to undergo expansion at temperatures below 800 °C. The Y-HA powder was the only material to exhibit a discernible expansion, which could be due to the material consisting of two distinct particle morphologies as a result of expansion during particle orientation therefrom.

DSC analysis of AR-HA and C-HA presented with two endothermic reaction at ~ 935 and 1315 °C, however, it was the latter event that was believed to pertain to phase transformation, as HA has been demonstrated to decompose above 1300 °C [298, 366,

423, 424]. Once again, the absence thereof in the Y-HA is attributed to the material's enhanced thermal stability.

6.4.2 The Effect of Calcination on Paste Properties

The effects of pre-calcination were also realised during subsequent processing steps. Both calcined powders led to the formulation of pastes with a higher solid loading (**Table 6-3**). In fact, the initial pastes formulated with the C-HA had to be repeated, because the pastes were difficult to handle post-extrusion. Water was observed to seep out of the paste, which indicated that a too excess distilled water content was used, and under pressure led to phase separation. On the second attempt with a solid loading of 42 vol%, the extrudates were notably stiffer, and were able to be handled post-extrusion. Despite the higher solid loading, a considerably lower extrusion force was required for extruding calcined pastes, which infers that a better binder coverage of the primary particles was achieved.

Fig. 6-31 illustrates the microstructure observed in green body samples. In the AR-HA paste micrograph (**Fig. 6-31 (a)**), outlines of the agglomerates were clearly observed, thereby confirming the previously postulated notion with regards to binder coating of agglomerates. In the previous chapter, it was reasoned that the high extrusion forces required for the as-received HA extrudates were as a result of particles in a state of direct contact with one another, and thus necessitated particle-particle contact flow. In contrast, examining the green bodies of calcined extrudates demonstrated the lack of agglomeration formation, and consequently complete lubrication of primary particles were attained. Hence, these micrographs confirmed that the AR-HA required an additional treatment to improve the overall processing thereof. From an industrial perspective, reducing the solvent content by simply calcining the powders could reduce the overall running costs.

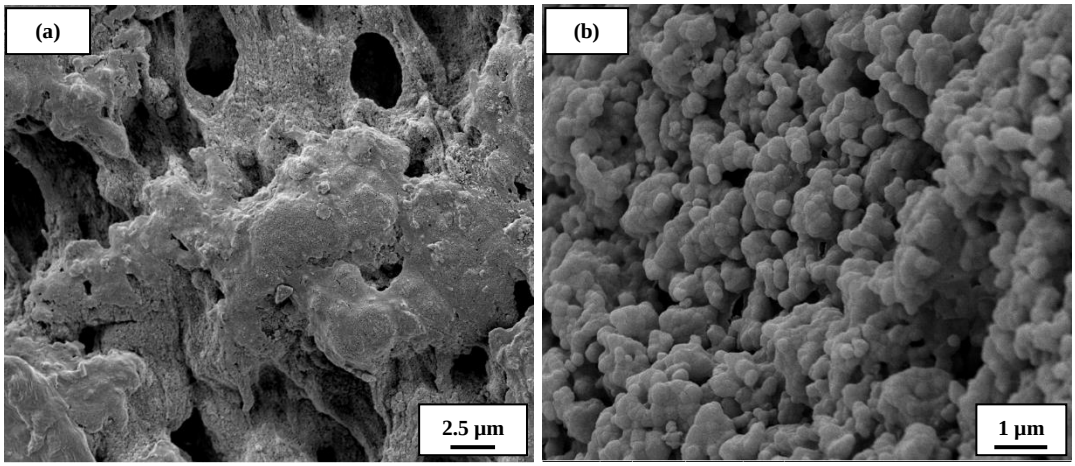

Fig. 6-31. *SEM (SE) micrographs of green extrudates in* ***(a)*** *AR-HA* ***(b)*** *C-HA pastes. Binder coating in AR-HA appeared to coat agglomerates, and not the individual primary particles. The ideal green extrudate should have the binder coating the individual primary particles, and thereby preventing particle-particle contact during extrusion that would result in high extrusion forces.*

6.4.3 The Effects of Calcination on Scaffold Properties

Pre-calcination affected the scaffold's chemical, physical, mechanical and microstructural properties. In addition to achieving remarkable compressive strength values, a greater bulk porosity was attained: both of which would result in scaffolds with improved clinical outcome. The colour change occurred once again, which is attributed to manganese, but paler. Alterations to the microstructure and chemical structure were also observed.

6.4.3.1 Chemical Properties

6.4.3.1.1 XRD

The chemical structure of the calcined scaffolds resulted in scaffolds with higher crystallinity. Comparing the hydroxyapatite peak intensities of the two calcined samples revealed that sintering at 1250 °C resulted in the Y-HA/S exhibiting greater HA peaks than its counterpart, having previously demonstrated relatively lower intensities at 1000 and 1200 °C (**Fig. 6-32**). Furthermore, the HA peaks in Y-HA/S were found to shift to higher angles, with respect to the HA peaks in C-HA/S. This is believed to be caused by yttrium, which has a similar atomic radii to calcium but a lower ionic radii, entering the HA lattice and eliciting the peak shift to the right [165]. In addition, the yttria phase in Y-

HA/S were found to decrease in peak intensity upon sintering, and thus, further corroborating the inclusion of yttrium into the HA lattice. Examining the relative intensity between the largest hydroxyapatite and yttria peaks, at 31.7 and 29.1 ° two-theta, respectively, (**Fig. 6-5** and **Fig. 6-12**) revealed the ration of HA:Y_2O_3 increased from 1.77 to 2.33 to 2.46, at 1000, 1200 and 1250 °C, respectively; which is a total by 39.0%.

Hydroxyapatite's tendency to decompose into other calcium phosphate phases could explain the cause of the decrease in HA intensity at 1250 °C from 1200 °C in the AR-HA/S and C-HA/S. Thus, it can be deduced from the XRD data that the incorporation of Y_2O_3 resulted in a more phase-stable HA at 1250 °C, thereby mitigating its tendency to decompose into other calcium phosphate phases.

6.4.3.1.2 FTIR

FTIR analysis further established the enhanced phase stability of the calcined scaffolds over the AR-HA/S. Only the AR-HA/S exhibited a functional group pertaining to a calcium phosphate other than HA. The re-hydroxylation that occurred during the calcination step provided C-HA/S and Y-HA/S with the incorporation of the hydroxyl group into the apatite structure, which consequently resulted in a more stable, stoichiometric HA; and therewithal with the increased thermal stability as a consequence of calcination, precluded the decomposition into anhydrous products.

The Y-HA/S presented with a relatively lower OH^- group at 3570 and 630 cm^{-1} with respect to C-HA/S. This is in agreement with a previous study, who also calcined HA with 10 wt% yttria [405]. They attributed the change in hydroxyl peak intensities to the charge compensation as a result of Ca^{2+} substitution by Y^{3+}. Indeed, if the inclusion of yttria facilitated de-hydroxylation, then the EDS map would have presented with an oxygen-deficient area at the grain boundaries (**Fig. 6-30**).

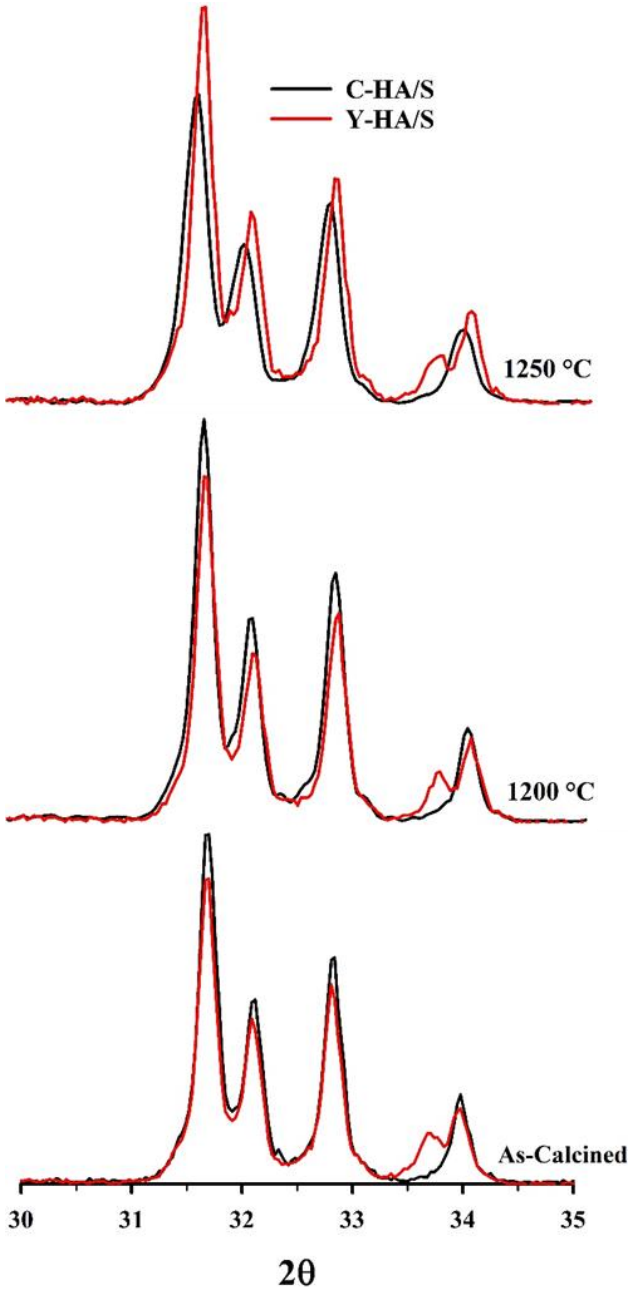

Fig. 6-32. *Superimposed XRD patterns of the calcined and Y-HA scaffolds, ranging from 30 to 35 two-theta. The hydroxyapatite peaks in Y-HA/S shifted to the right with increasing temperature. Additionally, at 1250 °C, the hydroxyapatite peak intensities were greater than that of C-HA/S, which was not observed at 1000 (as-calcined) and 1200 °C.*

6.4.3.2 Physical and Mechanical Properties

As expected from characterising the powders, the calcined scaffolds underwent a lower degree of shrinkage, which resulted in an increase to both cell lengths and strut thickness. The significance of this was that the increase in cell length was attributed to the increase

in bulk porosity, whereas the increase in strut thickness enhanced the compressive strength. An increase in strut thickness equated to a larger area for the load to be applied, however, the increase in compressive strength, particularly at 1250 °C, was disproportionate to the increases observed in strut thicknesses, in comparison to the AR-HA/S struts. Thus, the increase in compressive strength can only be partly ascribed to the increase in strut thickness. Other contributing factors were believed to include the decrease in shrinkage, which is associated with fewer defects; improved thermal stability; and the lack of β-TCP secondary phases, since this phase is inherently weaker than HA.

The effect of yttria on the compressive strength, from comparable values at 1200 °C to significantly different at 1250 °C, can again be partly attributed to the aforementioned reasons, and also to the difference observed at the microstructural level. To the author's best knowledge, this is the first experiment to be conducted on HA scaffolds using yttria as the dopant. Previous studies using other dopants were also successful in attaining calcium phosphate scaffolds with improved mechanical properties, and have ascertained the cause to higher thermal stability [169] and increased densification [425].

6.4.4 Microstructural Properties

6.4.4.1 Secondary Imaging

While composed of markedly larger primary particles, the calcined scaffolds presented with smaller grain sizes at both sintering temperatures: such is the advantage of using raw powders that do not exhibit enhanced sintering.

Both calcined samples progressed slower through the sintering process than the AR-HA/S, particularly at 1200 °C, where the microstructure demonstrated early sintering neck formation, and was more pronounced in the Y-HA/S. At 1250 °C, the temperature difference was sufficient in increasing the thickness of the sintering necks to great effect, thereby transitioning a sintering stage. Equally, the level of micro-porosity significantly decreased. The relationship between porosity and compressive strength is non-linear, and in certain conditions, exponential. In this study, the decrease in micro-porosity was a consequence of the increase in the thickness of sintering necks, which disappeared at 1250 °C due to adjacent grains merging.

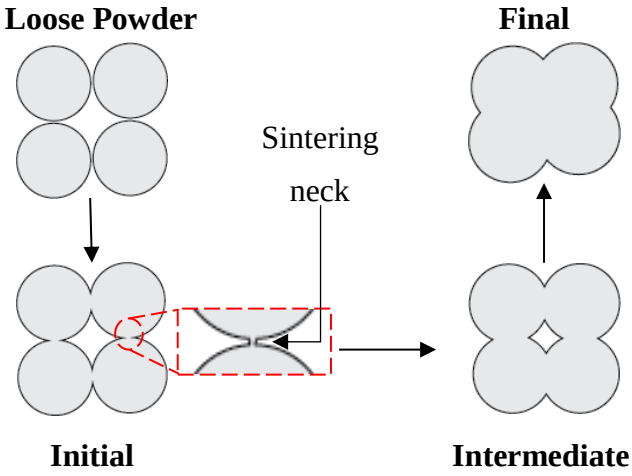

Fig. 6-33. *The stages of sintering. The initial stage of sintering begins with the formation of the sintering necks between adjacent primary particles at their point of contact. The size of the necks continues to grow, closing the voids in between the particles. The final stage is complete densification of the system. It was believed than increasing the sintering temperature from 1200 to 1250 °C resulted in C-HA/S and Y-HA/S transitioning from the initial to the intermediate sintering stage.*

The more coalesced microstructure observed at 1250 °C could also explain the remarkable rise in compressive strength, over a relatively short increase in temperature. Densification in ceramics is a sigmoidal event [227], whereby certain temperature ranges will exhibit greater densification to others comparable in range; and previous studies have demonstrated that hydroxyapatite is no different [342, 426, 427]. As compressive strength is a function of densification, it stands to reason that the mechanical properties also follow a sigmoidal trajectory [428], with other factors being constant. An earlier study examining the effects of sintering on ceramics have also noted significant increases in density when the temperature was increased by 50 °C, and wherein slight density enhancements were descried by the same increment before and after the particular inflexion point [429].

The cause of the delayed sintering in the calcined samples can be attributed to an increase in solid loading and the considerably lower surface area of the calcined powders. In a particulate system, the reduction in surface area reduces the sintering driving force, and thus suppresses densification. Similarly, more particles within the system would require more heat for sintering to occur.

Furthermore, the prevalence of secondary grain structures was significantly reduced in the calcined scaffolds, and seldom descried in the Y-HA/S. The incorporation of yttria may have mitigated the formations of phases (e.g. β-tricalcium phosphate and tetracalcium phospate) with conflicting thermal expansion to hydroxyapatite, thereby strengthening the overall structure. As for the yttria grains in Y-HA/S, they appeared to bond well with the hydroxyapatite grains, and evidence of fractures as a result of their bonding were not observed. On the contrary, the yttria grains near fracture sites were relatively intact, and were referred to as 'yttria bridges', because of their appearance over micro-fissures. The micrographs inferred that the yttria phase provided reinforcement to the HA matrix, and thus contributed towards the significant increase in the compressive strength at 1250 °C, with respect to C-HA/S. Moreover, said features comprised grain sizes in the nano region, thereby requiring greater energy for the cracks to propagate [117, 430, 431].

6.4.4.2 EDS Analysis

EDS maps revealed that the grain boundaries were the cause of the discrepancy in oxygen intensity. This is unsurprising, given that the energy at the boundary is higher than that of the grain body, and hence the primary site for oxygen liberation. De-hydroxylation of the grains prefigure phase transformation, and hence why the nucleation thereof also occurred at the grain boundary.

Furthermore, EDS maps highlighted the presence of yttrium in HA grains (**Fig. 6-30**). The changes elicited by yttrium to the hydroxyapatite's chemical structure observed in XRD and FTIR analyses unequivocally suggest that yttrium was incorporated within the HA lattice, as opposed to bonding superficially to the HA grains. The EDS maps further verified yttrium's stronger bond to oxygen than calcium, as the presence of oxygen-deficient sites were not observed, indicating that the stronger bond between oxygen and yttrium minimised the liberation of the former at the grain boundary. This could also explain the higher hydroxyapatite XRD peak intensities observed in **Fig. 6-12**.

6.5 Comparison to Other Work

The higher porosity and remarkable increase in compressive strength accomplished in the present study widens honeycomb extruded-scaffolds application in bone graft substitution where both aspects may have been a limiting factor in scaffolds fabricated using the as-received powder. As mentioned in the **1.1,** only three studies known to the author have reported hydroxyapatite scaffolds with compressive strengths above 100 MPa. The porosity values obtained herein were in the cancellous bone region but the compressive strengths are akin to cortical bone. Optimising the honeycomb extrusion process could further yield higher strengths. Examples of optimisation include pore geometry, sintering parameters, and the use of additional organic additives to increase the solid loading of HA pastes.

Surveying the literature for ionically substituted hydroxyapatite scaffolds have yielded far more impressive proportionate increases in compressive strength as a result of doping. However, as **Fig. 6-34** portrays, such increase tend to be in compressive strength from below to above 1 MPa, and hence the final compressive values are unimposing. As **Fig. 6-34** illustrates, it is much more difficult to increase the compressive strength when the undoped values are above 100 MPa, for example in dense bodies, and thus, increases of less than 100% are the norm. It will be interesting to see if such increases observed in the weaker structures can be replicated by the process utilised in this study; for example, when doping with zirconia (**Fig. 6-34**). The remarkable increases observed when the calcium in β-TCP scaffolds were ionically substituted with other cations merits a mention [169, 432], as it further demonstrates the utility of ionic substitution for tailoring the properties of other calcium phosphate scaffolds.

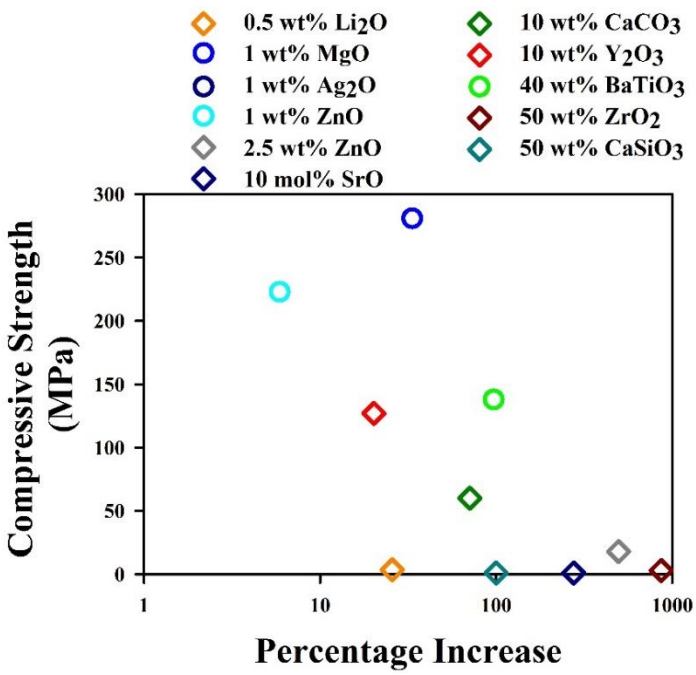

Fig. 6-34. *Select collection of data that have reported the compressive strength of doped HA, presented as a function of percentage increase to their respective undoped HA sample (open diamonds are scaffolds; open circles are dense materials; [260, 385, 425, 432-436]. The red, open diamond is that of Y-HA fabricated in the present study. The graph illustrates a moderate percentage increase in compressive strength was obtained by doping hydroxyapatite with yttria. Furthermore, larger percentage increases were typically seen with materials possessing lower compressive strengths.*

When porosity is taken into account, the Y-HA/S results obtained in this study are impressive, and exceeded other biphasic ceramic composites, in which high-strength ceramics were composited with HA for their crack arresting mechanisms [437], as illustrated in **Fig. 6-35**. The figure also includes examples of dense scaffolds composited with bioactive metals, which additionally demonstrates the impressiveness of the Y-HA/S properties.

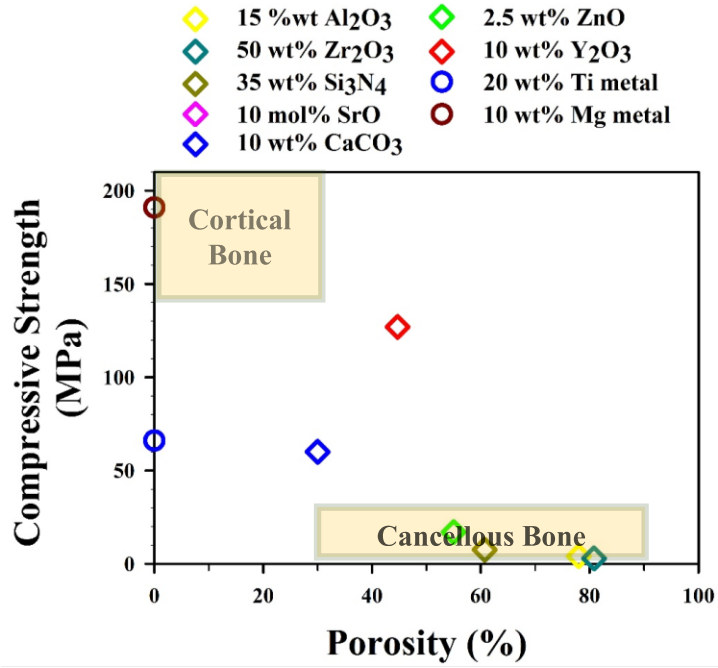

Fig. 6-35. *Compressive strength as a function of porosity of composite HA. The open diamonds denote HA-ceramic composite; open circles denote HA-metal composite [260, 432, 435, 436, 438-441]. The red, open diamond represents the data obtained in the present study. The values of cortical bone [442, 443] and cancellous bone [444-446] are included for comparison. The strength of the Y-HA (red, open diamond) can be seen to possess a unique balance between compressive strength and porosity, in contrast to other researchers' findings.*

6.6 Summary of Chapter

Altering the powder morphology by pre-calcination resulted in a cascade of positive effects within the fabrication process, which culminated in scaffolds with a high compressive strength that soared from 20.4 MPa to 127.3 MPa. In addition, the bulk porosity increased; for example, when scaffolds processed at 1250 °C the increase was from 40 vol% in the AR-HA/S to 45 vol% in the C-HA/S. The main advantages determined by pre-calcination were: (a) attaining a higher solid loading; and (b) an increase in surface area. In concert, the effects reduced the shrinkage characteristic of the scaffolds, thereby mitigating defects associated with shrinkage. The reduced shrinkage also resulted in wider struts that were able to sustain larger compressive loads. In addition, SEM analyses of the scaffolds revealed that pre-calcining the powders resulted in a microstructure with finer grain sizes, a decrease in dehydroxylation and phase decomposition, and an increase in micro-porosity; all of which have been reported to

enhance the compressive strength of ceramics. All of the aforementioned feats may have synergistically enhanced the compressive strength of scaffolds fabricated using the calcined powders.

In addition, the chapter demonstrated the positive affect of doping the raw material with 10 wt% Y_2O_3. The oxide further supressed densification, de-hydroxylation and crack propagation. No significant difference in compressive strength was observed between the undoped and yttria-doped calcined HA at 1200 °C, however a significant difference was observed at 1250 °C.

As stated in the introduction, the ionic substitution and co-substitution, whereby more than one element is incorporated, of hydroxyapatite has been extensively explored. These investigations were not without merit, as human bone is comprised of nonstoichiometric hydroxyapatite with trace elements of carbon, magnesium, sodium, potassium, chlorine and fluorine [447]. Doping of hydroxyapatite is a means of tailoring the physical and biological properties thereof, and, unlike certain facets of honeycomb extrusion, can be translated and utilised in different fabrication techniques. Thus, pursuing such investigations would have a greater research impact in the field of bone graft substitution. The relatively simple compositing procedure work presented in this chapter was necessary insofar as it demonstrated compositing can improve the mechanical properties, and provided a suitable foundation for understanding the effects of compositing HA on the extrusion process. The next objective will be to fabricate a composite with more of the abovementioned ions incorporated.

Chapter 7: Porous Hydroxyapatite-Bioactive Glass Hybrid Scaffolds

Materials from different categories have been assessed as potential scaffolds for synthetic bone grafting. Each material class has its respective advantages and disadvantages. Recent advances in the composite field have demonstrated that distinct materials can be combined to address the other's shortcomings, but also may produce a new material with characteristics different from the parent materials. To advance the work from the previous chapter, where several ions prevalent in bone are to be incorporated in the HA scaffolds, and thereby achieving greater compositional mimicry; as well as keeping in-line with the project's objectives of finding approaches to improving the mechanical properties of extruded HA scaffolds, this chapter details the research conducted into HA-bioactive glass composites. HA composited with bioactive glass has been explored for over two decades, however, this is the first study to utilise this approach with a fabrication technique that forms aligned porous architecture. Furthermore, this is the first study to demonstrate the use of ceramic extrusion for fabricating ceramic-glass composites.

7.1 Introduction

In the previous chapter, it was demonstrated how pre-processing of the hydroxyapatite (HA) powder can be applied to augment the mechanical properties of scaffolds in a simple manner yet yields effective results. However, concentrating on the mechanical properties would be to focus on one of the triad of qualities that are required for a bone graft; the other two being porosity and biological properties (**Fig. 7-1**). Hydroxyapatite, albeit possessing relatively high mechanical properties for a calcium phosphate (CaP), is considered to bear poor bioresorbability, which is the chief criticism for its use as a bone graft. Oonishi et al. (2000) investigated the *in vivo* bioresorbability of synthetic HA particles and discovered that the material failed to resorb within the twenty-four week assessment [448]. The same study investigated Bioglass® powders, a bioactive glass, and demonstrated its enhanced bone formation and resorpability over HA.

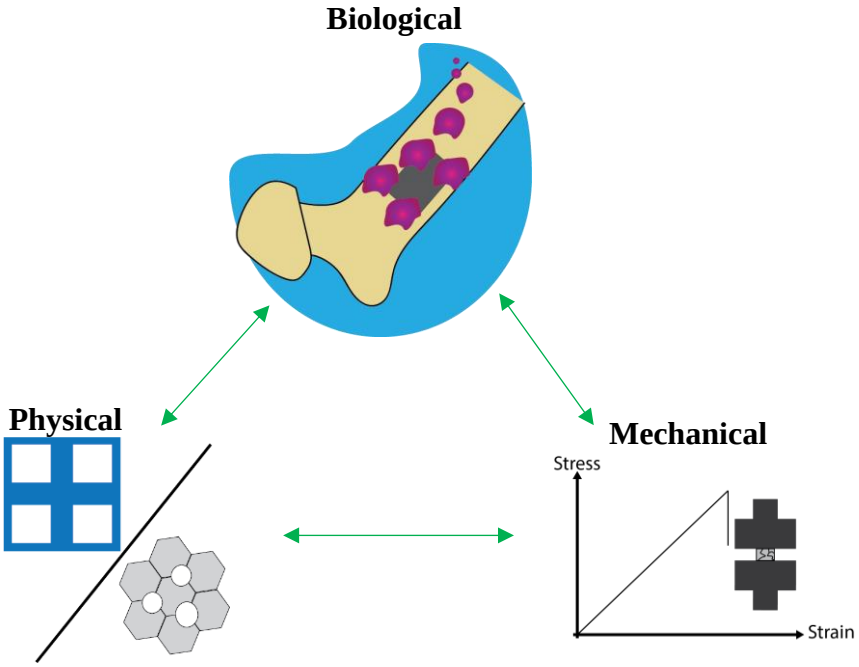

Fig. 7-1. *The triad of properties that govern the efficacy of a scaffold. When fabricating a bone scaffold, one has to consider the biological, physical (e.g. porosity) and mechanical properties (e.g. compressive strength) thereof.*

The bioactive silicate glass, 45S5 Bioglass® was the first man-made biomaterial discovered to bond to living bone and tissues [449-451]. Bioglass® (BG) comprises 45 wt% silica, 24.5 wt% calcium oxide, 24.5 wt% sodium oxide and 6 wt% phosphate, wherein the latter three oxides naturally occur in bone. Silica is one of few oxides required to form a glass, and its cytotoxicity is inconclusive. However, the oxide is known to facilitate bone bonding by forming a Si-rich layer at the interface. BG forms a strong bond with bones when exposed to physiological body fluids. The biomaterial has been proven to induce vascularisation *in vivo*, increase osteogenic and angiogenic gene expression *in vitro*, and promote mineralisation. Moreover, BG degrades in physiological milieu, and the ionic dissolution products may enhance new bone formation through a direct control over genes that regulate cell induction and proliferation. Furthermore, Bioglass® induces the formation of a hydroxycarbonate apatite (HCA) layer that bonds the biomaterial to the surface of bone. Thus, for bioactivity, Bioglass® is preferred over HA. A drawback of Bioglass® is its lack of structural viability, and is used mainly in the form of powders pressed into bone defects, as surgical putty or as coatings for metal

implants [451, 452]. Thus, as one addresses the other's shortcomings, a HA and BG composite has been regarded as a promising material for bone graft substitute.

Research into HA reinforced with BG has been conducted for over two decades. Research has demonstrated that the addition of ≤ 5 wt% of BG® [453, 454], as well as other bioactive glass [455], can improve the biological properties of HA. Equally, increases in mechanical properties were also reported when BG was added, and for other bioresorbable ceramics as well [220, 290, 456]. At typical HA sintering temperatures, the glasses melt, and through capillary forces and particle rearrangement, enhances the densification of HA [455-458]. This type of sintering is commonly referred to as liquid phase sintering, whereby the liquid phase occupies the voids in between the ceramic particles, and binds them together. The simultaneous improvements to both mechanical and biological properties were the primary reasons for compositing bioactive glass with HA: to address HA's drawbacks. Other justifications for the ceramic-glass approach include:

- Glass itself can be tailored with respect to composition, which can further expand the hybrid system's versatility to meet specific demands;
- Unlike bioactive polymers, glasses are thermally treated at temperatures comparable to ceramics;
- The liquid phase sintering aspect of glasses may accommodate the inclusion of metals that cannot bind directly to ceramics by conventional sintering;
- And, since ceramic-glass composites have not been explored via honeycomb extrusion, the technology can be translated to other fields and open new opportunities, such as solid oxide fuel cells.

In general, glasses containing CaO-P_2O_5-Na_2O have been considered as having an enormous potential because of their analogous elemental composition to the inorganic component of bone [459]. Another bioactive glass with great potential is canasite. When transformed into a glass-ceramic, canasite demonstrates exceptional mechanical properties in comparison to BG. Furthermore, canasite contains additional beneficial compounds that have elements prevalent in bone [454] but not found in BG, which are

calcium fluoride (CaF_2) and potassium oxide (K_2O)[8]. The former has been demonstrated to form a fluorapatite layer *in vivo*, which is more chemically stable than a HCA layer; and the latter reduces the glass's tendency to crystallise [460]. Hence, the aforementioned benefits make canasite an attractive candidate for compositing with HA.

In this study, the results of hydroxyapatite scaffolds reinforced with three different bioactive glasses are reported. The glasses investigated were stoichiometric Bioglass® (BG1), canasite (CAN) and a calcium-excess Bioglass® (BG2). The principle aim was to fabricate a hybrid scaffold that combines the advantages of HA with said bioactive glasses. The glasses were added as 10 wt% of the overall HA-bioactive glass admixture, which in the previous chapter was demonstrated as a sufficient proportion in obtaining a biphasic material. The chapter will first detail the synthesis, and the grinding of the glass into a fine powder suitable for extrusion. Subsequently, the melting point and crystallisation behaviour were identified before finalising the heating profile; the former being pertinent in identifying temperatures that conduce a liquid phase of the glass. Once confirmed, the fabrication of a HA reinforced with 10 wt% glass proceeded, and thereafter the obtained scaffolds were characterised in the same manner as in earlier chapters.

7.2 Experimental Procedure

7.2.1 Materials

7.2.1.1 Hydroxyapatite

The commercial hydroxyapatite powder was again used, and prior to mixing with the bioactive glass powder, was calcined as detailed in section **6.2**.

7.2.1.2 Bioactive Glass

The bioactive glass powder was synthesised *in-house* using the melt-derived route. The source materials used were Sand (SiO_2), Limestone ($CaCO_3$), Soda Ash (Na_2CO_3)

[8] This is an added benefit of using canasite over other glasses, namely glasses containing ions that are not naturally found in the body (e.g. titanium oxide) or that are detrimental to bone (e.g. lithium oxide in lithium-substituted bioactive glasses).

(Glassworks Services, UK) and ammonium dihydrogen phosphate (ADP) (Acros Organics, UK). For the preparation of canasite, Pot Ash (K_2CO_3) (Glassworks Services, UK) and analytical grade calcium fluoride (Fisher Scientific, UK) were used. **Table 7-1** enumerates the oxide composition of all three bioactive glasses. Once the composition was determined, the source materials were left to dry overnight in a furnace at 180 °C, except for the ADP which had a melting temperature of 190 °C and was dried overnight at 120 °C. The source materials were then weighed and mixed thoroughly until large agglomerates were removed and a homogenous powder colour was obtained. The mixture procedure comprised a high-shear energy mixer and manual mixing using an industrial palette knife. Once mixed, the batch powder was poured into a plastic bag and sealed until melting.

Table 7-1. *Theoretical glass composition of the bioactive glass used in this study.*

Glass component	CAN, mass%	BG1, mass%	BG2, mass%
SiO_2	58.4	45	45
P_2O_5	4.6	6	6
Na_2O	3.7	24.5	19.5
CaO	15.5	24.5	29.5
K_2O	7.6	N/A	N/A
CaF_2	10.2	N/A	N/A

Melting was performed in mullite crucibles[9], which prior to the day of melting where placed in a furnace that was gradually heated to 1100 °C at a rate of 1 °C/min in order to prevent thermal shocking of the crucible. Once left to dwell for 1.5 hours after reaching said temperature, the mullite crucible was then transferred using steel tongs to a furnace which was already pre-heated to the melting temperature of 1450 °C, and left to thermally equilibrate for 15 minutes. Once equilibrated, the crucible was removed from the furnace and the source materials were poured using an alumina scoop. The addition

[9] fabricated *in-house* via slip casting; three-part alumina, two-part silica.

of the source materials was performed in three tranches to avoid overflowing the crucible. The powder was melted for 4 hours before casted as a frit in a bucket filled with distilled water. A basket was placed inside of the bucket to collect the frit. The frit, illustrated in **Fig. 7-2**, was then crushed and ground into fine glass powder. The grinding procedure is detailed in the results section.

Fig. 7-2. *Image representative of glass frit. The image was of the BG2 sample, taken a few minutes after quenching in distilled water. This was then needed to be comminuted into particle sizes that can be processed prior to formulating an extrudable paste.*

7.2.2 Paste Preparation

Paste preparation was a similar protocol to that used previously, except the inorganic components of the paste (i.e. glass and HA powders) were mixed before the addition of the binder. The mixing of the inorganic components was performed at 800 rpm, for five minutes. The final paste composition is summarised in **Table 7-2**.

Table 7-2. *Paste composition for all hybrid pastes.*

Component	mass (g)	Mass (%)
HA	217	60.4
Bioactive Glass	24	6.7
Methocel®	18	5.0
Distilled Water	100	27.9

7.2.3 Extrusion

Extrusion was performed using the parameters detailed in section **4.2**.

7.2.4 Heat Treatment

Drying was performed at ambient conditions for at least twenty-four hours. The de-binding protocol was as follows:

- Ramp to 200 °C at a rate of 1 °C/min, and dwell for one hour
- Ramp to 300 °C at a rate of 1 °C/min, and dwell for one hour
- Ramp to 400 °C at a rate of 1 °C/min, and dwell for three hours
- Cooled to ambient temperature at a rate of 2 °C/min.

Following de-binding, the HA-bioactive extrudates were subjected to the following sintering protocol:

- Heat to 600 °C at a rate of 5 °C/min
- Heat to 800 °C at a rate of 2 °C/min, and dwell for 1 hours
- Heat to 1200 °C, at a rate of 5 °C/min, and dwell for 8 hours
- Cool down to ambient temperature at a rate of 2.5 °C/min.

Once sintered, the extrudates were sectioned until a 3 x 3 cell cubic scaffold was attained. Characterisation of the scaffolds ensued.

7.3 Results

Porous HA-bioactive glass hybrid scaffolds were successfully fashioned, with 10 wt% Bioglass®, canasite, and a calcium-rich Bioglass®, using ceramic honeycomb extrusion. Bioactive glasses were synthesised using the melt-derived approach, which yielded large quantities of glass, however, comminution thereof was required to provide particle sizes suitable for extrusion. Thus, before the glass can be mixed with HA and formulated into an extrudable paste, the glass frits were crushed and ground into particles sizes suitable for extrusion.

7.3.1 Comminution and Powder Properties

Comminution is the technical term for reducing a material to fine powders [461]. The target was to achieve particle sizes of less than a nominal value of 100 µm, and with limited comminution in order to prevent contamination by the milling process. The effects of glass particle size were not of interest to the current study, nonetheless, the narrowest gap found in the die is 560 µm, and thus obtaining particles sizes below 100 µm will preclude clogging of the die during extrusion. All glass frits were crushed using an *in-house* percussion mortar, and subsequently ground using a planetary mill (Pulveriser 6, Fritsch, Germany). Preliminary particle size analysis presented with varying results. As **Fig. 7-3** and **Fig. 7-4** illustrate, planetary milling was successful in attaining CAN particle sizes of less than a 100 µm, with the majority of particles exhibiting sizes of less than 50 µm. In contrast, BG particle sizes greater than 100 µm were observed. Subjecting the glass to further bouts on the planetary mill had no effect on the particle size.

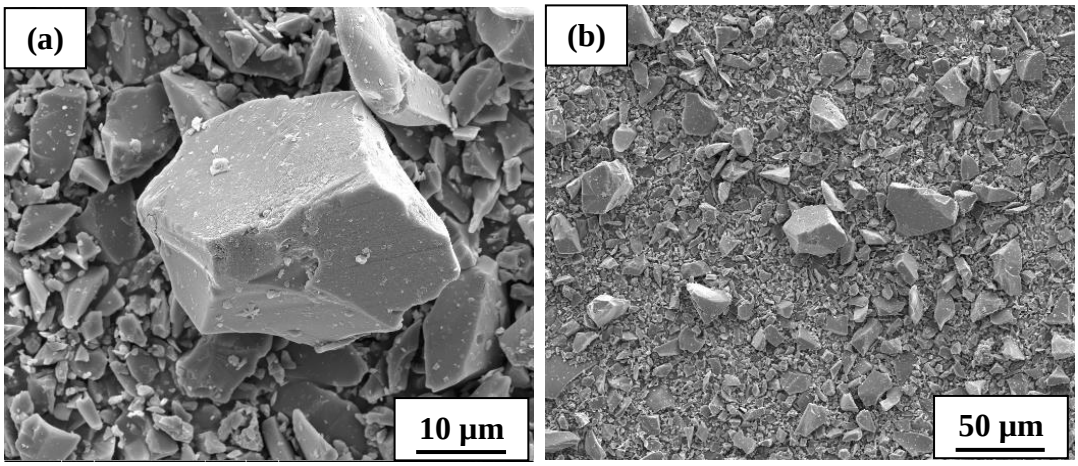

Fig. 7-3. *SEM (SE) micrographs of the as-sieved canasite powder taken at magnifications of* ***(a)*** *x5,000 and* ***(b)*** *x1,000. The micrographs revealed the effectiveness of planetary milling in reducing the particle size to below 100 µm.*

In order to reduce the particle sizes of the BG samples, attrition milling was utilised (Lab Attritor, Union Process, U.S.A). The milling media were in the micron range, in contrast to that of the planetary mill which had milling media with diameters in the millimetre

range[10]. Initially, the samples were subjected to 45 minutes, and subsequently analysed using a particle size analyser. The analysis revealed that attrition milling was successful in attaining BG1 powders with particle sizes of less than 100 µm.

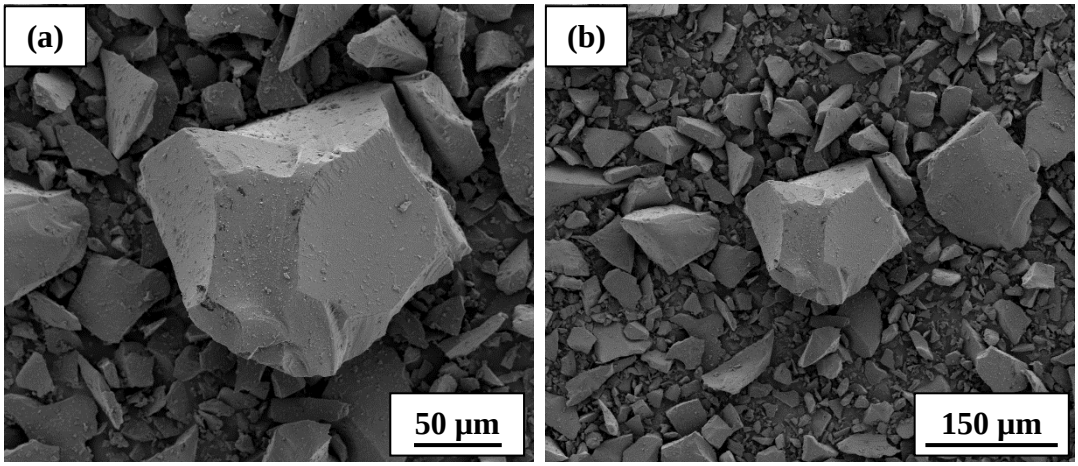

Fig. 7-4. *SEM (SE) micrographs typifying the as-sieved BG powder taken at magnifications of* ***(a)*** *x1,000 and* ***(b)*** *x500. After the initial planetary milling, the particles were still larger than the targeted 100 µm.*

The BG2 powder required a further 60 minutes on the attrition mill to achieve the targeted particle size; as **Fig. 7-5 (a)** illustrates, attrition milling the BG2 powder for 105 minutes reduced the mode particle size from 101 to 15 µm. The final comminution step was to sieve the powders through a 53 µm mesh sieve. The final particle size distribution is presented in **Fig. 7-5 (b).** It was discovered that particle sizes above 53 µm were detected for all the samples. It is plausible that the analyser detected agglomerates. It is equally plausible that particles exhibiting a high aspect ratio (**Fig. 7-3** & **Fig. 7-4**) passed through the sieve at facets smaller than the mesh size.

Table 7-3 lists the d_{50} particle sizes, density and surface area of all three glass powders. BG2 possessed, statistically significant, a lower d_{50} and powder density, but a higher surface area, than BG1. The canasite powder exhibited the smallest powder density

[10] At a certain point in comminution, smaller milling media sizes are needed. This is because particles can be trapped in voids in-between the milling media, and thus the particles will be inefficiently ground.

and surface area, but the largest d_{50}, which again was determined to be statistically different.

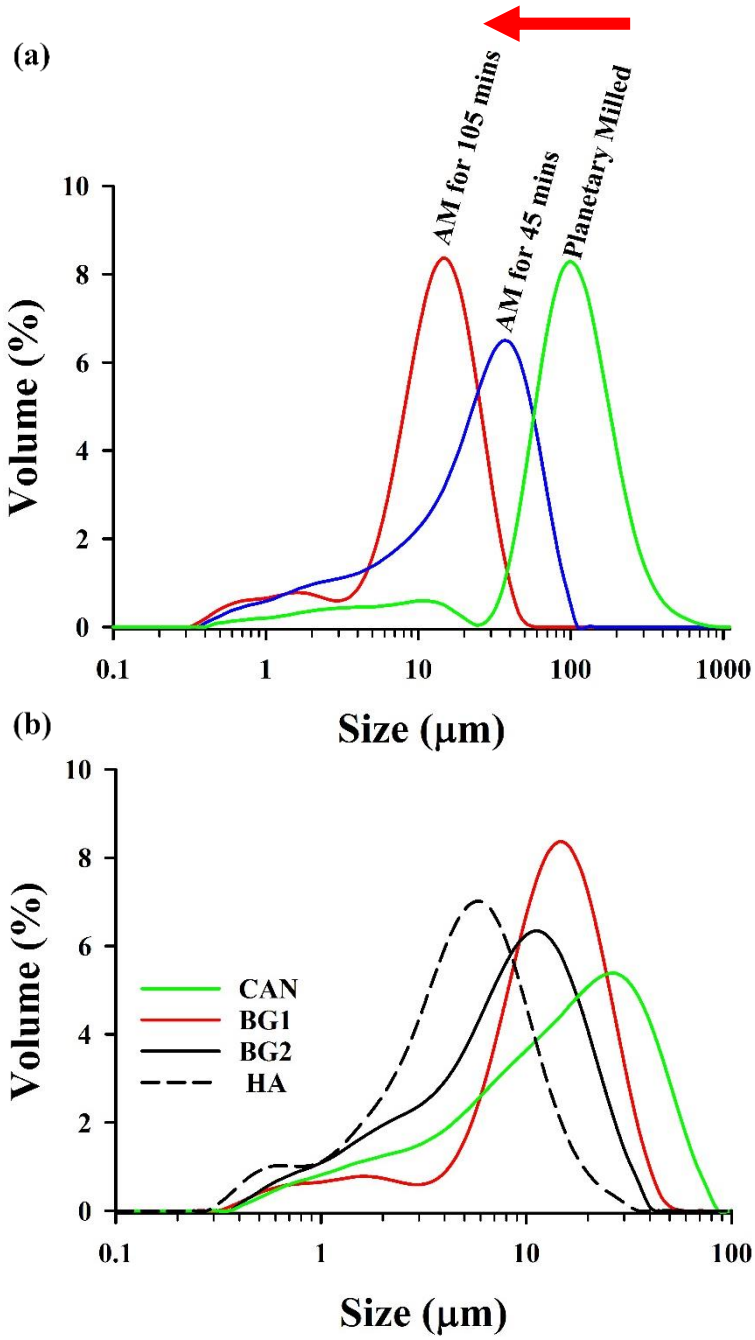

Fig. 7-5. *Particle size distribution of the glass powders.* ***(a)*** *illustrates the results of the BG2 powder after planetary milling, and both stages of attrition milling (AM), whereas* ***(b)*** *is the final particle size distribution of the different powders. The melt-derived approach of synthesising glass produced large particle sizes. The data demonstrates the effectiveness of the comminution protocol employed in reducing the particle sizes to below 100 μm, and thereby ensuring the prevention of particle-clogging of the die during extrusion.*

Table 7-3. *The physical properties of the glass powders used for the fabrication of hybrid scaffolds. The table presents the particle size (n = 5), powder density (n = 3) and BET surface area (n = 3) of the raw glass powders following comminution.*

Sample	D_{50} (µm)[a]	Powder density[a] (g/cm^3)	BET Surface[a] area (m^2/g)
BG1	13.56 ± 0.30	2.75 ± 0.1	3.10 ± 1.1
BG2	8.83 ± 0.19	2.73 ± 0.1	3.57 ± 1.5
CAN	15.9 ± 0.22	2.63 ± 0.2	2.25 ± 1.0

[a] a one-way ANOVA revealed the difference to be statistically insignificant between all powdered samples ($P < 0.05$).

7.3.1.1 Chemical Properties of Bioactive Glass Powder

Once the desired particle sizes were obtained, X-ray Fluorescence (XRF) was performed to inspect the starting raw powder for signs of possible contamination. Agate (SiO_2) pots and milling media were purposefully selected to avoid contamination during planetary milling, however, this option of using milling materials with compounds already found in the raw glass was not available for attrition milling. The milling media used for attrition milling was yttria-stabilised zirconia, and as **Table 7-4** demonstrates, neither yttrium nor zirconium was detected. However, both post-planetary and post-attrition milling XRF analyses detected the existence of aluminium in the powder, which is likely to have originated from the dissolution of the mullite crucible during glass melting, if not already present in the source chemicals. Thus, the comminution strategies utilised did not result in unwanted elemental contamination.

X-ray diffraction (XRD) was performed on the raw glass powders to determine their chemical structure. If properly synthesised, the glass powders should be amorphous. **Fig. 7-6** illustrates the XRD pattern of the glass samples after the comminution steps. All glass samples displayed a broad hump at a low two-theta angle. The pattern demonstrates that all bioactive glasses were completely amorphous with no diffraction peaks. This indicated that no crystallite was precipitated during the melting and quenching process, nor significant contamination had occurred that could initiate crystallisation.

Table 7-4. *XRF elemental analysis of the BG2 before and after attrition milling.*

Element concentration	Post-Planetary Milling (mass%)	Post-Attrition Milling (mass%)
Ca	65.4	68.1
Si	23.0	21.2
P	4.4	4.0
Na	4.3	3.7
Al	2.2	2.0

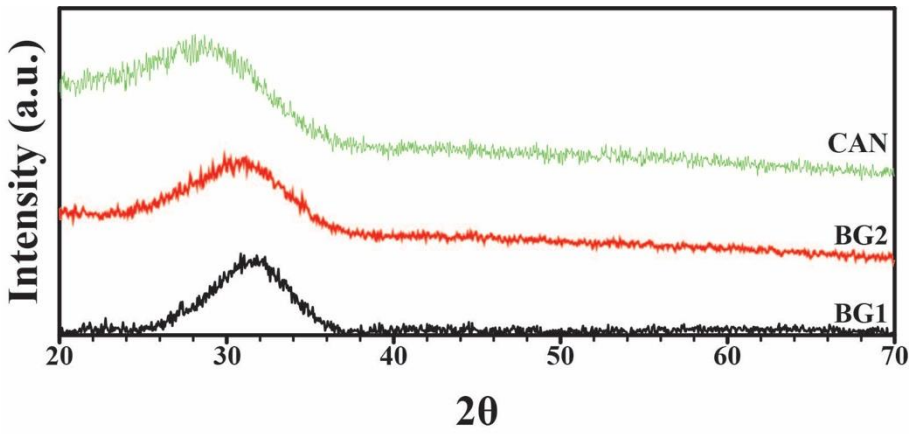

Fig. 7-6. *XRD pattern of the as-milled glass samples. The data confirms the amorphousness of all glass powders.*

FTIR analysis was also performed on the glass powders, and the results are illustrated in **Fig. 7-7**. The BG samples displayed similar spectra, with silica peaks detected at 1035, 930, 745, 502 cm^{-1}; and a phosphate peak at 605 cm^{-1}. The BG spectra concurs with ref. [462-465] Silica peaks in the canasite were detected at 1040, 777 and 470 cm^{-1}, and a phosphate band between 606-575 cm^{-1}. The canasite spectrum concurs with previous work [466]. Both XRD and FTIR demonstrated the successful synthesis of the desired glass powders, and corroborated with the XRF data that the powders exhibited no significant contamination as a result of comminution.

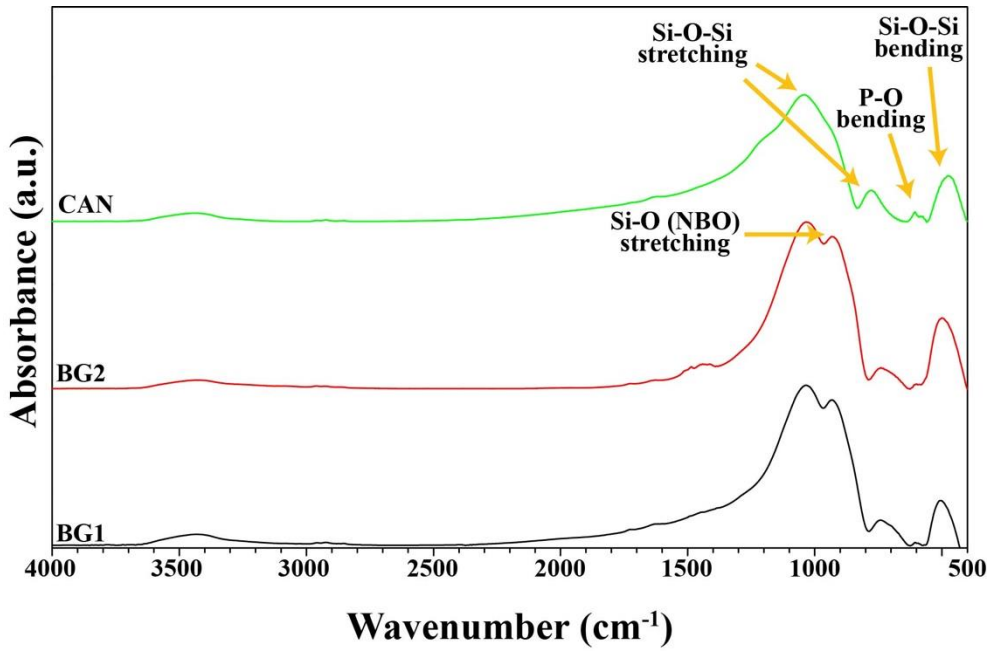

Fig. 7-7. *FTIR spectra of BG1, BG2 and CAN. The data confirmed the raw glass were amorphous.*

7.3.1.2 Evolution of Crystallisation with Increasing Temperature

Fig. 7-8 are XRD patterns illustrating the evolution of glass crystallisation at temperatures ranging from 600 to 900 °C for BG1 and BG2, and 700 to 1100 °C for CAN. These experiments were performed to determine whether the respective glasses would crystallise into their expected glass-ceramics, and if the synthesises stage affected their crystallisation kinetics.

The BG1 sample remained amorphous at 600 °C, and traces of crystallisation at 33.5 and 48.5° were first detected at 650 °C. The peaks pertained to a sodium calcium silicate phase ($Na_2Ca_2Si_3O_9$), which became more prominent at 700 °C. Additional peaks were observed at 800 °C at 32 and 47^o (denoted by the letter P), which were identified as belonging to silicorhenanite ($Na_2Ca_4(PO_4)_2SiO_4$). The BG2 sample displayed the same crystallisation phases, except crystallisation had occurred at a later temperature (**Fig. 7-8 (b)**)[11]. At 1000 °C, both BG samples reacted with the mullite crucibles, hence the data for BG was limited to 900 °C. The crystalline phases detected were in agreement with that

[11] Although the data is not included, XRD analysis was initially performed on BG2 powder heated at 650 and 655 °C, wherein no crystallisation was not observed.

of others [465, 467-469]. Thus, the substitution of 5 wt% CaO for 5 wt% Na_2O did not result in changes to the crystalline phases of Bioglass®.

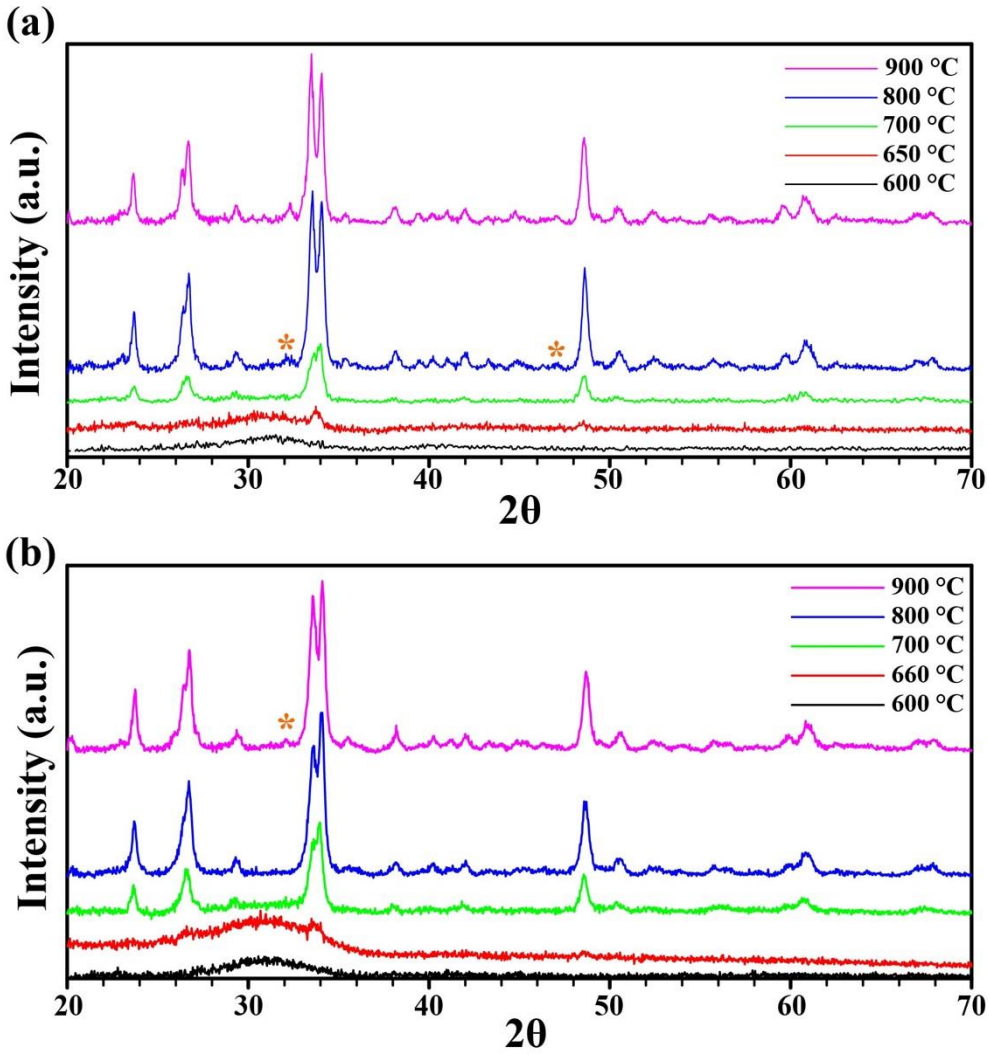

Fig. 7-8. *XRD pattern of* ***(a)*** *BG1 and* ***(b)*** *BG2 when heated at different temperatures. The figure demonstrates that BG2, with a higher calcium content, did not alter the crystallisation phases of Bioglass®; however, the phosphate phase (indicated by the orange asterisks) required higher temperatures for crystallisation thereof.*

The crystallisation of canasite is portrayed in **Fig. 7-9**. Crystallisation of the powder was first detected at 700 °C, which became more prominent by 800 °C. These peaks pertained to canasite. At 900 °C frankamenite peaks were detected, which decreased in intensity when the powder was heated to 1000 °C. At 1100 °C, canasite peaks decreased, and the frankamenite peaks vanished. However, new peaks had emerged, and were assigned to xonotlite, and one to fluorapatite [470].

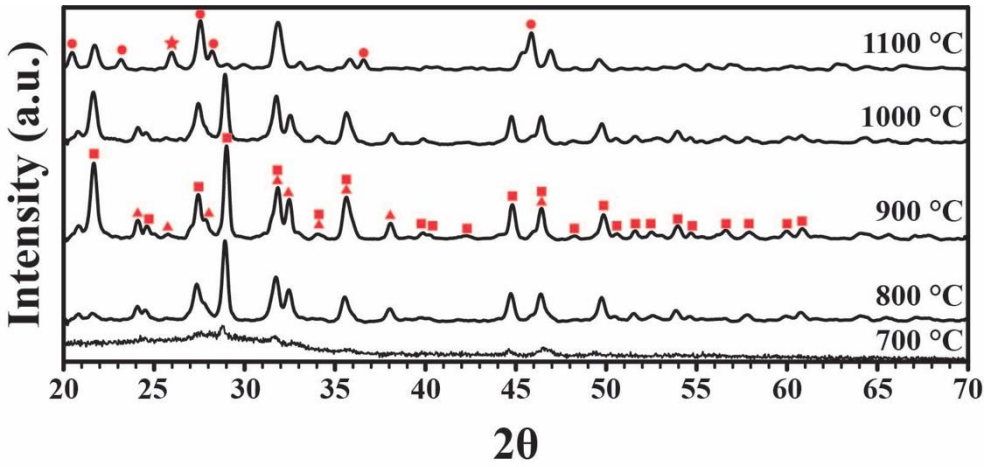

***Fig. 7-9**. XRD pattern of the canasite powder when heated at different temperatures. The figure illustrates the evolution of canasite into typical glass-ceramic phases thereof (square – canasite; triangle – frankamenite; circle – xonotlite; star – fluoroapatite)*

7.3.1.3 Thermal Properties of the Raw Glass Powders

7.3.1.3.1 Heating

The thermal behaviour of the bioactive glass powder is central to defining a sintering profile for the hybrid extrudates. In addition, the XRD data in **Fig. 7-8** revealed that BG2 was more thermally stable than stoichiometric BG, and hence thermal analysis was needed to clarify whether the glass would melt at the appropriate temperatures. A simultaneous thermal analyser (STA) was employed to elucidate the thermal characteristics of the starting raw material. **Fig. 7-10** delineates the DSC and TGA results, as red and green curves, respectively. The analysis was primarily performed to determine the melting temperature of the glasses, and hence suitable temperatures for achieving liquid phase sintering. Endothermic troughs indicative of melting for CAN, BG1 and BG2 were observed at 1220, 1170 and 1195 °C, respectively. Therefore, and in keeping with the previous work, it was decided that the sintering temperatures for both BG samples were to be 1200, 1250 and 1300 °C. Since CAN melted after 1200 °C, it was determined that HA-CAN hybrids were to be sintered at 1250 and 1300 °C. All of the melting points were accompanied by a sharp and transient mass loss, which was equally followed by a sharp rise in mass; hence the glass samples gained mass after melting in the STA. The overall mass loss was less than 1.2% for both BG powders, and less than 2.5% for the

canasite powder. According to Jiang et al. (2017), this level of mass loss ensures stable glass components during liquid-phase sintering [471].

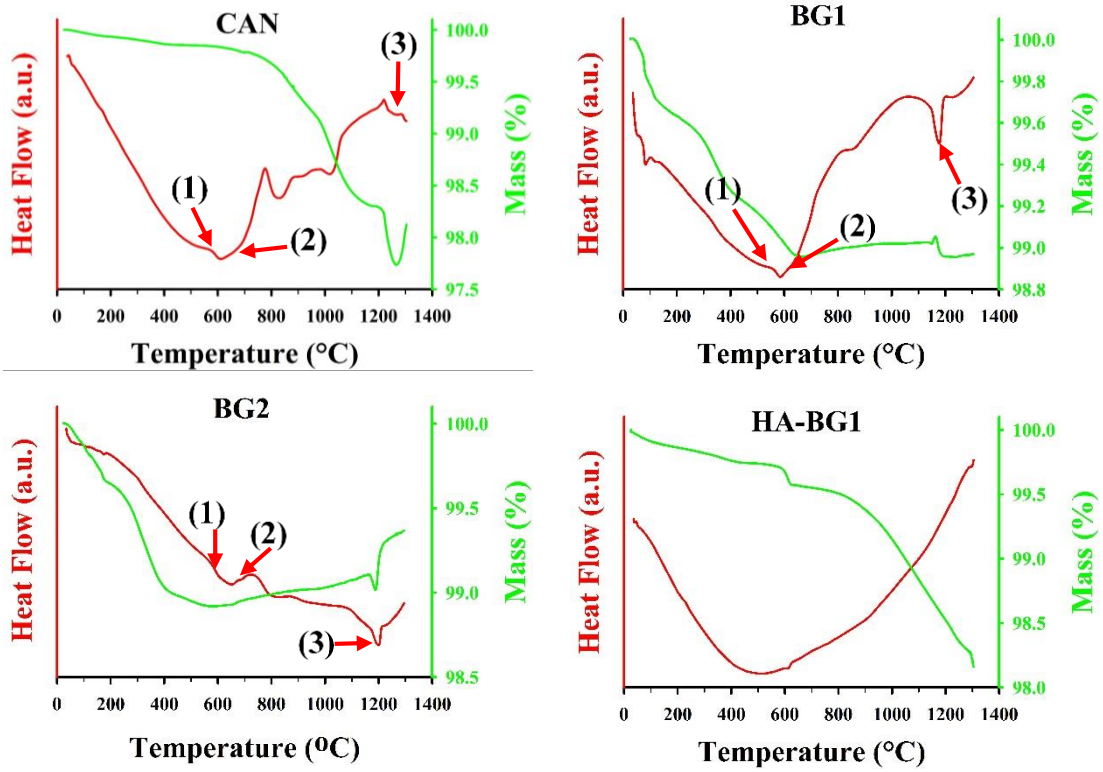

***Fig. 7-10**. Thermographs depicting the DSC (red) and TGA (green) curves of CAN, BG1, BG2 and a hybrid HA- 10wt% BG1 powder. The numbers in parenthesis are used to demarcate the first T_g (1) and T_c (2), as well as the T_m (3) (endothermic down). It was revealed that BG2 possessed higher T_g, T_c and T_m compared to BG1. Furthermore, TGA data revealed that all samples exhibited a mass loss of less than 2.5%.*

The glass transition temperatures (T_g) and crystallisation temperature (T_c) were also revealed by the STA. In addition to exhibiting a higher melting point, the BG2 powder presented with higher T_g and T_c temperatures, with respect to the BG1 powder, further highlighting the higher thermal stability of the former. All temperature characteristics are tabulated in **Table 7-5**. The thermal characteristics determined for BG [472-474] and CAN [475-477] are in agreement with others.

Table 7-5. *The different temperature points (°C) of the glass samples. T_{g1} and T_{g2} are the glass transition temperatures, T_c and T_m are the crystallisation and melting temperatures of the glasses, respectively (n = 1).*

Sample	T_{g1}	T_{g2}	T_c	T_m
BG1	54	787	618	1158
BG2	570	752	646	1183
CAN	570	775	667	1230

STA analysis was also performed on HA mixed with 10 wt% BG1 (**Fig. 7-10 (d)**). As the curves illustrate, an endothermic trough was observed at 615 °C. The T_g, T_c and T_m temperatures of the glass were not observed to the same extent as that of the STA of pure raw glass powder. A bimodal mass loss was observed, with the overall loss of < 2%.

7.3.1.3.2 Cooling

The DSC and TGA data for the BG1, CAN and HA-BG1 powder during cooling are presented in **Fig. 7-11**. Upon cooling, BG1 displayed two exothermic peaks at approximately 815 °C and then approximately 615 °C (**Fig. 7-11 (b)**), which were not detected in the hybrid powder; however, a minute increase in mass of 1.36% was observed in the latter (**Fig. 7-11 (c)**). The canasite results were unremarkable (**Fig. 7-11 (a)**). The results infer that BG may crystallise during cooling but not in the presence of hydroxyapatite. The crystallisation events were not evinced in CAN, which could be due to the potassium oxide reducing the tendency of glass to crystallise, as mentioned in the introduction (**7.1**).

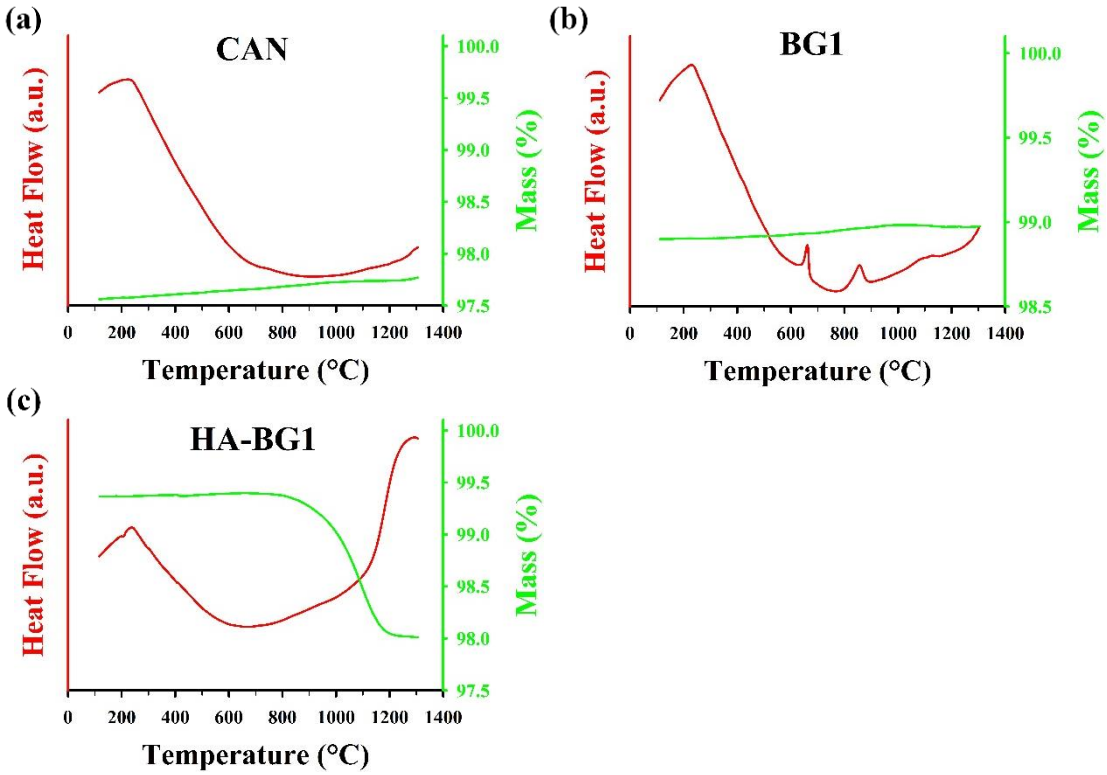

Fig. 7-11. *Cooling DSC (red) and TGA (green) curves of* ***(a)*** *CAN,* ***(b)*** *BG1 and* ***(c)*** *HA-BG1 (endothermic down). The results are used to illustrate that only Bioglass® powders crystallised upon cooling, however, this was not observed in the presence of HA* ***(c)****.*

7.3.2 Paste Properties

Fig. 7-12 portrays representative extrusion curves of the BG1 and CAN pastes formulated. A representative HA plot is included for comparison. The extrusion forces required for paste flow via the die were comparable to that of HA-only pastes. However, it was discovered that in the hybrid samples a relatively smaller pressure drop was observed, followed by a plateau until the end of the extrusion run, relative to the pure HA pastes. Data for BG2 pastes could not be included[12], however, the extrusion force was 19.68 ± 3.56 kN; a one-way ANOVA revealed this to be statistically indifferent to BG1 and CAN pastes, which were determined as 24.67 ± 2.87 and 20.5 ± 0.92 kN, respectively.

[12] Data was lost.

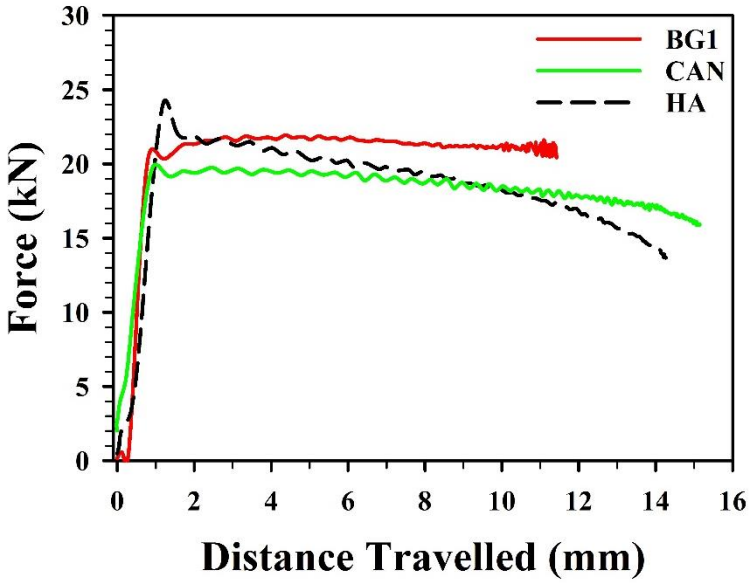

Fig. 7-12. *Representative extrusion plots of BG1, CAN and HA. The addition of glass particles resulted in a stable plateau following the pressure drop. This was in contrast to glass-free hydroxyapatite paste that presented with a decrease in force following the pressure drop. Furthermore, glass-containing pastes possessed a smaller pressure drop. A one-way ANOVA test revealed the peak extrusion force to be statistically invariable.*

7.3.3 Scaffold Properties

HA scaffolds with 10 wt% glass were successfully extruded, and sintered at different temperatures. The first notable difference between the HA-bioactive glass and HA-only scaffolds was the colour of the scaffold. Previously, extrudates presented with a blue colour, whereas the hybrid extrudates were white (**Error! Reference source not found.**). **Fig. 7-13** are various images representative of the fashioned BG2 scaffolds. For this study, the scaffolds were sintered at 1200, 1250 and 1300 °C. However, canasite samples sintered at 1250 °C cracked when removed from the furnace and handled; hence, only the complete data of the HA-CAN samples sintered at 1300 °C are presented.

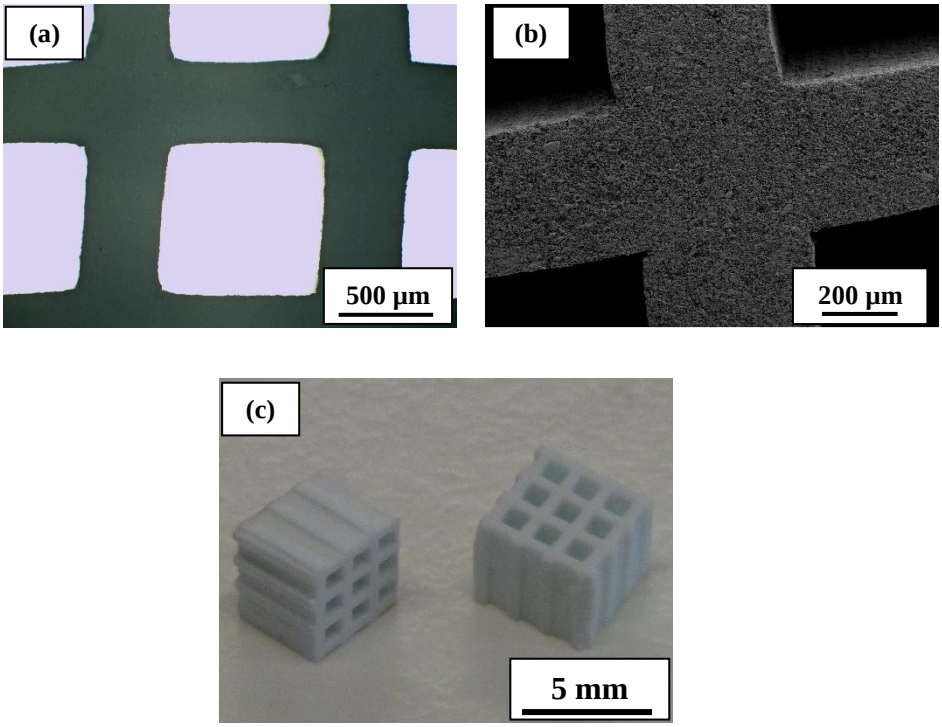

Fig. 7-13. *Images of BG2 scaffolds, taken using* ***(a)*** *an optical microscope,* ***(b)*** *SEM and* ***(c)*** *a digital camera. The images demonstrate the cell morphology.*

7.3.3.1 Chemical Structure of the Sintered Scaffolds.

Chemical analyses were performed on crushed scaffold specimens to determine their chemical structure. **Fig. 7-14** portrays XRD patterns of the BG samples sintered at 1200, 1250 and 1300 °C. The scaffolds were revealed to comprise hydroxyapatite, β-TCP (β-TCP), and calcium silicate ($CaSiO_3$) phases, as denoted in **Fig. 7-14**. The peak at 23.9 °, which appeared to increase in intensity with increasing temperature, could not be identified.

In the BG1 sample, the dominant peaks pertained to β-TCP, and continued to remain dominant until 1300 °C, albeit decreasing in intensity. This decrease was mirrored by increases to HA and $CaSiO_3$ peaks. At 1300 °C the large peaks pertaining to β-TCP and HA at 31 and 31.7°, respectively, were almost comparable in intensity. The ratio of β-TCP to HA at said two-theta decreased from 1.33 at 1200 °C to 1.01 at 1300 °C, as enumerated in **Table 7-6**; which corresponded to a decrease of 24%. Furthermore, it was discovered that HA peaks above 40° became less defined with increasing temperature.

BG2 exhibited near-comparable β-TCP and HA peak intensities at 1200 °C, and as the sintering temperature was raised, the HA phases dominated (**Fig. 7-14 (a)**). The

peak intensity ratio of β-TCP and HA at 31 and 31.7°, respectively, are listed in **Table 7-6**, where a decrease of 12% in ratio can be observed from 1200 to 1300 °C.

In addition, BG2 exhibited relatively larger $CaSiO_3$ phases, which also grew as the sintering temperature increased. HA peaks above 40° were again observed to lose their definition with increasing temperature. In both hybrids, the phases pertaining to crystalline Bioglass® (**Fig. 7-8**) were not observed, which is in accordance with previous work [290, 478, 479].

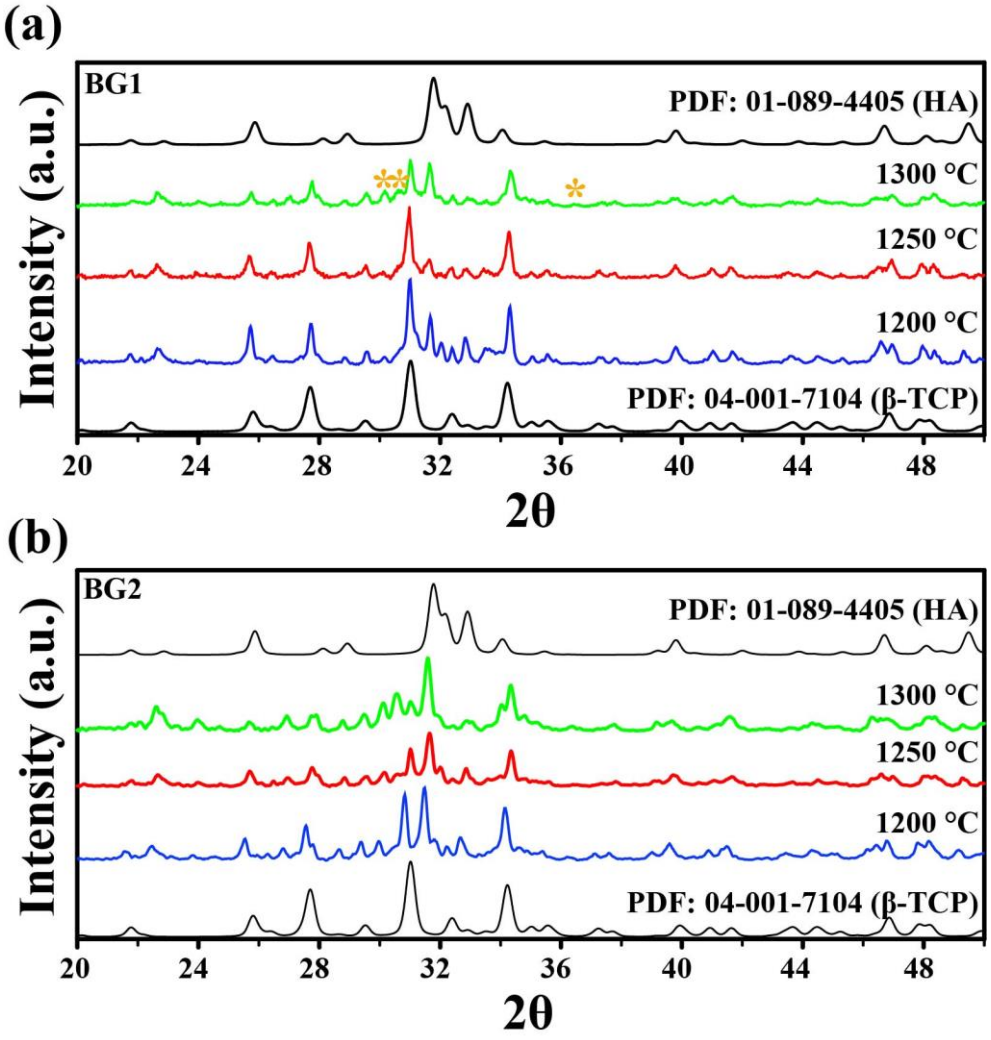

Fig. 7-14. *XRD pattern of the* ***(a)*** *BG1 and* ***(b)*** *BG2 scaffolds. The addition of 10 wt% glass resulted in the detection of hydroxyapatite, β-tricalcium phosphate and calcium silicate phases. The presence of Bioglass® glass-ceramic phases observed in* ***Fig. 7-8*** *were not observed (asterisks – calcium silicate peaks).*

Fig. 7-15 depicts the XRD patterns of canasite scaffolds sintered at 1300 °C. The scaffolds also consisted of β-TCP, HA and calcium silicate phases. Although samples sintered at 1250 °C fractured upon handling, the XRD data was included for comparison,

wherein it was again observed that raising the sintering temperature resulted in decreases to β-TCP peaks; and was once more mirrored by increases to HA and $CaSiO_3$ peaks, as presented in **Table 7-6**. The decrease of β-TCP to HA ratio was by 27%, and the decrease of β-TCP to calcium silicate ratio was by 48%. Crystalline phases of canasite (**Fig. 7-9**) were not detected.

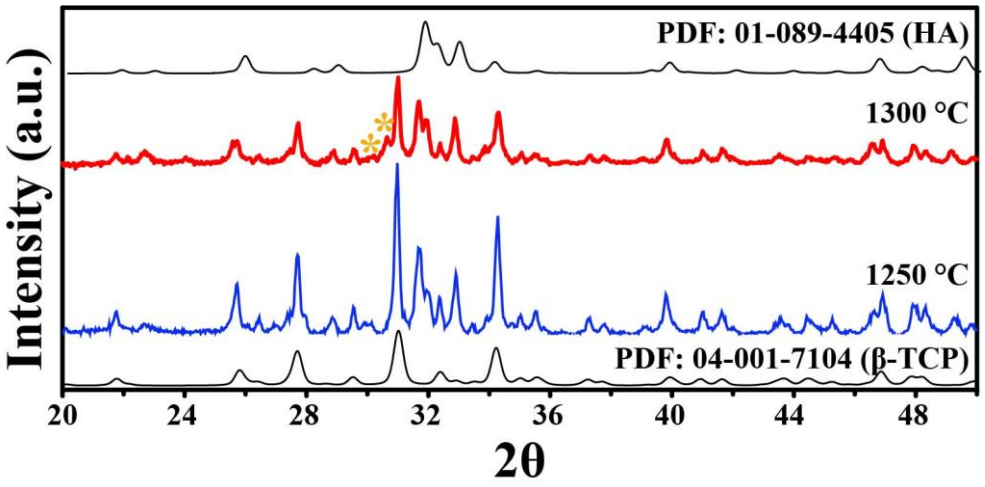

Fig. 7-15. *XRD pattern of canasite scaffolds sintered at 1250 and 1300 °C. Again, the detection of hydroxyapatite, β-tricalcium phosphate, and calcium silicate phases were detected; and the presence of canasite glass-ceramic phases observed in* ***Fig. 7-9*** *were not detected (asterisks – calcium silicate).*

Table 7-6. *Peak intensity ratio of β-TCP (β) taken at 31.0°, hydroxyapatite (HA) taken at 31.7°, and calcium silicate (CS) taken at 30.2°. The table demonstrates the decrease in β-TCP peak intensity in relation to the other two phases.*

	BG1			**BG2**			**CAN**		
	β/HA	β/CS	HA/CS	β/HA	β/CS	HA/CS	β/HA	β/CS	HA/CS
1200 °C	1.33	2.03	1.55	0.95	1.48	1.55	-	-	-
1250 °C	1.30	1.41	1.08	0.92	1.14	1.24	1.46	2.45	1.68
1300 °C	1.01	1.13	1.11	0.84	0.84	1.19	1.07	1.28	1.19

FTIR analysis of the BG samples detected functional groups pertaining to β-TCP, HA and calcium silicate, and the results are portrayed in **Fig. 7-16**. Phosphate groups pertaining to β-TCP are believed to be the bands detected at 1120, 1080, 1043, 945, 604 and 550 cm^{-1}; whereas those pertaining to HA are believed to be the peaks detected at

1010, 980, 880, 590 and 565 cm^{-1}; the hydroxyl group indicative of HA was detected at 3570 cm^{-1} in samples sintered at 1200 and 1250 °C. The peaks were observed to decrease in intensity with increasing sintering temperature, which was a similar behaviour to that observed in previous chapters when the sintering temperature was raised.

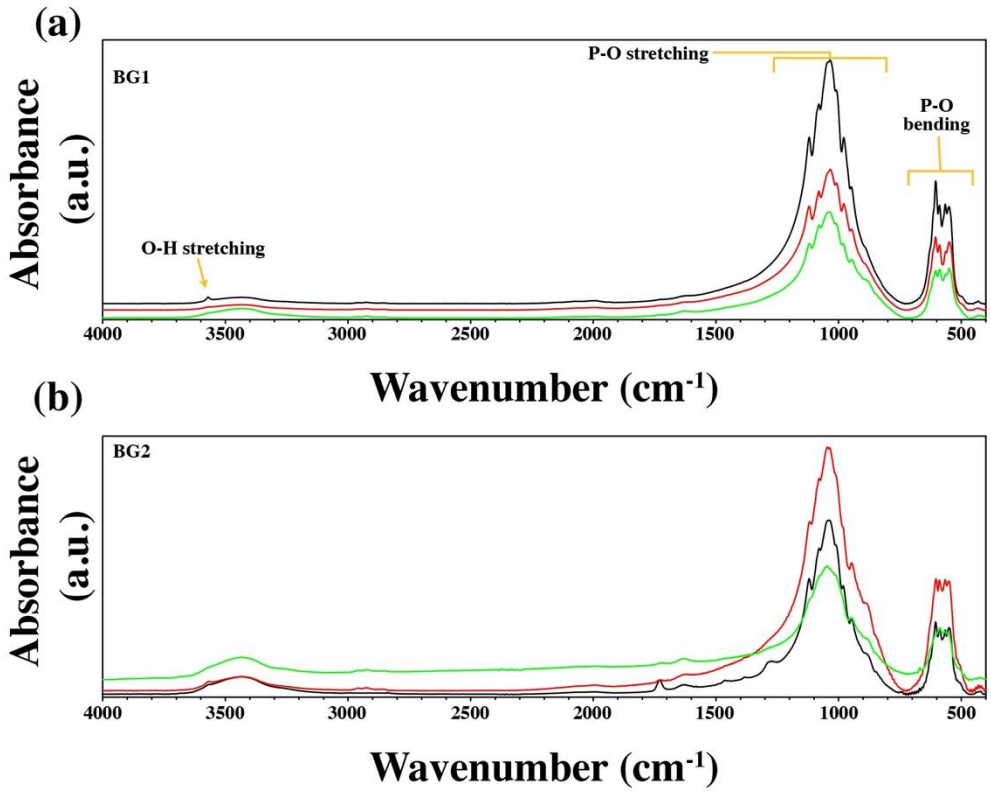

Fig. 7-16. *FTIR spectra of BG1 and BG2 at various sintering temperatures. FTIR revealed the HA-BG samples to possess both HA and β-TCP functional groups.*

Fig. 7-17 is the FTIR data obtained for HA-CAN samples sintered at 1250 and 1300 °C. In contrast, the phosphate functional groups detected at 1120, 1081, 1040, 966, 945, 604, 587 and 550 cm^{-1} were all ascribed to β-TCP. Only the 1250 °C sample presented with evidence of a hydroxyl group at 3530 cm^{-1}, which was lower than that of pure HA, as well as that of the HA-BG hybrids.

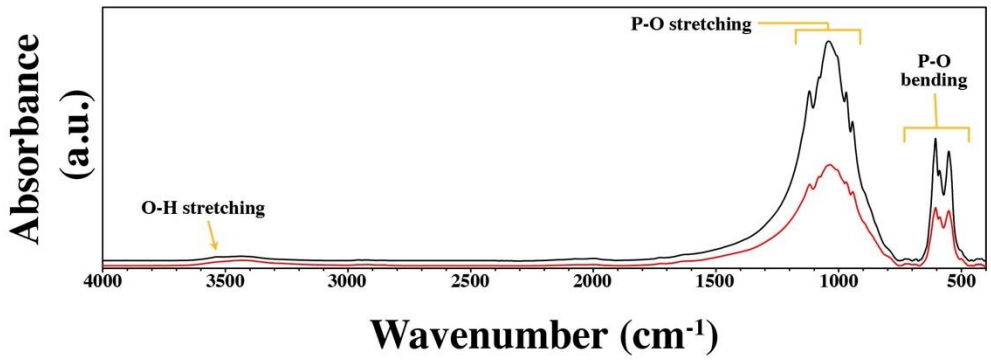

Fig. 7-17. *FTIR spectra of canasite sintered at two different temperatures. The analysis revealed the scaffold comprised both HA and β-TCP.*

7.3.3.2 Physical and Mechanical Properties of Sintered Scaffolds

The scaffold bulk porosity values are depicted in **Fig. 7-18**. The bulk porosity of BG1 scaffolds at 1200 °C was 71.6 ± 1.11 vol%, which decreased to 61.8 ± 0.9 and then 59.6 ± 1.0 vol% when the sintering temperature was raised to 1250 and 1300 °C, respectively.

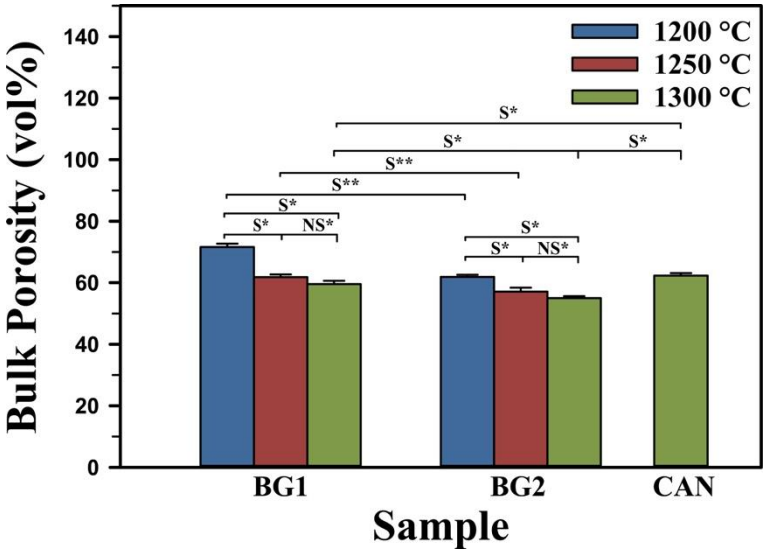

Fig. 7-18. *Bulk porosity of the three different hybrid scaffolds determined by a helium-pycnometer (n = 3; the error bars represent standard deviation; S* significantly different as determined by a one-way ANOVA test; S** significantly different as determined by an unpaired t-test; NS* data is not significant as determined by a one-way ANOVA test). The data revealed that HA-BG1 possessed higher bulk porosities than HA-BG2 at identical sintering temperatures. Furthermore, increasing the sintering temperature decreased the bulk porosity. The HA-CAN scaffolds failed when sintered below 1300 °C, hence the single data provided.*

Bulk porosity values for HA-BG2 scaffolds were significantly lower than their BG1 equivalent, with values of 61.9 ± 0.7, 57.1 ± 1.3 and 55.0 ± 0.6 vol% achieved for scaffolds sintered at 1200, 1250 and 1300 °C, respectively. The canasite scaffolds sintered at 1300 °C possessed a bulk porosity of 62.3 ± 0.8 vol%, which was significantly higher than HA-BG1 and HA-BG2 scaffolds processed at the same temperature.

Fig. 7-19 displays the corresponding maximum compressive strength values attained for the hybrid scaffolds when loaded parallel to the cell direction. The analysis revealed that HA-BG1 samples possessed compressive strengths of 9.8 ± 1.7, 24.1 ± 3.3 and 30.3 ± 3.9 MPa at 1200, 1250 and 1300 °C, respectively; which corresponded to an increase of 145% between 1200 and 1250 °C, and 26% between 1250 and 1300 °C. The strength of HA-BG2 samples were 16.7 ± 1.1, 48.4 ± 5.2 and 56.7 ± 6.9 MPa, at identical sintering temperatures; which meant an increase of 189% between 1200 and 1250 °C, and 17% between 1250 and 1300 °C. Sintering the canasite hybrid scaffold at 1300 °C resulted in a value of 11.4 ± 3.1 MPa. Statistical analysis revealed that increasing the sintering temperature resulted in scaffolds possessing significantly higher compressive strengths. Moreover, the scaffolds formed using BG2 possessed statistically significantly higher strengths than BG1 at all temperature points.

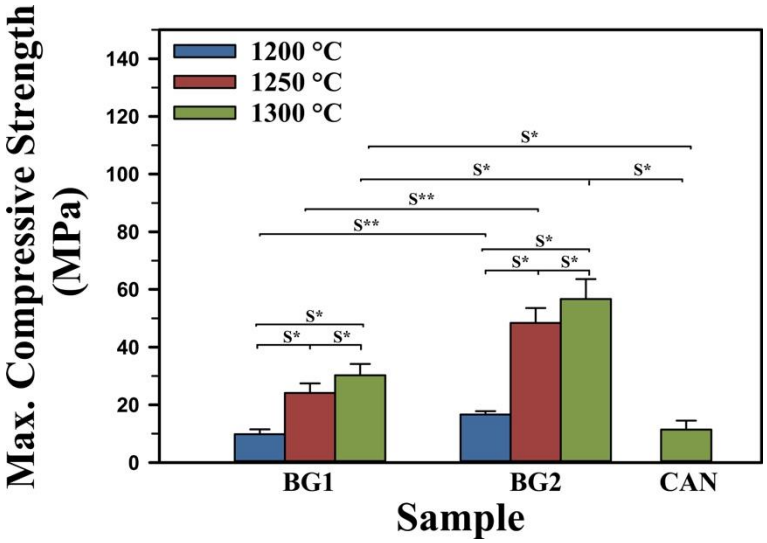

***Fig. 7-19**. The maximum compressive strength of the three hybrid scaffolds when loaded in the A-axis (n = >8; error bars are standard deviation; S* significantly different as determined by a one-way ANOVA test; S** significantly different as determined by an unpaired t-test). The data revealed HA-BG2 scaffolds to possess comparatively greater compressive strength than HA-BG1 at 1200, 1250 and 1300 °C. Furthermore, increasing the sintering temperature improved the compressive strength for both HA-BG scaffolds. The HA-CAN scaffolds failed when sintered below 1300 °C, hence the single data provided.*

Optical microscopy was utilised to determine the macro-pore size and strut thickness achieved. HA-BG1 scaffolds had macro-pores and strut thicknesses ranging from 840-940 and 435-440 µm, respectively; BG2 had macro-pores and strut thicknesses of 750-830 and 400-425 µm, respectively; whereas the canasite scaffolds sintered at 1300 °C exhibited macro-pores and strut thicknesses of approximately 880 and 450 µm, respectively.

7.3.3.3 Microstructure

The microstructure of fractured hybrid scaffolds was investigated. It was discovered that the scaffolds fractured at approximately the mid-point of the struts, as depicted in **Fig. 7-20**, which was similar to that of pure HA scaffolds. Mix-mode fracturing was observed in all hybrid scaffolds.

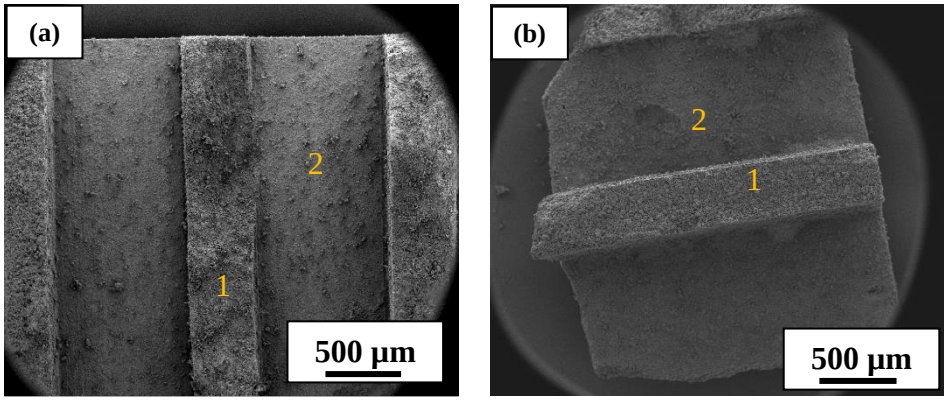

Fig. 7-20. *SEM (secondary electron mode) micrograph depicting the fracture of a BG2 sample sintered at 1200 °C* ***(a)*** *and a canasite scaffold* ***(b)****. The micrographs illustrate that the scaffolds were once more found to fracture at the midpoint when loaded in the A-axis during a compression test.*

Higher magnification images of the fracture surface were taken, and the results are displayed in **Fig. 7-21** and **Fig. 7-22**. When sintered at 1200 and 1250 °C, both BG samples presented with small sintering necks (**Fig. 7-21**), which became noticeably thicker when scaffolds were processed at 1300 °C (**Fig. 7-22 (a & b)**). This behaviour was matched by a decrease to the level of micro-porosity in said samples, which is indicative of higher densification. Previous studies have also found the densification of hybrid scaffolds improved with increasing sintering temperature findings [455, 457, 479].

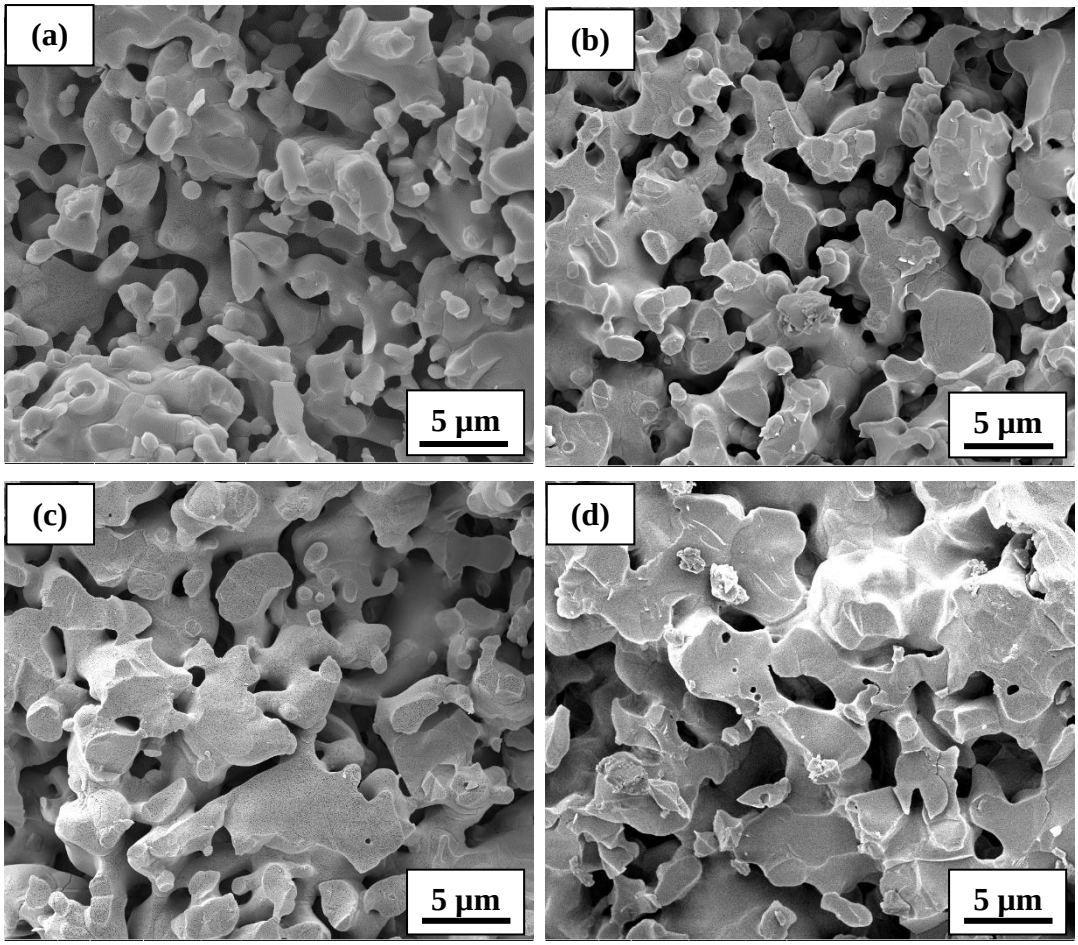

Fig. 7-21. *SEM (Secondary electron mode) micrographs depicting the fracture surface of BG1* ***(a & c)*** *and BG2* ***(b & d)*** *at 1200 (top images) and 1250 °C (bottom images). (Images were taken at x10,000 magnification). The micrographs illustrate that BG1 and BG2 possessed a porous microstructure.*

The canasite scaffolds sintered at 1300 °C presented with thinner sintering necks (**Fig. 7-22 (c)**), in comparison to the BG1 and BG2 scaffolds sintered at the same temperature; and accordingly, the level of micro-porosity was greater. A micrograph of a calcined HA microstructure sintered at 1250 °C is provided to highlight the difference in sintering progression (**Fig. 7-22 (d)**). It can be observed that the hybrid scaffolds were less dense than the pure HA scaffolds, albeit the former were sintered at a higher temperature. Relative to pure HA (**Fig. 7-22 (d)**), the HA-CAN samples (**Fig. 7-22 (c)**) displayed a less angular morphology.

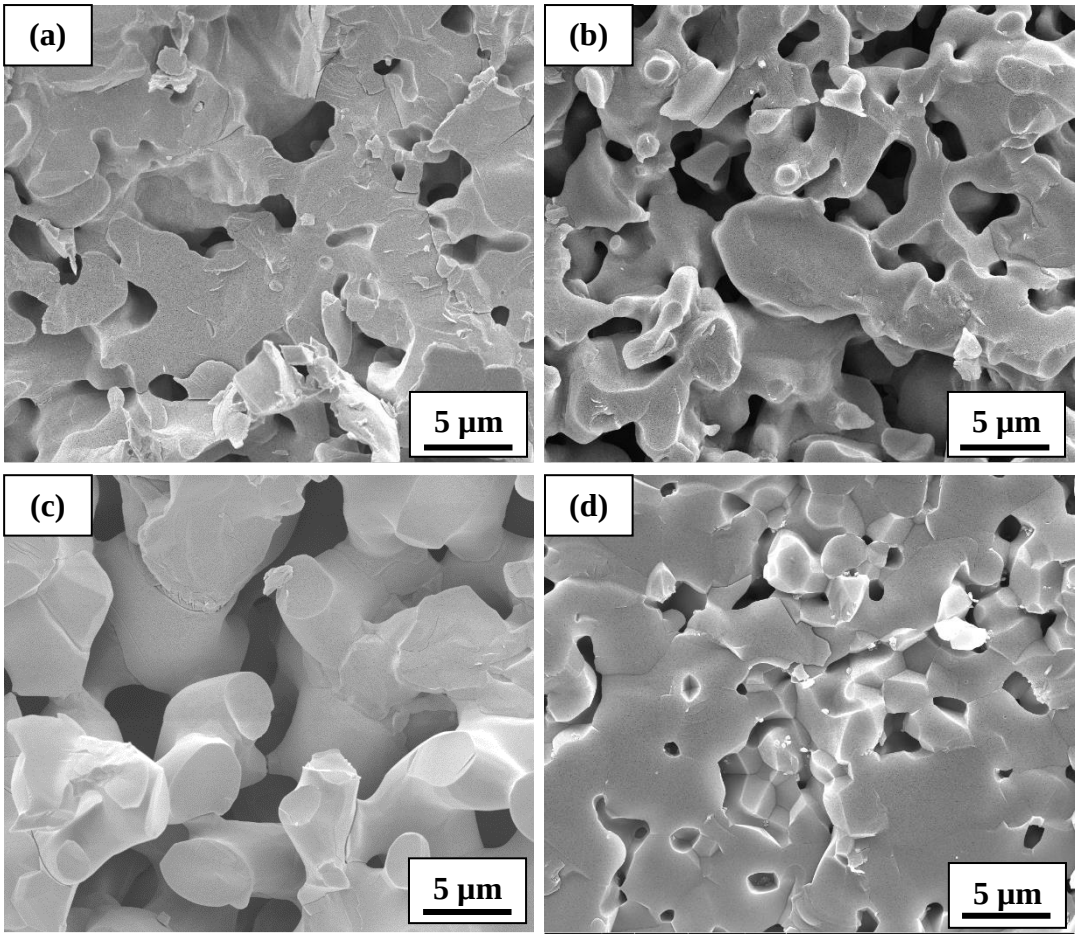

Fig. 7-22. *SEM (secondary electron mode) micrographs depicting the fracture surface of BG1* ***(a)****, BG2* ***(b)****, CAN* ***(c)*** *sintered at 1300 °C. The figure also includes the fracture surface of HA sintered at 1250 °C* ***(d)*** *for comparison. (Images were taken at x10,000 magnification). Compared to the HA sample, BG1, BG2 and CAN were less dense, albeit sintered at a higher temperature.*

Site 2 in **Fig. 7-20** was examined using SEM in an attempt to characterise the morphology of the grains. However, the grain morphology could not be examined, as **Fig. 7-23**, **Fig. 7-24** and **Fig. 7-25** can attest to, the glass had melted and enveloped the HA grains, thereby impeding the observation thereof. Furthermore, micro-porosity was observed in all samples analysed, and, in the case of the BG samples (**Fig. 7-23** and **Fig. 7-24**), increasing the sintering temperature led to a noticeable reduction in micro-porosity. The micro-pore morphology was mixed, with circular, angular and elliptical micro-pores observed. Micro-cracks on the amorphous phase were observed in these regions, which were not observed in previous HA scaffolds (AR-HA/S, C-HA/S and Y-HA/S).

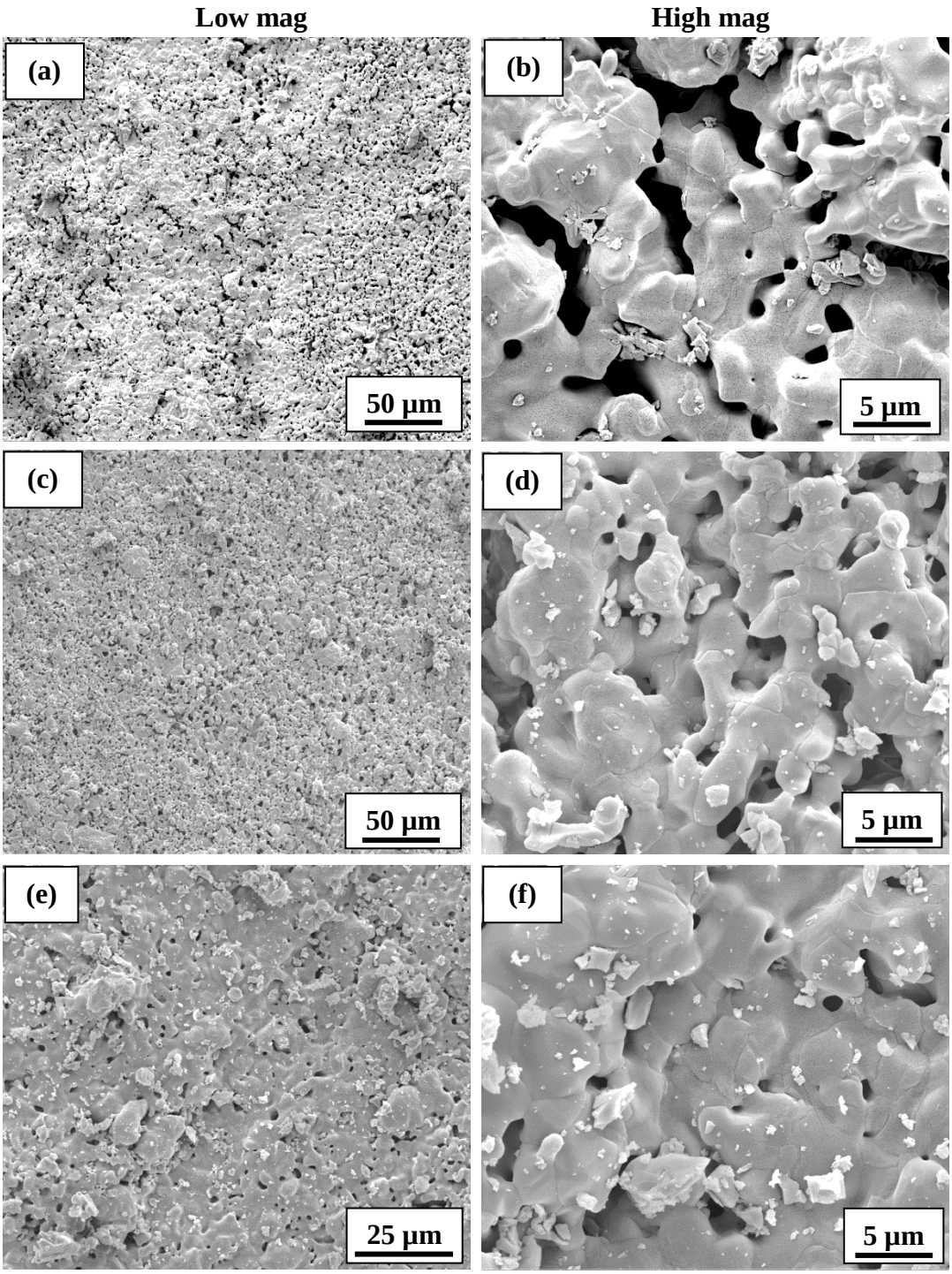

Fig. 7-23. *SEM (secondary electron mode) micrographs depicting the microstructure at Site 2 of BG1 at 1200* ***(a & b)****, 1250* ***(c & d)*** *and 1300 °C* ***(e & f)****. The micrographs demonstrate the porous microstructure of BG1 at all three sintering temperatures, wherein the porosity was observed to decrease with increasing sintering temperature. Furthermore, the glass had melted and impeded the observation of the HA grain morphology; for example, compared to* ***Fig. 6-23****, clear delineation of the grain boundaries could not be observed.*

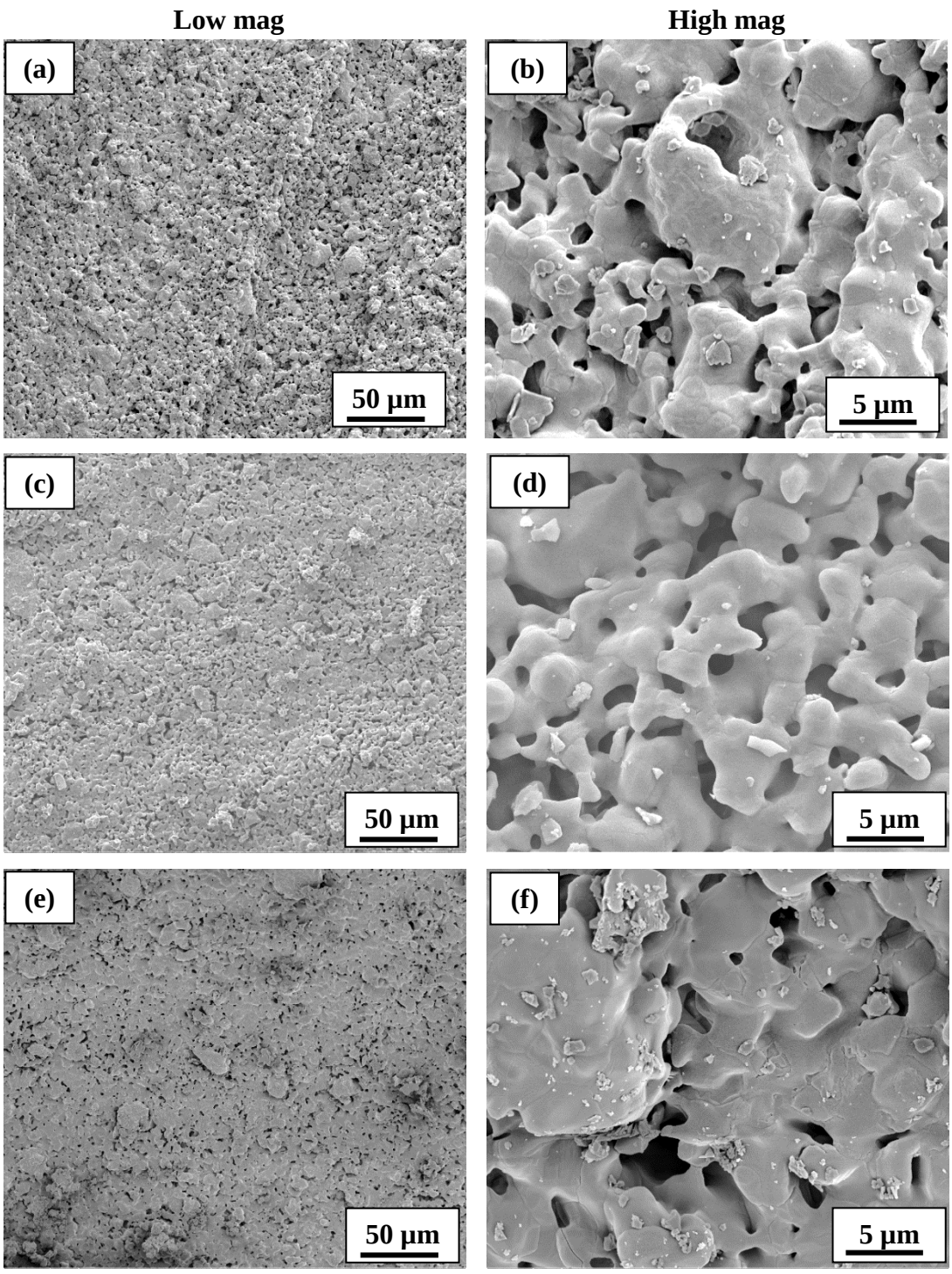

Fig. 7-24. *SEM (secondary electron mode) micrographs depicting the microstructure at Site 2 of BG2 at 1200* ***(a & b)****, 1250* ***(c & d)*** *and 1300 °C* ***(e & f)****. The micrographs demonstrate that BG2 possessed a porous microstructure at all three sintering temperatures. Furthermore, the complete grain morphology of HA, as seen in* ***Fig. 6-23****, could not be observed due to the melting of the glass impeding its observation.*

The microstructure of the CAN samples sintered at 1300 °C was akin to the BG samples sintered at 1200 °C, as demonstrated in **Fig. 7-25**. The variant micro-pore morphology was again observed, as well as mix-mode fracturing. In comparison to pure HA, the grain morphology of HA-CAN were notably more rounded, and hence the microstructure appeared comparatively smoother. The softening of calcium phosphate grains in the presence of Bioglass® has been previously attributed to sodium originating from the latter [290].

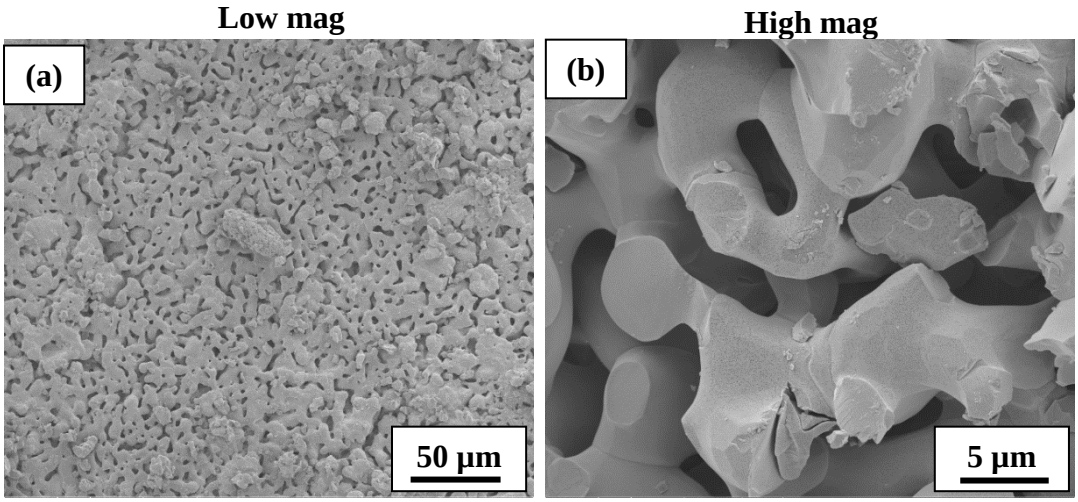

Fig. 7-25. *SEM (secondary electron mode) micrographs of the canasite microstructure taken at Site 2. The incorporation of 10 wt% canasite glass to HA resulted in a microstructure that was considerably more porous than that of pure HA, despite being sintered at the higher temperature of 1300 °C. Furthermore, the hydroxyapatite grains appeared to soften in the presence of canasite.*

7.4 Discussion

The main aims of the investigation were to improve both the biological and mechanical strength of the HA scaffolds by incorporating 10 wt% glass. This was carried-out by using Bioglass®, the most widely researched and commercially used bioactive glass; and canasite, a glass with improved biological properties. In addition, a modified Bioglass® was used, whereby 5 wt% Na_2O was substituted by 5 wt% CaO, and thus yielding a calcium-excess variant. It was hypothesised that compositing with a calcium-excess Bioglass® would produce hybrid scaffolds with greater compressive strength compared to compositing with stoichiometric-Bioglass®. The extra calcium concentration in the

system would minimise the commonly reported phase transformation of HA to β-TCP during sintering. The effects of Ca^{2+}-excess BG will be discussed below.

7.4.1 The Effect of Glass on Paste Properties

A relatively stable extrusion profile was observed with the HA-bioactive glass pastes compared to pastes formed using the as-received HA (**Chapter 5**) and the calcined HA (**Chapter 6**). In pure HA scaffolds, an initial rise in extrusion force was observed, followed by a decrease in force, which corresponds to a decrease in paste viscosity. As detailed in **Chapter 4**, the viscosity of all shear-thinning pastes continues until the stable infinite shear region is reached (**4.1.2.1**). This was not observed in the HA-bioactive glass samples, as **Fig. 7-26** demonstrates. In this study, sodium ions may have leached from the glass to the water [290], causing an increase to the local pH; consequently reducing the viscosity of the paste [480, 481] and thus accelerating the rheological stability thereof. Alternatively, the increase in mean particle size may have elicited the stable flow. An increase in particle size may have facilitated binder coverage, which explains why, despite the increase in particle size, HA-BG pastes resulted in the lowest extrusion pressure generated and a stable flow thereafter.

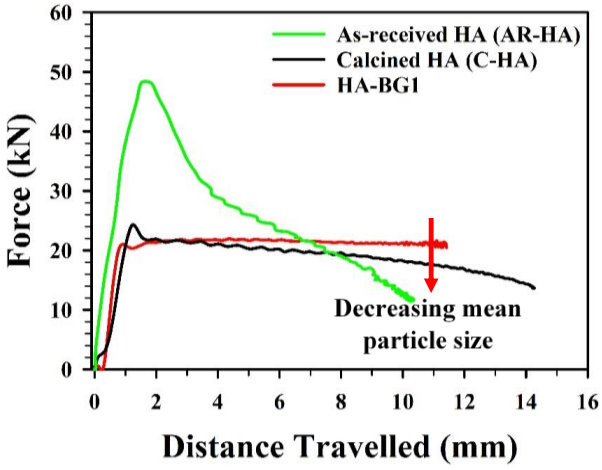

Fig. 7-26. *Extrusion plot of as-received HA, calcined HA and HA-BG1 hybrid pastes. The hybrid pastes were found to lack a decrease in force following the pressure drop, as previously seen in glass-free hydroxyapatite pastes, thereby resulting in a relatively stable plateau following the pressure drop. In addition, the hybrid pastes were found to possess the smallest pressure drop.*

7.4.2 The Effects of Bioactive Glass on Honeycomb Extruded Scaffolds

The incorporation of 10 wt% bioactive glass reduced the compressive strengths of hydroxyapatite scaffolds fabricated by honeycomb extrusion. Analysing the hybrid scaffolds revealed probable causes to said decrease.

7.4.2.1 Glass-induced Phase Transformation

The salient effect of incorporating 10 wt% glass was the phase transformation of HA into β-TCP. As mentioned, bioactive glass-induced phase transformation of HA into β-TCP is well documented [479, 482-486]. Indeed, at high enough temperatures, thermally-induced phase transformation can also occur without the presence of glass, as reported in **Chapter 5**. However, the hydroxyapatite used in this study was the same as the C-HA used in **Chapter 6**. This particular starting material exhibited enhanced thermal stability, whereby sintering at 1250 °C produced no evidence of phase transformation, according to the XRD and FTIR results. Therefore, it was deduced that the inclusion of glass was conducive to the phase transformation of HA. Generally, once HA has started to decompose, increasing the sintering temperature further produces more decomposed products, which was not observed in this study. On the contrary, increasing the sintering temperature reduced the intensity of the β-TCP phase, and thus added further credence to the notion that the phase transformation was glass-induced.

The bioactive glass-induced phase transformation can be ascribed to the imbalance in calcium concentration between HA and the glasses, thereby establishing a calcium concentration gradient. Calcium, in the form of calcium oxide, diffused from the hydroxyapatite and along the concentration gradient and into the glassy phase, which were relatively deficient in calcium. The following reaction was proposed to have taken place:

$$\mathbf{Ca_{10}(PO_4)_6(OH)_2 \longrightarrow 3Ca_3(PO_4)_2 + CaO + H_2O}$$

The calcium oxide could have further reacted with the phosphate and silica group from the glass to yield additional tricalcium phosphate and calcium silicate, respectively:

$$\mathbf{4CaO + (45SiO_2{\cdot}24.5CaO{\cdot}24.5Na_2O{\cdot}6P_2O_5) \longrightarrow Ca_3(PO_4)_2 + CaSiO_3 + (44SiO_2{\cdot}24.5CaO{\cdot}24.5Na_2O{\cdot}5P_2O_5)}$$

This reaction also explains why the hybrid containing BG2 exhibited less of a phase transformation. BG2, with a higher calcium concentration than BG1, alleviated the imbalance and hence reduced the driving force for Ca^{2+} to migrate from the HA. Therefore, it can be concluded that increasing the calcium quantity in a glass will reduce the level of phase transformation in HA-glass hybrids.

A concentration gradient for sodium and silicon may have also been established. Both ions are known to substitute for calcium and phosphate, respectively, and indeed HA peak shifts with respect to pure HA were observed. This can also explain why crystallisation of the bioactive glass did not occur, despite using a relatively slow cooling rate of 2.5 °C/min. As discovered in **Fig. 7-11**, BG does not crystallise in the presence of HA during cooling, which may be due to the glass losing the aforementioned ions, and thus unable to form a crystalline structure. From biological perspective, amorphous phases are favoured as they exhibit a higher bioactivity [487]. Further work is needed to confirm this hypothesis, particularly in-depth XRD analyses to confirm the exact substitution mechanisms that may have occurred herein.

Decreasing β-TCP phase with increasing sintering temperature has been previously reported, although an explanation for this effect has not been postulated. One possible explanation is that with increasing temperature the interfacial area over which the calcium ions can migrate decreases, thereby reducing the driving force for calcium diffusion. The minor calcium silicate phase was also observed to increase in intensity with increasing sintering temperature. Similarly, increasing the sintering temperature may have reduced the viscosity of the glass melt, which may have wetted more of the HA grains, thereby increasing the interfacial surface for Si to diffuse out of the glass. Therefore, factors that govern the surface area of the HA, and viscosity of the glass, may affect bioactive glass-induced phase transformation.

7.4.2.2 The Effect of Glass on Hydroxyapatite Microstructure

The microstructure revealed that the addition of 10 wt% bioactive glass perturbed the densification of the HA structure. The hindrance in HA densification observed in the present study as a result of bioactive glass incorporation has been previously disclosed [459, 482, 488]. Perusing the literature for studies into the fabrication of calcium phosphate or calcium silicate composited with bioactive glass has revealed that all but

one of the studies reported either a decrease or an insignificant change to the densification when compared to the respective glass-free scaffolds (**Table 7-7**). Hence, with regards to mechanical properties, most did not benefit from liquid-phase sintering. As a consequence of the suppressed densification, the current study demonstrated that the sintering necks were underdeveloped, and thus the microstructure was markedly more porous than that of pure HA. Improvements to the densification were achieved by increasing the sintering temperature.

Due to the complexity of the hybrid mixture, it is difficult to ascertain what caused the suppression in densification without additional analysis, namely transmission electron microscopy. Indeed, the presence of TCP may have contributed to the retardation of densification. Another plausible contributor is presence of silicon, which in the presence of calcium phosphates has been demonstrated to raise the densification temperature [275, 489]. Dilatometry analysis revealed that the addition of 25 wt% of silicon suppressed the densification of calcium phosphate [490]. Other work investigating HA-calcium silicate systems demonstrated a decrease in linear shrinkage when the CS phase increased [377].

Alternatively, ion migration from and to the hydroxyapatite grains may have altered the local defect chemistry of the HA making it Ca^{2+}-deficient, and thereby suppressing the densification thereof. Santos et al. (1994) investigated both Bioglass® and $CaO\text{-}P_2O_5$ binary glass systems [479]. The authors reported an increase in tricalcium phosphate phase with the incorporation of Biolgass®, but not with the binary glass; thus they concluded that the presence of Na^+ in the former accelerated HA decomposition, and thereby hindered densification. This is in agreement with the present study, whereby a decrease in sodium content increased densification. It can be reasoned that reducing either Si and/or Na^+ in bioactive glasses, or using sodium-free binary glasses, will enhance densification of HA-bioactive glass hybrids. However, Bellucci et al. (2013) compared the 40 wt% addition of both CaO-rich and stoichiometric Bioglass®, and reported the latter, which possessed a markedly higher Na content, resulted in a greater densification when sintered at 1150 °C [491]. Hence, the effects of Na^+ may differ depending on the ratio of HA to Bioglass®, and the processing parameters used.

Reducing the proportion of bioactive glass in the hybrid system is one approach of attenuating the effects of silicon- or sodium-induced decomposition. Tancred et al. (2001) reported a decrease in densification with the incorporation of Bioglass®, from as little as 2.5 wt% addition, to 50 wt%. The authors reported the decrease in densification

was exacerbated with increasing Bioglass® content [492]. The inclusion of both Na and Si are required for achieving desirable biological properties, hence, this must be factored if both elements are to be minimised.

7.4.2.3 The Resultant Compressive Strength and Comparison to Other Studies

HA-bioactive glass scaffolds had a lower compressive strength than HA-only scaffolds due to the aforementioned effects of glass on HA: (1) the presence of β-TCP, which is mechanically weaker than HA; and (2) a notable decrease in densification with smaller sintering necks. Similar findings were observed by Lee et al. (2006), whereby the addition of 30-35 wt% Bioglass® reduced the mechanical properties by up to 25% [488]. The increase in mechanical properties with increasing sintering temperature has also been reported [478, 479]. This was achieved herein without further decomposition of HA into α-tricalcium phosphate (α-TCP), which is in disagreement to previous work [485, 492]; both studies used finer particle sizes which may have accelerated the decomposition process. The same studies observed a decrease in mechanical properties with the introduction of α-TCP.

The hybrid scaffold synthesised with the calcium-excess BG exhibited higher mechanical properties, which was ascribed to a decrease in β-TCP phase, but also an increase in calcium silicate phase, which has been previously demonstrated to enhance the compressive strengths of HA-CS composites as the proportion of CS in the admixture was increased [493]. Therefore, the research herein has demonstrated that an increase of 5 wt% calcium oxide content of the raw Bioglass® powder was sufficient enough to impact the compressive strength of the HA scaffold. Desogus et al. (2015) [494] investigated CaO-rich versus stoichiometric Bioglass® using spark plasma sintering for dense HA. In addition to demonstrating that the former exhibited delayed devitrification, they revealed the CaO-rich Bioglass® displayed higher Vickers hardness values, and a generally higher elastic modulus; and were able to descry a higher-level densification attained by the CaO-rich BG.

The HA-CAN scaffolds sintered at 1300 °C possessed the weakest compressive strength. The micrograph images portrayed an equally low densification rate had transpired; the microstructure of CAN at 1300 °C was comparable to that of the BG samples at 1200 °C.

Table 7-7. *Examples of calcium phosphate-bioactive glass hybrids, and their respective bioactive glass composition, sintering temperature, dwell time, decomposition products and final density relative to pure calcium phosphate. (HA- hydroxyapatite; BG-Bioglass®; TCP- tricalcium phosphate; CaSiO – calcium silicate; Si-HA – silicon substituted hydroxyapatite).*

Study	Starting Hybrid	Glass mass%	Sintering (°C)	Dwell time (h)	Products	Density relative to pure CaP
Present study	HA/BG	10	1200-1300	8	HA, β-TCP, $CaSiO_3$	Decreased
Present study	HA/Canasite	10	1300	8	HA, β-TCP, $CaSiO_3$	Decreased
Santos [479]	HA/BG	5	1200-1300	1	α-TCP,β-TCP, Si-HA	Decreased
Bellucci [491]	HA/BG_Ca	40	1150	3	HA	Decreased
Lopes [290]	TCP/BG	7.5	1200	2	α-TCP,β-TCP	No change
Goller [495]	HA/BG	10	1200 & 1300	4	Si-HA, $Ca_2P_2O_7$, Na_2HPO_4	N/A
Yazdanpanah[455]	HA/Sodalime glass	5	800-1200	2	HA	Decreased
Lin [456]	CaSiO/BG	5	1100	3	CaSiO	Increased
Knowles [457]	HA/Na_2-CaO-P_2O_5	2	1200-1350	1	HA	No Change
	HA/Na_2-CaO-P_2O_5	4	1200-1350	1	α-TCP,β-TCP, HA	Decreased
Tancred [458]	HA/Phosphate glass	10	1150-1350	3	α-TCP,β-TCP, HA	Decreased
Tancred [492]	HA/BG	2.5-50	1050-1200	3	β-TCP, HA	Decreased
Demirkiran [482]	HA/BG	10	1200	4	Si-HA,β-TCP	Decreased

Therefore, it can be inferred that the failure of the extrudates sintered at 1250 °C was due to insufficient densification of the hybrid material. This may be due to canasite's higher thermal stability, which will require more energy for densification (**Fig. 7-10**). Moreover, previous research has determined that bioactive glasses containinga higher number of oxides reduced the binding effects thereof [459, 479]. Hence, as canasite contains an additional two compounds (K_2O and CaF_2) in comparison to the Bioglass®, the same may have been true in the present study.

Most of the glassy phase sintering work has concentrated on dense ceramics. A few have investigated the reinforcement in porous bioceramic scaffolds. To the author's best knowledge, the present study is the first to report the compressive strength of porous-controlled HA-Bioglass®, and certainly HA-canasite scaffold. The compressive data reported is comparable to that of dense HA-BG hybrids [455, 496]. Previous work has also sought to combine HA with phosphate-based glass, and the compressive strength and porosity thereof are comparable to that obtained herein [497, 498]. Similarly, BG has been combined with other bioceramics, such as β-TCP and calcium sulphate, which have attained compressive strengths below that obtained in this study [290, 499, 500]. By far the most promising work was by Lin et al. (2009), wherein 10 wt% BG was added to calcium silicate resulted in compressive strengths comparable to that of bone [456]. Calcium silicate is a biodegradable bioceramics capable of inducing bone regeneration *in vivo* [501]. The aforementioned study fabricated the hybrid scaffold using traditional routes of fabricating porous scaffolds whereby a stochastic porous architecture was generated. Thus, the fabrication of CS-BG using ceramic extrusion may yield a biodegradable scaffold with an unprecedented level of mechanical strength.

Comparing the mechanical properties to the commercially available hybrid BGS Bonelike®, the results are again an improvement. Bonelike®, which has been stated as a promising material with enhanced bioactivity compared to HA-only material [149, 502], and is suitable for direct clinical use, consists of HA with 4 wt% bioactive glass. Though the porosity values are comparable to that of the samples examined in the present study, the compressive strengths and macro-pore sizes are, respectively, 2 MPa and 100 μm [498]. Hence, the hybrid scaffolds fabricated herein, comprised of a higher glass content, remarkably greater compressive strength and larger pore sizes, would be more desirable for BGS.

7.5 Summary of Chapter

In this chapter, the fabrication of three different hybrid scaffolds, comprising hydroxyapatite with three different bioactive glasses, was investigated. The addition of 10 wt% stoichiometric Bioglass®, a calcium-excess Bioglass® and canasite were added to HA and sintered at temperatures conducive of liquid phase sintering (LPS). However, the benefit of LPS with respect to compressive strength was not observed. The scaffolds presented with an unexpected phase transformation of the HA, which was induced by the glasses. Preliminary investigations demonstrated that the glass crystallises into their respective glass-ceramics, with thermal analyses of BG samples inferring that crystallisation thereof can occur during cooling. However, a chemical reaction between HA and glass transpired that prevented the latter from crystallising. Instead, the sintered scaffolds consisted of HA, β-TCP, $CaSiO_3$ and a glassy phase. The compressive strength determined were 9.8-30.3, 16.7-56.7 and 11.4 MPa for HA-BG1, HA-BG2 and HA-CAN scaffolds, respectively. Furthermore, the results revealed that Bioglass® comprising a higher amount of calcium improved the densification of the system and hence resulted in an increase in mechanical properties. Thus, it was concluded that the composition of glass is a determinant of the hybrid scaffold's mechanical properties, albeit forming 10 wt% of the system. The composition can be modified to yield different ratios of HA and β-TCP, as well as to yield varying compressive strengths.

Chapter 8: Conclusion

The rationale behind the objectives pursued for this project was primarily to yield honeycomb extruded scaffolds with compressive strengths comparable to cortical bone. The honeycomb extrusion process was modified with regards to particle morphology and composited with different materials to produce novel scaffolds with remarkable properties for BGS. Scaffolds with macro-pore sizes exceeding the requirements were fashioned. The porosity volume exceeded that of cortical bone, with the compressive strength comparable thereto. The thesis demonstrated that the mechanical properties of HA scaffolds were governed by many factors, and hence a thorough control over all aspects of the fabrication process was needed, from synthesising the raw powders to the sintering stage.

General Observation on the Effects of Powder Morphology & Purity

The study has established that the raw powder properties can be modified to yield high-strength scaffolds. The thesis revealed that powders comprising of nano-sized primary particles resulted in poorly lubricated ceramic powder, and consequently resulted in a lower solid loading with a high extrusion force needed. Through calcination, it was demonstrated that this relatively simple approach resulted in HA powders that were easier to lubricate and hence a higher solids loading was attained, as well as a reducing the extrusion force needed. The solid loading mass was found to increase by 17.7%, whilst the extrusion force was reduced to approximately 23 kN, from approximately 44 kN.

Further, the calcined powders were found to result in wider strut thickness, which partly explained why significantly higher compressive strengths were obtained, as more load was sustained with thicker struts. The strut thickness increased from 350 μm to 425 μm, an increase of 21.4%. Less shrinkage also resulted in a higher bulk porosity, which increased from 40 to 45 vol% when the powders were calcined. The main advantages determined by pre-calcination were: (a) attaining a higher solid loading; and (b) an increase in surface area. In addition, the pre-calcined scaffolds exhibited finer grains, and considerably fewer secondary structures that also contributed to the enhanced compressive strength by mitigating crack propagation. The grain sizes reduced from 2.4

to 1.7 μm at 1200 ^{o}C, and from 5.9 to 3.2 μm at 1250 ^{o}C. These correspond to a decrease of by 29% and 46%, respectively.

In addition, the present work demonstrated that honeycomb-extruded scaffolds exhibited anisotropic mechanical properties; whereby a greater stress can be sustained by applying the load parallel to the cell direction, rather than perpendicular to the cell direction. This was attributed to the fracture mechanism, wherein the latter exhibited flexural stress, which ceramics are known to be weaker in compared to compression. Nonetheless, a compressive strength of 32.3 MPa is greater than scaffolds fabricated through traditional techniques.

Composite Scaffolds

Original work was conducted to increase the mechanical properties through compositing HA with other materials. Although, the addition of either 10 wt% yttria or bioactive glass did not affect the extrusion process, as evidenced by comparable extrusion behaviour to pure HA, the incorporation of yttria was found to enhance the compressive strengths of HA, from 105.9 to 127.3 MPa, an increase of 20%; whereas the latter reduced the strength from 105.9 MPa to the best achieved 56.7 MPa, a decrease of 46%. Yttria was found to mitigate HA decomposition into its weaker β-tricalcium phosphate counterpart, whereas compositing with bioactive glass induced the phase transformation thereto. The glass-induced phase transformation was lessened when glass was synthesised with a higher calcium oxide content, and consequently increased the compressive strength; thereby adding further credence to mitigating transformation of HA into its mechanically weaker phases. However, HA-bioactive glass composites possessed larger macro-pore sizes, increasing from 750 μm in glass-free HA scaffolds to a maximum of 940 μm; and greater bulk porosity, from a maximum of 52 vol% in glass-free HA scaffolds to 71.6 vol%. The work demonstrated that honeycomb extrusion is a feasible method for fabricating composite scaffolds, which can be used to tailor the strength and porosity.

The presence of β-TCP phase and densification were key determinants to improving the mechanical properties of honeycomb-extruded scaffolds. In all cases, including compositing with bioactive glass, increasing the sintering temperature, thereby improving the level of densification, resulted in an increase in compressive strength. This was because the sintering necks that formed between adjacent particles grew in thickness,

and thus were able to sustain a greater load. However, the presence of β-TCP phases may have perturbed grain interfacial bonding, and hence, HA scaffolds exhibiting phases thereof had the weakest compressive values.

For HA-glass composites, densification was also believed to be the reason why sintering at higher temperatures resulted in less HA phase transformation: an increase in densification decreased the interfacial area between HA and glass, thereby mitigating the rate of calcium oxide migration from the former to the latter. Additionally, yttria was found to be an ideal oxide for compositing, as grain bonding was achieved between the two phases, whilst yttria grain size were maintained in the nano region. As previously stated, finer grains contribute to enhanced mechanical properties.

Honeycomb extrusion is verily a promising technique for fabricating HA scaffolds. It requires low running and capital costs, it can attain structured and interconnected porosity, and high strengths can be achieved. Furthermore, unlike other techniques such as co-extrusion and freeze-casting, which can achieve a porous structure with high compressive strength but require understanding the solvent crystallisation kinetics for imparting porosity, honeycomb extrusion does not require such high-skilled knowledge. For example, if the pore sizes or pore shape need to be altered, this can be achieved easily by changing the die, whereas for freeze casting and co-extrusion crystal freezing dynamics will need to be investigated. Moreover, honeycomb extrusion is suitable for compositing of HA to other materials, including glass. In addition, the abovementioned advantageous extend the applications of honeycomb extrusion to other biomedical engineering fields, such as drug delivery devices. Scaffolds fabricated by this process yielded strengths that are remarkably greater than the commercially available Endobon® and Bonelike® (2 MPa), hence demonstrating the necessity for honeycomb extruded-scaffolds therewithal the shortcomings of contemporary fabrication techniques (e.g. freeze-casting and robocasting).

Limitations and Future Work

A chief limitation of honeycomb extrusion is the lack of complete interconnected porosity. In the present study, only unidirectional interconnected pores were formed. Thus, a means of controlling both longitudinal and lateral interconnected porosity will need to be sought, as this will enhance the osseointegration of scaffolds. Furthermore,

although extrusion is ideal if a fixed cross-sectional geometry is needed, bone defects typically require complex geometries. For this reason, there is a shift in perspective in biomedical engineering from *off-the-shelf* products to products that are personalised to the individual's needs, thereby improving the efficacy of the treatment. Consideration must be given to obtaining complex geometries if honeycomb extrusion is to fabricate potent bone graft substitutes.

Honeycomb extrusion was found to be a versatile technique, accommodating binders with different rheological characteristics, as well as raw ceramic powders with different particle morphology. Such versatility opens the opportunities to explore multiple research avenues in the search for achieving high strength. Building on the present study, future work will need to optimise the HA-bioactive glass composite to augment the mechanical properties. Factors to investigate include HA-glass ratio, glass composition and sintering conditions. The ideal composition will result in high strength, without sacrifice to bioactivity.

Factors not considered in the present study were the effect of macro-pore size and shape (e.g. hexagonal pores) on scaffold mechanical properties. Previous work has shown that hexagonal pores increased the compressive strength by 29% from rectangular pores (1), which could easily be implemented herein as a means of improving mechanical properties.

The inclusion of dispersants and lubricants were not investigated for paste formulation, which can provide an alternative route to minimising agglomeration of nano primary particles. Optimisation of paste formulation with said additives can improve the efficiency of extrusions, as well as subsequent processes. Furthermore, the work has started to identify suitable rheological characteristics suitable for honeycomb extrusion, and a more thorough rheological investigation is needed to establish the ideal rheological properties. Rheology can be a powerful tool for predicting extrudate quality without costly empirical experiments. Ultimately, further rheological research into the parameters that effect honeycomb extrusion, such as the effect of particle morphology on viscosity and shear modulus, will be beneficial, as the knowledge can be translated to other extrusion-based techniques, such as the *state of the art* robocasting.

Biological assessments of the synthetic bone scaffolds will need to be performed to determine their suitability. As mentioned in **Chapter 2**, bone possesses both organic

and inorganic matter, and has a vascular system to supply oxygen and nutrients to the cells involved in the healing process. Hence, biological tests will need to demonstrate the potential of a synthetic scaffold to generate new inorganic and organic phases, as well as forming new blood vessels. An *in vitro* cell viability will be needed to confirm whether the final products' biocompatibility and their potential for cell proliferation. The test will be performed ideally using human-derived bone cells, and also mesenchymal stem cells (MSC): to determine the effect of the scaffold on MSC differentiation into bone cells by staining for osteogenic differentiation markers, such as alkaline phosphates activtiy. Further tests that can be performed *in vitro* include immunofluorescence staining for calcium (using Alizarin Red S Stain Assay) to observe calcium deposition; and collagen (sirus red stain assay) to observe production thereof. If the results are promising, then *in vivo* tests can be performed thereafter; where histological tests can be performed on explants to quantify bone formation and the healing process, using histomorphometric analyses. In addition, immunofluorescence staining of endothelial cell markers, such as CD31, can be performed to determine the effect of scaffold on neovascularisation.

References

[1] M.A. Adams, Functional anatomy of the musculoskeletal system, Elsevier2016.
[2] B. Clarke, Normal Bone Anatomy and Physiology, Clinical Journal of the American Society of Nephrology : CJASN, 3 (2008) S131-S139.
[3] E.N. Marieb, K. Hoehn, Human Anatomy & Physiology: Pearson New International Edition, Pearson Education M.U.A.2013.
[4] E.F. Eriksen, Alexrod, D.W., Melsen, F., Bone Histomorphometry, Raven Press, New York, 1994.
[5] R.C. Manske, Shankman, G.A., Bone Healing, in: G.A. Skankman, Manske, R.C. (Ed.) Fundamental Orthopaedic Management: for the physical therapist assistant, Mosby, Missouri, 2011.
[6] T. Hildebrand, A. Laib, R. Müller, J. Dequeker, P. Rüegsegger, Direct Three-Dimensional Morphometric Analysis of Human Cancellous Bone: Microstructural Data from Spine, Femur, Iliac Crest, and Calcaneus, Journal of Bone and Mineral Research, 14 (1999) 1167-1174.
[7] E. Storey, S.A. Feik, Remodelling of bone and bones. Effects of altered mechanical stress on anlages, British journal of experimental pathology, 63 (1982) 184-193.
[8] J.F. Griffith, Bone Marrow Changes in Osteoporosis, in: G. Guglielmi (Ed.) Osteoporosis and Bone Densitometry Measurements, Spriner-Verlag, Berlin, 2013.
[9] A.J. Freemont, (I) bone, Current Orthopaedics, 12 (1998) 181-192.
[10] S. Qiu, D.P. Fyhrie, S. Palnitkar, D.S. Rao, Histomorphometric assessment of Haversian canal and osteocyte lacunae in different-sized osteons in human rib, The Anatomical Record Part A: Discoveries in Molecular, Cellular, and Evolutionary Biology, 272A (2003) 520-525.
[11] S.A. Goldstein, R. Goulet, D. McCubbrey, Measurement and significance of three-dimensional architecture to the mechanical integrity of trabecular bone, Calcified Tissue International, 53 (1993) S127-S133.
[12] R.M.V. Pidaparti, D.B. Burr, Collagen fiber orientation and geometry effects on the mechanical properties of secondary osteons, Journal of Biomechanics, 25 (1992) 869-880.
[13] S. Viguet-Carrin, P. Garnero, P.D. Delmas, The role of collagen in bone strength, Osteoporosis International, 17 (2006) 319-336.
[14] D.R. Carter, W.C. Hayes, Fatigue life of compact bone—I effects of stress amplitude, temperature and density, Journal of Biomechanics, 9 (1976) 27-34.
[15] P. Augat, S. Schorlemmer, The role of cortical bone and its microstructure in bone strength, Age and Ageing, 35 (2006) ii27-ii31.
[16] J.D. Currey, The effect of porosity and mineral content on the Young's modulus of elasticity of compact bone, Journal of Biomechanics, 21 (1988) 131-139.
[17] A.L. Boskey, E. DiCarlo, E. Paschalis, P. West, R. Mendelsohn, Comparison of mineral quality and quantity in iliac crest biopsies from high- and low-turnover osteoporosis: an FT-IR microspectroscopic investigation, Osteoporosis International, 16 (2005) 2031-2038.
[18] V. Zaichick, M. Tzaphlidou, Calcium and phosphorus concentrations and the calcium/phosphorus ratio in trabecular bone from the femoral neck of healthy humans as determined by neutron activation analysis, Applied Radiation and Isotopes, 58 (2003) 623-627.

[19] A. Bigi, G. Cojazzi, S. Panzavolta, A. Ripamonti, N. Roveri, M. Romanello, K. Noris Suarez, L. Moro, Chemical and structural characterization of the mineral phase from cortical and trabecular bone, Journal of Inorganic Biochemistry, 68 (1997) 45-51.
[20] L.L. Klepinger, Nutritional Assessment From Bone, Annual Review of Anthropology, 13 (1984) 75-96.
[21] R. Legros, N. Balmain, G. Bonel, Age-related changes in mineral of rat and bovine cortical bone, Calcified Tissue International, 41 (1987) 137-144.
[22] S. Bohic, C. Rey, A. Legrand, H. Sfihi, R. Rohanizadeh, C. Martel, A. Barbier, G. Daculsi, Characterization of the trabecular rat bone mineral: effect of ovariectomy and bisphosphonate treatment, Bone, 26 (2000) 341-348.
[23] N. Kourkoumelis, I. Balatsoukas, M. Tzaphlidou, Ca/P concentration ratio at different sites of normal and osteoporotic rabbit bones evaluated by Auger and energy dispersive X-ray spectroscopy, Journal of Biological Physics, 38 (2012) 279-291.
[24] S.M. Best, A.E. Porter, E.S. Thian, J. Huang, Bioceramics: Past, present and for the future, Journal of the European Ceramic Society, 28 (2008) 1319-1327.
[25] M.M. Huttunen, I. Tillman, H.T. Viljakainen, J. Tuukkanen, Z. Peng, M. Pekkinen, C.J. Lamberg-Allardt, High Dietary Phosphate Intake Reduces Bone Strength in the Growing Rat Skeleton, Journal of Bone and Mineral Research, 22 (2007) 83-92.
[26] B.G. Shah, G.V.G. Krishnarao, H.H. Draper, The Relationship of Ca and P Nutrition during Adult Life and Osteoporosis in Aged Mice, The Journal of Nutrition, 92 (1967) 30-42.
[27] D.M. Black, C.J. Rosen, Postmenopausal Osteoporosis, New England Journal of Medicine, 374 (2016) 254-262.
[28] W.J. Boyle, W.S. Simonet, D.L. Lacey, Osteoclast differentiation and activation, Nature, 423 (2003) 337.
[29] R. Baron, Molecular mechanisms of bone resorption An update, Acta Orthopaedica Scandinavica, 66 (1995) 66-70.
[30] H.K. Vaananen, H. Zhao, M. Mulari, J.M. Halleen, The cell biology of osteoclast function, Journal of Cell Science, 113 (2000) 377-381.
[31] C. Jane Dixon, W.B. Bowler, C.A. Walsh, J.A. Gallagher, Effects of extracellular nucleotides on single cells and populations of human osteoblasts: contribution of cell heterogeneity to relative potencies, British Journal of Pharmacology, 120 (1997) 777-780.
[32] G.Y. Rochefort, S. Pallu, C.L. Benhamou, Osteocyte: the unrecognized side of bone tissue, Osteoporosis International, 21 (2010) 1457-1469.
[33] Y. Hui, R. Zhang, Y. Ren, Y. Liu, J. Wang, J. Feng, The dual function of osteocytes in both demineralization and remineralization processes during bone remodeling, The FASEB Journal, 30 (2016) 1039.1034.
[34] T.A. Franz-Odendaal, B.K. Hall, P.E. Witten, Buried alive: How osteoblasts become osteocytes, Developmental Dynamics, 235 (2006) 176-190.
[35] Y. Gu, W. Zhang, Q. Sun, Y. Hao, J. Zilberberg, W.Y. Lee, Microbead-guided reconstruction of the 3D osteocyte network during microfluidic perfusion culture, Journal of Materials Chemistry B, 3 (2015) 3625-3633.
[36] G.J. Atkins, D.M. Findlay, Osteocyte regulation of bone mineral: a little give and take, Osteoporosis International, 23 (2012) 2067-2079.
[37] L.I. Plotkin, S.C. Manolagas, T. Bellido, Transduction of Cell Survival Signals by Connexin-43 Hemichannels, Journal of Biological Chemistry, 277 (2002) 8648-8657.
[38] L.I. Plotkin, J.I. Aguirre, S. Kousteni, S.C. Manolagas, T. Bellido, Bisphosphonates and Estrogens Inhibit Osteocyte Apoptosis via Distinct Molecular Mechanisms

Downstream of Extracellular Signal-regulated Kinase Activation, Journal of Biological Chemistry, 280 (2005) 7317-7325.
[39] M.N. Wein, Bone Lining Cells: Normal Physiology and Role in Response to Anabolic Osteoporosis Treatments, Current Molecular Biology Reports, 3 (2017) 79-84.
[40] OpenStax, Anatomy & Physiology, 2014.
[41] P.V. Hauschka, A.E. Mavrakos, M.D. Iafrati, S.E. Doleman, M. Klagsbrun, Growth factors in bone matrix. Isolation of multiple types by affinity chromatography on heparin-Sepharose, Journal of Biological Chemistry, 261 (1986) 12665-12674.
[42] M.J. Glimcher, Recent studies of the mineral phase in bone and its possible linkage to the organic matrix by protein-bound phosphate bonds, Philosophical Transactions of the Royal Society of London. B, Biological Sciences, 304 (1984) 479-508.
[43] L. Hessle, K.A. Johnson, H.C. Anderson, S. Narisawa, A. Sali, J.W. Goding, R. Terkeltaub, J.L. Millán, Tissue-nonspecific alkaline phosphatase and plasma cell membrane glycoprotein-1 are central antagonistic regulators of bone mineralization, Proceedings of the National Academy of Sciences, 99 (2002) 9445-9449.
[44] A. Zieba, G. Sethuraman, F. Perez, G.H. Nancollas, D. Cameron, Influence of Organic Phosphonates on Hydroxyapatite Crystal Growth Kinetics, Langmuir, 12 (1996) 2853-2858.
[45] J. An, S. Leeuwenburgh, J. Wolke, J. Jansen, 4 - Mineralization processes in hard tissue: Bone, in: C. Aparicio, M.-P. Ginebra (Eds.) Biomineralization and Biomaterials, Woodhead Publishing, Boston, 2016, pp. 129-146.
[46] J. Christoffersen, W.J. Landis, A contribution with review to the description of mineralization of bone and other calcified tissues in vivo, The Anatomical Record, 230 (1991) 435-450.
[47] P.J. Meunier, G. Boivin, Bone mineral density reflects bone mass but also the degree of mineralization of bone: Therapeutic implications, Bone, 21 (1997) 373-377.
[48] Y.N. Yeni, C.U. Brown, T.L. Norman, Influence of Bone Composition and Apparent Density on Fracture Toughness of the Human Femur and Tibia, Bone, 22 (1998) 79-84.
[49] A. Boskey, Bone mineral crystal size, Osteoporosis International, 14 (2003) 16-21.
[50] A. Bigi, E. Boanini, M. Gazzano, 7 - Ion substitution in biological and synthetic apatites, in: C. Aparicio, M.-P. Ginebra (Eds.) Biomineralization and Biomaterials, Woodhead Publishing, Boston, 2016, pp. 235-266.
[51] G. Montel, G. Bonel, J.C. Heughebaert, J.C. Trombe, C. Rey, New concepts in the composition, crystallization and growth of the mineral component of calcified tissues, Journal of Crystal Growth, 53 (1981) 74-99.
[52] C. Rey, C. Combes, C. Drouet, M.J. Glimcher, Bone mineral: update on chemical composition and structure, Osteoporosis international : a journal established as result of cooperation between the European Foundation for Osteoporosis and the National Osteoporosis Foundation of the USA, 20 (2009) 1013-1021.
[53] A.E. Sobel, P.A. Laurence, Crystal growth in mineralizing tissues, Biochimica et Biophysica Acta, 41 (1960) 1-8.
[54] C. Rey, C. Combes, 3 - Physical chemistry of biological apatites, in: C. Aparicio, M.-P. Ginebra (Eds.) Biomineralization and Biomaterials, Woodhead Publishing, Boston, 2016, pp. 95-127.
[55] C. Rey, B. Collins, T. Goehl, I.R. Dickson, M.J. Glimcher, The carbonate environment in bone mineral: A resolution-enhanced fourier transform infrared spectroscopy study, Calcified Tissue International, 45 (1989) 157-164.
[56] J.-M. Delaissé, T.L. Andersen, M.T. Engsig, K. Henriksen, T. Troen, L. Blavier, Matrix metalloproteinases (MMP) and cathepsin K contribute differently to osteoclastic activities, Microscopy Research and Technique, 61 (2003) 504-513.

[57] R. Florencio-Silva, G.R.d.S. Sasso, E. Sasso-Cerri, M.J. Simões, P.S. Cerri, Biology of Bone Tissue: Structure, Function, and Factors That Influence Bone Cells, BioMed Research International, 2015 (2015) 421746.
[58] E.A. Zimmermann, B. Busse, R.O. Ritchie, The fracture mechanics of human bone: influence of disease and treatment, BoneKEy Rep, 4 (2015).
[59] L. Libuda, U. Alexy, T. Remer, P. Stehle, E. Schoenau, M. Kersting, Association between long-term consumption of soft drinks and variables of bone modeling and remodeling in a sample of healthy German children and adolescents, The American Journal of Clinical Nutrition, 88 (2008) 1670-1677.
[60] U. Alexy, T. Remer, F. Manz, C.M. Neu, E. Schoenau, Long-term protein intake and dietary potential renal acid load are associated with bone modeling and remodeling at the proximal radius in healthy children, The American Journal of Clinical Nutrition, 82 (2005) 1107-1114.
[61] B.N. Epker, H.M. Frost, Periosteal appositional bone growth from age two to age seventy in man. A tetracycline evaluation, The Anatomical Record, 154 (1966) 573-577.
[62] B. Langdahl, S. Ferrari, D.W. Dempster, Bone modeling and remodeling: potential as therapeutic targets for the treatment of osteoporosis, Therapeutic Advances in Musculoskeletal Disease, 8 (2016) 225-235.
[63] S. Kontulainen, H. Sievänen, P. Kannus, M. Pasanen, I. Vuori, Effect of Long-Term Impact-Loading on Mass, Size, and Estimated Strength of Humerus and Radius of Female Racquet-Sports Players: A Peripheral Quantitative Computed Tomography Study Between Young and Old Starters and Controls, Journal of Bone and Mineral Research, 17 (2002) 2281-2289.
[64] M.S. Ominsky, C. Libanati, Q.-T. Niu, R.W. Boyce, P.J. Kostenuik, R.B. Wagman, R. Baron, D.W. Dempster, Sustained Modeling-Based Bone Formation During Adulthood in Cynomolgus Monkeys May Contribute to Continuous BMD Gains With Denosumab, Journal of Bone and Mineral Research, 30 (2015) 1280-1289.
[65] P. Tranquilli Leali, C. Doria, A. Zachos, A. Ruggiu, F. Milia, F. Barca, Bone fragility: current reviews and clinical features, Clinical Cases in Mineral and Bone Metabolism, 6 (2009) 109-113.
[66] L.J. Fraher, Biochemical markers of bone turnover, Clinical Biochemistry, 26 (1993) 431-432.
[67] I.A.-G. Fernández-Tresguerres-Hernández-Gil, MA; del-Canto-Pingarrón, M; Blanco-Jerez, L., Physiological bases of bone regeneration II. The remodeling process., Medicina Oral Patologia Oral y Cirugia Bucal, 11 (2006) E151-E157.
[68] U. Kini, B.N. Nandeesh, Physiology of Bone Formation, Remodeling, and Metabolism, in: I. Fogelman, G. Gnanasegaran, H. van der Wall (Eds.) Radionuclide and Hybrid Bone Imaging, Springer Berlin Heidelberg, Berlin, Heidelberg, 2012, pp. 29-57.
[69] S.C. Manolagas, Birth and Death of Bone Cells: Basic Regulatory Mechanisms and Implications for the Pathogenesis and Treatment of Osteoporosis*, Endocrine Reviews, 21 (2000) 115-137.
[70] T.C. Lee, A. Staines, D. Taylor, Bone adaptation to load: microdamage as a stimulus for bone remodelling, Journal of Anatomy, 201 (2002) 437-446.
[71] D.J. HADJIDAKIS, I.I. ANDROULAKIS, Bone Remodeling, Annals of the New York Academy of Sciences, 1092 (2006) 385-396.
[72] A.W. Friedman, Important Determinants of Bone Strength: Beyond Bone Mineral Density, Journal of Clinical Rheumatology, 12 (2006) 70-77.
[73] R. Marsell, T.A. Einhorn, THE BIOLOGY OF FRACTURE HEALING, Injury, 42 (2011) 551-555.

[74] M.S. Ghiasi, J. Chen, A. Vaziri, E.K. Rodriguez, A. Nazarian, Bone fracture healing in mechanobiological modeling: A review of principles and methods, Bone Reports, 6 (2017) 87-100.
[75] Iain H. Kalfas, Principles of bone healing, Neurosurgical Focus, 10 (2001) 1-4.
[76] Surgery and the NHS in numbers, 2014.
[77] A. Oryan, S. Alidadi, A. Moshiri, N. Maffulli, Bone regenerative medicine: classic options, novel strategies, and future directions, Journal of Orthopaedic Surgery and Research, 9 (2014) 18.
[78] A.S. Brydone, D. Meek, S. Maclaine, Bone grafting, orthopaedic biomaterials, and the clinical need for bone engineering, Proceedings of the Institution of Mechanical Engineers. Part H, Journal of engineering in medicine, 224 (2010) 1329-1343.
[79] J.O. Hollinger, Winn, S., Bonadio, J. , Options for tissue engineering to address challenges of ageing skeleton, Tissue Engineering, 6 (2000) 341-350.
[80] G.B.F. Dickson, Marsh, D., Harkin-Jones, E., Little, U. McCaigue, M., Orthopaedic tissue engineering and bone regeneration., Technology and Healthcare, 15 (2007) 57-67.
[81] M.S. Gaston, A.H.R.W. Simpson, Inhibition of fracture healing, Journal of Bone & Joint Surgery, British Volume, 89-B (2007) 1553-1560.
[82] I.D. Cameron, J.S. Chen, L.M. March, J.M. Simpson, R.G. Cumming, M.J. Seibel, P.N. Sambrook, Hip fracture causes excess mortality owing to cardiovascular and infectious disease in institutionalized older people: A prospective 5-year study, Journal of Bone and Mineral Research, 25 (2010) 866-872.
[83] G.G. Teng, e.R. Curtis, K.G. Saag, Mortality and osteoporotic fractures: is the link causal, and is it modifiable?, Clinical and experimental rheumatology, 26 (2008) S125-S137.
[84] G. Mathew, B.P. Hanson, Global burden of trauma: Need for effective fracture therapies, Indian Journal of Orthopaedics, 43 (2009) 111-116.
[85] K. Azuma, Y. Adachi, H. Hayashi, K.-Y. Kubo, Chronic Psychological Stress as a Risk Factor of Osteoporosis, Journal of UOEH, 37 (2015) 245-253.
[86] J. Zhang, K. Jameson, A.A. Sayer, S. Robinson, C. Cooper, E. Dennison, Accumulation of risk factors associated with poor bone health in older adults, Archives of Osteoporosis, 11 (2016) 3.
[87] A.Z. LaCroix, J.M. Guralnik, L.F. Berkman, R.B. Wallace, S. Satterfield, Maintaining Mobility in Late Life. II. Smoking, Alcohol Consumption, Physical Activity, and Body Mass Index, American Journal of Epidemiology, 137 (1993) 858-869.
[88] S. Scholes, S. Panesar, N.J. Shelton, R.M. Francis, S. Mirza, J.S. Mindell, L.J. Donaldson, Epidemiology of lifetime fracture prevalence in England: a population study of adults aged 55 years and over, Age and Ageing, 43 (2014) 234-240.
[89] D. Donati, C. Zolezzi, P. Tomba, A. Viganò, Bone grafting: historical and conceptual review, starting with an old manuscript by Vittorio Putti, Acta Orthopaedica, 78 (2007) 19-25.
[90] B.J. McEntire, B.S. Bal, M.N. Rahaman, J. Chevalier, G. Pezzotti, Ceramics and ceramic coatings in orthopaedics, Journal of the European Ceramic Society, 35 (2015) 4327-4369.
[91] R. Eyre, R.G. Feltbower, P.W. James, K. Blakey, E. Mubwandarikwa, D. Forman, P.A. McKinney, M.S. Pearce, R.J. McNally, The epidemiology of bone cancer in 0 - 39 year olds in northern England, 1981 - 2002, BMC Cancer, 10 (2010) 357.
[92] H.D. Dorfman, Czerniak, B., Kotz, R., Vanel, D., Park, Y.K., Unni, K.K., WHO Classification of Bone Tumours.
[93] R. Rajagopal, G. Tobin, Radioactivity in drinking water: Expert opinion and policy choices, Environmental Geochemistry and Health, 12 (1990) 267-276.

[94] K.P. Anfinsen, T. Grotmol, O.S. Bruland, T.J. Jonasdottir, Primary bone cancer in Leonbergers may be associated with a higher bodyweight during adolescence, Preventive Veterinary Medicine, 119 (2015) 48-53.
[95] J. Perez-Garcia, E. Muñoz-Couselo, J. Cortes, Bone metastases: Causes, consequences and therapeutic opportunities, European Journal of Cancer Supplements, 11 (2013) 254-256.
[96] R.B. Heimann, Bioceramic Materials, Classic and Advanced Ceramics, Wiley-VCH Verlag GmbH & Co. KGaA2010, pp. 347-419.
[97] M. Navarro, A. Michiardi, O. Castaño, J.A. Planell, Biomaterials in orthopaedics, Journal of the Royal Society Interface, 5 (2008) 1137-1158.
[98] M. Bohner, Resorbable biomaterials as bone graft substitutes, Materials Today, 13 (2010) 24-30.
[99] M. Fröhlich, W.L. Grayson, L.Q. Wan, D. Marolt, M. Drobnic, G. Vunjak-Novakovic, Tissue Engineered Bone Grafts: Biological Requirements, Tissue Culture and Clinical Relevance, Current stem cell research & therapy, 3 (2008) 254-264.
[100] G. Hannink, J.J.C. Arts, Bioresorbability, porosity and mechanical strength of bone substitutes: What is optimal for bone regeneration?, Injury, 42, Supplement 2 (2011) S22-S25.
[101] B.J. Story, Wagner, W.R., Gaisser, D.M., Cook, S.D., Rust-Dawick. A.M., In vivo performance of a modified CSTi dental implant coating, International Journal of Oral Maxillofac Implants, 13 (1998) 749-757.
[102] V. Karageorgiou, D. Kaplan, Porosity of 3D biomaterial scaffolds and osteogenesis, Biomaterials, 26 (2005) 5474-5491.
[103] R.Z. LeGeros, S. Lin, R. Rohanizadeh, D. Mijares, J.P. LeGeros, Biphasic calcium phosphate bioceramics: preparation, properties and applications, J Mater Sci: Mater Med, 14 (2003) 201-209.
[104] P.S. EGGLI, W. MOLLER, R.K. SCHENK, Porous Hydroxyapatite and Tricalcium Phosphate Cylinders with Two Different Pore Size Ranges Implanted in the Cancellous Bone of Rabbits: A Comparative Histomorphometric and Histologic Study of Bony Ingrowth and Implant Substitution, Clinical Orthopaedics and Related Research, 232 (1988) 127-138.
[105] J. Vivanco, A. Aiyangar, A. Araneda, H.-L. Ploeg, Mechanical characterization of injection-molded macro porous bioceramic bone scaffolds, Journal of the Mechanical Behavior of Biomedical Materials, 9 (2012) 137-152.
[106] Y.H. An, Draughn, R.A., Mechanical testing of bone and the bone-implant interface, CRC Press, Boca Raton, 2000.
[107] M.P. Ginebra, 10 - Calcium phosphate bone cements A2 - Deb, Sanjukta, Orthopaedic Bone Cements, Woodhead Publishing2008, pp. 206-230.
[108] T.J. Cypher, J.P. Grossman, Biological principles of bone graft healing, The Journal of Foot and Ankle Surgery, 35 (1996) 413-417.
[109] W. Wang, K.W.K. Yeung, Bone grafts and biomaterials substitutes for bone defect repair: A review, Bioactive Materials, 2 (2017) 224-247.
[110] C.G. Finkemeier, Bone-Grafting and Bone-Graft Substitutes, The Journal of Bone & Joint Surgery, 84 (2002) 454-464.
[111] A.R. Gazdag, J.M. Lane, D. Glaser, R.A. Forster, Alternatives to Autogenous Bone Graft: Efficacy and Indications, JAAOS - Journal of the American Academy of Orthopaedic Surgeons, 3 (1995) 1-8.
[112] E.R. Carlisle, J.S. Fischgrund, CHAPTER 27 - Bone Graft and Fusion Enhancement A2 - Errico, Thomas J, in: B.S. Lonner, A.W. Moulton (Eds.) Surgical Management of Spinal Deformities, W.B. Saunders, Philadelphia, 2009, pp. 433-448.

[113] B.K. Culpepper, P.P. Bonvallet, M.S. Reddy, S. Ponnazhagan, S.L. Bellis, Polyglutamate directed coupling of bioactive peptides for the delivery of osteoinductive signals on allograft bone, Biomaterials, 34 (2013) 1506-1513.
[114] V.-V. Välimäki, H.T. Aro, Molecular Basis for Action of Bioactive Glasses as Bone Graft Substitute, Scandinavian Journal of Surgery, 95 (2006) 95-102.
[115] J.B. Park, Metallic Implant Materials, Biomaterials Science and Engineering, Springer US, Boston, MA, 1984, pp. 193-233.
[116] H. Hermawan, Ramdan, D., Djuansjah, R.P., Metals for Biomedical Applications, in: R. Fazel-Rezai (Ed.) Biomedical Engineering - From Theory to Applications, Intech2011.
[117] M.Z. Ibrahim, A.A.D. Sarhan, F. Yusuf, M. Hamdi, Biomedical materials and techniques to improve the tribological, mechanical and biomedical properties of orthopedic implants – A review article, Journal of Alloys and Compounds, 714 (2017) 636-667.
[118] V. Sansone, D. Pagani, M. Melato, The effects on bone cells of metal ions released from orthopaedic implants. A review, Clinical Cases in Mineral and Bone Metabolism, 10 (2013) 34-40.
[119] Q. Chen, G.A. Thouas, Metallic implant biomaterials, Materials Science and Engineering: R: Reports, 87 (2015) 1-57.
[120] A. Muñoz, M. Costa, Elucidating the mechanisms of nickel compound uptake: A review of particulate and nano-nickel endocytosis and toxicity, Toxicology and Applied Pharmacology, 260 (2012) 1-16.
[121] P. Stenlund, O. Omar, U. Brohede, S. Norgren, B. Norlindh, A. Johansson, J. Lausmaa, P. Thomsen, A. Palmquist, Bone response to a novel Ti–Ta–Nb–Zr alloy, Acta Biomaterialia, 20 (2015) 165-175.
[122] C. Aguilar, C. Guerra, S. Lascano, D. Guzman, P.A. Rojas, M. Thirumurugan, L. Bejar, A. Medina, Synthesis and characterization of Ti–Ta–Nb–Mn foams, Materials Science and Engineering: C, 58 (2016) 420-431.
[123] H. Matsuno, A. Yokoyama, F. Watari, M. Uo, T. Kawasaki, Biocompatibility and osteogenesis of refractory metal implants, titanium, hafnium, niobium, tantalum and rhenium, Biomaterials, 22 (2001) 1253-1262.
[124] M. Vallet-Regí, J.M. González-Calbet, Calcium phosphates as substitution of bone tissues, Progress in Solid State Chemistry, 32 (2004) 1-31.
[125] B.G.X. Zhang, D.E. Myers, G.G. Wallace, M. Brandt, P.F.M. Choong, Bioactive Coatings for Orthopaedic Implants—Recent Trends in Development of Implant Coatings, International Journal of Molecular Sciences, 15 (2014) 11878-11921.
[126] K. Søballe, Hydroxyapatite ceramic coating for bone implant fixation, Acta Orthopaedica Scandinavica, 64 (1993) 1-58.
[127] J.C. Middleton, A.J. Tipton, Synthetic biodegradable polymers as orthopedic devices, Biomaterials, 21 (2000) 2335-2346.
[128] R. Kroeze, M. Helder, L. Govaert, T. Smit, Biodegradable Polymers in Bone Tissue Engineering, Materials, 2 (2009) 833.
[129] M.C. Meikle, S. Papaioannou, T.J. Ratledge, P.M. Speight, S.R. Watt-Smith, P.A. Hill, J.J. Reynolds, Effect of poly DL-lactide-co-glycolide implants and xenogeneic bone matrix-derived growth factors on calvarial bone repair in the rabbit, Biomaterials, 15 (1994) 513-521.
[130] Q. Yao, J.G.L. Cosme, T. Xu, J.M. Miszuk, P.H.S. Picciani, H. Fong, H. Sun, Three dimensional electrospun PCL/PLA blend nanofibrous scaffolds with significantly improved stem cells osteogenic differentiation and cranial bone formation, Biomaterials, 115 (2017) 115-127.

[131] P. Fabbri, V. Cannillo, A. Sola, A. Dorigato, F. Chiellini, Highly porous polycaprolactone-45S5 Bioglass® scaffolds for bone tissue engineering, Composites Science and Technology, 70 (2010) 1869-1878.
[132] S. Eshraghi, S. Das, Mechanical and microstructural properties of polycaprolactone scaffolds with one-dimensional, two-dimensional, and three-dimensional orthogonally oriented porous architectures produced by selective laser sintering, Acta Biomaterialia, 6 (2010) 2467-2476.
[133] K. Khoshroo, T.S. Jafarzadeh Kashi, F. Moztarzadeh, M. Tahriri, H.E. Jazayeri, L. Tayebi, Development of 3D PCL microsphere/TiO2 nanotube composite scaffolds for bone tissue engineering, Materials Science and Engineering: C, 70 (2017) 586-598.
[134] X. Li, S. Zhang, X. Zhang, S. Xie, G. Zhao, L. Zhang, Biocompatibility and physicochemical characteristics of poly(Ɛ-caprolactone)/poly(lactide-co-glycolide)/nano-hydroxyapatite composite scaffolds for bone tissue engineering, Materials & Design, 114 (2017) 149-160.
[135] H.-Y. Cheung, K.-T. Lau, T.-P. Lu, D. Hui, A critical review on polymer-based bio-engineered materials for scaffold development, Composites Part B: Engineering, 38 (2007) 291-300.
[136] S. Bose, M. Roy, A. Bandyopadhyay, Recent advances in bone tissue engineering scaffolds, Trends in Biotechnology, 30 (2012) 546-554.
[137] K.M. Ainslie, S.L. Tao, K.C. Popat, H. Daniels, V. Hardev, C.A. Grimes, T.A. Desai, In vitro inflammatory response of nanostructured titania, silicon oxide, and polycaprolactone, Journal of Biomedical Materials Research Part A, 91A (2009) 647-655.
[138] L.L. Hench, R.J. Splinter, W.C. Allen, T.K. Greenlee, Bonding mechanisms at the interface of ceramic prosthetic materials, Journal of Biomedical Materials Research, 5 (1971) 117-141.
[139] L.-C. Gerhardt, A.R. Boccaccini, Bioactive Glass and Glass-Ceramic Scaffolds for Bone Tissue Engineering, Materials, 3 (2010) 3867.
[140] S. Radin, G. Reilly, G. Bhargave, P.S. Leboy, P. Ducheyne, Osteogenic effects of bioactive glass on bone marrow stromal cells, Journal of Biomedical Materials Research Part A, 73A (2005) 21-29.
[141] L.L. Hench, J.K. West, Biological applications of bioactive glasses, Harwood Academic Publishers1996.
[142] A. Mahato, B. Kundu, P. Mukherjee, S.K. Nandi, Applications of Different Bioactive Glass and Glass-Ceramic Materials for Osteoconductivity and Osteoinductivity, Transactions of the Indian Ceramic Society, 76 (2017) 149-158.
[143] N. Drnovšek, S. Novak, U. Dragin, M. Čeh, M. Gorenšek, M. Gradišar, Bioactive glass enhances bone ingrowth into the porous titanium coating on orthopaedic implants, International Orthopaedics, 36 (2012) 1739-1745.
[144] L. Floroian, Popescu, A., Serban, N., Mihailescu, I., Polymer-Bioglass Composite Coatings: A Promising Alternative For Advanced Biomedical Implants, in: Cuppoletti (Ed.) Metal, Ceramic and Polymeric Composites for Various Uses, Intech2011.
[145] S.-I. Roohani-Esfahani, P. Newman, H. Zreiqat, Design and Fabrication of 3D printed Scaffolds with a Mechanical Strength Comparable to Cortical Bone to Repair Large Bone Defects, Scientific Reports, 6 (2016) 19468.
[146] I.D. Thompson, L.L. Hench, Mechanical properties of bioactive glasses, glass-ceramics and composites, Proceedings of the Institution of Mechanical Engineers, Part H: Journal of Engineering in Medicine, 212 (1998) 127-136.

[147] J.M. M. Elbadawi, L. Hopkins and I. Reaney, Progress in Bioactive Metal and, Ceramic Implants for Load- Bearing Application, in: A.R.Z.a.J.B.d. Miranda (Ed.) Advanced Techniques in Bone Regeneration2016.
[148] H. Wang, W. Zhi, X. Lu, X. Li, K. Duan, R. Duan, Y. Mu, J. Weng, Comparative studies on ectopic bone formation in porous hydroxyapatite scaffolds with complementary pore structures, Acta Biomaterialia, 9 (2013) 8413-8421.
[149] D. Bellucci, A. Sola, V. Cannillo, Hydroxyapatite and tricalcium phosphate composites with bioactive glass as second phase: State of the art and current applications, Journal of Biomedical Materials Research Part A, 104 (2016) 1030-1056.
[150] L. Lin, K.L. Chow, Y. Leng, Study of hydroxyapatite osteoinductivity with an osteogenic differentiation of mesenchymal stem cells, Journal of Biomedical Materials Research Part A, 89A (2009) 326-335.
[151] E. Tsiridis, A. Bhalla, Z. Ali, N. Gurav, M. Heliotis, S. Deb, L. DiSilvio, Enhancing the osteoinductive properties of hydroxyapatite by the addition of human mesenchymal stem cells, and recombinant human osteogenic protein-1 (BMP-7) in vitro, Injury, 37 (2006) S25-S32.
[152] G. Daculsi, R.Z. Legeros, E. Nery, K. Lynch, B. Kerebel, Transformation of biphasic calcium phosphate ceramics in vivo: Ultrastructural and physicochemical characterization, Journal of Biomedical Materials Research, 23 (1989) 883-894.
[153] F. Barrère, C.A. van Blitterswijk, K. de Groot, Bone regeneration: molecular and cellular interactions with calcium phosphate ceramics, International Journal of Nanomedicine, 1 (2006) 317-332.
[154] C. Rey, Calcium phosphate biomaterials and bone mineral. Differences in composition, structures and properties, Biomaterials, 11 (1990) 13-15.
[155] S. Joschek, B. Nies, R. Krotz, A. Göpferich, Chemical and physicochemical characterization of porous hydroxyapatite ceramics made of natural bone, Biomaterials, 21 (2000) 1645-1658.
[156] M. Yamada, M. Shiota, Y. Yamashita, S. Kasugai, Histological and histomorphometrical comparative study of the degradation and osteoconductive characteristics of α- and β-tricalcium phosphate in block grafts, Journal of Biomedical Materials Research Part B: Applied Biomaterials, 82B (2007) 139-148.
[157] M. Kamitakahara, C. Ohtsuki, T. Miyazaki, Review Paper: Behavior of Ceramic Biomaterials Derived from Tricalcium Phosphate in Physiological Condition, Journal of Biomaterials Applications, 23 (2008) 197-212.
[158] N. Rangavittal, A.R. Landa-Cánovas, J.M. González-Calbet, M. Vallet-Regí, Structural study and stability of hydroxyapatite and β-tricalcium phosphate: Two important bioceramics, Journal of Biomedical Materials Research, 51 (2000) 660-668.
[159] D. Shi, G. Jiang, J. Bauer, The effect of structural characteristics on the in vitro bioactivity of hydroxyapatite, Journal of Biomedical Materials Research, 63 (2002) 71-78.
[160] V. Uskoković, The role of hydroxyl channel in defining selected physicochemical peculiarities exhibited by hydroxyapatite, RSC Advances, 5 (2015) 36614-36633.
[161] N. Matsumoto, K. Yoshida, K. Hashimoto, Y. Toda, Thermal stability of β-tricalcium phosphate doped with monovalent metal ions, Materials Research Bulletin, 44 (2009) 1889-1894.
[162] M. Okazaki, M. Sato, Computer graphics of hydroxyapatite and β-tricalcium phosphate, Biomaterials, 11 (1990) 573-578.
[163] J.D. Pasteris, B. Wopenka, J.J. Freeman, K. Rogers, E. Valsami-Jones, J.A.M. van der Houwen, M.J. Silva, Lack of OH in nanocrystalline apatite as a function of degree of atomic order: implications for bone and biomaterials, Biomaterials, 25 (2004) 229-238.

[164] A. El-Ghannam, C.Q. Ning, J. Mehta, Cyclosilicate nanocomposite: A novel resorbable bioactive tissue engineering scaffold for BMP and bone-marrow cell delivery, Journal of Biomedical Materials Research Part A, 71A (2004) 377-390.
[165] J.C. Elliott, Structure and chemistry of the apatites and other calcium orthophosphates, Amsterdam London : Elsevier, c19941994.
[166] X. Li, A. Ito, Y. Sogo, X. Wang, R.Z. LeGeros, Solubility of Mg-containing β-tricalcium phosphate at 25°C, Acta Biomaterialia, 5 (2009) 508-517.
[167] M. Schumacher, A. Henß, M. Rohnke, M. Gelinsky, A novel and easy-to-prepare strontium(II) modified calcium phosphate bone cement with enhanced mechanical properties, Acta Biomaterialia, 9 (2013) 7536-7544.
[168] I. Uysal, F. Severcan, A. Tezcaner, Z. Evis, Co-doping of hydroxyapatite with zinc and fluoride improves mechanical and biological properties of hydroxyapatite, Progress in Natural Science: Materials International, 24 (2014) 340-349.
[169] H.-S. Ryu, K.S. Hong, J.-K. Lee, D.J. Kim, J.H. Lee, B.-S. Chang, D.-h. Lee, C.-K. Lee, S.-S. Chung, Magnesia-doped HA/β-TCP ceramics and evaluation of their biocompatibility, Biomaterials, 25 (2004) 393-401.
[170] A. Royer, J.C. Viguie, M. Heughebaert, J.C. Heughebaert, Stoichiometry of hydroxyapatite: influence on the flexural strength, J Mater Sci: Mater Med, 4 (1993) 76-82.
[171] W. Suchanek, M. Yoshimura, Processing and properties of hydroxyapatite-based biomaterials for use as hard tissue replacement implants, Journal of Materials Research, 13 (2011) 94-117.
[172] J.-S. Bow, S.-C. Liou, S.-Y. Chen, Structural characterization of room-temperature synthesized nano-sized β-tricalcium phosphate, Biomaterials, 25 (2004) 3155-3161.
[173] L. Pighinelli, M. Kucharska, Chitosan–hydroxyapatite composites, Carbohydrate Polymers, 93 (2013) 256-262.
[174] H.-M. Kim, T. Himeno, T. Kokubo, T. Nakamura, Process and kinetics of bonelike apatite formation on sintered hydroxyapatite in a simulated body fluid, Biomaterials, 26 (2005) 4366-4373.
[175] J. Vandiver, D. Dean, N. Patel, W. Bonfield, C. Ortiz, Nanoscale variation in surface charge of synthetic hydroxyapatite detected by chemically and spatially specific high-resolution force spectroscopy, Biomaterials, 26 (2005) 271-283.
[176] S. Nakamura, T. Kobayashi, M. Nakamura, S. Itoh, K. Yamashita, Electrostatic surface charge acceleration of bone ingrowth of porous hydroxyapatite/β-tricalcium phosphate ceramics, Journal of Biomedical Materials Research Part A, 92A (2010) 267-275.
[177] E. Fujii, M. Ohkubo, K. Tsuru, S. Hayakawa, A. Osaka, K. Kawabata, C. Bonhomme, F. Babonneau, Selective protein adsorption property and characterization of nano-crystalline zinc-containing hydroxyapatite, Acta Biomaterialia, 2 (2006) 69-74.
[178] W.-H. Lee, C.-Y. Loo, R. Rohanizadeh, A review of chemical surface modification of bioceramics: Effects on protein adsorption and cellular response, Colloids and Surfaces B: Biointerfaces, 122 (2014) 823-834.
[179] E.A. dos Santos, M. Farina, G.A. Soares, K. Anselme, Surface energy of hydroxyapatite and β-tricalcium phosphate ceramics driving serum protein adsorption and osteoblast adhesion, J Mater Sci: Mater Med, 19 (2008) 2307-2316.
[180] Z. Sheikh, M.-N. Abdallah, A.A. Hanafi, S. Misbahuddin, H. Rashid, M. Glogauer, Mechanisms of in Vivo Degradation and Resorption of Calcium Phosphate Based Biomaterials, Materials, 8 (2015) 7913-7925.
[181] J.F. Osborn, H. Newesely, The material science of calcium phosphate ceramics, Biomaterials, 1 (1980) 108-111.

[182] W. Qiao, Q. Liu, Z. Li, H. Zhang, Z. Chen, Changes in physicochemical and biological properties of porcine bone derived hydroxyapatite induced by the incorporation of fluoride, Science and Technology of Advanced Materials, 18 (2017) 110-121.
[183] S. Samavedi, A.R. Whittington, A.S. Goldstein, Calcium phosphate ceramics in bone tissue engineering: A review of properties and their influence on cell behavior, Acta Biomaterialia, 9 (2013) 8037-8045.
[184] A. Boskey, Paschalis, E., Matrix proteins and biomineralization, in: J. Davies (Ed.) Bone Engineering, EM Square Incorporated, Toronto, 2001, pp. 44-61.
[185] M. Neo, T. Nakamura, C. Ohtsuki, T. Kokubo, T. Yamamuro, Apatite formation on three kinds of bioactive material at an early stage in vivo: A comparative study by transmission electron microscopy, Journal of Biomedical Materials Research, 27 (1993) 999-1006.
[186] S.J. Kalita, A. Bhardwaj, H.A. Bhatt, Nanocrystalline calcium phosphate ceramics in biomedical engineering, Materials Science and Engineering: C, 27 (2007) 441-449.
[187] I. Denry, L.T. Kuhn, Design and Characterization of Calcium Phosphate Ceramic Scaffolds for Bone Tissue Engineering, Dental materials : official publication of the Academy of Dental Materials, 32 (2016) 43-53.
[188] Y. Li, Q. Li, S. Zhu, E. Luo, J. Li, G. Feng, Y. Liao, J. Hu, The effect of strontium-substituted hydroxyapatite coating on implant fixation in ovariectomized rats, Biomaterials, 31 (2010) 9006-9014.
[189] A.E. Porter, N. Patel, J.N. Skepper, S.M. Best, W. Bonfield, Comparison of in vivo dissolution processes in hydroxyapatite and silicon-substituted hydroxyapatite bioceramics, Biomaterials, 24 (2003) 4609-4620.
[190] A. El-Ghannam, P. Ducheyne, 1.9 Bioactive Ceramics☆, Comprehensive Biomaterials II, Elsevier, Oxford, 2017, pp. 204-234.
[191] E.W.H. Bodde, J.G.C. Wolke, R.S.Z. Kowalski, J.A. Jansen, Bone regeneration of porous β-tricalcium phosphate (Conduit™ TCP) and of biphasic calcium phosphate ceramic (Biosel®) in trabecular defects in sheep, Journal of Biomedical Materials Research Part A, 82A (2007) 711-722.
[192] V. Kartsogiannis, K.W. Ng, Cell lines and primary cell cultures in the study of bone cell biology, Molecular and Cellular Endocrinology, 228 (2004) 79-102.
[193] Y. Hong, H. Fan, B. Li, B. Guo, M. Liu, X. Zhang, Fabrication, biological effects, and medical applications of calcium phosphate nanoceramics, Materials Science and Engineering: R: Reports, 70 (2010) 225-242.
[194] M.F. Ashby, Cellular ceramics [electronic resource] : structure, manufacturing, properties and applications, Weinheim : Wiley-VCH, 20052005.
[195] R. Gilissen, J.P. Erauw, A. Smolders, E. Vanswijgenhoven, J. Luyten, Gelcasting, a near net shape technique, Materials & Design, 21 (2000) 251-257.
[196] B. Chen, T. Zhang, J. Zhang, Q. Lin, D. Jiang, Microstructure and mechanical properties of hydroxyapatite obtained by gel-casting process, Ceramics International, 34 (2008) 359-364.
[197] B. Mondal, S. Mondal, A. Mondal, N. Mandal, Fish scale derived hydroxyapatite scaffold for bone tissue engineering, Materials Characterization, 121 (2016) 112-124.
[198] M. Trunec, Z. Chlup, Subtractive manufacturing of customized hydroxyapatite scaffolds for bone regeneration, Ceramics International, 43 (2017) 11265-11273.
[199] C. Vakifahmetoglu, D. Zeydanli, P. Colombo, Porous polymer derived ceramics, Materials Science and Engineering: R: Reports, 106 (2016) 1-30.

[200] J. Anita Lett, M. Sundareswari, K. Ravichandran, Porous hydroxyapatite scaffolds for orthopedic and dental applications - the role of binders, Materials Today: Proceedings, 3 (2016) 1672-1677.
[201] G. Tripathi, B. Basu, A porous hydroxyapatite scaffold for bone tissue engineering: Physico-mechanical and biological evaluations, Ceramics International, 38 (2012) 341-349.
[202] S.K. Swain, S. Bhattacharyya, D. Sarkar, Preparation of porous scaffold from hydroxyapatite powders, Materials Science and Engineering: C, 31 (2011) 1240-1244.
[203] J. Wang, Y. Zhu, M. Wang, D. Liu, X. Chen, X. Zhu, X. Yang, K. Zhang, Y. Fan, X. Zhang, Fabrication and preliminary biological evaluation of a highly porous biphasic calcium phosphate scaffold with nano-hydroxyapatite surface coating, Ceramics International, 44 (2018) 1304-1311.
[204] J.-H. Lee, H.-E. Kim, Y.-H. Koh, Highly porous titanium (Ti) scaffolds with bioactive microporous hydroxyapatite/TiO2 hybrid coating layer, Materials Letters, 63 (2009) 1995-1998.
[205] K.H. Zuo, Y. Zhang, Y.-P. Zeng, D. Jiang, Pore-forming agent induced microstructure evolution of freeze casted hydroxyapatite, Ceramics International, 37 (2011) 407-410.
[206] Z. Chen, X. Zhang, Y. Yang, K. Zhou, N. Wragg, Y. Liu, M. Lewis, C. Liu, Fabrication and characterization of 3D complex hydroxyapatite scaffolds with hierarchical porosity of different features for optimal bioactive performance, Ceramics International, 43 (2017) 336-344.
[207] D.-M. LIU Fabrication of hydroxyapatite ceramic with controlled porosity, J Mater Sci: Mater Med, 8 (1997) 227-232.
[208] D.-M. Liu, Preparation and characterisation of porous hydroxyapatite bioceramic via a slip-casting route, Ceramics International, 24 (1998) 441-446.
[209] S.R. Dash, R. Sarkar, S. Bhattacharyya, Gel casting of hydroxyapatite with naphthalene as pore former, Ceramics International, 41 (2015) 3775-3790.
[210] Y.-H. Koh, H.-W. Kim, H.-E. Kim, J.W. Halloran, Fabrication of Macrochannelled-Hydroxyapatite Bioceramic by a Coextrusion Process, Journal of the American Ceramic Society, 85 (2002) 2578-2580.
[211] H.J. Kim, I.K. Park, J.H. Kim, C.S. Cho, M.S. Kim, Gas foaming fabrication of porous biphasic calcium phosphate for bone regeneration, Tissue Engineering and Regenerative Medicine, 9 (2012) 63-68.
[212] H. Janik, M. Marzec, A review: Fabrication of porous polyurethane scaffolds, Materials Science and Engineering: C, 48 (2015) 586-591.
[213] S. Deville, E. Saiz, A.P. Tomsia, Freeze casting of hydroxyapatite scaffolds for bone tissue engineering, Biomaterials, 27 (2006) 5480-5489.
[214] H.D. Espinosa, R. Soler-Crespo, Lessons from tooth enamel, Nature, 543 (2017) 42.
[215] J. Cihlář, M. Tranec, Injection moulded hydroxyapatite ceramics, Biomaterials, 17 (1996) 1905-1911.
[216] A.B.M. Azlina, A.A.S. Norazlini, I.M. Hussain, Tribology study of hydroxyapatite (HAp) scaffold blended single based binder via rheology and mechanical properties, Industrial Lubrication and Tribology, 69 (2017) 414-419.
[217] A. Dehghan-Manshadi, M.J. Bermingham, M.S. Dargusch, D.H. StJohn, M. Qian, Metal injection moulding of titanium and titanium alloys: Challenges and recent development, Powder Technology, 319 (2017) 289-301.
[218] L. Zema, G. Loreti, A. Melocchi, A. Maroni, A. Gazzaniga, Injection Molding and its application to drug delivery, Journal of Controlled Release, 159 (2012) 324-331.

[219] P.K. Zysset, X. Edward Guo, C. Edward Hoffler, K.E. Moore, S.A. Goldstein, Elastic modulus and hardness of cortical and trabecular bone lamellae measured by nanoindentation in the human femur, Journal of Biomechanics, 32 (1999) 1005-1012.
[220] J. Liu, C. Gao, P. Feng, S. Peng, C. Shuai, Selective laser sintering of β-TCP/nano-58S composite scaffolds with improved mechanical properties, Materials & Design, 84 (2015) 395-401.
[221] B. Derby, Inkjet printing ceramics: From drops to solid, Journal of the European Ceramic Society, 31 (2011) 2543-2550.
[222] J.G. Dellinger, A.M. Wojtowicz, R.D. Jamison, Effects of degradation and porosity on the load bearing properties of model hydroxyapatite bone scaffolds, Journal of Biomedical Materials Research Part A, 77 (2006) 563-571.
[223] D.J. Shanefield, Organic additives and ceramic processing : with applications in powder metallurgy, ink, and paint, Boston London : Kluwer Academic, c1995, Boston, London, 1995.
[224] N.Y. Mostafa, H.M. Hassan, F.H. Mohamed, Sintering behavior and thermal stability of Na+, SiO44− and CO32− co-substituted hydroxyapatites, Journal of Alloys and Compounds, 479 (2009) 692-698.
[225] S. Best, W. Bonfield, Processing behaviour of hydroxyapatite powders with contrasting morphology, J Mater Sci: Mater Med, 5 (1994) 516-521.
[226] A. Banerjee, A. Bandyopadhyay, S. Bose, Hydroxyapatite nanopowders: Synthesis, densification and cell–materials interaction, Materials Science and Engineering: C, 27 (2007) 729-735.
[227] M.N. Rahaman, Ceramic Processing and Sintering, Taylor & Francis Group, Florida, 2003.
[228] G.C. Robinson, Ceramic Processing Before Firing, Wiley-Interscience Publications1978.
[229] D.W. Richerson, Modern ceramic engineering : properties, processing, and use in design, 3rd ed. ed., Boca Raton, Fla. London : CRC, 2006, Boca Raton, Fla. London, 2006.
[230] S. Spath, P. Drescher, H. Seitz, Impact of Particle Size of Ceramic Granule Blends on Mechanical Strength and Porosity of 3D Printed Scaffolds, Materials, 8 (2015) 4720.
[231] E. Cunningham, N. Dunne, G. Walker, F. Buchanan, High-solid-content hydroxyapatite slurry for the production of bone substitute scaffolds, Proceedings of the Institution of Mechanical Engineers, Part H: Journal of Engineering in Medicine, 223 (2009) 727-737.
[232] Z. Kaviani, A. Zamanian, Effect of Nanohydroxyapatite Addition on the Pore Morphology and Mechanical Properties of Freeze Cast Hydroxyapatite Scaffolds, Procedia Materials Science, 11 (2015) 190-195.
[233] A. Zamanian, S. Farhangdoust, M. Yasaei, M. Khorami, M. Hafezi, The Effect of Particle Size on the Mechanical and Microstructural Properties of Freeze-Casted Macroporous Hydroxyapatite Scaffolds, International Journal of Applied Ceramic Technology, 11 (2014) 12-21.
[234] S. Michna, W. Wu, J.A. Lewis, Concentrated hydroxyapatite inks for direct-write assembly of 3-D periodic scaffolds, Biomaterials, 26 (2005) 5632-5639.
[235] Y. Ryabenkova, A. Pinnock, P.A. Quadros, R.L. Goodchild, G. Möbus, A. Crawford, P.V. Hatton, C.A. Miller, The relationship between particle morphology and rheological properties in injectable nano-hydroxyapatite bone graft substitutes, Materials Science and Engineering: C, 75 (2017) 1083-1090.

[236] J. Marchi, P. Greil, J.C. Bressiani, A. Bressiani, F. Müller, Influence of Synthesis Conditions on the Characteristics of Biphasic Calcium Phosphate Powders, International Journal of Applied Ceramic Technology, 6 (2009) 60-71.
[237] C.Y. Tang, P.S. Uskokovic, C.P. Tsui, D. Veljovic, R. Petrovic, D. Janackovic, Influence of microstructure and phase composition on the nanoindentation characterization of bioceramic materials based on hydroxyapatite, Ceramics International, 35 (2009) 2171-2178.
[238] S. Kannan, J.H.G. Rocha, J.M.G. Ventura, A.F. Lemos, J.M.F. Ferreira, Effect of Ca/P ratio of precursors on the formation of different calcium apatitic ceramics—An X-ray diffraction study, Scripta Materialia, 53 (2005) 1259-1262.
[239] F. Gervaso, F. Scalera, S. Kunjalukkal Padmanabhan, A. Sannino, A. Licciulli, High-Performance Hydroxyapatite Scaffolds for Bone Tissue Engineering Applications, International Journal of Applied Ceramic Technology, 9 (2012) 507-516.
[240] A.A. Chaudhry, H. Yan, K. Gong, F. Inam, G. Viola, M.J. Reece, J.B.M. Goodall, I. ur Rehman, F.K. McNeil-Watson, J.C.W. Corbett, J.C. Knowles, J.A. Darr, High-strength nanograined and translucent hydroxyapatite monoliths via continuous hydrothermal synthesis and optimized spark plasma sintering, Acta Biomaterialia, 7 (2011) 791-799.
[241] J.C. Merry, I.R. Gibson, S.M. Best, W. Bonfield, Synthesis and characterization of carbonate hydroxyapatite, J Mater Sci: Mater Med, 9 (1998) 779-783.
[242] S. Raynaud, E. Champion, J.P. Lafon, D. Bernache-Assollant, Calcium phosphate apatites with variable Ca/P atomic ratio III. Mechanical properties and degradation in solution of hot pressed ceramics, Biomaterials, 23 (2002) 1081-1089.
[243] N.Y. Mostafa, Characterization, thermal stability and sintering of hydroxyapatite powders prepared by different routes, Materials Chemistry and Physics, 94 (2005) 333-341.
[244] S. Raynaud, E. Champion, D. Bernache-Assollant, P. Thomas, Calcium phosphate apatites with variable Ca/P atomic ratio I. Synthesis, characterisation and thermal stability of powders, Biomaterials, 23 (2002) 1065-1072.
[245] C. Durucan, P.W. Brown, α-Tricalcium phosphate hydrolysis to hydroxyapatite at and near physiological temperature, J Mater Sci: Mater Med, 11 (2000) 365-371.
[246] F. Apfelbaum, H. Diab, I. Mayer, J.D.B. Featherstone, An FTIR study of carbonate in synthetic apatites, Journal of Inorganic Biochemistry, 45 (1992) 277-282.
[247] H.R. Ramay, M. Zhang, Preparation of porous hydroxyapatite scaffolds by combination of the gel-casting and polymer sponge methods, Biomaterials, 24 (2003) 3293-3302.
[248] Y.-M. Soon, K.-H. Shin, Y.-H. Koh, J.-H. Lee, W.-Y. Choi, H.-E. Kim, Fabrication and compressive strength of porous hydroxyapatite scaffolds with a functionally graded core/shell structure, Journal of the European Ceramic Society, 31 (2011) 13-18.
[249] I. Sabree, J.E. Gough, B. Derby, Mechanical properties of porous ceramic scaffolds: Influence of internal dimensions, Ceramics International, 41 (2015) 8425-8432.
[250] T.Y. Yang, J.M. Lee, S.Y. Yoon, H.C. Park, Hydroxyapatite scaffolds processed using a TBA-based freeze-gel casting/polymer sponge technique, J Mater Sci: Mater Med, 21 (2010) 1495-1502.
[251] A.F. Lemos, J.M.F. Ferreira, Combining Foaming and Starch Consolidation Methods to Develop Macroporous Hydroxyapatite Implants, Key Engineering Materials, 254-256 (2004) 1041-1044.
[252] J.R. Woodard, A.J. Hilldore, S.K. Lan, C.J. Park, A.W. Morgan, J.A.C. Eurell, S.G. Clark, M.B. Wheeler, R.D. Jamison, A.J. Wagoner Johnson, The mechanical properties

and osteoconductivity of hydroxyapatite bone scaffolds with multi-scale porosity, Biomaterials, 28 (2007) 45-54.
[253] J.G. Dellinger, J. Cesarano, R.D. Jamison, Robotic deposition of model hydroxyapatite scaffolds with multiple architectures and multiscale porosity for bone tissue engineering, Journal of Biomedical Materials Research Part A, 82A (2007) 383-394.
[254] L.M. Rodríguez-Lorenzo, M. Vallet-Regí, J.M.F. Ferreira, Fabrication of porous hydroxyapatite bodies by a new direct consolidation method: starch consolidation, Journal of Biomedical Materials Research, 60 (2002) 232-240.
[255] E. Munch, J. Franco, S. Deville, P. Hunger, E. Saiz, A.P. Tomsia, Porous ceramic scaffolds with complex architectures, JOM, 60 (2008) 54-58.
[256] L. Gorjan, L. Reiff, A. Liersch, F. Clemens, Ethylene vinyl acetate as a binder for additive manufacturing of tricalcium phosphate bio-ceramics, Ceramics International, 44 (2018) 15817-15823.
[257] C.F. Marques, F.H. Perera, A. Marote, S. Ferreira, S.I. Vieira, S. Olhero, P. Miranda, J.M.F. Ferreira, Biphasic calcium phosphate scaffolds fabricated by direct write assembly: Mechanical, anti-microbial and osteoblastic properties, Journal of the European Ceramic Society, 37 (2017) 359-368.
[258] C. Vitale-Brovarone, F. Baino, E. Verné, High strength bioactive glass-ceramic scaffolds for bone regeneration, J Mater Sci: Mater Med, 20 (2009) 643-653.
[259] S. Sánchez-Salcedo, A. Nieto, M. Vallet-Regí, Hydroxyapatite/β-tricalcium phosphate/agarose macroporous scaffolds for bone tissue engineering, Chemical Engineering Journal, 137 (2008) 62-71.
[260] S.-H. An, T. Matsumoto, H. Miyajima, A. Nakahira, K.-H. Kim, S. Imazato, Porous zirconia/hydroxyapatite scaffolds for bone reconstruction, Dental Materials, 28 (2012) 1221-1231.
[261] P.K. Wongwitwichot, J; Chua, K.H; Ruszymah, B.H.I., Comparison of TCP and TCP/HA Hybrid Scaffolds for Osteoconductive Activity, The Open Biomedical Engineering Journal, 4 (2010) 279-285.
[262] H.-W. Kim, S.-Y. Lee, C.-J. Bae, Y.-J. Noh, H.-E. Kim, H.-M. Kim, J.S. Ko, Porous ZrO2 bone scaffold coated with hydroxyapatite with fluorapatite intermediate layer, Biomaterials, 24 (2003) 3277-3284.
[263] Y. Chen, B. Feng, Y. Zhu, J. Weng, J. Wang, X. Lu, Preparation and characterization of a novel porous titanium scaffold with 3D hierarchical porous structures, J Mater Sci: Mater Med, 22 (2011) 839-844.
[264] J. Lee, M.M. Farag, E.K. Park, J. Lim, H.-s. Yun, A simultaneous process of 3D magnesium phosphate scaffold fabrication and bioactive substance loading for hard tissue regeneration, Materials Science and Engineering: C, 36 (2014) 252-260.
[265] F.R. Rose, L.A. Cyster, D.M. Grant, C.A. Scotchford, S.M. Howdle, K.M. Shakesheff, In vitro assessment of cell penetration into porous hydroxyapatite scaffolds with a central aligned channel, Biomaterials, 25 (2004) 5507-5514.
[266] J.M. Oliveira, M.T. Rodrigues, S.S. Silva, P.B. Malafaya, M.E. Gomes, C.A. Viegas, I.R. Dias, J.T. Azevedo, J.F. Mano, R.L. Reis, Novel hydroxyapatite/chitosan bilayered scaffold for osteochondral tissue-engineering applications: Scaffold design and its performance when seeded with goat bone marrow stromal cells, Biomaterials, 27 (2006) 6123-6137.
[267] B. Leukers, H. Gülkan, S.H. Irsen, S. Milz, C. Tille, H. Seitz, M. Schieker, Biocompatibility of ceramic scaffolds for bone replacement made by 3D printing, Materialwissenschaft und Werkstofftechnik, 36 (2005) 781-787.

[268] S. Feng, F. He, J. Ye, Fabrication and characterization of honeycomb β-tricalcium phosphate scaffolds through an extrusion technique, Ceramics International, 43 (2017) 6778-6785.
[269] F.E. Wiria, B.Y. Tay, E. Ghassemieh, Morphological and Cell Growth Assessment in Near Dense Hydroxyapatite Scaffold, Journal of Materials, 2013 (2013) 8.
[270] S. Chamary, D. Hautcoeur, J.-C. Hornez, A. Leriche, F. Cambier, Bio-inspired hydroxyapatite dual core-shell structure for bone substitutes, Journal of the European Ceramic Society, 37 (2017) 5321-5327.
[271] J.G. Dellinger, J.A.C. Eurell, R.D. Jamison, Bone response to 3D periodic hydroxyapatite scaffolds with and without tailored microporosity to deliver bone morphogenetic protein 2, Journal of Biomedical Materials Research Part A, 76A (2006) 366-376.
[272] A. Thomas, K.C.R. Kolan, M.C. Leu, G.E. Hilmas, Freeform extrusion fabrication of titanium fiber reinforced 13–93 bioactive glass scaffolds, Journal of the Mechanical Behavior of Biomedical Materials, 69 (2017) 153-162.
[273] H.-W. Kim, J.C. Knowles, H.-E. Kim, Hydroxyapatite/poly(ε-caprolactone) composite coatings on hydroxyapatite porous bone scaffold for drug delivery, Biomaterials, 25 (2004) 1279-1287.
[274] S. Teixeira, M.H. Fernandes, M.P. Ferraz, F.J. Monteiro, Proliferation and mineralization of bone marrow cells cultured on macroporous hydroxyapatite scaffolds functionalized with collagen type I for bone tissue regeneration, Journal of Biomedical Materials Research Part A, 95A (2010) 1-8.
[275] P. Miranda, E. Saiz, K. Gryn, A.P. Tomsia, Sintering and robocasting of β-tricalcium phosphate scaffolds for orthopaedic applications, Acta Biomaterialia, 2 (2006) 457-466.
[276] M. Descamps, J.C. Hornez, A. Leriche, Manufacture of hydroxyapatite beads for medical applications, Journal of the European Ceramic Society, 29 (2009) 369-375.
[277] F.J. Martínez-Vázquez, F.H. Perera, P. Miranda, A. Pajares, F. Guiberteau, Improving the compressive strength of bioceramic robocast scaffolds by polymer infiltration, Acta Biomaterialia, 6 (2010) 4361-4368.
[278] J.R. Jones, G. Poologasundarampillai, R.C. Atwood, D. Bernard, P.D. Lee, Non-destructive quantitative 3D analysis for the optimisation of tissue scaffolds, Biomaterials, 28 (2007) 1404-1413.
[279] F. Barrera-Méndez, J.C. Escobedo-Bocardo, D.A. Cortés-Hernández, J.M. Almanza-Robles, E.M. Múzquiz-Ramos, Gentamicin sulphate release from lost foam wollastonite scaffolds using poly(dl-lactide-co-glycolide) acid, Ceramics International, 37 (2011) 2445-2451.
[280] Y. Ben, L. Zhang, S. Wei, T. Zhou, Z. Li, H. Yang, Y. Wang, F.A. Selim, C. Wong, H. Chen, PVB modified spherical granules of β-TCP by spray drying for 3D ceramic printing, Journal of Alloys and Compounds, 721 (2017) 312-319.
[281] S.-C. Wu, H.-C. Hsu, S.-K. Hsu, W.-H. Wang, W.-F. Ho, Preparation and characterization of four different compositions of calcium phosphate scaffolds for bone tissue engineering, Materials Characterization, 62 (2011) 526-534.
[282] C. Wang, Y. Duan, B. Markovic, J. Barbara, C. Rolfe Howlett, X. Zhang, H. Zreiqat, Proliferation and bone-related gene expression of osteoblasts grown on hydroxyapatite ceramics sintered at different temperature, Biomaterials, 25 (2004) 2949-2956.
[283] P. Frayssinet, N. Rouquet, J. Fages, M. Durand, P.O. Vidalain, G. Bonel, The influence of sintering temperature on the proliferation of fibroblastic cells in contact with HA-bioceramics, Journal of Biomedical Materials Research, 35 (1997) 337-347.

[284] K. Hwang, Y. Lim, Chemical and structural changes of hydroxyapatite films by using a sol–gel method, Surface and Coatings Technology, 115 (1999) 172-175.
[285] F. Scalera, F. Gervaso, K.P. Sanosh, A. Sannino, A. Licciulli, Influence of the calcination temperature on morphological and mechanical properties of highly porous hydroxyapatite scaffolds, Ceramics International, 39 (2013) 4839-4846.
[286] H. Li, K.A. Khor, P. Cheang, Titanium dioxide reinforced hydroxyapatite coatings deposited by high velocity oxy-fuel (HVOF) spray, Biomaterials, 23 (2002) 85-91.
[287] P.M.C. Torres, J.C.C. Abrantes, A. Kaushal, S. Pina, N. Döbelin, M. Bohner, J.M.F. Ferreira, Influence of Mg-doping, calcium pyrophosphate impurities and cooling rate on the allotropic α↔β-tricalcium phosphate phase transformations, Journal of the European Ceramic Society, 36 (2016) 817-827.
[288] D. Brazete, P.M.C. Torres, J.C.C. Abrantes, J.M.F. Ferreira, Influence of the Ca/P ratio and cooling rate on the allotropic α↔β-tricalcium phosphate phase transformations, Ceramics International, 44 (2018) 8249-8256.
[289] A.S. Posner, Crystal chemistry of bone mineral, Physiological Reviews, 49 (1969) 760-792.
[290] J.H. Lopes, J.A. Magalhães, R.F. Gouveia, C.A. Bertran, M. Motisuke, S.E.A. Camargo, E.d.S. Trichês, Hierarchical structures of β-TCP/45S5 bioglass hybrid scaffolds prepared by gelcasting, Journal of the Mechanical Behavior of Biomedical Materials, 62 (2016) 10-23.
[291] A.F. Vásquez, S. Domínguez, L.A. Loureiro dos Santos, α-TCP cements prepared by syringe-foaming: Influence of Na2HPO4 and surfactant concentration, Materials Science and Engineering: C, 81 (2017) 148-155.
[292] V. Jokanović, B. Čolović, Synthesis of TTCP by using inverse micelle method, Materials Chemistry and Physics, 143 (2014) 1481-1488.
[293] A.C.S. Talari, M.A.G. Martinez, Z. Movasaghi, S. Rehman, I.U. Rehman, Advances in Fourier transform infrared (FTIR) spectroscopy of biological tissues, Applied Spectroscopy Reviews, 52 (2017) 456-506.
[294] B.O. Fowler, Infrared studies of apatites. I. Vibrational assignments for calcium, strontium, and barium hydroxyapatites utilizing isotopic substitution, Inorganic Chemistry, 13 (1974) 194-207.
[295] G. PENEL, G. LEROY, C. REY, B. SOMBRET, J.P. HUVENNE, E. BRES, Infrared and Raman microspectrometry study of fluor-fluor-hydroxy and hydroxy-apatite powders, J Mater Sci: Mater Med, 8 (1997) 271-276.
[296] T. Uchino, T. Sakka, M. Iwasaki, Interpretation of Hydrated States of Sodium Silicate Glasses by Infrared and Raman Analysis, Journal of the American Ceramic Society, 74 (1991) 306-313.
[297] K.C. Blakeslee, R.A. Condrate, Vibrational Spectra of Hydrothermally Prepared Hydroxyapatites, Journal of the American Ceramic Society, 54 (1971) 559-563.
[298] C.-J. Liao, F.-H. Lin, K.-S. Chen, J.-S. Sun, Thermal decomposition and reconstitution of hydroxyapatite in air atmosphere, Biomaterials, 20 (1999) 1807-1813.
[299] I. REHMAN, W. BONFIELD, Characterization of hydroxyapatite and carbonated apatite by photo acoustic FTIR spectroscopy, J Mater Sci: Mater Med, 8 (1997) 1-4.
[300] V. Balla, S. Bose, N. Davies, A. Bandyopadhyay, Tantalum—A bioactive metal for implants, The Journal of The Minerals, Metals & Materials Society (TMS), 62 (2010) 61-64.
[301] W.E. Brown, L.C. Chow, Chemical Properties of Bone Mineral, Annual Review of Materials Science, 6 (1976) 213-236.
[302] W.E. Klee, G. Engel, I.R. spectra of the phosphate ions in various apatites, Journal of Inorganic and Nuclear Chemistry, 32 (1970) 1837-1843.

[303] C.B. Baddiel, E.E. Berry, Spectra structure correlations in hydroxy and fluorapatite, Spectrochimica Acta, 22 (1966) 1407-1416.
[304] V.M. Bhatnagar, Infrared spectrum of strontium hydroxyapatite, Experientia, 23 (1967) 697-699.
[305] I.R. Gibson, I. Rehman, S.M. Best, W. Bonfield*, Characterization of the transformation from calcium-deficient apatite to β-tricalcium phosphate, J Mater Sci: Mater Med, 11 (2000) 533-539.
[306] I. Manjubala, M. Sivakumar, In-situ synthesis of biphasic calcium phosphate ceramics using microwave irradiation, Materials Chemistry and Physics, 71 (2001) 272-278.
[307] S.R. Radin, P. Ducheyne, Plasma spraying induced changes of calcium phosphate ceramic characteristics and the effect onin vitro stability, J Mater Sci: Mater Med, 3 (1992) 33-42.
[308] I. Cacciotti, A. Bianco, M. Lombardi, L. Montanaro, Mg-substituted hydroxyapatite nanopowders: Synthesis, thermal stability and sintering behaviour, Journal of the European Ceramic Society, 29 (2009) 2969-2978.
[309] C.Y. Ooi, M. Hamdi, S. Ramesh, Properties of hydroxyapatite produced by annealing of bovine bone, Ceramics International, 33 (2007) 1171-1177.
[310] S. Meejoo, W. Maneeprakorn, P. Winotai, Phase and thermal stability of nanocrystalline hydroxyapatite prepared via microwave heating, Thermochimica Acta, 447 (2006) 115-120.
[311] A. Ślósarczyk, C. Paluszkiewicz, M. Gawlicki, Z. Paszkiewicz, The FTIR spectroscopy and QXRD studies of calcium phosphate based materials produced from the powder precursors with different CaP ratios, Ceramics International, 23 (1997) 297-304.
[312] M. Malakauskaite-Petruleviciene, Z. Stankeviciute, G. Niaura, E. Garskaite, A. Beganskiene, A. Kareiva, Characterization of sol-gel processing of calcium phosphate thin films on silicon substrate by FTIR spectroscopy, Vibrational Spectroscopy, 85 (2016) 16-21.
[313] S. Pramanik, A.K. Agarwal, K.N. Rai, A. Garg, Development of high strength hydroxyapatite by solid-state-sintering process, Ceramics International, 33 (2007) 419-426.
[314] F. Händle, Extrusion in Ceramics, Springer Berlin Heidelberg, Berlin, Heidelberg, 2007.
[315] D.M. Beall, C.J. Malarkey, G.A. Merkel, Low expansion, high porosity, high strength cordierite body and method, Google Patents, 2002.
[316] J.P. Day, Extruded ceramic honeycomb and method, Google Patents, 1995.
[317] K.E. Rudman, R.M. Aspden, J.R. Meakin, Compression or tension? The stress distribution in the proximal femur, BioMedical Engineering OnLine, 5 (2006) 12-12.
[318] L.J.a.A. Gibson, M. F., Cellular solids : structure and properties, 2nd ed., 1st pbk. ed. with corr. ed., Cambridge : Cambridge University Press, 1999, Cambridge, 1999.
[319] C. Petit, S. Meille, E. Maire, S. Tadier, J. Adrien, Mechanical behaviour of a β-TCP ceramic with a random porosity: Study of the fracture path with X-ray tomography, Journal of the European Ceramic Society, 36 (2016) 3225-3233.
[320] E. Saiz, L. Gremillard, G. Menendez, P. Miranda, K. Gryn, A.P. Tomsia, Preparation of porous hydroxyapatite scaffolds, Materials Science and Engineering: C, 27 (2007) 546-550.
[321] E.C.G. Moreno, T.M.; Brown, W.E., Preparation and solubility of hydroxyapatite, Journal of Research of the National Bureau of Standards, 72A (1968) 773-782.

[322] Y. Zhang, N. Zhou, W. Li, J. Li, S. Nian, X. Li, J. Sui, Fabrication and characterization of bone china using synthetic bone powder as raw materials, Ceramics International, 42 (2016) 14910-14917.
[323] M.D. O'Donnell, Melt-Derived Bioactive Glass, Bio-Glasses, John Wiley & Sons, Ltd2012, pp. 13-27.
[324] H.I.o. Mineralogy, Canasite, 2017.
[325] P.A.a.O. Webb, C., Analytical Methods in Fine Particle Technology, Micromeritics instrument corp, Norcross, GA USA, 1997.
[326] J. Meredith, K.K. Mallick, High-strength scaffolds for bone regeneration, Bioinspired, Biomimetic and Nanobiomaterials, 4 48-58.
[327] R. Bayer, M. Knarr, Thermal precipitation or gelling behaviour of dissolved methylcellulose (MC) derivatives—Behaviour in water and influence on the extrusion of ceramic pastes. Part 1: Fundamentals of MC-derivatives, Journal of the European Ceramic Society, 32 (2012) 1007-1018.
[328] J.A. Grover, CHAPTER 18 - METHYLCELLULOSE AND ITS DERIVATIVES, Industrial Gums (Third Edition), Academic Press, London, 1993, pp. 475-504.
[329] B.-R. Lee, E.-S. Oh, Effect of Molecular Weight and Degree of Substitution of a Sodium-Carboxymethyl Cellulose Binder on Li4Ti5O12 Anodic Performance, The Journal of Physical Chemistry C, 117 (2013) 4404-4409.
[330] J. Moon, J.E. Grau, V. Knezevic, M.J. Cima, E.M. Sachs, Ink-Jet Printing of Binders for Ceramic Components, Journal of the American Ceramic Society, 85 (2002) 755-762.
[331] J.-K. Song, W.-S. Um, H.-S. Lee, M.-S. Kang, K.-W. Chung, J.-H. Park, Effect of polymer molecular weight variations on PZT slip for tape casting, Journal of the European Ceramic Society, 20 (2000) 685-688.
[332] J. Benbow, Paste flow and extrusion, Oxford : Oxford University Press, 1993, Oxford, 1993.
[333] G.W. Crume, Ceramic compositions for improved extrusion, Google Patents, 2014.
[334] D.K. Buslov, N.I. Sushko, O.N. Tretinnikov, Study of thermal gelation of methylcellulose in water using FTIR-ATR spectroscopy, Journal of Applied Spectroscopy, 75 (2008) 514-518.
[335] J.-H. Zhu, X.-Q. Yang, I. Ahmad, Y. Jiang, X.-Y. Wang, L.-Y. Wu, Effect of guar gum on the rheological, thermal and textural properties of soybean β-conglycinin gel, International Journal of Food Science & Technology, 44 (2009) 1314-1322.
[336] F.-J. Liu, K.-S. Chou, Determining critical ceramic powder volume concentration from viscosity measurements, Ceramics International, 26 (2000) 159-164.
[337] R.L. Feddersen, S.N. Thorp, CHAPTER 20 - SODIUM CARBOXYMETHYLCELLULOSE, Industrial Gums (Third Edition), Academic Press, London, 1993, pp. 537-578.
[338] G.R. Filho, R.M.N. de Assunção, J.G. Vieira, C.d.S. Meireles, D.A. Cerqueira, H. da Silva Barud, S.J.L. Ribeiro, Y. Messaddeq, Characterization of methylcellulose produced from sugar cane bagasse cellulose: Crystallinity and thermal properties, Polymer Degradation and Stability, 92 (2007) 205-210.
[339] W. Habraken, P. Habibovic, M. Epple, M. Bohner, Calcium phosphates in biomedical applications: materials for the future?, Materials Today, 19 (2016) 69-87.
[340] J.P. Moseley, M.E. Carroll, J.D. McCanless, O. Schulz, A. Fronk, Composite bone graft substitute cement and articles produced therefrom, Google Patents, 2014.
[341] R.V. da Silva, C.A. Bertran, E.Y. Kawachi, J.A. Camilli, Repair of Cranial Bone Defects With Calcium Phosphate Ceramic Implant or Autogenous Bone Graft, Journal of Craniofacial Surgery, 18 (2007) 281-286.

[342] G. Muralithran, S. Ramesh, The effects of sintering temperature on the properties of hydroxyapatite, Ceramics International, 26 (2000) 221-230.
[343] P. Landuyt, F. Li, J. Keustermans, J. Streydio, F. Delannay, E. Munting, The influence of high sintering temperatures on the mechanical properties of hydroxylapatite, Official Journal of the European Society for Biomaterials, 6 (1995) 8-13.
[344] M. Houmard, Q. Fu, M. Genet, E. Saiz, A.P. Tomsia, On the structural, mechanical, and biodegradation properties of HA/β-TCP robocast scaffolds, Journal of Biomedical Materials Research Part B: Applied Biomaterials, 101 (2013) 1233-1242.
[345] C. Shuai, P. Li, J. Liu, S. Peng, Optimization of TCP/HAP ratio for better properties of calcium phosphate scaffold via selective laser sintering, Materials Characterization, 77 (2013) 23-31.
[346] M. Schumacher, U. Deisinger, R. Detsch, G. Ziegler, Indirect rapid prototyping of biphasic calcium phosphate scaffolds as bone substitutes: influence of phase composition, macroporosity and pore geometry on mechanical properties, J Mater Sci: Mater Med, 21 (2010) 3119-3127.
[347] A.J. Wagoner Johnson, B.A. Herschler, A review of the mechanical behavior of CaP and CaP/polymer composites for applications in bone replacement and repair, Acta Biomaterialia, 7 (2011) 16-30.
[348] Q. Wu, X. Zhang, B. Wu, W. Huang, Effects of microwave sintering on the properties of porous hydroxyapatite scaffolds, Ceramics International, 39 (2013) 2389-2395.
[349] P. Feng, M. Niu, C. Gao, S. Peng, C. Shuai, A novel two-step sintering for nano-hydroxyapatite scaffolds for bone tissue engineering, Scientific Reports, 4 (2014) 5599.
[350] S. Ramesh, K.L. Aw, R. Tolouei, M. Amiriyan, C.Y. Tan, M. Hamdi, J. Purbolaksono, M.A. Hassan, W.D. Teng, Sintering properties of hydroxyapatite powders prepared using different methods, Ceramics International, 39 (2013) 111-119.
[351] S. Ramesh, C.Y. Tan, S.B. Bhaduri, W.D. Teng, Rapid densification of nanocrystalline hydroxyapatite for biomedical applications, Ceramics International, 33 (2007) 1363-1367.
[352] D.J. Curran, T.J. Fleming, M.R. Towler, S. Hampshire, Mechanical parameters of strontium doped hydroxyapatite sintered using microwave and conventional methods, Journal of the Mechanical Behavior of Biomedical Materials, 4 (2011) 2063-2073.
[353] M.R. Saadati, A. Maleki, B. Niroumand, A.R. Allafchian, A novel low cost method for the synthesis of ceramic nano silicon oxycarbide powder, Ceramics International, 42 (2016) 8531-8536.
[354] H.R.R. Ramay, M. Zhang, Biphasic calcium phosphate nanocomposite porous scaffolds for load-bearing bone tissue engineering, Biomaterials, 25 (2004) 5171-5180.
[355] S. Cazalbou, G. Bertrand, C. Drouet, Tetracycline-loaded biomimetic apatite: an adsorption study, The journal of physical chemistry. B, 119 (2015) 3014.
[356] I.H. Arita, D.S. Wilkinson, M.A. Mondragón, V.M. Castaño, Chemistry and sintering behaviour of thin hydroxyapatite ceramics with controlled porosity, Biomaterials, 16 (1995) 403-408.
[357] F. Heidari, M. Razavi, M. Ghaedi, M. Forooghi, M. Tahriri, L. Tayebi, Investigation of mechanical properties of natural hydroxyapatite samples prepared by cold isostatic pressing method, Journal of Alloys and Compounds, 693 (2017) 1150-1156.
[358] D.J. Shanefield, Organic Additives and Ceramic Processing, Kluwer Academic Publishers, Massachusetts, USA, 1995.
[359] M.T. Zilm, S.D.; Wei, M., A Comparative Study of the Sintering Behavior of Pure and Manganese-Substituted Hydroxyapatite, Materials, 8 (2015) 6419-6436.

[360] Y. Li, C.P.A.T. Klein, X. Zhang, K. de Groot, Relationship between the colour change of hydroxyapatite and the trace element manganese, Biomaterials, 14 (1993) 969-972.
[361] N. Mustafa, Ibrahim, M.H.I., Asmawi, R., Amin, A.M, Hydroxyapatite Extracted from Waste Fish Bones and Scales via Calcination Method, Applied Mechanics and Materials, 773-774 (2015) 287-290.
[362] R.G. Carrodeguas, S. De Aza, α-Tricalcium phosphate: Synthesis, properties and biomedical applications, Acta Biomaterialia, 7 (2011) 3536-3546.
[363] R. Famery, N. Richard, P. Boch, Preparation of α- and β-tricalcium phosphate ceramics, with and without magnesium addition, Ceramics International, 20 (1994) 327-336.
[364] H.-S. Ryu, H.-J. Youn, K. Sun Hong, B.-S. Chang, C.-K. Lee, S.-S. Chung, An improvement in sintering property of β-tricalcium phosphate by addition of calcium pyrophosphate, Biomaterials, 23 (2002) 909-914.
[365] K. Itatani, T. Nishioka, S. Seike, F.S. Howell, A. Kishioka, M. Kinoshita, Sinterability of β-Calcium Orthophosphate Powder Prepared by Spray-Pyrolysis, Journal of the American Ceramic Society, 77 (1994) 801-805.
[366] S.-F. Ou, S.-Y. Chiou, K.-L. Ou, Phase transformation on hydroxyapatite decomposition, Ceramics International, 39 (2013) 3809-3816.
[367] P.E. Wang, T.K. Chaki, Sintering behaviour and mechanical properties of hydroxyapatite and dicalcium phosphate, J Mater Sci: Mater Med, 4 (1993) 150-158.
[368] A.H. Heuer, Transgranular and Intergranular Fracture in Polycrystalline Alumina, Journal of the American Ceramic Society, 52 (1969) 510-511.
[369] M. Chen, H. Wang, H. Jin, X. Pan, Z. Jin, Effect of pores on crack propagation behavior for porous Si3N4 ceramics, Ceramics International, 42 (2016) 5642-5649.
[370] L.D.T. Topoleski, R. Rodriguez-Pinto, 6.602 - Bone Cement A2 - Ducheyne, Paul, Comprehensive Biomaterials, Elsevier, Oxford, 2011, pp. 11-28.
[371] E.D. Case, I.O. Smith, M.J. Baumann, Microcracking and porosity in calcium phosphates and the implications for bone tissue engineering, Materials Science and Engineering: A, 390 (2005) 246-254.
[372] Y. Kang, A. Scully, D.A. Young, S. Kim, H. Tsao, M. Sen, Y. Yang, Enhanced mechanical performance and biological evaluation of a PLGA coated β-TCP composite scaffold for load-bearing applications, European Polymer Journal, 47 (2011) 1569-1577.
[373] M. Xu, D. Zhai, J. Chang, C. Wu, In vitro assessment of three-dimensionally plotted nagelschmidtite bioceramic scaffolds with varied macropore morphologies, Acta Biomaterialia, 10 (2014) 463-476.
[374] S. Tarafder, N.M. Davies, A. Bandyopadhyay, S. Bose, 3D printed tricalcium phosphate bone tissue engineering scaffolds: effect of SrO and MgO doping on in vivo osteogenesis in a rat distal femoral defect model, Biomaterials Science, 1 (2013) 1250-1259.
[375] W. Bian, D. Li, Q. Lian, X. Li, W. Zhang, K. Wang, Z. Jin, Fabrication of a bio-inspired beta-Tricalcium phosphate/collagen scaffold based on ceramic stereolithography and gel casting for osteochondral tissue engineering, Rapid Prototyping Journal, 18 (2012) 68-80.
[376] N.A.S. Zairani, M. Jaafar, N. Ahmad, K. Abdul Razak, Fabrication and characterization of porous β-tricalcium phosphate scaffolds coated with alginate, Ceramics International, 42 (2016) 5141-5147.
[377] S. Kunjalukkal Padmanabhan, F. Gervaso, M. Carrozzo, F. Scalera, A. Sannino, A. Licciulli, Wollastonite/hydroxyapatite scaffolds with improved mechanical, bioactive

and biodegradable properties for bone tissue engineering, Ceramics International, 39 (2013) 619-627.
[378] J. Wu, C. Ruan, Y. Ma, Y. Wang, Y. Luo, Vital Role of Hydroxyapatite Particle Shape in Regulating the Porosity and Mechanical Properties of the Sintered Scaffolds, Journal of Materials Science & Technology.
[379] Y. Tang, K. Zhao, L. Hu, Z. Wu, Two-step freeze casting fabrication of hydroxyapatite porous scaffolds with bionic bone graded structure, Ceramics International, 39 (2013) 9703-9707.
[380] H.Y. Juang, M.H. Hon, Effect of calcination on sintering of hydroxyapatite, Biomaterials, 17 (1996) 2059-2064.
[381] M. Figueiredo, A. Fernando, G. Martins, J. Freitas, F. Judas, H. Figueiredo, Effect of the calcination temperature on the composition and microstructure of hydroxyapatite derived from human and animal bone, Ceramics International, 36 (2010) 2383-2393.
[382] A. Sobczak-Kupiec, Z. Wzorek, The influence of calcination parameters on free calcium oxide content in natural hydroxyapatite, Ceramics International, 38 (2012) 641-647.
[383] S.-H. Kwon, Y.-K. Jun, S.-H. Hong, H.-E. Kim, Synthesis and dissolution behavior of β-TCP and HA/β-TCP composite powders, Journal of the European Ceramic Society, 23 (2003) 1039-1045.
[384] S. Raynaud, E. Champion, D. Bernache-Assollant, Calcium phosphate apatites with variable Ca/P atomic ratio II. Calcination and sintering, Biomaterials, 23 (2002) 1073-1080.
[385] T. Sundararajan, S. Balasivanandha Prabu, Spark plasma sintering of microwave processed nanocrystalline barium titanate and their characterisations, Materials Chemistry and Physics, 139 (2013) 465-470.
[386] M. Hidouri, K. Bouzouita, F. Kooli, I. Khattech, Thermal behaviour of magnesium-containing fluorapatite, Materials Chemistry and Physics, 80 (2003) 496-505.
[387] M. Šupová, Substituted hydroxyapatites for biomedical applications: A review, Ceramics International, 41 (2015) 9203-9231.
[388] E. Boanini, M. Gazzano, A. Bigi, Ionic substitutions in calcium phosphates synthesized at low temperature, Acta Biomaterialia, 6 (2010) 1882-1894.
[389] E. Champion, Sintering of calcium phosphate bioceramics, Acta Biomaterialia, 9 (2013) 5855-5875.
[390] B. Basar, A. Tezcaner, D. Keskin, Z. Evis, Improvements in microstructural, mechanical, and biocompatibility properties of nano-sized hydroxyapatites doped with yttrium and fluoride, Ceramics International, 36 (2010) 1633-1643.
[391] M. Kavitha, R. Subramanian, R. Narayanan, V. Udhayabanu, Solution combustion synthesis and characterization of strontium substituted hydroxyapatite nanocrystals, Powder Technology, 253 (2014) 129-137.
[392] C. Ergun, Effect of Ti ion substitution on the structure of hydroxylapatite, Journal of the European Ceramic Society, 28 (2008) 2137-2149.
[393] M.A. Auger, B. Savoini, A. Muñoz, T. Leguey, M.A. Monge, R. Pareja, J. Victoria, Mechanical characteristics of porous hydroxyapatite/oxide composites produced by post-sintering hot isostatic pressing, Ceramics International, 35 (2009) 2373-2380.
[394] I.R. Gibson, W. Bonfield, Preparation and characterization of magnesium/carbonate co-substituted hydroxyapatites, J Mater Sci: Mater Med, 13 (2002) 685-693.
[395] M.A. Gülgün, R. Voytovych, I. Maclaren, M. Rühle, R.M. Cannon, Cation Segregation in an Oxide Ceramic with Low Solubility: Yttrium Doped α-Alumina, Interface Science, 10 (2002) 99-110.

[396] R.G. Luthardt, M.S. Holzhüter, H. Rudolph, V. Herold, M.H. Walter, CAD/CAM-machining effects on Y-TZP zirconia, Dental Materials, 20 (2004) 655-662.
[397] J. Chevalier, S. Deville, E. Münch, R. Jullian, F. Lair, Critical effect of cubic phase on aging in 3 mol% yttria-stabilized zirconia ceramics for hip replacement prosthesis, Biomaterials, 25 (2004) 5539-5545.
[398] J. Al-Haidary, M. Al-Haidari, S. Qrunfuleh, Effect of yttria addition on mechanical, physical and biological properties of bioactive MgO–CaO–SiO 2 –P 2 O 5 –CaF 2 glass ceramic, Biomedical Materials, 3 (2008) 015005.
[399] H. Owada, K. Yamashita, T. Umegaki, T. Kanazawa, M. Nagai, Humidity-sensitivity of yttrium substituted apatite ceramics, Solid State Ionics, 35 (1989) 401-404.
[400] M. Sato, M.A. Sambito, A. Aslani, N.M. Kalkhoran, E.B. Slamovich, T.J. Webster, Increased osteoblast functions on undoped and yttrium-doped nanocrystalline hydroxyapatite coatings on titanium, Biomaterials, 27 (2006) 2358-2369.
[401] J.C. Anderson, C. Eriksson, Piezoelectric Properties of Dry and Wet Bone, Nature, 227 (1970) 491.
[402] T.J. Webster, C. Ergun, R.H. Doremus, R. Bizios, Hydroxylapatite with substituted magnesium, zinc, cadmium, and yttrium. II. Mechanisms of osteoblast adhesion, Journal of Biomedical Materials Research, 59 (2002) 312-317.
[403] J. Zhang, C. Liu, Y. Li, J. Sun, P. Wang, K. Di, H. Chen, Y. Zhao, Effect of yttrium ion on the proliferation, differentiation and mineralization function of primary mouse osteoblasts in vitro, Journal of Rare Earths, 28 (2010) 466-470.
[404] A. Costantini, R. Fresa, A. Buri, F. Branda, Effect of the substitution of Y2O3 for CaO on the bioactivity of 2.5CaO · 2SiO2 glass, Biomaterials, 18 (1997) 453-458.
[405] P. Parente, B. Savoini, B. Ferrari, M.A. Monge, R. Pareja, A.J. Sanchez-Herencia, Effect of highly dispersed yttria addition on thermal stability of hydroxyapatite, Materials Science and Engineering: C, 33 (2013) 864-869.
[406] A. Aranzabal, D. Iturbe, M. Romero-Sáez, M.P. González-Marcos, J.R. González-Velasco, J.A. González-Marcos, Optimization of process parameters on the extrusion of honeycomb shaped monolith of H-ZSM-5 zeolite, Chemical Engineering Journal, 162 (2010) 415-423.
[407] M.K. Naskar, M. Chatterjee, A. Dey, K. Basu, Effects of processing parameters on the fabrication of near-net-shape fibre reinforced oxide ceramic matrix composites via sol–gel route, Ceramics International, 30 (2004) 257-265.
[408] Y. Cai, X. Li, J. Dong, Microstructure and mechanical properties of porous Si3N4–SiO2 ceramics fabricated by a process combining carbothermal reduction and sol–gel infiltration–sintering, Materials Science and Engineering: A, 601 (2014) 111-115.
[409] P.P. Nampi, S. Kume, Y. Hotta, K. Watari, M. Itoh, H. Toda, A. Matsutani, The effect of polyvinyl alcohol as a binder and stearic acid as an internal lubricant in the formation, and subsequent sintering of spray-dried alumina, Ceramics International, 37 (2011) 3445-3450.
[410] Y.-T. Huang, M. Imura, Y. Nemoto, C.-H. Cheng, Y. Yamauchi, Block-copolymer-assisted synthesis of hydroxyapatite nanoparticles with high surface area and uniform size, Science and Technology of Advanced Materials, 12 (2011) 045005.
[411] T.F. Al-Fariss, F.A.A. El-Aleem, Y. Arafat, K.A. El-Nagdy, A.A. El-Midany, Low Solubility of Calcined Phosphate: Surface Area Reduction or Chemical Composition Change?, Particulate Science and Technology, 32 (2014) 80-85.
[412] A. Nzihou, B. Adhikari, Effect of Oxides and Nitrates of Lead on the Sintering and Densification of Hydroxyapatite Adsorbents, Industrial & Engineering Chemistry Research, 43 (2004) 3325-3335.

[413] S. Bailliez, A. Nzihou, The kinetics of surface area reduction during isothermal sintering of hydroxyapatite adsorbent, Chemical Engineering Journal, 98 (2004) 141-152.
[414] J.A.F. Gamelas, A.G. Martins, Surface properties of carbonated and non-carbonated hydroxyapatites obtained after bone calcination at different temperatures, Colloids and Surfaces A: Physicochemical and Engineering Aspects, 478 (2015) 62-70.
[415] L.M. Rodríguez-Lorenzo, J.N. Hart, K.A. Gross, Influence of fluorine in the synthesis of apatites. Synthesis of solid solutions of hydroxy-fluorapatite, Biomaterials, 24 (2003) 3777-3785.
[416] U. Batra, S. Kapoor, S. Sharma, Influence of Magnesium Ion Substitution on Structural and Thermal Behavior of Nanodimensional Hydroxyapatite, Journal of Materials Engineering and Performance, 22 (2013) 1798-1806.
[417] J. G. M. Poralan, J.E. Gambe, E.M. Alcantara, R.M. Vequizo, X-ray diffraction and infrared spectroscopy analyses on the crystallinity of engineered biological hydroxyapatite for medical application, IOP Conference Series: Materials Science and Engineering, 79 (2015) 012028.
[418] R.C. Burk, T.W. Zawidzki, P.S. Apte, Particle Size Distribution and Its Relation to Sintering—A Case Study for UO2 Powders, Journal of the American Ceramic Society, 66 (1983) 815-818.
[419] B. Basu, L. Donzel, J. Van Humbeeck, J. Vleugels, R. Schaller, O. Van Der Biest, Thermal expansion and damping characteristics of Y-TZP, Scripta Materialia, 40 (1999) 759-765.
[420] X. Cheng, C. Yuan, N.R. Green, P.A. Withey, Sintering mechanisms of Yttria with different additives, Ceramics International, 39 (2013) 4791-4799.
[421] G.R. Fischer, P. Bardhan, J.E. Geiger, The lattice thermal expansion of hydroxyapatite, Journal of Materials Science Letters, 2 (1983) 577-578.
[422] S. Nakamura, R. Otsuka, H. Aoki, M. Akao, N. Miura, T. Yamamoto, Thermal expansion of hydroxyapatite-β-tricalcium phosphate ceramics, Thermochimica Acta, 165 (1990) 57-72.
[423] M. Aminzare, A. Eskandari, M.H. Baroonian, A. Berenov, Z. Razavi Hesabi, M. Taheri, S.K. Sadrnezhaad, Hydroxyapatite nanocomposites: Synthesis, sintering and mechanical properties, Ceramics International, 39 (2013) 2197-2206.
[424] V.P. Orlovskii, V.S. Komlev, S.M. Barinov, Hydroxyapatite and Hydroxyapatite-Based Ceramics, Inorganic Materials, 38 (2002) 973-984.
[425] Y. Wang, X. Yang, Z. Gu, H. Qin, L. Li, J. Liu, X. Yu, In vitro study on the degradation of lithium-doped hydroxyapatite for bone tissue engineering scaffold, Materials Science and Engineering: C, 66 (2016) 185-192.
[426] M.K. Herliansyah, M. Hamdi, A. Ide-Ektessabi, M.W. Wildan, J.A. Toque, The influence of sintering temperature on the properties of compacted bovine hydroxyapatite, Materials Science and Engineering: C, 29 (2009) 1674-1680.
[427] A.J. Ruys, M. Wei, C.C. Sorrell, M.R. Dickson, A. Brandwood, B.K. Milthorpe, Sintering effects on the strength of hydroxyapatite, Biomaterials, 16 (1995) 409-415.
[428] M. L. Munar, K.-i. Udoh, K. Ishikawa, S. Matsuya, M. Nakagawa, Effects of Sintering Temperature Over 1,300°C on the Physical and Compositional Properties of Porous Hydroxyapatite Foam, Dental Materials Journal, 25 (2006) 51-58.
[429] J. Liu, X. Lv, J. Li, L. Jiang, Pressureless sintered magnesium aluminate spinel with enhanced mechanical properties obtained by the two-step sintering method, Journal of Alloys and Compounds, 680 (2016) 133-138.
[430] A.A. Palmeira, M.J. Bondioli, K. Strecker, C.d. Santos, Densification and grain growth of nano- and micro-sized Y-TZP powders, Ceramics International, 42 (2016) 2662-2669.

[431] D. Veljović, I. Zalite, E. Palcevskis, I. Smiciklas, R. Petrović, D. Janaćković, Microwave sintering of fine grained HAP and HAP/TCP bioceramics, Ceramics International, 36 (2010) 595-603.
[432] P. Feng, P. Wei, C. Shuai, S. Peng, Characterization of Mechanical and Biological Properties of 3-D Scaffolds Reinforced with Zinc Oxide for Bone Tissue Engineering, PLOS ONE, 9 (2014) e87755.
[433] S.J. Kalita, H.A. Bhatt, Nanocrystalline hydroxyapatite doped with magnesium and zinc: Synthesis and characterization, Materials Science and Engineering: C, 27 (2007) 837-848.
[434] A. Dubnika, V. Zalite, Preparation and characterization of porous Ag doped hydroxyapatite bioceramic scaffolds, Ceramics International, 40 (2014) 9923-9930.
[435] I.S. M.C. Murad, C. Rohaida, Z. Ahmad, M. Reusmaazran, Fabrication and Characterization of Strontium-Doped Hydroxyapatite Bioceramics Scaffolds for Bone Implant Application: A Preliminary Study Advanced Materials Research, 93-94 (2010) 401-404.
[436] F. Heilmann, O.C. Standard, F.A. Müller, M. Hoffman, Development of graded hydroxyapatite/CaCO3 composite structures for bone ingrowth, J Mater Sci: Mater Med, 18 (2007) 1817-1824.
[437] S. Hesaraki, Feasibility of alumina and alumina-silica nanoparticles to fabricate strengthened betatricalcium phosphate scaffold with improved biological responses, Ceramics International, 42 (2016) 7593-7604.
[438] S.M.H. Ghazanfari, A. Zamanian, Phase transformation, microstructural and mechanical properties of hydroxyapatite/alumina nanocomposite scaffolds produced by freeze casting, Ceramics International, 39 (2013) 9835-9844.
[439] M. Precnerová, K. Bodišová, F. Frajkorová, D. Galusková, Z. Varchulová Nováková, J. Vojtaššák, Z. Lenčéš, P. Šajgalík, In vitro bioactivity of silicon nitride–hydroxyapatite composites, Ceramics International, 41 (2015) 8100-8108.
[440] A.Z.O. Arawi, R. Ramli, M.K. Talari, M. Tripathy, Effect of titanium addition on mechanical properties of hydroxyapatite - Titanium nanocomposite, 2011 IEEE Colloquium on Humanities, Science and Engineering, 2011, pp. 533-536.
[441] G. Xiong, Y. Nie, D. Ji, J. Li, C. Li, W. Li, Y. Zhu, H. Luo, Y. Wan, Characterization of biomedical hydroxyapatite/magnesium composites prepared by powder metallurgy assisted with microwave sintering, Current Applied Physics, 16 (2016) 830-836.
[442] R. Havaldar, S.C. Pilli, B.B. Putti, Insights into the effects of tensile and compressive loadings on human femur bone, Advanced Biomedical Research, 3 (2014) 101.
[443] X. Wang, Q. Ni, Determination of cortical bone porosity and pore size distribution using a low field pulsed NMR approach, Journal of Orthopaedic Research, 21 (2003) 312-319.
[444] L. Røhl, E. Larsen, F. Linde, A. Odgaard, J. Jørgensen, Tensile and compressive properties of cancellous bone, Journal of Biomechanics, 24 (1991) 1143-1149.
[445] M. Martens, R. Van Audekercke, P. Delport, P. De Meester, J.C. Mulier, The mechanical characteristics of cancellous bone at the upper femoral region, Journal of Biomechanics, 16 (1983) 971-983.
[446] S.P. Samuel, G.R. Baran, Y. Wei, B.L. Davis, Biomechanics - Part II, in: J.S. Khurana (Ed.) Bone Pathology, Humana Press, Totowa, NJ, 2009, pp. 69-77.
[447] I. Zipkin, The Inorganic Composition of Bones and Teeth, in: H. Schraer (Ed.) Biological Calcification: Cellular and Molecular Aspects, Springer US, Boston, MA, 1970, pp. 69-103.

[448] H. Oonishi, L.L. Hench, J. Wilson, F. Sugihara, E. Tsuji, M. Matsuura, S. Kin, T. Yamamoto, S. Mizokawa, Quantitative comparison of bone growth behavior in granules of Bioglass®, A-W glass-ceramic, and hydroxyapatite, Journal of Biomedical Materials Research, 51 (2000) 37-46.
[449] L.L. Hench, The story of Bioglass®, J Mater Sci: Mater Med, 17 (2006) 967-978.
[450] M. Montazerian, E.D. Zanotto, A guided walk through Larry Hench's monumental discoveries, JOURNAL OF MATERIALS SCIENCE, (2017) 1-38.
[451] J.R. Jones, Reprint of: Review of bioactive glass: From Hench to hybrids, Acta Biomaterialia, 23, Supplement (2015) S53-S82.
[452] L. Altomare, D. Bellucci, G. Bolelli, B. Bonferroni, V. Cannillo, L. De Nardo, R. Gadow, A. Killinger, L. Lusvarghi, A. Sola, N. Stiegler, Microstructure and in vitro behaviour of 45S5 bioglass coatings deposited by high velocity suspension flame spraying (HVSFS), J Mater Sci: Mater Med, 22 (2011) 1303.
[453] V. Salih, G. Georgiou, J.C. Knowles, I. Olsen, Glass reinforced hydroxyapatite for hard tissue surgery—Part II: in vitro evaluation of bone cell growth and function, Biomaterials, 22 (2001) 2817-2824.
[454] G. Georgiou, J.C. Knowles, Glass reinforced hydroxyapatite for hard tissue surgery—Part 1: mechanical properties, Biomaterials, 22 (2001) 2811-2815.
[455] Z. Yazdanpanah, M.E. Bahrololoom, B. Hashemi, Evaluating morphology and mechanical properties of glass-reinforced natural hydroxyapatite composites, Journal of the Mechanical Behavior of Biomedical Materials, 41 (2015) 36-42.
[456] K. Lin, J. Chang, Z. Liu, Y. Zeng, R. Shen, Fabrication and characterization of 45S5 bioglass reinforced macroporous calcium silicate bioceramics, Journal of the European Ceramic Society, 29 (2009) 2937-2943.
[457] J.C. Knowles, S. Talal, J.D. Santos, Sintering effects in a glass reinforced hydroxyapatite, Biomaterials, 17 (1996) 1437-1442.
[458] D.C. Tancred, B.A.O. McCormack, A.J. Carr, A quantitative study of the sintering and mechanical properties of hydroxyapatite/phosphate glass composites, Biomaterials, 19 (1998) 1735-1743.
[459] J.D. Santos, R.L. Reis, F.J. Monteiro, J.C. Knowles, G.W. Hastings, Liquid phase sintering of hydroxyapatite by phosphate and silicate glass additions: structure and properties of the composites, J Mater Sci: Mater Med, 6 (1995) 348-352.
[460] S.M. Rabiee, N. Nazparvar, M. Azizian, D. Vashaee, L. Tayebi, Effect of ion substitution on properties of bioactive glasses: A review, Ceramics International, 41 (2015) 7241-7251.
[461] J.E. Funk, D.R. Dinger, Milling or Comminution, Predictive Process Control of Crowded Particulate Suspensions: Applied to Ceramic Manufacturing, Springer US, Boston, MA, 1994, pp. 373-394.
[462] M.D. O'Donnell, S.J. Watts, R.G. Hill, R.V. Law, The effect of phosphate content on the bioactivity of soda-lime-phosphosilicate glasses, J Mater Sci: Mater Med, 20 (2009) 1611-1618.
[463] Y. Li, S. Cai, G. Xu, S. Shen, M. Zhang, T. Zhang, X. Sun, Synthesis and characterization of a phytic acid/mesoporous 45S5 bioglass composite coating on a magnesium alloy and degradation behavior, RSC Advances, 5 (2015) 25708-25716.
[464] P. Sepulveda, J.R. Jones, L.L. Hench, In vitro dissolution of melt-derived 45S5 and sol-gel derived 58S bioactive glasses, Journal of Biomedical Materials Research, 61 (2002) 301-311.
[465] A.R. Boccaccini, Q. Chen, L. Lefebvre, L. Gremillard, J. Chevalier, Sintering, crystallisation and biodegradation behaviour of Bioglass[registered sign]-derived glass-ceramics, Faraday Discussions, 136 (2007) 27-44.

[466] M.M. Farag, A.M.I. El-Rashedi, C. Rüssel, In vitro biocompatibility evaluation of canasite-calcium phosphate glass-ceramics, Journal of Non-Crystalline Solids, 488 (2018) 24-35.
[467] O. Bretcanu, X. Chatzistavrou, K. Paraskevopoulos, R. Conradt, I. Thompson, A.R. Boccaccini, Sintering and crystallisation of 45S5 Bioglass® powder, Journal of the European Ceramic Society, 29 (2009) 3299-3306.
[468] Q.Z. Chen, I.D. Thompson, A.R. Boccaccini, 45S5 Bioglass®-derived glass–ceramic scaffolds for bone tissue engineering, Biomaterials, 27 (2006) 2414-2425.
[469] K. Fujikura, N. Karpukhina, T. Kasuga, D.S. Brauer, R.G. Hill, R.V. Law, Influence of strontium substitution on structure and crystallisation of Bioglass[registered sign] 45S5, Journal of Materials Chemistry, 22 (2012) 7395-7402.
[470] N. Kanchanarat, C.A. Miller, P.V. Hatton, P.F. James, I.M. Reaney, Early Stages of Crystallization in Canasite-Based Glass Ceramics, Journal of the American Ceramic Society, 88 (2005) 3198-3204.
[471] Y. Jiang, B. Jiang, X. Yuan, C. Wang, J. Fan, Q. Yang, P. Zhang, S. Chen, G. Zhang, X. Mao, L. Zhang, Preparation and luminescence of Ce: YAG transparent glass ceramics by liquid-phase sintering, Materials Letters, 195 (2017) 120-122.
[472] E.A. Aguilar-Reyes, C.A. León-Patiño, B. Jacinto-Diaz, L.-P. Lefebvre, Structural Characterization and Mechanical Evaluation of Bioactive Glass 45S5 Foams Obtained by a Powder Technology Approach, Journal of the American Ceramic Society, 95 (2012) 3776-3780.
[473] H. Pirayesh, J.A. Nychka, Sol–Gel Synthesis of Bioactive Glass-Ceramic 45S5 and its in vitro Dissolution and Mineralization Behavior, Journal of the American Ceramic Society, 96 (2013) 1643-1650.
[474] L. Lefebvre, L. Gremillard, J. Chevalier, R. Zenati, D. Bernache-Assolant, Sintering behaviour of 45S5 bioactive glass, Acta Biomaterialia, 4 (2008) 1894-1903.
[475] C.A. Miller, I.M. Reaney, P.V. Hatton, P.F. James, Crystallization of Canasite/Frankamenite-Based Glass-Ceramics, Chemistry of Materials, 16 (2004) 5736-5743.
[476] S. Pollington, R. van Noort, Manufacture, characterisation and properties of novel fluorcanasite glass–ceramics, Journal of Dentistry, 40 (2012) 1006-1017.
[477] C. Vitale-Brovarone, M. Miola, C. Balagna, E. Verné, 3D-glass–ceramic scaffolds with antibacterial properties for bone grafting, Chemical Engineering Journal, 137 (2008) 129-136.
[478] D. Bellucci, L. Desogus, S. Montinaro, R. Orrù, G. Cao, V. Cannillo, Innovative hydroxyapatite/bioactive glass composites processed by spark plasma sintering for bone tissue repair, Journal of the European Ceramic Society, 37 (2017) 1723-1733.
[479] J.D. Santos, J.C. Knowles, R.L. Reis, F.J. Monteiro, G.W. Hastings, Microstructural characterization of glass-reinforced hydroxyapatite composites, Biomaterials, 15 (1994) 5-10.
[480] Y. Bao, A.M.R. Senos, M. Almeida, L.J. Gauckler, Rheological behavior of aqueous suspensions of hydroxyapatite (HAP), J Mater Sci: Mater Med, 13 (2002) 639-643.
[481] Z. Sadeghian, J.G. Heinrich, F. Moztarzadeh, Preparation of highly concentrated aqueous hydroxyapatite suspensions for slip casting, JOURNAL OF MATERIALS SCIENCE, 40 (2005) 4619-4623.
[482] H. Demirkiran, A. Mohandas, M. Dohi, A. Fuentes, K. Nguyen, P. Aswath, Bioactivity and mineralization of hydroxyapatite with bioglass as sintering aid and bioceramics with Na3Ca6(PO4)5 and Ca5(PO4)2SiO4 in a silicate matrix, Materials Science and Engineering: C, 30 (2010) 263-272.

[483] L.-L. Wang, X.-F. Wang, X. Ding, H.-T. Jiang, Preparation of HA-Bioglass-Al2O3 Biological Composite, Materials and Manufacturing Processes, 28 (2013) 980-983.
[484] L.M. Atayde, P.P. Cortez, A. Afonso, M. Santos, A.C. Maurício, J.D. Santos, Morphology effect of bioglass-reinforced hydroxyapatite (Bonelike®) on osteoregeneration, Journal of Biomedical Materials Research Part B: Applied Biomaterials, 103 (2015) 292-304.
[485] C.-K. Katarzyna, K. Justyna, Ł. Maria, N. Łukasz, M. Wojciech, M.O. Anna, Gel-derived bioglass as a compound of hydroxyapatite composites, Biomedical Materials, 4 (2009) 055007.
[486] M.M. Sebdani, M.H. Fathi, Fabrication and Characterization of Hydroxyapatite–Forsterite–Bioactive Glass Composite Nanopowder for Biomedical Applications, International Journal of Applied Ceramic Technology, 8 (2011) 553-559.
[487] O.P. Filho, G.P. La Torre, L.L. Hench, Effect of crystallization on apatite-layer formation of bioactive glass 45S5, Journal of Biomedical Materials Research, 30 (1996) 509-514.
[488] E.-J. Lee, H.-E. Kim, H.-W. Kim, Production of Hydroxyapatite/Bioactive Glass Biomedical Composites by the Hot-Pressing Technique, Journal of the American Ceramic Society, 89 (2006) 3593-3596.
[489] I.R. Gibson, S.M. Best, W. Bonfield, Effect of Silicon Substitution on the Sintering and Microstructure of Hydroxyapatite, Journal of the American Ceramic Society, 85 (2002) 2771-2777.
[490] H.-S. Ryu, J.K. Lee, H. Kim, K.S. Hong, New type of bioactive materials: Hydroxyapatite/α-wollastonite composites, Journal of Materials Research, 20 (2011) 1154-1163.
[491] D. Bellucci, A. Sola, M. Gazzarri, F. Chiellini, V. Cannillo, A new hydroxyapatite-based biocomposite for bone replacement, Materials Science and Engineering: C, 33 (2013) 1091-1101.
[492] D.C. Tancred, A.J. Carr, B.A.O. McCormack, The sintering and mechanical behavior of hydroxyapatite with bioglass additions, J Mater Sci: Mater Med, 12 (2001) 81-93.
[493] H.H. Beheri, K.R. Mohamed, G.T. El-Bassyouni, Mechanical and microstructure of reinforced hydroxyapatite/calcium silicate nano-composites materials, Materials & Design, 44 (2013) 461-468.
[494] L. Desogus, A. Cuccu, S. Montinaro, R. Orrù, G. Cao, D. Bellucci, A. Sola, V. Cannillo, Classical Bioglass® and innovative CaO-rich bioglass powders processed by Spark Plasma Sintering: A comparative study, Journal of the European Ceramic Society, 35 (2015) 4277-4285.
[495] G. Goller, H. Demirkıran, F.N. Oktar, E. Demirkesen, Processing and characterization of bioglass reinforced hydroxyapatite composites, Ceramics International, 29 (2003) 721-724.
[496] S. Kapoor, Batra, U., Preparation and Bioactivity Evaluation of Bone like Hydroxyapatite - Bioglass Composite, Conference Preceedings, (2012).
[497] T.W. Kim, S.C. Ryu, B.K. Kim, S.Y. Yoon, H.C. Park, Porous hydroxyapatite scaffolds containing calcium phosphate glass-ceramics processed using a freeze/gel-casting technique, Metals and Materials International, 20 (2014) 135-140.
[498] M.H.P.d. Silva, A.F. Lemos, J.M.d.F. Ferreira, J.D. Santos, Mechanical characterisation of porous glass reinforced hydroxyapatite ceramics: Bonelike®, Materials Research, 6 (2003) 321-325.

[499] C. Shuai, J. Zhou, P. Wu, C. Gao, P. Feng, T. Xiao, Y. Deng, S. Peng, Enhanced Stability of Calcium Sulfate Scaffolds with 45S5 Bioglass for Bone Repair, Materials, 8 (2015) 5398.
[500] P. Feng, Y. Deng, S. Duan, C. Gao, C. Shuai, S. Peng, Liquid Phase Sintered Ceramic Bone Scaffolds by Combined Laser and Furnace, International Journal of Molecular Sciences, 15 (2014) 14574-14590.
[501] S. Xu, K. Lin, Z. Wang, J. Chang, L. Wang, J. Lu, C. Ning, Reconstruction of calvarial defect of rabbits using porous calcium silicate bioactive ceramics, Biomaterials, 29 (2008) 2588-2596.
[502] M. Gutierres, M.A. Lopes, N. Sooraj Hussain, A.F. Lemos, J.M.F. Ferreira, A. Afonso, A.T. Cabral, L. Almeida, J.D. Santos, Bone ingrowth in macroporous Bonelike® for orthopaedic applications, Acta Biomaterialia, 4 (2008) 370-377.